

UNIVERSITÉ DE NANTES
FACULTÉ DES SCIENCES ET TECHNIQUES

ÉCOLE DOCTORALE
3MPL: Matière, Molécules, Matériaux en Pays de la Loire

Année: 2010

N° attribué par la bibliothèque:

*Études du charme ouvert dans l'expérience STAR
auprès du collisionneur RHIC
dans les collisions p+p et A+A à $\sqrt{s_{\text{NN}}} = 200 \text{ GeV}$*

THÈSE DE DOCTORAT
Discipline: Physique Nucléaire
Spécialité: Physique des Ions Lourds

Présentée et soutenue publiquement par

Artemios GEROMITSOS

le 12 avril 2010, devant le jury ci-dessous:

| | | | |
|---------------------|----------|----------|---|
| Président: | Ginés | MARTINEZ | Chercheur, CNRS/IN2P3 |
| Rapporteurs: | Spyridon | MARGETIS | Professeur, Université de l'État à Kent |
| | Phillipe | CROCHET | Chercheur, CNRS/IN2P3 |
| Examinateurs: | James | DUNLOP | Chercheur, BNL |
| | André | MISCHKE | Professeur, Université d'Utrecht |
| Directeur de thèse: | Sonia | KABANA | Professeur, Université de Nantes |

UNIVERSITY OF NANTES
FACULTY OF SCIENCE AND TECHNOLOGY

DOCTORAL SCHOOL
3MPL: Matière, Molécules, Matériaux en Pays de la Loire

Year: 2010

Library index:



*Open charm measurements in the STAR
experiment at RHIC
in p+p and A+A collisions at $\sqrt{s_{\text{NN}}} = 200 \text{ GeV}$*

A thesis submitted
in Candidacy for the Degree
of
Doctor of Philosophy

*Publicly defended by
Artemios GEROMITSOS
on the 12th of April 2010, in front of the committee:*

| | | | |
|-----------------|-----------|----------|---|
| President: | Ginés | MARTINEZ | Researcher, CNRS/IN2P3 |
| Referees: | Spyridon | MARGETIS | Professor, Kent State University |
| | Phillippe | CROCHET | Researcher, CNRS/IN2P3 |
| Examinators: | James | DUNLOP | Research Scientist, BNL |
| | André | MISCHKE | Assistant Professor, Utrecht University |
| Thesis Advisor: | Sonia | KABANA | Professor, University of Nantes |

UNIVERSITÉ DE NANTES



*Études du charme ouvert dans l'expérience STAR
auprès du collisionneur RHIC
dans les collisions p+p et A+A à $\sqrt{s_{\text{NN}}} = 200 \text{ GeV}$*

*Open charm measurements in the STAR
experiment at RHIC
in p+p and A+A collisions at $\sqrt{s_{\text{NN}}} = 200 \text{ GeV}$*

Artemios GEROMITSOS

SUBATECH, Nantes, France, 2010

Στη μνήμη της Βασιλικής

Contents

| | |
|--|--------------|
| Contents | ix |
| List of Tables | xvii |
| List of Figures | xix |
| Acknowledgments | xxv |
| Abstract | xxvii |
| Outline | xxix |
| 1 Theoretical Introduction | 1 |
| 1.1 Quantum Chromodynamics | 1 |
| 1.2 The QCD Lagrangian | 2 |
| 1.2.1 The Color Factors | 3 |
| 1.3 The Running Coupling Constant | 3 |
| 1.4 The Asymptotic Freedom | 4 |
| 1.5 The Deconfinement of Quarks | 6 |
| 1.6 The QCD Phase Diagram | 6 |
| 1.7 The Physics of the Relativistic Heavy Ion Collisions | 7 |
| 1.8 The Quark Gluon Plasma | 9 |
| 1.8.1 The Jet Quenching | 10 |
| 1.8.2 The Enhancement of Strange Particle Production | 10 |
| 1.8.3 The Suppression of J/ψ | 10 |
| 1.8.4 Photons | 11 |
| 1.8.5 Di-leptons | 12 |
| 1.8.6 The Restoration of Chiral Symmetry | 13 |
| 1.9 The Nuclear Modification Factor | 13 |

| | | |
|----------|--|-----------|
| 1.10 | The Glauber Model | 13 |
| 1.11 | The Experimental Quantities | 15 |
| 1.11.1 | Rapidity | 15 |
| 1.11.2 | Pseudorapidity | 15 |
| 1.11.3 | The Transverse Momentum, Energy and Mass | 16 |
| 1.11.4 | The Energy Density | 16 |
| 1.11.5 | Luminosity | 17 |
| 1.12 | The Physics of Charm | 17 |
| 1.13 | The Azimuthal Angular Correlation Method | 19 |
| 2 | Experimental Aspects | 23 |
| 2.1 | The Relativistic Heavy Ion Collider | 23 |
| 2.2 | The RHIC Experimental Areas | 25 |
| 2.2.1 | PHOBOS | 25 |
| 2.2.2 | BRAHMS | 27 |
| 2.2.3 | PHENIX | 28 |
| 2.3 | STAR Overview | 29 |
| 2.3.1 | The Trigger System | 30 |
| 2.3.2 | The Trigger Levels | 30 |
| 2.3.3 | The Zero Degree Calorimeter | 31 |
| 2.3.4 | The Beam Beam Counters | 32 |
| 2.3.5 | The Central Trigger Barrel | 33 |
| 2.4 | The Physics of Semiconductors | 33 |
| 2.5 | The Semiconductor Doping | 34 |
| 2.5.1 | The n-doping | 35 |
| 2.5.2 | The p-doping | 35 |
| 2.6 | The Inversed PN Junction | 36 |
| 2.7 | The Semiconductors in Particle Detectors | 37 |
| 2.8 | The STAR Inner Silicon Detectors | 37 |
| 2.9 | The Silicon Vertex Tracker | 38 |
| 2.10 | The Silicon Strip Detector | 39 |
| 2.10.1 | The SSD Module | 41 |
| 2.11 | Energy Loss by Ionization | 42 |
| 2.12 | The Time Projection Chamber | 43 |
| 2.12.1 | The TPC Cluster Reconstruction | 44 |
| 2.12.2 | The TPC Laser System | 46 |
| 2.13 | The Forward TPC Modules | 47 |
| 2.14 | The STAR Calorimetry | 48 |
| 2.15 | The Endcap Electromagnetic Calorimeter | 48 |
| 2.15.1 | The Endcap Pre Shower Detector | 49 |
| 2.16 | The Barrel Electromagnetic Calorimeter | 49 |

| | | |
|----------|---|-----------|
| 2.16.1 | The Barrel Pre Shower Detector | 50 |
| 2.16.2 | The Barrel Shower Maximum Detector | 51 |
| 2.17 | The Forward Meson Spectrometer | 52 |
| 2.18 | The Forward GEM Tracker | 53 |
| 2.19 | The Time of Flight Detector | 54 |
| 2.20 | The Muon Telescope Detector | 56 |
| 2.21 | The Pseudo-Vertex Position Detectors | 57 |
| 2.22 | The Heavy Flavor Tracker | 57 |
| 2.23 | The DAQ1000 | 58 |
| 2.24 | The PPV and the MinuitVF Method | 59 |
| 3 | Data Analysis | 61 |
| 3.1 | Introduction | 61 |
| 3.2 | The Event Selection | 62 |
| 3.2.1 | Minimum Bias Triggered Events | 62 |
| 3.2.2 | High Tower Triggered Events | 62 |
| 3.2.3 | The Primary z -vertex Selection | 63 |
| 3.2.4 | The Charged Particle Event Multiplicity | 63 |
| 3.2.5 | Trigger Event Selection | 64 |
| 3.3 | The Track Quality Assurance Selection | 64 |
| 3.4 | The Role of the BEMC | 65 |
| 3.5 | The Electron Identification | 66 |
| 3.5.1 | The Role of the SMD | 68 |
| 3.5.2 | The dE/dx for the Electron Candidates | 69 |
| 3.5.3 | The Ratio $p_{\text{TPC}}/E_{\text{TOWER}}$ | 70 |
| 3.5.4 | The Distance Between the Extrapolated Track and the Tower | 70 |
| 3.5.5 | The Selection of the Non Photonic Electrons | 71 |
| 3.6 | The PID for the daughter tracks | 72 |
| 3.6.1 | The Charge Correlation between e and h | 72 |
| 3.6.2 | The nSigmaKaon and nSigmaPion Distributions | 72 |
| 3.7 | The Role of the Silicon Detectors | 72 |
| 3.8 | The D^0 Invariant Mass Reconstruction | 74 |
| 3.8.1 | The Ambiguity in the Daughters Mass Attribution | 74 |
| 3.9 | The Background Reconstruction | 75 |
| 3.9.1 | The Same-Sign Background | 75 |
| 3.9.2 | The Rotational Invariant Mass Background | 75 |
| 3.9.3 | The Polynomial Background | 77 |
| 3.10 | The Scaling of the Background | 78 |
| 3.10.1 | The Region above $2.1 \text{ GeV}/c^2$ | 79 |
| 3.10.2 | The Regions $[1.7, 1.8] \cup [1.9, 2.0] [\text{GeV}/c^2]$ | 80 |
| 3.11 | The Significance of a Signal | 81 |

| | |
|--|------------|
| 4 Microvertexing Technique | 83 |
| 4.1 Introduction | 83 |
| 4.2 The Calculation of the Microvertexing Variables | 84 |
| 4.2.1 The Coplanarity of the Decay Daughters | 87 |
| 4.2.2 The Angle θ_{POINTING} | 88 |
| 4.2.3 The Angle θ^* | 88 |
| 4.2.4 The Calculation of DCA_{xy} and DCA_z | 89 |
| 4.2.5 The Products $\text{DCA}_{xy}^1 \cdot \text{DCA}_{xy}^2$ and $d_0^{xy,1} \cdot d_0^{xy,2}$ | 92 |
| 4.3 The Resolution of the DCA in Tracking | 92 |
| 4.3.1 The Multiple Coulomb Scattering | 92 |
| 5 Simulation Study | 97 |
| 5.1 Introduction | 97 |
| 5.2 The STARSIM initial values | 99 |
| 5.3 The Tracking Resolution | 99 |
| 5.4 The Microvertexing Method Application on Monte Carlo | 100 |
| 5.4.1 The Impact of the Silicon Hits on the Microvertexing Variables . | 108 |
| 5.5 The Reconstructed Microvertexing Values Cut Study | 110 |
| 5.5.1 The <i>S/B</i> Study for $\text{SVT+SSD}>0$ hits | 111 |
| 5.5.2 The <i>S/B</i> Study for $\text{SVT+SSD}>1$ hits | 119 |
| 5.5.3 The <i>S/B</i> Study for $\text{SVT+SSD}>2$ hits | 127 |
| 5.5.4 The <i>S/B</i> Study for $\text{SVT+SSD}>3$ hits | 135 |
| 5.5.5 The <i>S/B</i> Study for the Rest of the Microvertexing Variables . | 143 |
| 6 Results in Cu+Cu collisions—year 2005 | 147 |
| 6.1 Introduction | 147 |
| 6.2 Applied Event Cuts | 148 |
| 6.2.1 Primary z -Vertex Cut | 148 |
| 6.2.2 BEMC Energy Threshold | 148 |
| 6.3 Applied Track Cuts | 148 |
| 6.3.1 Track Quality Cuts | 148 |
| 6.3.2 Particle Identification Cuts | 149 |
| 6.4 Charged Event Multiplicity and $\Delta\phi$ Cuts | 149 |
| 6.5 Microvertexing Cuts | 150 |
| 6.6 Invariant Mass Plots | 151 |
| 6.6.1 Results with Cutset c | 151 |
| 6.6.2 Results with Cutset d | 153 |
| 6.6.3 Results with Cutset e | 155 |
| 6.7 Discussion | 156 |

| | |
|--|------------|
| 7 Results in p+p collisions—year 2006 | 159 |
| 7.1 Introduction | 159 |
| 7.2 Applied Event Cuts | 160 |
| 7.2.1 Primary z -Vertex Cut | 160 |
| 7.2.2 BEMC Energy Threshold | 160 |
| 7.3 Applied Track Cuts | 161 |
| 7.3.1 Track Quality Cuts | 161 |
| 7.3.2 Particle Identification Cuts | 161 |
| 7.4 Invariant Mass Plots | 161 |
| 7.4.1 Results with $\Delta\phi = \pi$ | 161 |
| 7.4.2 Results with $\Delta\phi = 0$ | 162 |
| 7.4.3 Results with no $\Delta\phi$ cut | 162 |
| 7.5 Discussion | 163 |
| 8 Results in Au+Au collisions—year 2007 | 165 |
| 8.1 Introduction | 165 |
| 8.2 Applied Event Cuts | 165 |
| 8.2.1 Primary z -Vertex Cut | 165 |
| 8.2.2 Quality of Runs | 166 |
| 8.2.3 BEMC Energy Threshold | 167 |
| 8.3 Applied Track Cuts | 167 |
| 8.3.1 Track Quality Cuts | 167 |
| 8.3.2 Particle Identification Cuts | 167 |
| 8.4 Microvertexing Cuts | 167 |
| 8.5 Invariant Mass Plots | 168 |
| 8.5.1 Results on Minimum Biased Events | 168 |
| 8.5.2 Results on the $Btag$ Triggered Events | 169 |
| 8.6 Discussion | 169 |
| 9 Results in p+p and d+Au collisions—year 2008 | 171 |
| 9.1 Introduction | 171 |
| 9.2 Applied Event Cuts | 172 |
| 9.2.1 Primary z -Vertex Cut | 172 |
| 9.2.2 BEMC Energy Threshold | 172 |
| 9.3 Applied Track Cuts | 172 |
| 9.3.1 Track Quality Cuts | 172 |
| 9.3.2 Particle Identification Cuts | 173 |
| 9.4 Invariant Mass Plots | 173 |
| 9.4.1 Results in p+p | 173 |
| 9.4.2 Results in d+Au | 175 |
| 9.5 Discussion | 176 |

| | |
|---|------------|
| 10 Novel SSD Cluster Finder | 179 |
| 10.1 Introduction | 179 |
| 10.2 Calculation of the Noise | 179 |
| 10.3 Standard Cluster Finder | 181 |
| 10.4 TSpectrum ROOT Class | 181 |
| 10.5 Novel Cluster Finder | 182 |
| 10.6 Comparison Methodology | 183 |
| 10.7 Discussion | 183 |
| 11 Conclusion | 187 |
| 12 Résumé | 191 |
| 12.1 Soupçon de théorie de physique des noyaux | 191 |
| 12.1.1 Le plasma des Quarks et des Gluons | 193 |
| 12.2 Notions expérimentales | 197 |
| 12.2.1 La chambre à projection temporelle | 200 |
| 12.2.2 La calorimétrie du STAR | 204 |
| 12.2.3 La trajectographie interne du STAR | 204 |
| 12.3 Motivation pour l'étude de correlations angulaires | 206 |
| 12.4 Méthode d'analyse des données | 207 |
| 12.4.1 Selection des événements | 208 |
| 12.4.2 Identification des hadrons | 208 |
| 12.4.3 Identification des électrons | 209 |
| 12.4.4 La reconstruction de la masse invariante du D^0 | 210 |
| 12.5 La méthode du microvertexing | 210 |
| 12.5.1 Étude de Simulation | 211 |
| 12.6 Résultats | 213 |
| 12.7 Nouvelle méthode de collecte des amas de charge | 215 |
| 12.8 Conclusion | 216 |
| Appendices | |
| A Relativistic Calculation | 219 |
| A.1 Rapidity Relation Between Two Reference Frames | 219 |
| A.2 When $y \rightarrow \eta$ | 220 |
| A.3 The Gottfried-Jackson Reference Frame | 221 |
| A.4 Fixed Target and Collider Experiment Available \sqrt{s} | 222 |
| A.4.1 Fixed Target | 222 |
| A.4.2 Collider | 223 |

| | |
|---|------------|
| B Kinematics | 225 |
| B.1 Isotropic Decay | 225 |
| B.2 Sagitta | 226 |
| C Statistics | 229 |
| C.1 The Uniform Distribution | 229 |
| D Helix | 231 |
| D.1 Helix Parameterization | 231 |
| D.2 Calculation of the Particle Momentum | 233 |
| D.3 Distance Measurement Between a Point and a Helix | 233 |
| D.4 Distance of Closest Approach Between Two Helices | 235 |
| D.4.1 In the Transverse Plane | 235 |
| D.4.2 In 3 Dimensions | 236 |
| D.5 Intersection with a Cylinder | 236 |
| D.6 Intersection with a Plane | 237 |
| D.7 Limitations | 238 |
| D.8 The Case of the Absence of the Magnetic Field | 238 |
| E Primary and Global tracks | 239 |
| E.1 Track Fitting | 239 |
| F SSD p-and n-sides | 241 |
| F.1 Introduction | 241 |
| F.2 Signal and Noise vs. Strips for the Selected Wafers | 241 |
| F.3 Noise Distribution for the Selected Wafers | 243 |
| Index | 245 |
| Glossary | 249 |
| Bibliography | 253 |

List of Tables

| | | |
|------|---|-----|
| 1.1 | Quark and lepton species along with the force mediators | 5 |
| 1.2 | $e-K$ LS and ULS pairs vs. $\Delta\phi$ cases for C and B contribution | 21 |
| 2.1 | RHIC runs for the years 2000–2009 | 26 |
| 2.2 | SSD characteristics and operational nominal values | 40 |
| 3.1 | Primary z -vertex Cut for various datasets | 63 |
| 3.2 | Centrality definition values for Cu+Cu and Au+Au at $\sqrt{s_{\text{NN}}} = 200 \text{ GeV}$ | 65 |
| 3.3 | BEMC Tower energy thresholds for various datasets | 67 |
| 4.1 | Values of σDCA_{xy} , σDCA_z , at $p = 1 \text{ GeV}/c$ and SVT+SSD cases | 95 |
| 5.1 | SIMU values of σDCA_{xy} , σDCA_z , at $p = 1 \text{ GeV}/c$, for SVT+SSD cases | 101 |
| 5.2 | Mean values of the microvertexing variables for various SVT+SSD cases | 108 |
| 5.3 | S/B variation in the range 0–1 (cm) for $\text{SVT+SSD}>0$ hits | 113 |
| 5.4 | S/B variation in the range 0–0.09 (cm) for $\text{SVT+SSD}>0$ hits | 117 |
| 5.5 | S/B variation in the range 0–1 (cm) for $\text{SVT+SSD}>1$ hits | 121 |
| 5.6 | S/B variation in the range 0–0.09 (cm) for $\text{SVT+SSD}>1$ hits | 125 |
| 5.7 | S/B variation in the range 0–1 (cm) for $\text{SVT+SSD}>2$ hits | 129 |
| 5.8 | S/B variation in the range 0–0.09 (cm) for $\text{SVT+SSD}>2$ hits | 133 |
| 5.9 | S/B variation in the range 0–1 (cm) for $\text{SVT+SSD}>3$ hits | 137 |
| 5.10 | S/B variation in the range 0–0.09 (cm) for $\text{SVT+SSD}>3$ hits | 141 |
| 5.11 | S/B variation of $\cos\theta^*$, $\cos\theta_{\text{POINTING}}$ and ϕ_2 for $\text{SVT+SSD}>0$ hits | 145 |
| 6.1 | Cu+Cu 2005 D^0 invariant mass results for various $\Delta\phi$ cases | 158 |
| 7.1 | $p+p$ 2006 D^0 invariant mass results for various $\Delta\phi$ cases | 163 |
| 8.1 | Au+Au 2007 D^0 invariant mass results for various $\Delta\phi$ cases and triggers | 170 |

| | |
|---|-----|
| 9.1 d+Au and p+p 2008 D^0 invariant mass results for various $\Delta\phi$ cases . . . | 177 |
| A.1 AGS, SPS, RHIC and LHC Characteristics | 224 |
| B.1 Sagitta s , radius r , transverse momentum p_T and track length l | 227 |

List of Figures

| | | |
|------|---|----|
| 1.1 | Diagram of 3 and 4 interacting gluons | 2 |
| 1.2 | Running coupling constant as a function of Q | 4 |
| 1.3 | Phase diagram of the nuclear matter: T vs μ_B | 6 |
| 1.4 | Lattice QCD calculation for the energy density and pressure | 7 |
| 1.5 | Space time evolution of Quark Gluon Plasma | 8 |
| 1.6 | STAR result on Jet Quenching | 9 |
| 1.7 | LQCD calculation for two dynamical quark flavors | 12 |
| 1.8 | Cartoon depicting a peripheral and a central collision | 14 |
| 1.9 | R_{AA} for non-photonic electrons | 18 |
| 1.10 | Schematic decay of a $b\bar{b}$ and of a $c\bar{c}$ pair | 19 |
| 1.11 | Leading order PYTHIA e - D^0 azimuthal correlation for LS and ULS e - K . | 20 |
| 2.1 | Overview of RHIC facilities | 24 |
| 2.2 | Geometrical acceptance of PHOBOS Silicon Detectors and overview . . | 27 |
| 2.3 | Overview of BRAHMS Experiment | 27 |
| 2.4 | Beam view and side view of PHENIX Experiment | 28 |
| 2.5 | Overview of STAR Experiment | 29 |
| 2.6 | Overview of STAR Trigger System | 30 |
| 2.7 | STAR Zero Degree Calorimeter | 31 |
| 2.8 | STAR Beam Beam Counters | 32 |
| 2.9 | STAR Central Trigger Barrel and module | 33 |
| 2.10 | Semiconductor energy bands | 34 |
| 2.11 | Doping in semiconductors | 35 |
| 2.12 | PN junction in forward and inverted bias | 36 |
| 2.13 | Passage of a charged particle through the SSD module | 37 |
| 2.14 | GEANT STAR Silicon Strip Detectors: SVT, SSD | 38 |
| 2.15 | STAR Silicon Vertex Tracker | 39 |
| 2.16 | Cartoon depicting the SSD ladder | 40 |

| | | |
|------|--|----|
| 2.17 | Sketch of the SSD module and stereoscopic view of the strips | 41 |
| 2.18 | Beam view of the TPC Endcap and overall view of the detector | 43 |
| 2.19 | Energy loss of particles in STAR TPC | 45 |
| 2.20 | Cartoon depicting a Pile-Up Event | 46 |
| 2.21 | STAR Forward Time Projection Chambers | 47 |
| 2.22 | STAR Endcap Electromagnetic Calorimeter | 48 |
| 2.23 | STAR Barrel Electromagnetic Calorimeter | 50 |
| 2.24 | Detail of the BEMC towers module | 51 |
| 2.25 | STAR Shower Maximum Detector | 51 |
| 2.26 | STAR Forward Meson Spectrometer | 53 |
| 2.27 | STAR Front Gem Tracker simulated in STARSIM | 54 |
| 2.28 | STAR Time of Flight module (MRPC) and Muon Telescope | 55 |
| 2.29 | STAR Vertex Position Detector | 57 |
| 2.30 | Sketch of STAR Heavy Flavor Tracker | 58 |
| 3.1 | Feynman diagram of $D^0 \rightarrow K^-\pi^+$ and SU(4) mesons 16-plet | 62 |
| 3.2 | z vertex distribution for various datasets at $\sqrt{s} = 200$ GeV | 63 |
| 3.3 | Multiplicity distributions for various datasets at $\sqrt{s} = 200$ GeV | 64 |
| 3.4 | TPC possible hits: nHitsFit vs nHitsFit/nHitsPoss | 66 |
| 3.5 | BEMC $\eta\phi$ acceptance for the run V and run VII | 66 |
| 3.6 | SMD Strips for hadron and electron showers | 68 |
| 3.7 | $\frac{dE}{dx}$ vs rigidity for all tracks and for the electron cut | 69 |
| 3.8 | $\frac{p}{E_{\text{TOWER}}}$ distributions for hadrons and electrons | 70 |
| 3.9 | γ -ray STAR tomography and invariant mass of $e^\pm e^\pm/e^\pm e^\mp$ | 71 |
| 3.10 | nSigmaPion for the range $3.75 < p_T < 4.0$ GeV/c | 73 |
| 3.11 | 2D plot of SVT, SSD hits for two different datasets: Cu+Cu, Au+Au . | 73 |
| 3.12 | Samesign invariant mass for $K^-\pi^-$, $K^+\pi^+$ and $\sqrt{K^-\pi^- \otimes K^+\pi^+}$. . | 76 |
| 3.13 | Cartoon of the rotation of a kaon's momentum by θ_{rot} and yields | 76 |
| 3.14 | Azimuthal acceptance for various SVT+SSD cases | 77 |
| 3.15 | Rotational and samesign invariant mass yield for SVT+SSD cases | 78 |
| 3.16 | D^0 Invariant Mass along with the polynomial fit $n=1\text{--}7$ degrees | 78 |
| 3.17 | Invariant Mass yield of $K^0(892) \rightarrow K\pi$ and $D^0 \rightarrow K\pi$ | 79 |
| 3.18 | Scale for (M_A, ∞) and $(M_A, M_B) \cup (M_C, M_D)$ | 80 |
| 3.19 | Invariant mass yields: $K^-\pi^+/K^+\pi^-$, scaled and unscaled backgrounds | 81 |
| 4.1 | Cartoon depicting the D^0 decay and the microvertexing variables | 85 |
| 4.2 | Cartoon depicting the angle between the planes of the decay particles . | 87 |
| 4.3 | True and a false $D^0 \rightarrow K^-\pi^+$ along with the daughter planes | 88 |
| 4.4 | Sketch of the θ_{POINTING} and θ^* | 89 |
| 4.5 | Distributions of DCA, σ DCA (xy and z) for the Cu+Cu (2005) run . | 90 |
| 4.6 | Distributions of DCA, σ DCA (xy and z) for the Au+Au (2007) run . | 91 |

| | | |
|------|---|-----|
| 4.7 | Tracking resolution in r - ϕ and z vs p^{-1} for Cu+Cu and Au+Au data | 94 |
| 5.1 | Primary z -vertex component for the simulated event | 98 |
| 5.2 | η - ϕ of daughter particles and DCA_{xy} vs. DCA_z for simulation of D^0 | 98 |
| 5.3 | p_T distribution and decay length distribution of a pure D^0 , STARSIM | 99 |
| 5.4 | STARSIM η distribution of a pure D^0 signal | 99 |
| 5.5 | Simulated $K^- \pi^+$ along with fit invariant mass yields | 100 |
| 5.6 | Tracking resolution in r - ϕ and z as a function of p^{-1} from simulation | 100 |
| 5.7 | Distribution of RECO – GEANT values for the 1^{ary} vertex | 102 |
| 5.8 | RECO vs. GEANT 2D plot for the primary vertex reconstruction | 103 |
| 5.9 | Distribution of RECO – GEANT values for the 2^{ary} vertex | 104 |
| 5.10 | RECO vs. GEANT 2D plot for the secondary vertex reconstruction | 105 |
| 5.11 | Distribution of RECO – GEANT values for the decay length | 106 |
| 5.12 | RECO vs. GEANT 2D values for the decay length | 107 |
| 5.13 | Microvertexing variables for various SVT+SSD cases | 109 |
| 5.14 | DCA between tracks S/B variation study for $SVT+SSD > 0$, 0–1 (cm) | 111 |
| 5.15 | D^0 decay length S/B variation study for $SVT+SSD > 0$, 0–1 (cm) | 112 |
| 5.16 | D^0 DCA to PV S/B variation study for $SVT+SSD > 0$, 0–1 (cm) | 114 |
| 5.17 | DCA between tracks S/B variation study for $SVT+SSD > 0$, 0–0.1 (cm) | 115 |
| 5.18 | D^0 decay length S/B variation study for $SVT+SSD > 0$, 0–0.1 (cm) | 116 |
| 5.19 | D^0 DCA to PV S/B variation study for $SVT+SSD > 0$, 0–0.1 (cm) | 118 |
| 5.20 | DCA between tracks S/B variation study for $SVT+SSD > 1$, 0–1 (cm) | 119 |
| 5.21 | D^0 decay length S/B variation study for $SVT+SSD > 1$, 0–1 (cm) | 120 |
| 5.22 | D^0 DCA to PV S/B variation study for $SVT+SSD > 1$, 0–1 (cm) | 122 |
| 5.23 | DCA between tracks S/B variation study for $SVT+SSD > 1$, 0–0.1 (cm) | 123 |
| 5.24 | D^0 decay length S/B variation study for $SVT+SSD > 1$, 0–0.1 (cm) | 124 |
| 5.25 | D^0 DCA to PV S/B variation study for $SVT+SSD > 1$, 0–0.1 (cm) | 126 |
| 5.26 | DCA between tracks S/B variation study for $SVT+SSD > 2$, 0–1 (cm) | 127 |
| 5.27 | D^0 decay length S/B variation study for $SVT+SSD > 2$, 0–1 (cm) | 128 |
| 5.28 | D^0 DCA to PV S/B variation study for $SVT+SSD > 2$, 0–1 cm | 130 |
| 5.29 | DCA between tracks S/B variation study for $SVT+SSD > 2$, 0–0.1 (cm) | 131 |
| 5.30 | D^0 decay length S/B variation study for $SVT+SSD > 2$, 0–0.1 (cm) | 132 |
| 5.31 | D^0 DCA to PV S/B variation study for $SVT+SSD > 2$, 0–0.1 (cm) | 134 |
| 5.32 | DCA between tracks S/B variation study for $SVT+SSD > 3$, 0–1 (cm) | 135 |
| 5.33 | D^0 decay length S/B variation study for $SVT+SSD > 3$, 0–1 (cm) | 136 |
| 5.34 | D^0 DCA to PV S/B variation study for $SVT+SSD > 3$, 0–1 (cm) | 138 |
| 5.35 | DCA between tracks S/B variation study for $SVT+SSD > 3$, 0–0.1 (cm) | 139 |
| 5.36 | D^0 decay length S/B variation study for $SVT+SSD > 3$, 0–0.1 (cm) | 140 |
| 5.37 | D^0 DCA to PV S/B variation study for $SVT+SSD > 3$, 0–0.1 (cm) | 142 |
| 5.38 | MC and data values for the angle between daughter planes, $\cos \theta_{\text{POINTING}}$ | 143 |
| 5.39 | Simulation and data for the $DCA_{xy}^K \cdot DCA_{xy}^\pi$ and $d_0^K \cdot d_0^\pi$ | 144 |

| | | |
|------|---|-----|
| 5.40 | Simulation and data for $\cos \theta_K^*$ and $\cos \theta_\pi^*$ | 144 |
| 6.1 | Primary z -vertex distribution for all events, Cu+Cu <i>High Tower</i> | 148 |
| 6.2 | Distribution of ULS and LS pairs for the Cu+Cu dataset | 149 |
| 6.3 | D^0/\bar{D}^0 Invariant Mass yields with $\Delta\phi = 0$, Cutset c | 152 |
| 6.4 | D^0/\bar{D}^0 Invariant Mass yields with $\Delta\phi = \pi$, Cutset c | 152 |
| 6.5 | D^0/\bar{D}^0 Invariant Mass yields with no $\Delta\phi$, Cutset c | 153 |
| 6.6 | D^0/\bar{D}^0 Invariant Mass yields with $\Delta\phi = 0$, Cutset d | 153 |
| 6.7 | D^0/\bar{D}^0 Invariant Mass yields with $\Delta\phi = \pi$, Cutset d | 154 |
| 6.8 | D^0/\bar{D}^0 Invariant Mass yields with no $\Delta\phi$, Cutset d | 154 |
| 6.9 | D^0/\bar{D}^0 Invariant Mass yields with $\Delta\phi = 0$, Cutset e | 155 |
| 6.10 | D^0/\bar{D}^0 Invariant Mass yields with $\Delta\phi = \pi$, Cutset e | 155 |
| 6.11 | D^0/\bar{D}^0 Invariant Mass yields with no $\Delta\phi$, Cutset e | 156 |
| 6.12 | D^0/\bar{D}^0 Invariant Mass yields with multiplicity < 74, $\Delta\phi = \pi$, Cutset e . | 157 |
| 7.1 | Primary z -vertex distribution for all events, p+p | 160 |
| 7.2 | D^0/\bar{D}^0 Invariant Mass yields with $\Delta\phi = \pi$ | 162 |
| 7.3 | D^0/\bar{D}^0 Invariant Mass yields with $\Delta\phi = 0$ | 162 |
| 7.4 | D^0/\bar{D}^0 Invariant Mass yields with no $\Delta\phi$ cut | 163 |
| 7.5 | $e-D^0$ $\Delta\phi$ results and $B/(B+D)$ contribution vs. the trigger p_T | 164 |
| 8.1 | Primary z -vertex distribution for all events, Au+Au <i>Btag</i> | 166 |
| 8.2 | Distribution of ULS and LS hadron pairs per event for the Au+Au case | 168 |
| 8.3 | D^0/\bar{D}^0 Invariant Mass yields with Cutset a | 169 |
| 8.4 | D^0/\bar{D}^0 Invariant Mass yields with $\Delta\phi = 180$ and Cutset b | 170 |
| 9.1 | Primary z -vertex distribution for all events in d+Au and p+p run | 172 |
| 9.2 | D^0/\bar{D}^0 Invariant Mass yields with $\Delta\phi = 0$ | 173 |
| 9.3 | D^0/\bar{D}^0 Invariant Mass yields with $\Delta\phi = \pi$ | 174 |
| 9.4 | D^0/\bar{D}^0 Invariant Mass yields with no $\Delta\phi$ cut | 174 |
| 9.5 | D^0/\bar{D}^0 Invariant Mass yields with $\Delta\phi = 0$ | 175 |
| 9.6 | D^0/\bar{D}^0 Invariant Mass yields with $\Delta\phi = \pi$ | 175 |
| 9.7 | D^0/\bar{D}^0 Invariant Mass yields with no $\Delta\phi$ cut | 176 |
| 10.1 | Overall signal and noise of the SSD | 180 |
| 10.2 | TSpectrum selection of peaks in a given spectrum | 182 |
| 10.3 | Clusters Found by SCF and Novel Cluster Finder | 184 |
| 10.4 | Correlation of the number of clusters obtained by both methods and fit | 185 |
| A.1 | Energy at the CMS for fixed target and collider experiment | 223 |
| B.1 | Distribution of the angle θ and $\cos \theta$ for an isotropic decay | 225 |
| B.2 | Cartoon of the sagitta s of a track, the radius r and the track length l . | 226 |

| | | |
|-----|--|-----|
| B.3 | Cartoon of the sagitta vs. the p_T for different track lengths | 227 |
| C.1 | Plot of the constant distribution using random numbers | 230 |
| D.1 | Helix parameterization in xy and sz plane | 232 |
| D.2 | Two intersecting helices in the xy plane | 235 |
| D.3 | Sketch of the intersection of the helix with a plane | 237 |
| F.1 | SSD 3D and 2D raw hits | 241 |
| F.2 | Fired strips for ladder 3, wafers: $\{5, 6, 8, 9 \text{ and } 10\}$, on both sides . . . | 242 |
| F.3 | Noise distribution for ladder 3, per wafer $\{5, 6, 8, 9 \text{ and } 10\}$, sides $p \& n$ | 243 |

Acknowledgments

I would like to begin my *thank you* note by expressing my gratitude to Ginés Martínez, for taking the difficult task to preside at the jury committee for the evaluation of the current work, and for the role of the examinator as well. I am also grateful to Spyridon Margetis and to Phillippe Crochet for having executed the task of the referee. Additionally I would like to thank James Dunlop and André Mischke for examining this work. My gratitude and profound appreciation goes to Sonia Kabana for being the advisor of this thesis and to Barbara Erazmus for accepting me to work in the SUBATECH-STAR group. I am also grateful to Lidia Didenko, Yuri Fisyak, Victor Perevoztchikov and Valeri Fine for the major support on the various STAR software issues (спасибо!). I would like also to thank Yuri Gorbunov for his precious help and advice during the neverending shifts. Jérôme Lauret for helping me to initiate the journey in STAR software (*merci*). The SSD group: Jim Thomas, Howard Matis, Micheal Levine, Jérôme Baudot, Stéphane Bouvier, Vi Nham Tram, Jonathan Bouchet, Gérard Guilloux and Cristophe Renard for introducing me to the Silicon Strip Detector. During my stay at BNL, I would like to thank Wayne Betts for helping me out with the various computer hardware/software issues I quite frequently came across. Levente Hadju, for his great help on SUMS. Lijuan Ruan for her kindness and instructive advice, 謝謝 . Lanny Ray and Gene van Buren for their useful advice and constant help throughout the QA shifts. The Heavy Flavor Group of STAR, and in particular the conveners: Xin Dong, Manuel Calderón de la Barca Sánchez and their successors Jaroslav Bielcik and Gang Wang. Although the short collaboration, I would like to thank Witek for the great help provided in the last few months (dziękuję). A major support and inspiration came from my fellow classmates dating back to ye good olde—UOA—times: Andy, Dimitrios and Giota, as well as Fanis and Angela. My gratitude finally goes to my parents, for their support throughout all these years kept me carrying on. Σας είμαι ευγνώμων.

Je souhaite remercier la direction du SUBATECH, en particulier Monsieur Jacques Martino et Christelle Roy de m'avoir accueilli au sein du laboratoire. Le directeur adjoint Pascal Lautridou pour les conseils sur la rédaction et la série des démarches administratives pour la soutenance. Je suis très reconnaissant à Frédéric Lefevre pour son aide énorme sur les outils informatiques ainsi que pour nos discussions constructives

durant mon séjour au labo. En outre Stéphane Peigne pour répondre à mes questions sur la théorie quantique de champs. J'ai bien apprécié les discussions avec Taklit Sami et Andrei Smilga. Que tous les membres du groupe PLASMA de SUBATECH soient enfin remerciés ici.

A.Γ.
Nantes, October 22, 2010

Abstract

The STAR experiment investigates the formation of the Quark Gluon Plasma via the heavy ion collisions taking place at the Relativistic Heavy Ion Collider (RHIC) situated at Brookhaven National Laboratory (BNL), Upton, NY. The production of charm quark (in $c\bar{c}$ pairs) occurs in the early stages of the heavy ion collisions dominantly via gluon fusion $gg \rightarrow c\bar{c}$. Due to the fact that the yield of charm is affected by the conditions of the early stages of the collision, the measurement of the charm production provides a useful tool for description of the initial stage that took place. One of the most important findings of the experiments at RHIC was the discovery of the anomalous quenching of jets when passing through the hot and dense matter build in nucleus nucleus collisions. Heavy quarks (charm C and beauty B together) measured through non photonic electron yields in heavy ion reactions at $\sqrt{s_{\text{NN}}} = 200 \text{ GeV}$ at RHIC, exhibit a larger suppression than expected from the theoretical considerations. In order to comprehend this puzzle and understand better the flavor dependence of the jet quenching, the separation of charm and beauty contributions as well as the measurement of their quenching is necessary. In the current work we investigate the D^0 yield in various datasets (Cu+Cu, Au+Au, d+Au and p+p) at $\sqrt{s_{\text{NN}}} = 200 \text{ GeV}$. For the Cu+Cu and Au+Au (run VII) for which the silicon strip detector of STAR has been used for data taking, a microvertexing technique was applied in the analysis, allowing the topological reconstruction of the D^0 charmed meson through its secondary vertex reconstruction. The Silicon Strip Detector (SSD) was first deployed in the year 2005 during the Cu+Cu at $\sqrt{s_{\text{NN}}} = 200 \text{ GeV}$ collisions, allowing the enhancement of the tracking capabilities by providing a connection between reconstructed tracks in the TPC and SVT (Silicon Vertex Tracker) points. It was observed that the detector loses a significant percentage of hits of the tracks recorded by the TPC. As a result the overall tracking reconstruction efficiency drops. A novel cluster finder method is proposed as a technical part of this thesis by looking for clusters independently on the p and n sides of the SSD. This study was performed on data taken from run VII. The new developments achieved in this thesis concern the successful application of the microvertexing techniques in the heavy ion environment, the extraction of the D^0 signal in the heavy ion collisions using these techniques through the study of $e-D^0$ correlations in p+p, Cu+Cu and Au+Au collisions.

Keywords: Quark-Gluon Plasma (QGP), Heavy Ion Collisions, Charm Physics, Silicon Strip Detector, STAR experiment, RHIC, BNL

Outline

In Chapter 1, (p. 1), we present a brief introduction to the theory of nuclear interactions, the theoretical predictions for the existence of the Quark Gluon Plasma, and the experimental observables of heavy-ion collisions. An introduction to the Heavy Flavor Physics is also presented, along with the theoretical motivation for the e - D^0 azimuthal correlations. In the latter method explication, it is also described how the experimental disentanglement of the contribution of charm and beauty during heavy ion collisions, is attained.

In Chapter 2, (p. 23) we carry on with a description of the experimental apparatus, namely the relativistic heavy ion collider (RHIC), along with the four experimental areas: PHOBOS, PHENIX, BRAHMS and STAR. The latter will be thoroughly presented and the various subsystems along with the future upgrades will be discussed as well. A short description of the Silicon Strip Detector (SSD) is also given along with its important role in the amelioration of the tracking of STAR.

In Chapter 3, (p. 61) we describe the analysis methodology that is applied on to the various datasets. In particular, the general applicable event cuts as well as the Quality Assurance (QA) cuts applied to the tracks, are also discussed. The D^0 invariant mass reconstruction method is presented, and the various techniques for the background subtraction are also discussed.

In Chapter 4, (p. 83) we describe the microvertexing technique that is applied in the Cu+Cu and Au+Au datasets, exploiting the better tracking capabilities offered by the STAR Silicon Detectors (SVT and SSD).

In Chapter 5, (p. 97) a Monte Carlo study on the microvertexing technique is presented, allowing to perform a test on the code concerning the functionality and QA. In the final sections of the Chapter 5, a comparison is being presented, between data (Cu+Cu at $\sqrt{s_{\text{NN}}} = 200 \text{ GeV}$) and MC having as a goal the optimization of cuts that will be used for the topological reconstruction of the D^0 .

Having taken into account the values of the optimized microvertexing cuts extracted by the analysis discussed in Chapter 4, the results on the Cu+Cu dataset are presented in Chapter 6, (p. 147).

We continue in Chapter 7 (p. 159) by presenting the results in the p+p dataset at $\sqrt{s} = 200 \text{ GeV}$ (run VI). In addition, in Chapter 8 (p. 165) we discuss the results

of Au+Au dataset at $\sqrt{s_{\text{NN}}} = 200 \text{ GeV}$ (run VII), obtained with the $e-D^0$ correlation technique as well as by applying the microvertexing technique.

Finally in Chapter 9 (p. 171) we discuss the results in the p+p and d+Au dataset at $\sqrt{s} = 200 \text{ GeV}$ of the year 2008. Concerning the technical part of the work, in Chapter 10, (p. 179) it is presented a new cluster finder method for the Silicon Strip Detector. It is also discussed the current cluster finder, and a comparison between these two methods is performed. The data used for this study is from Au+Au at $\sqrt{s_{\text{NN}}} = 200 \text{ GeV}$ (run VII). A conclusion of the work is drawn in Chapter 11 (p. 187), summarizing the results and the main aspects of the work.

Theoretical Introduction

The main focus of the current chapter is the theoretical introduction on the nuclear strong force along with the theoretical predictions for the existence of the Quark-Gluon Plasma. Some elements of the observable variables that are used in the experimental nuclear physics are also presented. The last paragraphs of the chapter are dedicated to the description of the charm formation and its important role in the study of the heavy ion collisions. In the conclusion of the chapter, it is also presented the theoretical motivation background for the e–D⁰ azimuthal correlation analysis.

1.1 Quantum Chromodynamics

Quantum Chromodynamics (QCD) is the theory that describes the strong interaction exerted among the elementary constituents of the nuclear matter, the quarks. The force carriers are called *gluons* and the fundamental aspect of this theory is that the mediators can interact among them, resulting in 3 or 4 gluon interaction vertices as can be seen in Figure 1.1. It was the discovery of the Δ^{++} baryon that led to the introduction of the *color* as a quantum number in order for the wave-function of the particle to be anti-symmetric, obeying to the Fermi-Dirac statistics. The specific baryon has a total spin of $J = \frac{3}{2}$ and can be obtained by combining 3 *spin-up* ($J_u = \frac{1}{2}$) *u* quarks. Therefore the total spin of the system hence can be written: $J = \frac{3}{2}$ ($u\uparrow u\uparrow u\uparrow$). Since the wave function was symmetric in space, flavor and spin, the introduction of color, solved this problem, since it was imposed that any permutation in color results in an anti-symmetric wavefunction $u_R\uparrow u_G\uparrow u_B\uparrow$.

A quark (q) can obtain one of the three colors, viz. red, green and blue, (RGB). The antiparticle, denoted by (\bar{q}), can obtain the anti-colors expressed as cyan, magenta and yellow (or *anti-red*, *anti-green* and *anti-blue* $\bar{R}\bar{G}\bar{B}$). Gluons carry always a pair of color and anti-color. The confined states of quarks are called hadrons and are *colorless*,

(white) entities, composed in such a way of quarks and anti-quarks that the overall color contribution is naught.

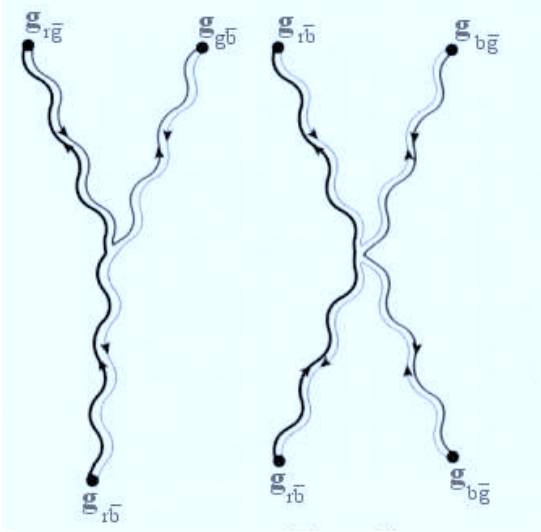


FIG. 1.1: Sketch depicting the interaction of 3 and 4 gluons, showing the exchange (*flow*) of color.

1.2 The QCD Lagrangian

The Lagrangian of the QCD is written:

$$\mathcal{L}_{\text{QCD}} = i \sum_f \bar{q}_f^i \gamma^\mu (D_\mu)_{ij} q_f^j - \sum_f m_f \bar{q}_f^i q_{fi} - \frac{1}{4} G_{\mu\nu}^\alpha G_\alpha^{\mu\nu} \quad (1.1)$$

with the indices i, j referring to the color, f to the quark flavor and μ, ν are the Lorentz indices. Also by q we define the quark spinor field of dimension 12 (color \otimes Dirac). The covariant derivative $(D_\mu)_{ij}$, reflecting the local gauge invariance, is expressed by the term $(D_\mu)_{ij} = \delta_{ij}\partial_\mu - ig_s \sum \frac{\lambda_{ij}^a}{2} A_\mu^a$ where λ_{ij}^a are the Gell-Mann matrices in the SU(3) flavor representation. Finally the interaction between the gluons is described by the term: $G_{\mu\nu}^\alpha = \partial_\mu A_\nu^\alpha - \partial_\nu A_\mu^\alpha + g_s f_{abc} A_\mu^b A_\nu^c$, where A_μ^a refers to the gluon field and f_{abc} are the fully anti-symmetric, structure constants. As mentioned above, for each N quark flavor there exist three corresponding colors. In other words for every quark it is assigned a *triplet* of the SU(3) color group. Unlike SU(N) flavor symmetry, the SU(3) color symmetry is expected to be conserved. On the other hand the gluons come in

$3^2 - 1 = 8$ different colors, or else said in a $SU(3)$ color *octet*:

$$R\bar{G}, R\bar{B}, G\bar{R}, G\bar{B}, B\bar{R}, B\bar{G}, \sqrt{\frac{1}{2}}(R\bar{R} - G\bar{G}), \sqrt{\frac{1}{6}}(R\bar{R} + G\bar{G} - 2B\bar{B})$$

Concerning the color *singlet*

$$\sqrt{\frac{1}{3}}(R\bar{R} + G\bar{G} + B\bar{B})$$

it cannot be the mediator between the color charges, since there is no color than can be carried.

1.2.1 The Color Factors

The coupling of the interaction between two colors via a gluon exchange is $\frac{1}{2}c_1c_2$, with c_1 and c_2 let be the color coefficients in the vertices of the interaction. By convention the quantity expressed in (1.2) is called *color factor*.

$$C_F \equiv \frac{1}{2}|c_1c_2| \quad (1.2)$$

1.3 The Running Coupling Constant

The potential between the two quarks at a distance r can be written in approximation as (1.3).

$$V(r) = -\frac{4\alpha_s}{3r} + kr \quad (1.3)$$

with α_s the strong coupling constant, and $k \sim 1\text{GeV/fm}$. The first term indicates the repulsion and dominates at small distances. The second term indicates the attraction and becomes significant at large distances, not allowing the separation of the quarks at this distance scale, thus talking about quark *confinement*. The running coupling constant a_s depends on the Q^2 , the value of the momentum transfer between partons $Q^2 = -(p_1 + p_2)^2$ and is expressed by (1.4).

$$\alpha_s(Q^2) = \frac{\alpha_s(\mu^2)}{1 + \frac{\alpha_s(\mu^2)}{12\pi}(11n - 2f)\ln\frac{Q^2}{\mu^2}} \quad (1.4)$$

Also let n be the number of colors (3 in the S.M.) and f be the number of flavors (6 in the S.M.), as stated in Table 1.1. The term $\alpha_s(\mu^2)$ refers to the screening and in specific $\alpha(0) = \frac{1}{137}$. We also note that there is no restriction on the value of μ ,

as long as $a_s(\mu^2) < 1$. Evolving all results to the rest energy of the Z^0 boson, the new world average of $\alpha_s(M_Z)$ is determined from measurements which are based on QCD calculations in complete NNLO perturbation theory, yielding the following value $\alpha_s(M_Z) = 0.1183 \pm 0.0027$ [Bethke 03].

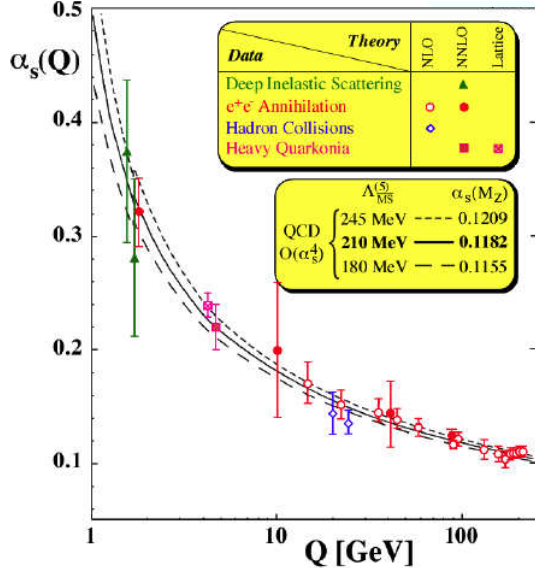


FIG. 1.2: Running coupling constant as a function of Q . Figure taken from [Bethke 03].

1.4 The Asymptotic Freedom

At short distances the strong force becomes weak and this is the feature, responsible for the *asymptotic freedom*. The consequences of the asymptotic freedom are the following:

- i. In large energies the running coupling constant is small, thus justifies the use of perturbation theory and explains the quasi partonic behavior of quarks and gluons in large energy scale; and
- ii. in large distance where the coupling constant is not small $\alpha_s \sim 1$, the perturbation theory ceases to be applicable and the infrared (IR) modes become of crucial importance. Along with the confinement, the spontaneous chiral symmetry breaking is also manifested.

TAB. 1.1: Overview of the three generations of quarks and leptons families, along with the mediators of all forces, except the gravitational. By q_e it is denoted the value of the electric charge of the electron ($q_e = 1.6 \cdot 10^{-19}$ Cb). Values are taken from [Amsler 08].

| PARTICLE FAMILY | SYMBOL | MASS [MeV/c ²] | ELECTRIC CHARGE [q_e] |
|-------------------|-------------------|----------------------------|-----------------------------|
| FIRST GENERATION | | | |
| Quarks | u | 1.5–4.0 | +2/3 |
| | d | 4.0–8.0 | -1/3 |
| Leptons | e^- | 0.511 | -1 |
| | $\bar{\nu}_e$ | $\leq 2.2 \cdot 10^{-6}$ | 0 |
| SECOND GENERATION | | | |
| Quarks | c | 1150–1350 | +2/3 |
| | s | 80–130 | -1/3 |
| Leptons | μ^- | 105.7 | -1 |
| | $\bar{\nu}_\mu$ | ≤ 0.17 | 0 |
| THIRD GENERATION | | | |
| Quarks | t | 170900 ± 1800 | +2/3 |
| | b | 4100–4400 | -1/3 |
| Leptons | τ^- | 1784.1 | -1 |
| | $\bar{\nu}_\tau$ | ≤ 15.5 | 0 |
| FORCE | GAUGE BOSONS | MASS [GeV/c ²] | ELECTRIC CHARGE [q_e] |
| Strong | g (8 gluons) | 0 | 0 |
| Electromagnetic | γ (photon) | 0 | 0 |
| Weak | W^\pm | 80.3980 ± 0.0250 | ± 1 |
| | Z^0 | 91.1876 ± 0.0021 | 0 |

1.5 The Deconfinement of Quarks

The study of the asymptotic freedom, can be attained with high energy collisions. At high density, the quarks and the gluons can be decoupled over a volume, much larger than the nucleonic ($\sim 1\text{fm}^3$).

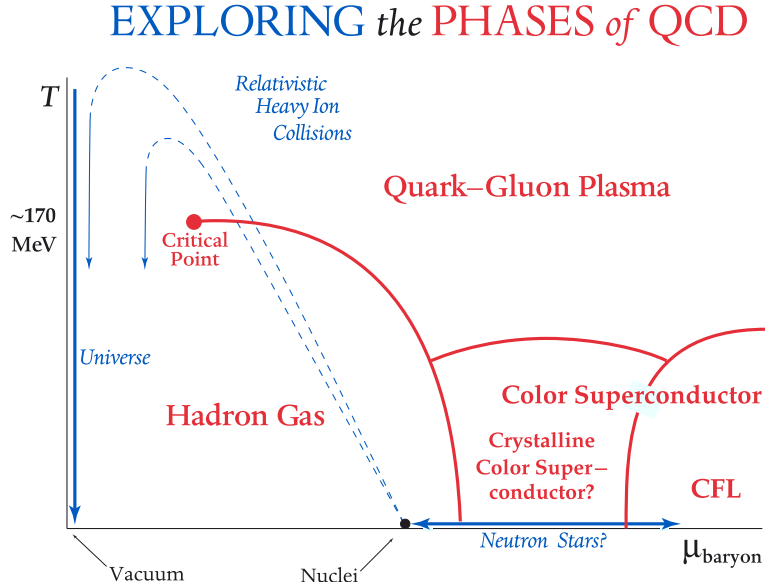


FIG. 1.3: Phase diagram of the nuclear matter. Heavy ion collisions at RHIC are expected to be of low baryon chemical potential (μ_B) and temperature (T) greater than 170 MeV. The hatched region indicates the current expectation for the phase boundary based on lattice QCD calculations at $\mu_B = 0$. Figure taken from [Rajagopal 09].

1.6 The QCD Phase Diagram

The phase diagram of the hadronic and partonic matter in terms of temperature T and baryo-chemical potential μ_B is presented in Figure 1.3. The hatched region indicates the current expectation for the phase boundary based on lattice QCD calculations for $\mu_B = 0$. The high temperature and the low μ_B region is expected to be accessible via heavy ion collisions. Colliders with various energies (LHC, RHIC, SPS, AGS, and SIS) can reach different regions in this phase diagram. The QGP matter that can be created in the laboratory is believed to have existed in the first few micro-seconds after the Big Bang. The expected high temperature and minimum baryonic chemical potential of the early universe when QGP matter was created is shown in the phase diagram. The region near the zero temperature and high μ_B is where the deconfined high-density phase is also predicted to exist (i.e. in the interior of neutron stars).

Numerical calculations of lattice QCD can be performed to check the dependence of the temperature on the energy density of the system. In a quark gluon plasma phase, due to the increase in the number of the degrees of freedom, it is expected that there will be a change in the energy density. Such a dependence of the energy density ϵ , divided by T^4 on $T = T_c$ is presented in Figure 1.4. The number of the degrees of freedom rises steeply for temperatures above the critical value denoted by T_c , corresponding to a transition of the system to a state where the quarks and gluons are deconfined (cf. Section 1.5). Let us add also that the *critical* temperature is predicted to be in the region of 150–190 MeV.

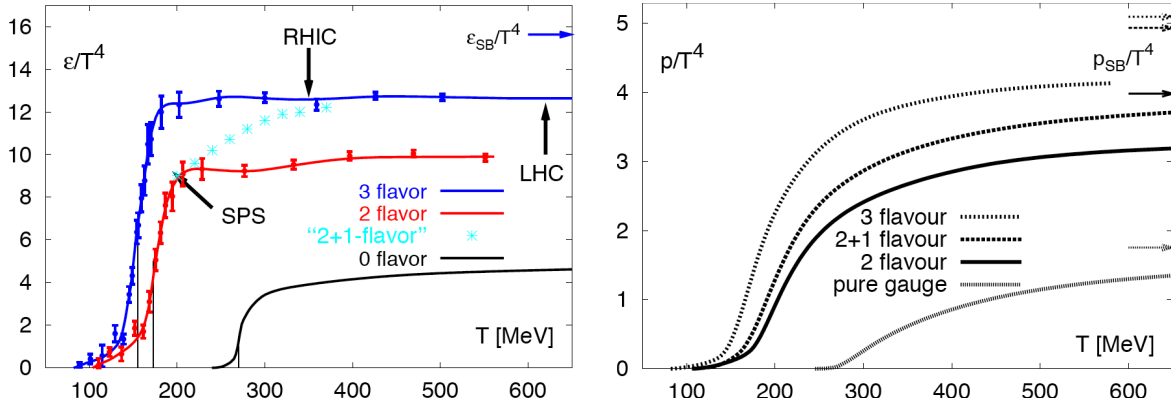


FIG. 1.4: *Left:* The energy density (ϵ) as a function of the temperature (T) scaled by T^4 from lattice QCD calculation. The realistic case is for $N = 2 + 1$ flavors. *Right:* The pressure (p) as a function of temperature (T) scaled by T^4 . Note that the pressure is continuous in the region where there is a sharp change in the energy density. Figure taken from [Gyulassy 05].

1.7 The Physics of the Relativistic Heavy Ion Collisions

According to the Bjorken scenario [Bjorken 82], during a heavy ion collision the following phases occur in a chronological order, as depicted in Figure 1.5. In particular:

- i. Pre-equilibrium state (when formation of the elementary constituents takes place). During this phase, the nucleons pass through each other and parton-parton interactions occur, where a parton is defined as a quark or a gluon. Due to high energy density, the released partons can re-scatter multiple times, losing part of their initial energy in the interaction region. A *fireball* of interacting quarks and gluons expands and the baryon chemical potential (μ_B) vanishes at mid-rapidity $y = 0$,

while the forward and the backwards regions, $y \neq 0$, are rich in baryons corresponding to the remnants of the colliding nuclei. At this stage the scattering of hard partons also occurs;

- ii. Chemical and thermal equilibrium: the nuclear matter reaches equilibrium at the proper time τ_0 (just before the QGP formation) through parton re-scattering in the medium. The energy density obtained in the collisions at RHIC is above the critical value, so when the interacting medium is thermalised, the QGP might be produced;
- iii. The QGP phase, evolving according to the laws of hydrodynamics;
- iv. The mixed phase of QGP and the Hadron Gas (HG); and
- v. the hadronization and freeze-out. In particular, the expanding QGP cools down fast and quickly reaches the transition temperature. It evolves into the phase of hadron gas, finally reaching the state known as *chemical* freeze-out. The resulting hadronic gas continues to expand, cooling down the interaction rate between the hadrons. Then the system evolves to the thermal equilibrium; this state is known as *thermal* freeze-out. After this moment, hadrons are able to move freely.

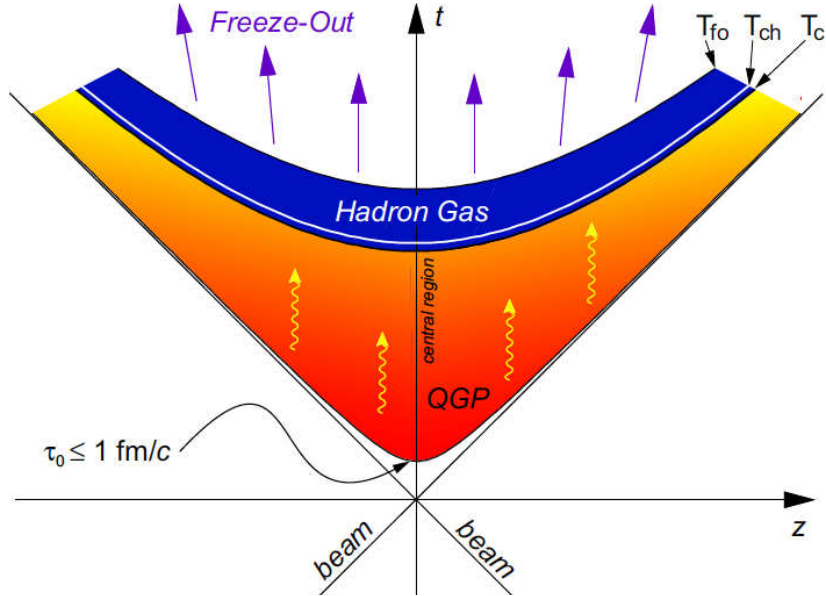


FIG. 1.5: Cartoon depicting the space-time evolution of Quark Gluon Plasma.

1.8 The Quark Gluon Plasma

Historically, the term Quark-Gluon plasma was first proposed by Shuryak [Shuryak 78]. Over the last 20 years many ideas have evolved and a lot of definitions have been presented. We shall restrain to the following one: *QGP can be a (locally) thermally equilibrated state of matter in which quarks and gluons are deconfined from hadrons, so that color degrees of freedom become manifest over nuclear, rather than merely nucleonic, volumes* [Adams 05]. Some theoretical predictions for the existence of QGP are:

- i. Enhancement of strange particle production;
- ii. J/ψ suppression;
- iii. the initial temperature of the medium can be measured from the thermal photons or di-leptons;
- iv. the jet quenching; and
- v. the restoration of the chiral symmetry.

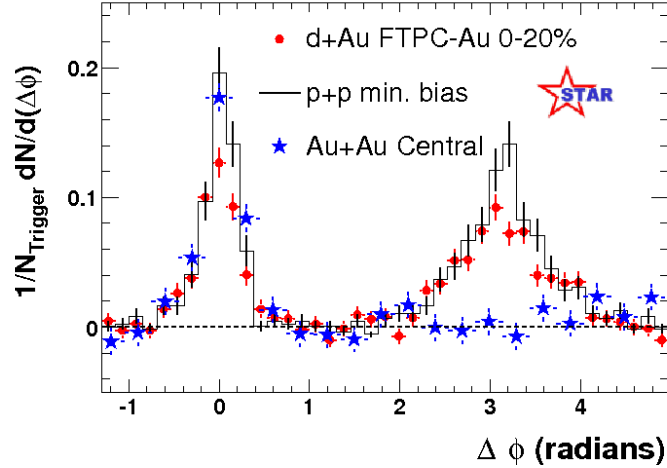


FIG. 1.6: Di-jet fragment azimuthal correlations in STAR experiment. In d+Au the di-jets remain unquenched relative to the mono jet correlation observed in central Au+Au collisions. All runs are at $\sqrt{s_{\text{NN}}} = 200$ GeV. It is believed that the existence of QGP is responsible for the creation of the jet quenching in Au+Au collisions, whereas in p+p and d+Au, no such a state of matter seems to be present. Figure taken from [Adams 03].

1.8.1 The Jet Quenching

It was predicted that at high momentum, partons lose energy via gluon radiation passing through the dense QGP matter [Gyulassy 91]. The latter is called *jet quenching* and can be studied using the Nuclear Modification factor, Section 1.9. The manifestation of the quenching of jets can be interpreted as:

- i. Suppression of the yield of high- p_{T} particles;
- ii. the ratio \bar{p}/p can be also quenched because of the different energy loss in the medium of gluons and quarks; and
- iii. a correlation of the impact parameter (Section 1.10 of the collision with the jet quenching yield. The phenomenon is favored in central collisions.

In Figure 1.6 it is presented results of STAR collaboration [Adams 03], denoting the jet quenching in Au+Au by the di-jet azimuthal correlation. The same quantity remains *unquenched* for the p+p and d+Au collisions at $\sqrt{s} = 200 \text{ GeV}$ as shown in the same plot.

1.8.2 The Enhancement of Strange Particle Production

Proposed by J. Rafelski and B. Müller in 1982 [Rafelski 82] as one of the prediction for the existence of the QGP, is the enhancement of strange hadrons. In particular inside the deconfined QGP medium, the strange quark (s) is saturated by $s\bar{s}$ pair production in $gg \rightarrow s\bar{s}$ and $q\bar{q} \rightarrow s\bar{s}$ (where $q = u, d$) reactions. The energy threshold for the s and \bar{s} production in QGP is 300 MeV, which is approximately the mass of the two quarks, yielding to the production of multi-strange baryons and strange antibaryons. Often the ratio of the yield of K/π is considered as the expression in order to quantify the strangeness enhancement. In other words in the QGP state the strange quarks have to be *thermalised*.

1.8.3 The Suppression of J/ψ

The idea was introduced in 1986 by Matsui and Satz [Matsui 86] that the charm quark (c), will be Debye-screened from its anti-quark \bar{c} , resulting in a J/ψ suppression. The potential between the quarks, as stated in Section 1.3, allows the formation of $c\bar{c}$, *charmonium* (J/ψ , ψ' , χ_c) and $b\bar{b}$ states called *bottomonium* such as Υ , χ_b , Υ' , etc. The NA50 collaboration [Beole 00], announced such a suppression in the channel $J/\psi \rightarrow \mu^-\mu^+$. Quantitatively the suppression of the J/ψ is measured with respect to the Drell-Yan muons process, where the latter process scales down with the number of the binary N+N collisions.

1.8.4 Photons

The photons can be created during heavy ion collisions, as a result of:

- i. In the early stages of the collisions the *prompt* photons initially are created by parton-parton scattering and this phase is common both in p+p and in A+A collisions;
- ii. during the QGP phase, photons are emitted as a result of the quarks undergoing collisions with other quarks and gluons in the created medium;
- iii. as the system expands and cools, the hadronization takes place at a temperature $T = 150\text{--}200\,\text{MeV}$ allowing the scattering of light unflavored mesons such as the π , ρ and ω . Also the light neutral mesons contribute via the decays $\pi^0 \rightarrow 2\gamma$ and $\eta \rightarrow 3\pi^0$ in the spectrum from a few MeV spanning to several GeV; and
- iv. finally through the kinetic freeze-out, the resonances contribute mostly in the photon spectrum in the energy domain of some MeV.

Direct photons are an interesting tool to study the possible QGP formation. They are produced in:

- i. $q + \bar{q} \rightarrow g + \gamma$: quark-antiquark annihilation; and
- ii. $q + g \rightarrow q + \gamma$: quark-gluon Compton scattering.

The direct photons do not come from hadronic decays. Theoretical models predict that the thermal photons should dominate the direct yield of photons at a low transverse momentum. As the yield of thermal photons falls off exponentially with transverse momentum, the direct photons from the initial hard scattering will dominate the spectrum at higher transverse momentum values. Additionally, a contribution of photons produced during parton fragmentation is observed. The measurements of *thermal photons* can provide information about temperature. Measurements of the *prompt photons* allow the study of the jet properties interacting with the medium.

The production of the prompt photons is represented by the nuclear modification factor (Section 1.9) with the yields of hadrons in A+A collisions relative to the scaled reference measured in p+p collisions. Thus direct photons provide a tool to check the binary collision scaling since their production is not affected by the medium produced in the final stage of the interaction. At RHIC energies it is possible to study direct photons in Au+Au, d+Au and p+p collisions. Prompt photons in p+p collisions provide an excellent test of QCD formation, while results from d+Au collisions may be used to investigate nuclear effects.

1.8.5 Di-leptons

Along with photons, the study of leptons is proven to be an interesting tool in order to deduce the properties of the formation of matter during heavy ion collisions. Due to the fact that leptons do not interact strongly with the medium, they exhibit a similar behavior like photons in terms of production stages. In particular, there exist *prompt* di-leptons created from the hard scattering processes, as well as *thermal* ones emitted from the QGP. Finally during the chemical freeze-out di-leptons are produced as byproducts of the meson decays.

Resonances such as ρ , ϕ and ω are the main sources for the *thermal* di-lepton creation below the energy domain of 1.5 GeV. Medium effects can broaden the width of the ρ resonance. In the region ≤ 2 GeV, the semileptonic decays of heavy flavor mesons and Drell-Yan processes ($q\bar{q} \rightarrow l^-l^+$) are favored, producing sufficient di-leptons. For higher energy scale the di-leptons can also be a result of the decay of J/ψ , ψ' , Υ , Υ' and Z^0 .

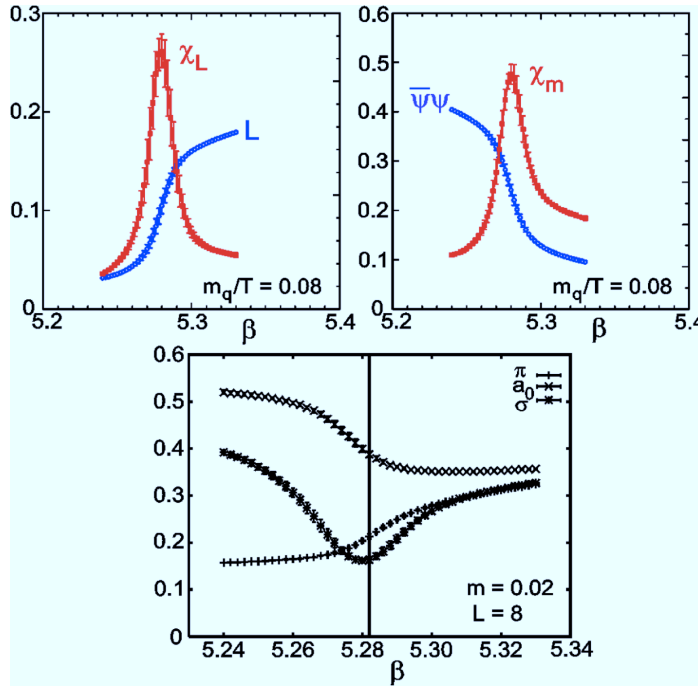


FIG. 1.7: *Upper:* LQCD calculations for two dynamical quark flavors showing the coincidence of the chiral symmetry restoration, marked by the rapid decrease of chiral condensate $\langle \bar{\psi}\psi \rangle$ (right frame) and deconfinement (left frame) phase transitions. *Lower:* The chiral transition leads toward a mass degeneracy of the pion with scalar meson masses. All plots are as a function of the bare coupling strength β used in the calculations; increasing β corresponds to decreasing lattice spacing and to increasing temperature. Figure taken from [Adams 05].

1.8.6 The Restoration of Chiral Symmetry

The expectation value $\langle \psi\bar{\psi} \rangle$ is often called *quark condensate* and gives a description of $q\bar{q}$ pairs found in the QCD vacuum. The breaking of the chiral symmetry, involves the confined quarks that do not have *zero mass*, but rather a few hundreds of MeV, cf. Table 1.1. At high temperature, the quark condensate tends to vanish, thus talking about the restoration of chiral symmetry. The phase during which neither confinement, nor chiral symmetry breaking occurs, is generally attributed to the presence of QGP.

Using lattice QCD (LQCD) calculations, in order to extract physically relevant predictions and to be extrapolated from the discrete case to the continuum (lattice spacing approaches zero), chiral (actual current quark mass) and thermodynamic (large volume) limits, the deconfinement transition may be accompanied by a chiral symmetry restoration transition, cf. Figure 1.7.

1.9 The Nuclear Modification Factor

The comparison of the particle spectra measured in Au+Au collisions and the spectra in which the QGP is not present, such as the d+Au and p+p systems, allows the better comprehension of the particle production mechanisms. A useful tool to achieve this comparison is the nuclear modification factor as defined in (1.5).

$$R_{AA}(p_T) = \frac{d^2N_{AA}/dp_T d\eta}{(\langle N_{coll} \rangle / \sigma_{pp})(d^2\sigma_{pp}/dp_T d\eta)} \quad (1.5)$$

The yield in nucleus-nucleus case (A+A) is contained in the numerator. The denominator contains a calculation of the Glauber Model, as described in Section 1.10. In particular, it scales down to the $\frac{d^2\sigma_{pp}}{dp_T d\eta}$ —for the p+p yield—and for a given centrality, by the number of binary collisions $\langle N_{coll} \rangle$ in the A+A case.

1.10 The Glauber Model

In the heavy ion collisions the values that describe the geometry of the collision are:

- i. The mean impact parameter $\langle b \rangle$, which is the distance between the centers of the 2 nucleons (cf. Figure 1.8);
- ii. the mean number of the participating nucleons $\langle N_{part} \rangle$, that take part in at least in one collision;
- iii. the mean number of the binary collisions $\langle N_{coll} \rangle$ since a nucleon can undergo more than one collision; and

- iv. the number of the nucleon-spectators, i.e. the nucleons that did not participate in the collision, (cf. Figure 1.8).

Experimentally we have no *direct* information about any of the above set of variables, rather than a measurement of the emitted charged particles given by the various sub-detectors. The Glauber model [Glauber 59], is a geometrical interpretation of the collision of the nuclei, allowing the deduction of the above collisional variables. In particular, this model considers the collision of the two nuclei in terms of the individual interactions of the constituent nucleons. The following assumptions are being made:

- i. The nucleons' trajectory is a straight line and parallel to the beam axis; and
- ii. a nucleus-nucleus ($A+A$) collision is considered as a superimposition of the subsequent nucleon-nucleon ($N+N$) collisions.

Furthermore the model considers a Woods-Saxon density (1.6) for the space distribution $\rho(r)_{\text{ch}}$ of the nucleons:

$$\rho_{\text{ch}}(r) = \frac{\rho_0}{1 + e^{\frac{r-r_c}{c}}} \quad (1.6)$$

where $r_c = r_0 \cdot A^{\frac{1}{3}}$. The parameters to be determined are r_c and c . Concerning the constant ρ_0 , it is calculated in that way in order to fulfill (1.7) [Cottingham 01].

$$\int \rho_{\text{ch}}(r) d^3\mathbf{r} = 4\pi \int_0^\infty \rho_{\text{ch}}(r) r^2 dr = Z \quad (1.7)$$

As an application of (1.7), we also note that ρ_0 , r_0 and c are constants, e.g. in the case of the Au nuclei, the constants are $r_0 = 6.38 \text{ fm}$, $c = 0.535 \text{ fm}$ yielding $\rho_0 = 0.169 \text{ fm}^{-3}$.

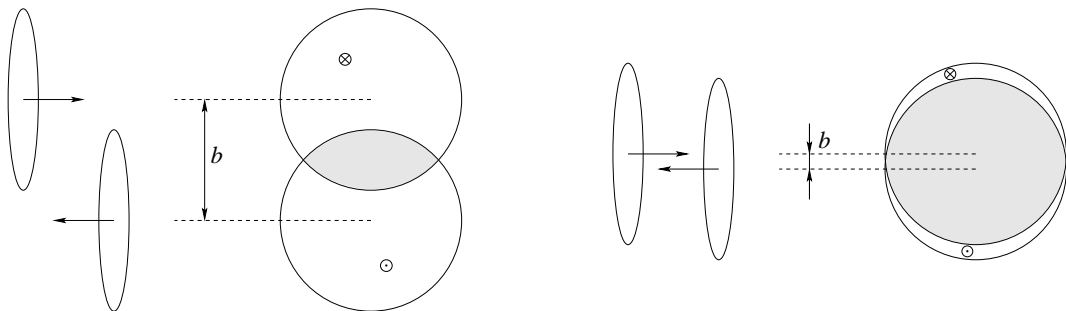


FIG. 1.8: *Left:* Cartoon depicting a peripheral collision. *Right:* Cartoon depicting a central collision. In both figures it is also represented the z -(*left*) and transverse (*right*) profile of each collision.

1.11 The Experimental Quantities

In the experimental nuclear and particle physics, the phase space observables of particles emerging from a heavy-ion collision are the following:

1.11.1 Rapidity

Let us consider a particle with a 4-momentum given by (1.8)

$$p^\mu = (E, p_x, p_y, p_z) \quad (1.8)$$

The rapidity y is hence defined by (1.9)

$$y \equiv \frac{1}{2} \ln \frac{E + p_L}{E - p_L} \quad (1.9)$$

where p_L is the longitudinal momentum (1.10) component usually—for convenience—considered along the beam direction. Also, the angle of emission is denoted by θ .

$$p_L = p \cos \theta \quad (1.10)$$

Under a Lorentz transformation along the beam axis, the value is additive $y' = y + a$, (Appendix A.1). The latter is of extreme importance when comparing collider to fixed target experiments. For collider experiments the center of the momentum frame coincides with the laboratory frame (cf. Appendix A.4).

1.11.2 Pseudorapidity

The purely experimental value of a particle's track, since the exact value of the particle mass remains unknown only until after the particle identification (PID) is called pseudorapidity η and is being defined as:

$$\eta \equiv -\ln \tan \frac{\theta}{2} \quad (1.11)$$

When the momentum of a particle becomes comparable to its energy ($p \approx E$), then the value of pseudo-rapidity is approximately equal to the value of rapidity ($\eta \rightarrow y$), (cf. Appendix A.2). In the mid-rapidity region the distributions of dN/dy and $dN/d\eta$ are correlated with a factor depending on the mass of the particle.

1.11.3 The Transverse Momentum, Energy and Mass

For a particle with a 4-momentum as in (1.8), the transverse momentum p_T is being defined as

$$p_T \equiv \sqrt{p_x^2 + p_y^2} \quad (1.12)$$

and is Lorentz invariant under transformations in the z -axis. Since it originates from the collision energy, it offers a tool for the study of the collision dynamics. In a similar way, the transverse mass is defined by (1.13)

$$m_T^2 = m^2 + p_T^2 \quad (1.13)$$

Also the transverse energy E_T is given by (1.14).

$$E_T = mc p_T \quad (1.14)$$

Finally a very useful expression is (1.15).

$$E_T = E \cdot \sin \theta \quad (1.15)$$

Let us also note that (1.15) will be used later for our analysis, in particular it will serve to identify the *towers* that are above the threshold (cf. Table 3.3) in the Barrel Electromagnetic Calorimeter (BEMC) as it is stated in Section 2.16.

1.11.4 The Energy Density

The idea is attributed to Bjorken, that in order to explore the QGP we need to know the energy available (in the order of magnitude of GeV/fm³) [Bjorken 83]. In particular during the collisions the nuclei due to Lorentz contraction, are forced to re-shape into discs, in the lab frame. The total kinetic energy of the nuclei, becomes the initial conditions for the creation of the medium. The energy density (ϵ), is therefore proportional to the transverse energy E_T per rapidity unit as measured in the mid-rapidity ($y = 0$) of the center-of-mass reference frame.

$$\epsilon = \frac{1}{A_\tau \tau_0} \cdot \frac{dE_T}{dy} \Big|_{y=0} \quad (1.16)$$

The τ_0 corresponds to a typical order of magnitude of 1 fm/c, the time necessary for the hydrodynamic evolution to be established. The A_τ corresponds to the transverse surface where the energy was deposited. For a *perfectly* central collision, it can be used as the surface of the disc $A_\tau = \pi \cdot R^2$.

1.11.5 Luminosity

The rate R of a physical process with a cross section denoted by σ , is given by the:

$$R = \sigma \cdot \mathbb{L} \quad (1.17)$$

where \mathbb{L} stands for the luminosity, described by the formula:

$$\mathbb{L} = f \frac{N_1 N_2}{4\pi \sigma_x \sigma_y} \quad (1.18)$$

where f is the frequency of the collisions, N_1, N_2 are the numbers of ions included in each packet, *bunch*, of each beam and the σ_x, σ_y are the Gaussian transverse profiles of the beams. In Table 2.1, the values of the integrated luminosities of the RHIC for the operating years 2000—2009 are described.

1.12 The Physics of Charm

The production of the charm quark (in $c\bar{c}$ pairs) occurs in the early stages of the heavy ion collisions dominantly via the gluon fusion $gg \rightarrow c\bar{c}$ [Abelev 08]. Due to the fact that the yield of charm is affected by the conditions of the early stages of the collision, the measurement of the charm production provides a useful tool for the description of the initial stage that took place. Due to their large mass ($m > 1 \text{ GeV}/c^2$), the heavy quarks (charm and bottom) are to be primarily produced by hard scattering processes (high momentum transfer) in the early stages of the collision and, therefore, are sensitive to the initial gluon density [Lin 95]. The production of the heavy quark by thermal processes later in the collision is low since the expected energy available for particle production in the medium ($\sim 0.5 \text{ GeV}/c^2$) is smaller than the energy needed to produce a heavy quark pair ($> 2.4 \text{ GeV}/c^2$). The study of the energy loss of partons in the hot and dense QCD matter can be performed at RHIC energies. The energy loss of a heavy quark, is expected to be lower than that of the light one. This result is explained because of the suppression of the gluon radiation at small angles, according to the *dead cone* effect [Dokshitzer 01, Djordjevic 05]. The production of the J/ψ in nuclear collisions is suppressed due to the *Debye screening* of the $c\bar{c}$ pairs.

The states of the $c\bar{c}$ such as the χ_c and ψ' , as they are more dissociated, are suppressed even more than the J/ψ . The energy loss of the heavy quark mesons is studied through the measurements of the p_T spectra of their decay electrons. At high p_T , the mechanism of electron production is dominant enough to reliably subtract other sources of electrons like conversions from photons and π^0 Dalitz decays. RHIC measurements in central Au+Au collisions have shown that the high p_T yield of electrons from semileptonic charm and bottom decays is suppressed relative to properly scaled p+p collisions, usually quantified in the nuclear modification factor R_{AA} [Abelev 07, Adare 07].

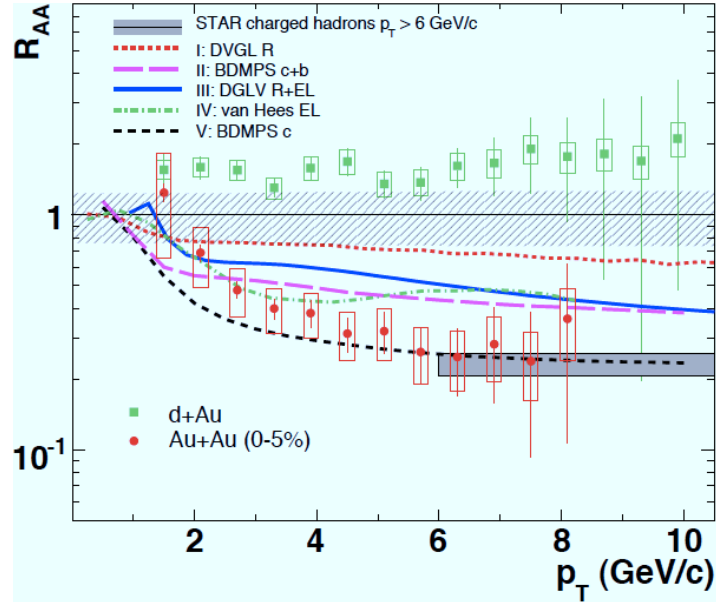


FIG. 1.9: Nuclear Modification Factor R_{AA} for the non-photonic electrons. Figure taken from [Bielcik 06].

The nuclear modification factor (R_{AA}), shown in cf. Figure 1.9, exhibits an unexpectedly similar amount of suppression as observed for light quark hadrons, suggesting substantial energy loss of heavy quarks in the produced medium. The energy loss models, incorporating contributions from charm C and bottom B , do not explain the observed suppression sufficiently [Djordjevic 06, Armesto 06]. Although it has been realized that the energy loss by elastic parton scattering causing collisional energy loss is probably of comparable importance to the energy loss by gluon radiation [Wicks 07, van Hess 06], the quantitative description of the suppression is still not satisfying. Furthermore, it has been shown that the collisional dissociation of heavy meson in the medium may be significant in heavy-ion collisions [Adil 07].

However, the theoretical models which include energy loss from charm only describe the observed suppression reasonably well [Cacciari 05]. The observed discrepancy between the data and the model calculations could indicate that the dominance over D mesons starts at higher p_T as expected. Theoretical calculations implying perturbative QCD (pQCD) have shown that the crossing point where bottom decay electrons start to dominate over charm decay electrons is largely unknown [Cacciari 05, Vogt 08]. Therefore, the relative contributions from charm and bottom meson decays to electrons have to be determined separately. In Section 1.13 it is presented an experimental disentanglement method of the contribution of the C and B .

1.13 The Azimuthal Angular Correlation Method

In Quantum Chromodynamics (QCD), due to the flavor conservation, it is imposed that the heavy quarks are produced in quark anti-quark pairs (namely $c\bar{c}$ and $b\bar{b}$). A more detailed understanding of the underlying production process may be obtained from events in which both heavy-quark particles are detected. In addition, due to momentum conservation, these heavy-quark anti-quarks pairs are correlated in relative azimuth ($\Delta\phi$) in the transverse plane with respect to the colliding beams, leading to the characteristic back-to-back oriented sprays of particles (di-jet).

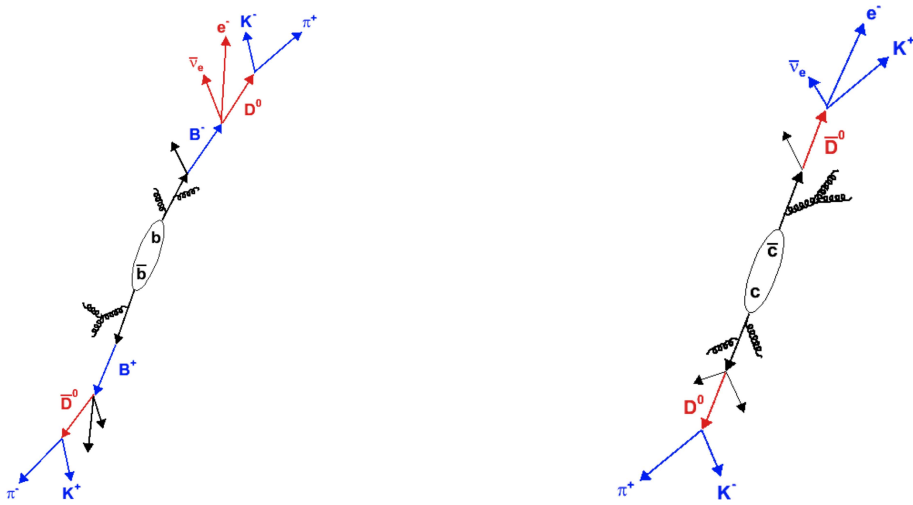


FIG. 1.10: Fragmentation of a $b\bar{b}$ pair (left) and of a $c\bar{c}$ (right). Figures taken from [Mischke 09a].

We can consider the typical decays of $c\bar{c}$ and $b\bar{b}$ as they are shown in Figure 1.10. This di-jet signal appears in the azimuthal correlation distribution as two distinct back-to-back Gaussian-like peaks around $\Delta\phi = 0$ (near side) and $\Delta\phi = \pi$ (away side), shown in Figure 1.11. The correlation in their azimuthal opening angle survives the fragmentation process to a large extent in $p+p$ collisions. Studies exploiting the angular correlations of pairs of high p_T particles, have successfully been performed in order to investigate on a statistical basis the properties of the produced jets [Arsene 05]. In the current correlation method, the charm and the bottom production events are identified using the characteristic decay topology of the jets. In particular, charm quarks (c) predominantly hadronize to D^0 mesons via (1.19) while bottom quarks produce D^0 via the intermediate B meson decay as in (1.20) [Amsler 08].

$$c \rightarrow D^0 + X, \quad \text{B.R.} = 56.5 \pm 3.2\% \quad (1.19)$$

$$b \rightarrow B^-/\bar{B}^0/\bar{B}_s^0 \rightarrow D^0 + X, \quad \text{B.R.} = 59.6 \pm 2.9\% \quad (1.20)$$

The branching ratio for charm and bottom quark decays is given in (1.21)–(1.22).

$$c \rightarrow e + \text{anything}, \quad \text{B.R.} = 9.60\% \quad (1.21)$$

$$b \rightarrow e + \text{anything}, \quad \text{B.R.} = 10.86\% \quad (1.22)$$

While triggering on the leading electron (*trigger* particle), the balancing heavy quark, identified by the D^0 meson through the hadronic decay (1.23), is used to determine the underlying production mechanism (*probe* side).

$$D^0 \rightarrow K^-\pi^+, \quad \text{B.R.} = 3.89\% \quad (1.23)$$

$$B \rightarrow \bar{D}^0 + X, \quad \text{B.R.} = 59.60\% \quad (1.24)$$

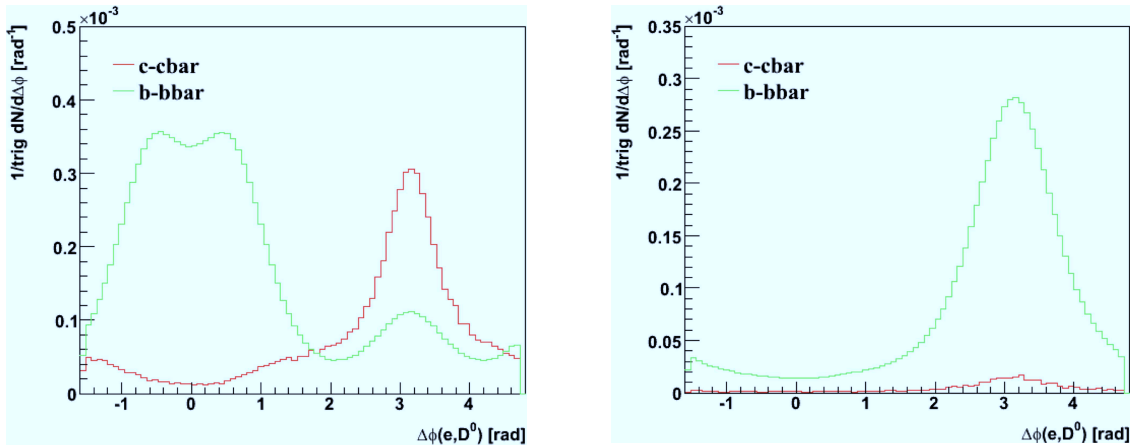


FIG. 1.11: Leading order PYTHIA azimuthal correlation distribution of non-photonic electrons and D^0 mesons from charm and bottom contribution. *Left:* for like-sign $e-K$ pair. *Right:* for unlike-sign $e-K$ pair. Figures taken from [Mischke 07].

A charge sign requirement between the trigger electrons (e) and the decay kaon (K) provides a powerful tool in order to separate events originating either from a $c\bar{c}$ or a $b\bar{b}$ fragmentation channel. As an example, in Figure 1.10 it is illustrated a schematic view of the fragmentation of a $b\bar{b}$ (*left*) and a $c\bar{c}$ pair (*right*), respectively. The corresponding azimuthal correlations (of the $e-D^0$) are shown in Figure 1.11. Assuming that the trigger lepton is an electron e^- coming from the fragmentation of a \bar{c} or b quark, the partner charm quark has to be a c , therefore producing a pair $K^-\pi^+$. The bottom quark on the opposite side is a \bar{b} which produces $K^+\pi^-$ pairs via the dominant decay mode (1.24). However there is another channel [Amsler 08], less probable as stated in (1.25) yielding adequately $K^-\pi^+$ pairs.

$$B \rightarrow D^0 + X, \quad \text{B.R.} = 9.1\% \quad (1.25)$$

$$B^- \rightarrow D^0 + e^- \bar{\nu}_e \quad (1.26)$$

In addition, both semileptonic B decays (1.22) and (1.26) are expected yielding adequately: e^-K^- and e^+K^+ pairs. As a consequence, the electron-kaon pairs with opposite charge sign, called unlike sign (ULS), can prompt the identification of B decays on the away-side of the azimuthal correlation distribution between decay electrons and D^0 mesons. By requiring the like-sign (LS) $e-K$ pairs, it is possible to select the bottom contribution on the near side and charm, as well as a small contribution from bottom ($\sim 15\%$) on the away side of the $e-D^0$ correlation function. In Table 1.2, the $\Delta\phi$ azimuthal correlation between e and D^0 along with the charge demand between trigger particle (e) and kaon candidate (K), along with the *probe* side decay (D^0 or \bar{D}^0) and the adequate C or B contribution are summarized. Requiring $e-D^0$ coincidence in the same event significantly improves the signal to background ratio over either technique individually. Moreover, the decay electrons provide an efficient trigger for the heavy-quark production events. The shape of the azimuthal correlation distribution allows a more differential comparison between the charm and bottom contributions owing to their different decay kinematics.

TAB. 1.2: Like Sign (LS, marked in *blue*) and unlike sign (ULS, in *red*) charge demand for the $e-K$ pairs and for various $\Delta\phi = \phi_e - \phi_{D^0}$ azimuthal correlations, allowing the experimental disentanglement of the contribution of C and B fragmentation channel. The trigger side along with the probe decay side for each case is also noted. In boldface it is marked the dominant contributing source (fragmentation channel).

| PAIR | $\Delta\phi :$ | 0° | | 180° | | PROBE |
|------|----------------|----------------|--------|-----------------------|--|-------|
| | | TRIGGER | PROBE | TRIGGER | PROBE | |
| LS: | | e^- e^+ | bottom | charm , bottom | $\mathbf{K}^-\pi^+ (D^0)$ $\mathbf{K}^+\pi^- (\bar{D}^0)$ | |
| ULS: | | e^- e^+ | n/a | bottom , charm | $\mathbf{K}^+\pi^-$ $\mathbf{K}^-\pi^+$ | |

Chapter 2

Experimental Aspects

In this chapter a description of the experimental facilities is given, in particular the Relativistic Heavy Ion Collider, RHIC, along with the 4 experiments. Emphasis will be put on STAR experiment with some brief description of the various sub-systems. The STAR Inner Silicon Trackers will be presented insisting on the Silicon Strip Detector. Also some notions of the recent and future upgrades that will take place in STAR experiment will be presented. The chapter concludes by mentioning some basic elements of STAR vertex reconstruction software.

2.1 The Relativistic Heavy Ion Collider

The Relativistic Heavy Ion Collider (RHIC) is located at Brookhaven National Laboratory, Upton NY. RHIC has been operational since the summer of year 2000 and measures 1.2 km in diameter. A remarkable achievement in the field of high energy nuclear physics, RHIC was the first machine ever being built with the capability of colliding mixed species. RHIC can collide ion species as light as protons and deuterons and as heavy as Uranium at a variety of energies. RHIC consists of two independent accelerator storage rings with six interaction points and a system of superconducting magnets. The acceleration of heavy ions is a complex process that unfolds in stages. Since RHIC uses superconductivity (most of the RHIC components operate at temperature close to the absolute zero, the RHIC ramp rate is relatively slow. It takes a week to cool down the RHIC superconducting magnets from room to operating temperature which is 4.2 K [Harrison 03]. Moreover, the accelerator is not a stand-alone machine, it is part of a complex that includes other components—ion sources and initial accelerators (Linear Accelerator (LINAC)—is used in order to accelerate protons whether Tandem Van de Graaff accelerators are used for heavier ions), electron-stripping foils, a Booster ring, and the Alternating Gradient Synchrotron (AGS). Before reaching RHIC,

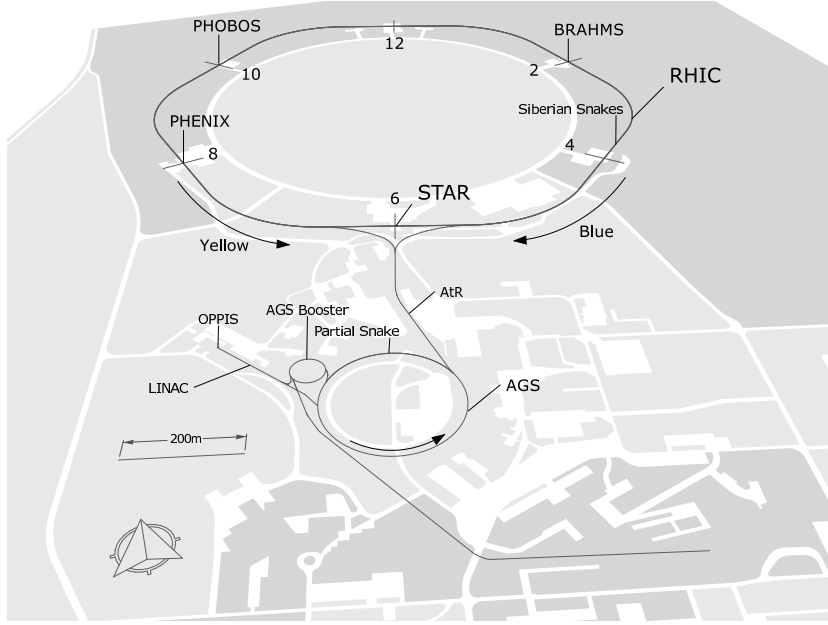


FIG. 2.1: Layout of the RHIC facilities at Brookhaven National Laboratory. The locations of STAR, PHENIX, PHOBOS and BRAHMS are clearly seen around the RHIC ring. Figure taken from [Sakuma 10].

the atoms are ionized and accelerated.

A brief description of the RHIC operation using Au atoms as an example follows: The negatively charged ^{197}Au ions are produced in a source and accelerated into and through the Tandem Van de Graaff accelerator, which has a terminal voltage of 14 MV. At the terminal the ions pass through the stripping foils, they lose their negative charge and acquire a positive charge, which for gold ions is of +12 units. The ions are accelerated from the terminal to ground potential, increasing their energy by 168 MeV (at this point the energy of each Au ion is about 1 MeV/nucleon). As the ions exit the Van de Graaff, they are stripped further and pass into the Booster via a transfer line. In the Booster the ions are bunched into six bunches, they are accelerated further, and as they exit the Booster, they are stripped of all except the K-shell electrons. After this stage, the Alternating Gradient Synchrotron (AGS) receives the bunches from the Booster, and gathers the ions into bunches. Each AGS bunch is equivalent to six Booster bunches.

The next step is the acceleration and the transportation to RHIC with energy of 8.86 GeV per nucleon. Before entering RHIC, however, the ions are stripped of the remaining electrons. The bunches can then be stored and further accelerated inside RHIC. A second Tandem Van de Graaff accelerator is available to provide a second species for asymmetrical collisions(such as the d+Au). For the injection of protons

the proton Linear Accelerator (LINAC) is used. For the polarized proton program, the challenge is to keep the beam polarized through out the acceleration process. To maintain the desired polarization, two polarimeters and one partial *Siberian snake* are installed to RHIC. From their source in the LINAC, the protons are inserted into the Booster and then into the AGS. From there, at 25 GeV/particle, the beam is transferred to RHIC. Both the ion and proton injection processes are illustrated in Figure 2.1.

At the end of the heavy ion injection, each RHIC ring holds a total of 6×10^{10} particles. When the injection is performed with the light ions, this number may be up to two orders of magnitude larger [Harrison 03]. Once the beams are inside the RHIC, they travel inside the two rings in opposite directions. One ring is called *blue* for reference, in it the beam travels in the clockwise direction as viewed from above. The other ring is often referred to as the *yellow* ring. In the latter case the beam moves in the counter-clockwise direction. Finally, in the pivot Table 2.1, it is summarized the runs that were taken from the beginning of the operations until today.

In the near future RHIC will upgrade its aging Tandem Van de Graaff with an Electron Beam Ion Source (EBIS) [Alessi 05]. This source and linac based pre-injector can produce all ion species up to uranium, including noble gases and polarized ^3He .

2.2 The RHIC Experimental Areas

There are six interaction areas along the perimeter of RHIC. Four of these are used for experimental reasons, the fifth by the collider-accelerator department (C-AD), and the sixth remains vacant. As of today, two out of four experiment still are under the process of data acquisition: PHENIX (Section 2.2.3) and STAR (Section 2.3). Along with PHOBOS (Section 2.2.1) and BRAHMS (Section 2.2.2), they constitute the ensemble of the experimental facilities at RHIC.

2.2.1 PHOBOS

Named after the larger of the two moons of planet Mars, PHOBOS* experiment has as a goal to detect events where QGP may have been present. The experiment was designed to measure particles with transverse momentum p_{T} as low as 10 MeV/c. The experimental apparatus, consists of fast Si pad detectors (covering in $|\eta| < 5.4$ as can be seen in Figure 2.2). In addition the experiment is equipped with a TOF detector. The trigger is provided by the paddle counters (16 scintillation detectors located around the beam pipe in $3.2 < \eta < 4.5$). The PHOBOS ZDC's are identical to what STAR experiment is actually using and are described in Section 2.3.3. The PHOBOS collaboration has carried out measurements of particle multiplicity, particle/anti-particle

*Initially the name proposal for the experiment was MARS: Modular Array for RHIC spectroscopy, but was soon rejected.

TAB. 2.1: Colliding nuclei species for the different RHIC runs throughout the years 2000–2009. Luminosity values are taken from [Dunlop 08a].

| RUN | YEAR | COLLIDING SPECIES | BEAM ENERGY [GeV/u] | INTEGRATED LUMINOSITY [pb ⁻¹] |
|------|-----------|-------------------|------------------------|--|
| I | 2000 | Au+Au | 27.9 65.2 | < 10 ⁻⁹ 20 · 10 ⁻⁶ |
| II | 2001–2002 | p+p | 100.0 | 1.4 |
| | | Au+Au | 9.8 | 258 · 10 ⁻⁶ 0.4 · 10 ⁻⁶ |
| III | 2002–2003 | d+Au | 100.0 | 73 · 10 ⁻³ |
| | | p+p | | 5.5 |
| IV | 2003–2004 | Au+Au | | 3740 · 10 ⁻⁶ |
| | | p+p | 100.0 | 67 · 10 ⁻⁶ 7.1 |
| V | 2004–2005 | Cu+Cu | 11.2 100.0 31.2 | 0.02 · 10 ⁻⁶ 42.10 · 10 ⁻⁶ 1.50 · 10 ⁻³ |
| | | p+p | 100.0 204.9 | 29.5 0.1 |
| | | | | |
| | | | | |
| | | | | |
| VI | 2006 | p+p | 100.0 31.2 | 93.3 1.05 |
| VII | 2006–2007 | Au+Au | 100.0 | 7250 · 10 ⁻⁶ |
| VIII | 2008–2009 | d+Au | | 33.95 · 10 ⁻³ |
| | | p+p | 100.0 | 2.5 |

ratios and collective flow [Back 03]. As of the year 2005, the collaboration has seized its operation [Franz 06].

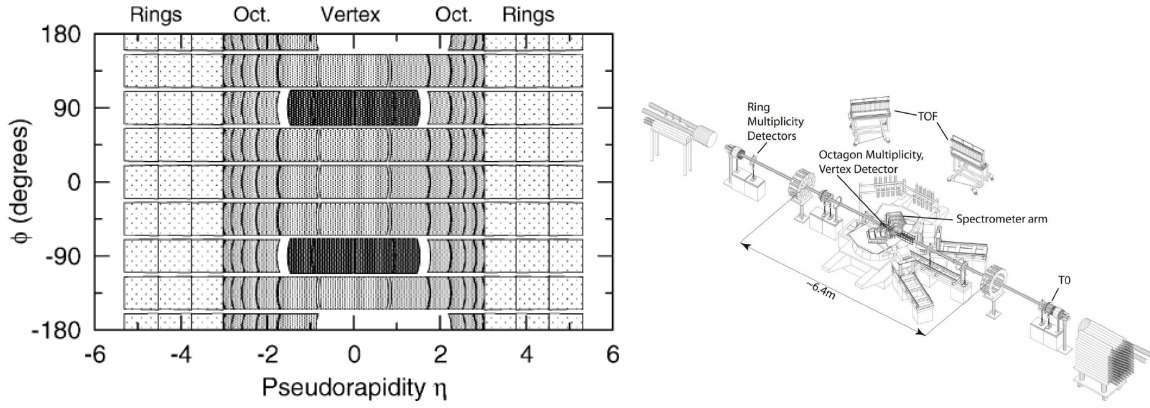


FIG. 2.2: *Left:* Geometrical acceptance of PHOBOS Silicon Detectors. *Right:* Overview of PHOBOS experiment. Figures taken from [Back 03].

2.2.2 BRAHMS

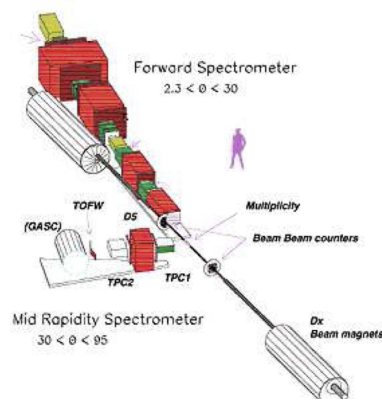


FIG. 2.3: Overview of BRAHMS Experiment. Figure taken from [Adamczyk 03].

The Broad Range Hadron Magnetic Spectrometer (BRAHMS) [Adamczyk 03], serves to measure the particle spectra (such as p^\pm, K^\pm and π^\pm). The specific experiment has two separate movable spectrometer arms for the high and the low transverse momentum p_T particles. It consists of the Forward Spectrometer (FS) at Mid Rapidity Spectrometer (MRS), as seen in Figure 2.3, situated at 2.3° and 90° with respect to the beam axis. The particle identification (PID) is performed with the standard spectrometer

components like the Time of Flight (TOF), threshold and ring-imaging Cherenkov detectors and tracking devices like drift (DC) and time-projection (TPC) chambers. The TPC's are of standard design with 21.8 cm drift and electric field of 229 V/cm using Ar/CO₂, (90:10) and STAR front-end-electronics (FEE). The DC's have 10 layers with x, y pattern and a $\pm 18^\circ$ wire planes using a Ar/C₄H₁₀ (67 : 33) gas mixture with a 9 °C alcohol bubbler.

2.2.3 PHENIX

The Pioneering High Energy Nuclear Interaction experiment (PHENIX), is a compound detector primarily oriented to perform electromagnetic probes. The various sub-detector systems are able to capture hundreds of heavy ion events per second, 10 kHz [Adcox 03]. The rare probes as a sign of the QGP formation, is the PHENIX physics goal. The apparatus consists of two large central arms, positioned symmetrically on equidistant sides, of the beam line. As it can be seen in Figure 2.4, there are

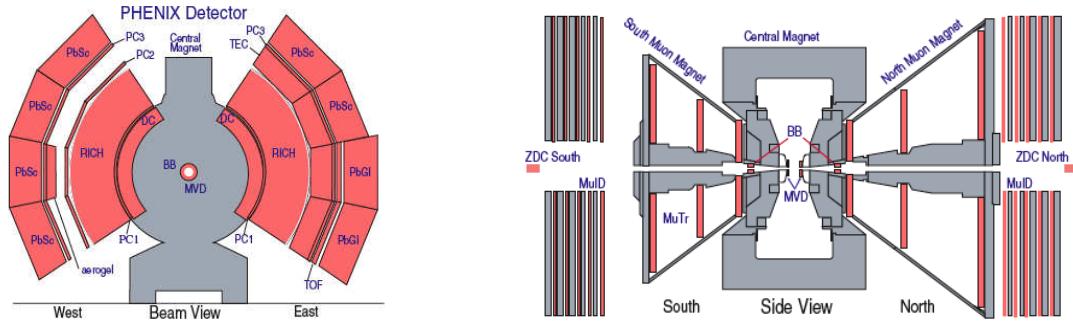


FIG. 2.4: Views of the PHENIX experiment. *Left:* Beam-view. *Right:* Side-view Figures taken from [Adcox 03, Franz 08].

two muon forward spectrometers, covering $1.1 < |\eta| < 2.2$. They consist of a muon tracker (consecutive layers of drift chambers) and a muon identifier (absorber made of steel and layers with streamer tubes [Adcox 03, Franz 08] of *Iarocci* type [Iarocci 83]). PHENIX possesses two calorimeters in PbSc (Lead-Silicon) and PbGl (lead-glass) as can be seen on the left side of Figure 2.4. They serve to reconstruct the π^0 and η neutral mesons. In the central arms, the particle identification is being performed where particles such as (e^\pm, π with p_T up to 4 GeV/c) are detected using the Ring Imaging Cherenkov (RICH). For the π^\pm, K^\pm up to $p_T = 1.5$ GeV/c and the p^\pm up to 3.5 GeV/c the Time of Flight (TOF) serves for their identification [Adcox 03, Franz 08]. In addition, the muon arm serves to identify the charmed particle J/ψ and in particular its muonic decay $J/\psi \rightarrow \mu^+ \mu^-$.

2.3 STAR Overview

The Solenoidal Tracker at RHIC experiment, is a collaboration that consists of 616 physicists from 52 institutions in 12 countries. An overview of the apparatus is shown in Figure 2.5. STAR experiment excels in measuring hadron production over a large solid angle. It features detector systems for the high precision tracking, momentum analysis, and particle identification at the center of mass rapidity.

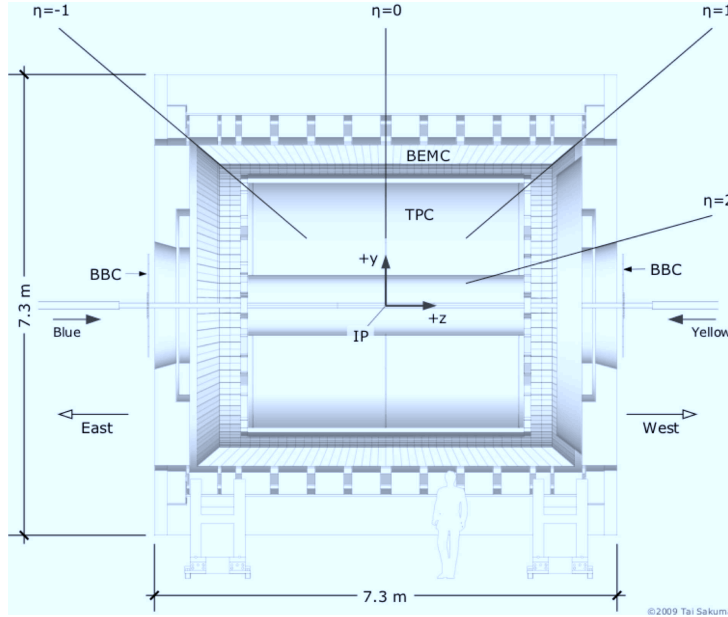


FIG. 2.5: Overview of the STAR experiment. The z axis is parallel to the beam direction, and at $z = 0$ the TPC membrane is situated as depicted by the vertical line. Figure taken from [Sakuma 10].

The major subdetector is the large TPC serving for tracking and particle identification (PID) together with the 3 layer silicon vertex tracker (SVT), and a single layer silicon strip detector (SSD). The electromagnetic calorimetry surrounds the TPC, namely the Barrel Electromagnetic Calorimeter (BEMC), described in Section 2.16. The tracking of approximately 2000 charged particles per central event in the TPC is performed by the application of a Kalman Filter [Liko 92] and Hough transform which points the tracks back to the SVT/SSD, Section 2.8. Finally the smaller angles are covered by two small forward TPC's (Section 2.13) with a radial drift. In addition, the new STAR upgrades such as the FGT and the HFT that will allow the improvement on the measurement and the opening of a window to new physics.

2.3.1 The Trigger System

The STAR trigger system consists of the Zero Degree Calorimeter (ZDC), the Central Trigger Barrel (CTB) and the Electromagnetic Calorimeter (EMC). The EMC can be used to select events with rare probes, or electrons from J/ψ and Υ decays. The trigger is used in order to select peripheral, central, or events that contain high energy particles in A+A collisions.

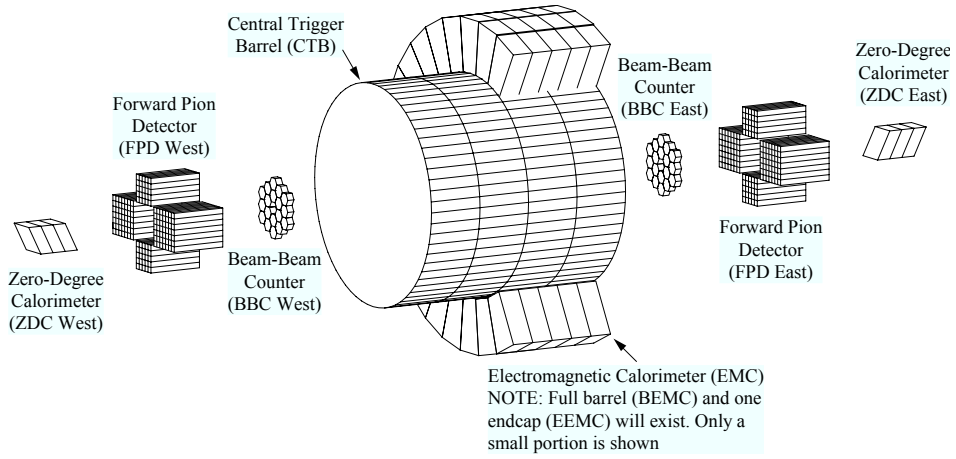


FIG. 2.6: Overview of STAR Trigger System. Figure taken from [Judd 03].

2.3.2 The Trigger Levels

The 3 trigger levels of STAR experiment provide a decision in order to classify the corresponding event. In particular:

- i. The CTB along with ZDC form the level $L0$ of decision. The coincidence of signals in ZDC along with the RHIC clock, are used in order to deduce the exact time of the bunch crossing. This trigger decision is fast: $1.5\ \mu s$. If this trigger level is satisfied, the CTB signal is used to extract the multiplicity. An event that passes $L0$, triggers the response of the other detectors and their signal is also taken under consideration.
- ii. The level $L1$ corresponds to the time that the electrons drift in the TPC volume. The time that this level needs is of the order of $100\ \mu s$.
- iii. The next level of decision is $L2$ and it is used by the fast detectors. During this time ($10\ ms$), the digitization of the TPC tracks is being performed.

- iv. Finally the L_3 is the online track reconstruction. Its total duration is 200 ms. An estimation of the vertex position is also being done during this period of time, and a particle identification of the high p_T particles is being performed as well [Adler 03].

2.3.3 The Zero Degree Calorimeter

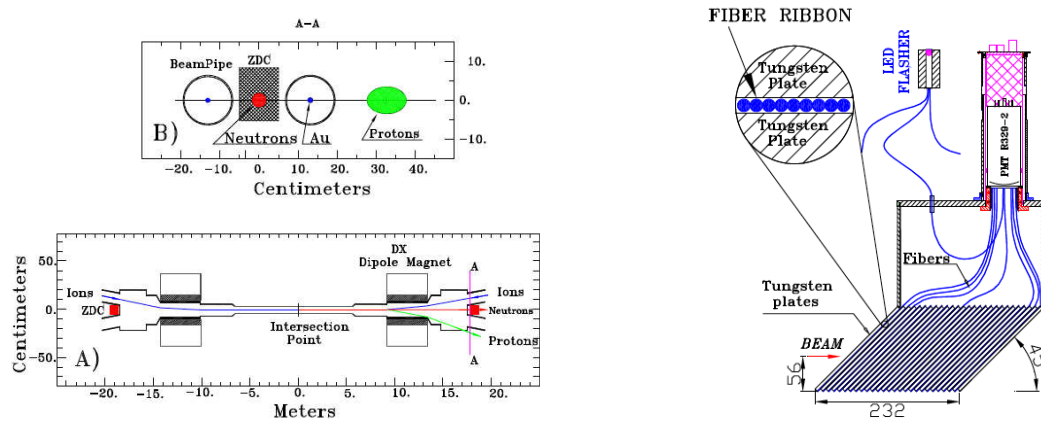


FIG. 2.7: *Left:* Transverse view of the collision region depicting the interaction point, the beam pipe as well as the Zero Degree Calorimeter. *Right:* Detail of ZDC modules. Figures taken from [Adler 01].

Located at a distance of 18 m from the origin of axis z (in both sides), as shown in Figure 2.7, the Zero Degree Calorimeters (ZDC), serve as the Minimum Bias Trigger and contribute to the deduction of the centrality in heavy ion collisions [Adler 01]. Their dimension is only 10 cm wide. In particular, the dipole magnet Dx situated at 10 m serves in order to deflect the charged fragments of the beam, as shown in the upper left part of Figure 2.7. Since neutrons are not affected by the presence of the magnetic field, and due to their forward rapidities, they carry a large probability that are not by products of the collision. The detector layout as shown in Figure 2.7, is made of 3 modules. Each module consists of Tungsten absorber layers and Cherenkov fibers with a total length of 0.7 m, able to measure the energy of the neutrons emitted as fragments after each collision in 2.5 mrad acceptance around the beam pipe [Adler 01]. The accumulated measured energy is proportional to the neutron multiplicity, thus giving a measurement of the collision geometry, hence the deduction of centrality. In addition, the same type of the ZDC modules are placed in all four RHIC experimental facilities, monitoring the beam luminosity.

2.3.4 The Beam Beam Counters

The STAR Beam-Beam Counters (BBC) are located at a distance of $z = \pm 3.7$ m from the central TPC membrane at $z = 0$, outside of the pole-tip of STAR magnet. Each BBC module is divided in two areas: inner and outer. The former of radius between 9.6 cm to 48 cm covers $3.4 < |\eta| < 5.0$, when the latter is located between 38 cm and 193 cm covers $2.1 < |\eta| < 3.6$. Their main purpose is to serve as a trigger in collisions where the use of ZDC (cf. Section 2.3.3) is impractical (e.g. in p+p collisions). They consist of 18 large hexagonal scintillation tiles as shown in Figure 2.8 which are connected to the Photo-Multipliers (PMT). The inner part of each BBC is constructed by small tiles made of scintillating material and a coincidence in at least one of the 18 small inner tiles on both sides, provides a trigger for p+p collisions. The BBC's can be also used for vertex position determination. In particular, the comparison of the time of arrival between East and West, can determine the vertex z position. Also, let us note that large values in time of flight are associated with the passage of beam halo and the corresponding trigger is being rejected.

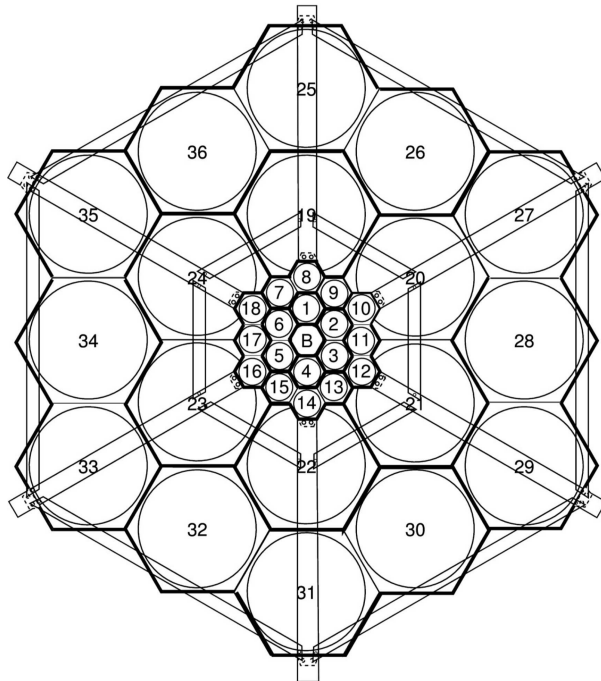


FIG. 2.8: Schematic depiction of a STAR Beam-Beam Counter. The beam pipe can be seen depicted by the letter **B**, in the center of the image. Figure taken from [Bieser 03].

2.3.5 The Central Trigger Barrel

The Central Trigger Barrel [Bieser 03] surrounds the TPC Barrel and covers in pseudo-rapidity $|\eta| < 1$, as shown in Figure 2.5. It consists of an array of 240 scintillator slats covering 2π in azimuth [Bieser 03], as shown in Figure 2.9. The signal of each slat is proportional to the number of particles that traversed it. The CTB along with the ZDC (cf. Section 2.3.3) served as a quick method of the multiplicity determination, without the intervention of the time-consuming event reconstruction. It does succeed to perform so, by counting the charged particles emerging from the point of interaction. In particular, just by using the ZDC and CTB information, e.g. minor energy deposits in the ZDC and large amount of counts in the CTB, indicates a collision with small impact parameter (cf. Section 1.10) that occurs during central events. In the contrary case, where the amount of deposit is large in the ZDC and few counts are recorded in the CTB, the collision is characterized as peripheral, therefore with a large value of the impact parameter. The year 2007 was the last operational period for the CTB.

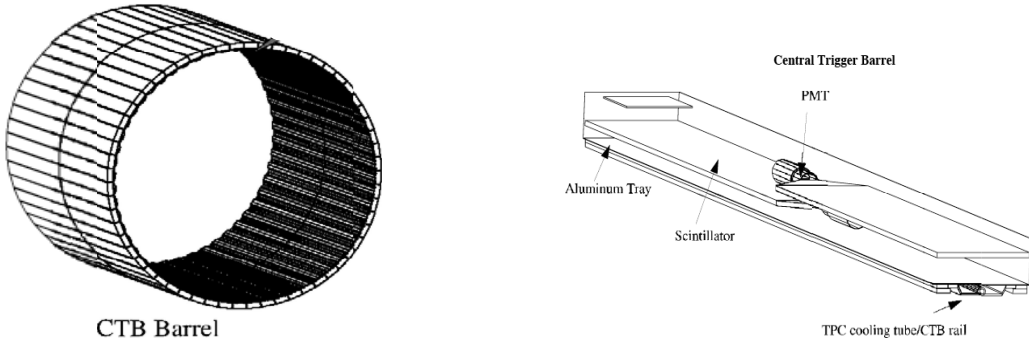


FIG. 2.9: *Left:* View of STAR Central Trigger Barrel that serves as a trigger. *Right:* Detail of the CTB module. Figures taken from [Bieser 03].

2.4 The Physics of Semiconductors

As in other solids, the electrons in semiconductors can have energies only within certain bands (i.e. ranges of levels of energy) between the energy of the ground state, corresponding to electrons tightly bound to the atomic nuclei of the material, and the free electron energy, which is the energy required for an electron to escape entirely from the material. The energy bands correspond to a large number of discrete quantum states of the electrons. Most of the states with low energy are full, up to a particular band called the *valence band*. Semiconductors along with insulators are distinguished from metals because the valence band in the semiconductor materials is nearly filled under usual operating conditions. This requirement can cause more electrons to be available in the *conduction band* which is the band immediately above the valence band. The

ease with which electrons in a semiconductor can be excited from the valence band to the conduction band depends on the gap between the bands, and it is the size of this energy band gap that serves as an arbitrary dividing line (roughly 4 eV) between semiconductors and insulators. Finally the *gap band* is the energy difference between the top of the valence band and the bottom of the conduction band in insulators and semiconductors. It is possible to modify the balance between the electrons and holes population in a silicon crystal lattice by embedding to the crystal, atoms of other element. This technique is called *doping*. In particular, atoms with one more valence electron than silicon can be used to produce the *n-type* semiconductor material, which adds electrons to the conduction band, resulting to the enhancement of the number of electrons.

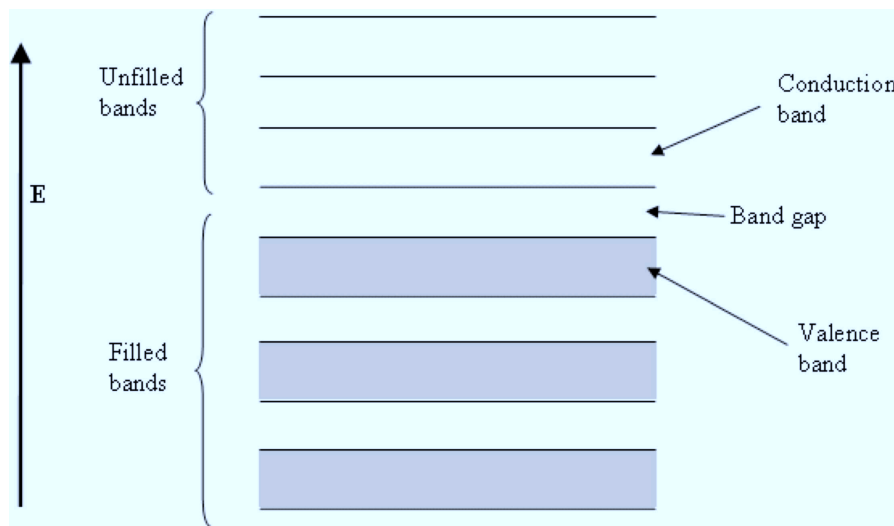


FIG. 2.10: Sketch of the semiconductor energy bands.

2.5 The Semiconductor Doping

On the other hand atoms with one less valence electron can be used in order to result in *p-type* material. In the latter type material, the number of electrons trapped in bonds is higher, thus effectively increasing the number of holes. In doped material, there is always an excess of one type of carrier compared to the abundance of the other. The type of carrier with the higher concentration is called a *majority carrier* while the lower concentration carrier is called a *minority carrier*. The amount of impurity, or dopant, added to an *intrinsic* (pure) semiconductor can differentiate the level of conductivity. Doped semiconductors are also often referred to, as *extrinsic*. Let us examine the case

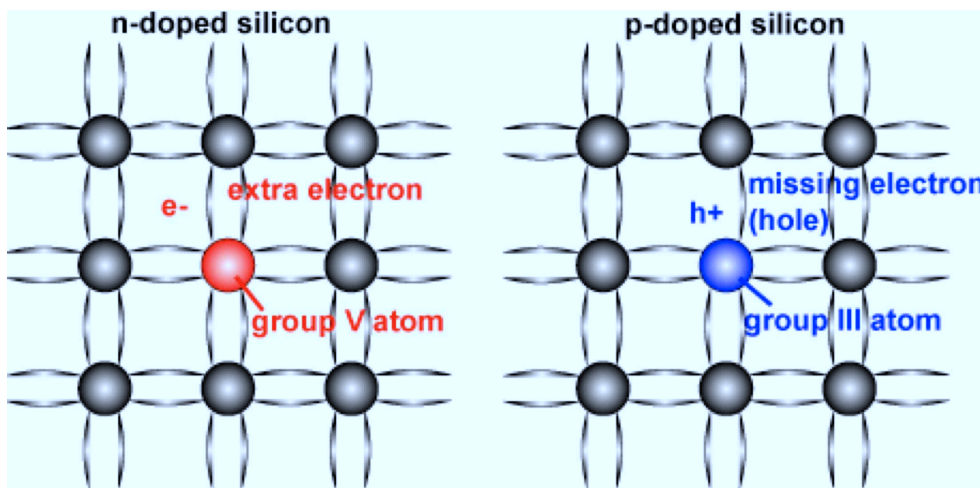


FIG. 2.11: Sketch depicting the *n* (left) and *p* (right) doping in silicon.

of silicon, a tetravalent element, which is doped with other elements that have 3 or 5 valence electrons. In this manner charge carriers in a quasi-free energy state are created.

2.5.1 The n-doping

A pentavalent dopant is called *donor* Figure 2.11 (*left side*) because one of the valence electrons is in a relatively *loose* bound state. The supplementary ionised electrons can create holes in every atom of the dopant. The holes not being able to move in the region, force a valence electron to migrate towards the energy state of a free electron of the dopant material, making available energy sum of E_G . Overall, the doping has two effects. First of all it creates an asymmetry between the charge carrier. In the case of a doping with an element V of the periodical table, the carriers are the electrons when at the same time the holes are the minority. As a global effect, the material conductivity is enhanced.

2.5.2 The p-doping

In the case of the doping using a trivalent atom Figure 2.11 (*right side*), an acceptor is introduced over the higher energy level of the valence energy band. The conduction process is performed primarily via the holes, e.g. a valence electron can create a hole in the valence band that is free to move. The conductivity of the doped semiconductors is a lot more enhanced than that of the *intrinsic* ones. The usage of the such a material for particle detection purposes, could not have been attained, had it not been for the

pn junction presenting a relatively low conductivity. The latter will be the topic of discussion of Section 2.6.

2.6 The Inversed PN Junction

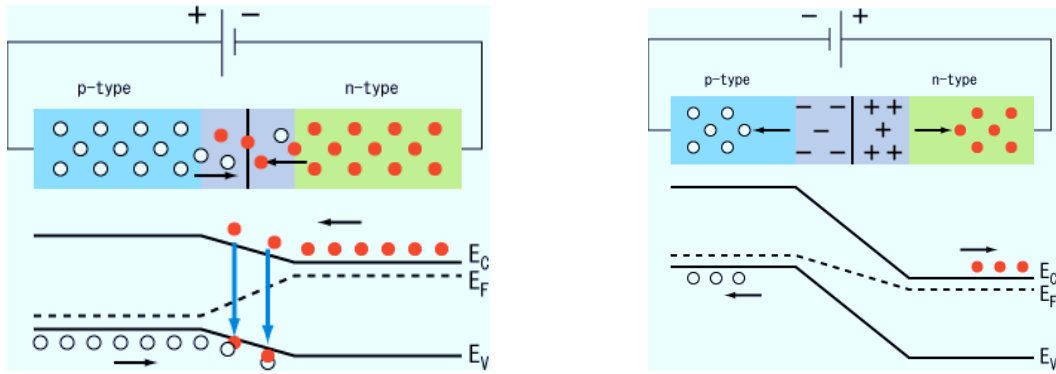


FIG. 2.12: PN Junction. *Left:* In forward bias. *Right:* In inverse bias.

Let us consider a *n*-type crystal, with a concentration N_D of atoms-donors. Also let us call N_A the concentration of atom-acceptors. In this zone where, $N_A \gg N_D$ the conduction is performed by the holes that drift in the *n* region leaving the atom acceptor –where they originate– with negative charge. In the same way, electrons coming from a *n* region, will drift towards the *p* region, resulting in positive atom donors. The intermediate zone *p-n* contains no more drifting charges, cf. Figure 2.12, thus called *space charge region* or *depletion layer*. The above procedure has as a result, the creation of ionized zones. In the zone of contact of *n-p* there are no more volatile charges, thus calling it *deserted*. In addition, due to the separation of different species of charges, an electric field is created. In the state of (thermal) equilibrium, and in the absence of an external electric field, there is no diffusion of holes and electrons. Obeying to the Fermi-Dirac statistics, the chemical potential for the two zones are equal. The difference of energy levels of the E_V (*p*-type) and E_C (*n*-type) is around 1 eV that the external field has to overcome. Therefore the applicable voltage is of the order of few Volts region and the deserted zone extends to a few microns. In order to augment the number of carriers in the silicon, an external field is to be applied (potential V_{pn}) between the *p* and *n* regions, thus talking about inverted voltage, in the deserted region.

2.7 The Semiconductors in Particle Detectors

Materials like Silicon and Germanium, can be used in order to detect charged particle. In particular, when a charged particle passes through the semiconductor medium, electron-hole pairs are generated Figure 2.13, which later on are collected by the applied electric field. Due to their density, semiconductors, offer a greater *stopping power* than gaseous. An extra advantage of the semiconducting over the gaseous detectors is that the energy for the creation of an electron-hole pair is around 10 times smaller than the gas ionization [Leo 92], allowing an increased energy resolution. Except for silicon, in general these detectors require cooling, in order to operate, to low temperature. Also due to their crystalline material structure, they are severely affected by the radiation damage, yielding in a limited long term use.

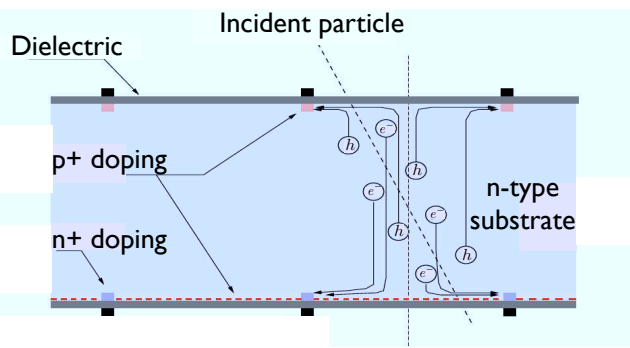


FIG. 2.13: Cartoon of a charged particle passing through the SSD module creating pairs of electrons (e^-) and holes (h^+).

2.8 The STAR Inner Silicon Detectors

The Inner Silicon Tracking system of STAR experiment, consists of the Silicon Vertex Tracker (SVT) and the Silicon Strip Detector (SSD), as seen in Figure 2.14. The detector was included in the runs for years 2004 to 2007. Both detectors have served the *strangeness* physics program [Timmins 09a], and oriented towards the physics of *charm*. The alignment and the drift velocity calibrations were re-visited to see if it is possible to perform direct D -meson measurement and whether the B -meson tagging is feasible. Finally, the ensemble of the silicon detectors, will be substituted by one of the future STAR upgrades: the HFT (cf. Section 2.22), keeping the SSD as the third layer.

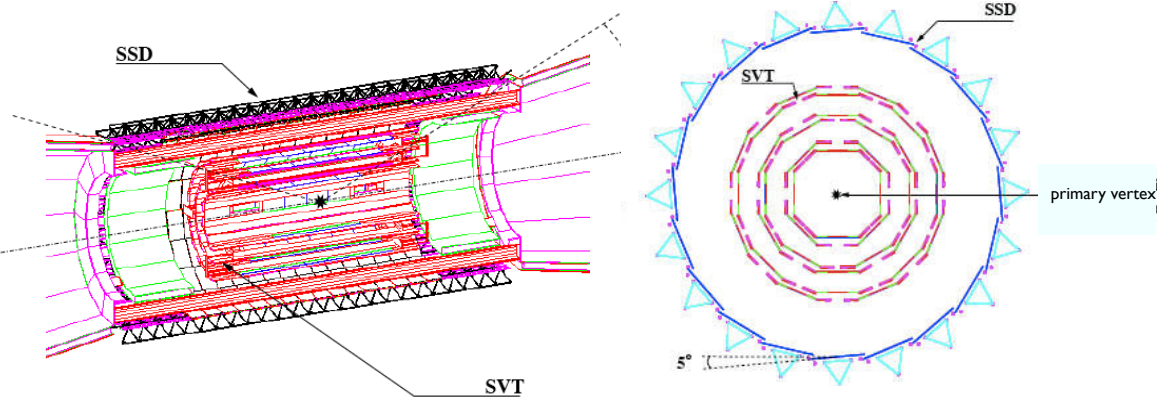


FIG. 2.14: Schematic depiction of the Inner Silicon Detectors of STAR. *Left:* Inside the beam cone. *Right:* Beam view (xy). Figures taken from [Suire 01].

2.9 The Silicon Vertex Tracker

In order to improve the tracking of the low transverse momentum ($p_T < 150 \text{ MeV}/c$) particles and detection of short-lived hadrons such as strange baryons and K_S^0 , STAR experiment is equipped with a tracker that sits close to the beam pipe and has high resolution, $25 \mu\text{m}$ for space points and $500 \mu\text{m}$ for a two-track resolution. The Silicon Vertex Tracker (SVT) shown in Figure 2.14, consists of three cylinder layers of silicon drift detectors with their inner boundaries at distances $r = 6.37, 10.38$ and 14.19 cm from the center of the beam pipe. The SVT consists of 216 p -type $6.3 \times 6.3 \times 280$ ($[W \text{ [cm]} \times L \text{ [cm]} \times H \text{ [\mu m]}$) silicon wafers [Bellwied 03], distributed as follows:

1st layer: 8 ladders (4 wafers);

2nd layer: 12 ladders (6 wafers); and

3rd layer: 16 ladders (7 wafers);

Each detector's layer is relatively thick ($1.5 X_0$) and the intrinsic spatial resolution is $\sigma_{r-\phi} < 80 \mu\text{m}$ and $\sigma_z < 80 \mu\text{m}$. Each wafer is divided into two halves by a central cathode to minimize the drift distance for the electrons (Figure 2.15).

The electrons drift to the nearest anode, located at opposite ends of the silicon wafer. There are 240 anodes in each drift direction. The electron drift speed at the maximum applied anode voltage of 1500 V (which corresponds to a field of approximately 500 V/cm) is $6.75 \mu\text{m/ns}$, yielding a maximum drift time of $4.5 \mu\text{s}$ [Bellwied 03]. The SVT combines two principle of detection: *semiconductivity* and *ionization*, both of which are discussed in Sections 2.4 and 2.11.

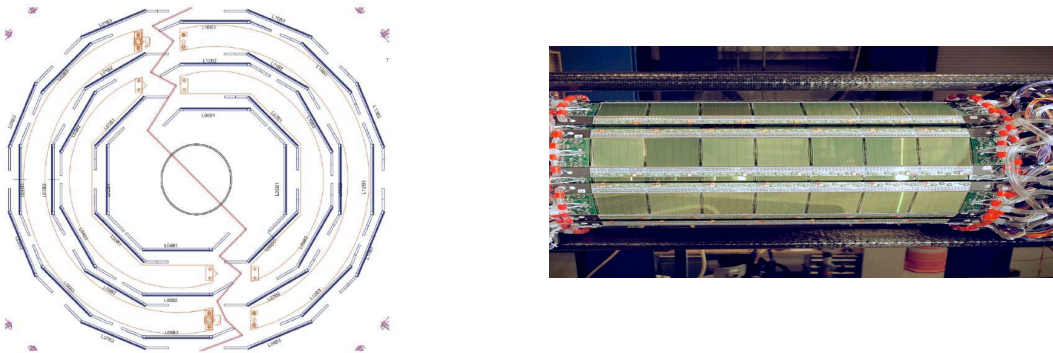


FIG. 2.15: The STAR Silicon Vertex Tracker. *Left:* Sketch of the detector in transverse view. Figure taken from [Matis 95]. *Right:* z view, installed inside the STAR beam cone. Figure taken from [Fisyak 07].

2.10 The Silicon Strip Detector

Then main purpose of the SSD, is to provide an intermediate, non-drifting point for track matching between the TPC and the SVT. The Silicon Strip Detector was partially installed for Run IV, and used for the physics analysis Cu+Cu dataset at $\sqrt{s_{\text{NN}}} = 200 \text{ GeV}$ (run V) data. It consists of 20 ladders of 100.60 cm in length and radius of 23 cm, (cf. Figure 2.16), covering a full azimuth and $|\eta| < 1.2$. Every ladder consists of 16 wafers, and each wafer of two sides, p and n -type. Every side of each wafer has 768 Si strips, resulting in a total detection material surface of $\sim 1 \text{ m}^2$. The orientation of the strips can be seen in Figure 2.17. The *pitch* ($95 \mu\text{m}$) which is the distance between the strips, is chosen taking into account the accuracy of position measurement and the number of the read outs channels. Also the stereo-angle between the p and n -strips: is 35 mrad. Finally, the intrinsic resolution of the detector is $30 \mu\text{m}$ for the transverse and $860 \mu\text{m}$ in the z -direction.

When a minimum ionizing particle (*MIP*) traverses the $320 \mu\text{m}$ of the Silicon (Figure 2.13), loses approximately 84 keV . This energy is spent in the creation of approximately 23000 electron-hole pairs. The role of the SSD is to serve as an intermediate associative layer between the SVT and the TPC hits. In particular SSD will enhance the efficiency of the inner tracking ability, allowing a more precise measurement of the tracks emerging from the primary vertex. In addition to the above, the SSD can help the reconstruction of the strange particles from a secondary vertex, such as K_S^0 , Ξ^\pm , Λ and Ω^\pm . The *PN* inverted junction, Section 2.6 is used as the detection module which is kept under electric tension of couple of tenths of Volts. In Table 2.2 the characteristics of the detector are summarized.

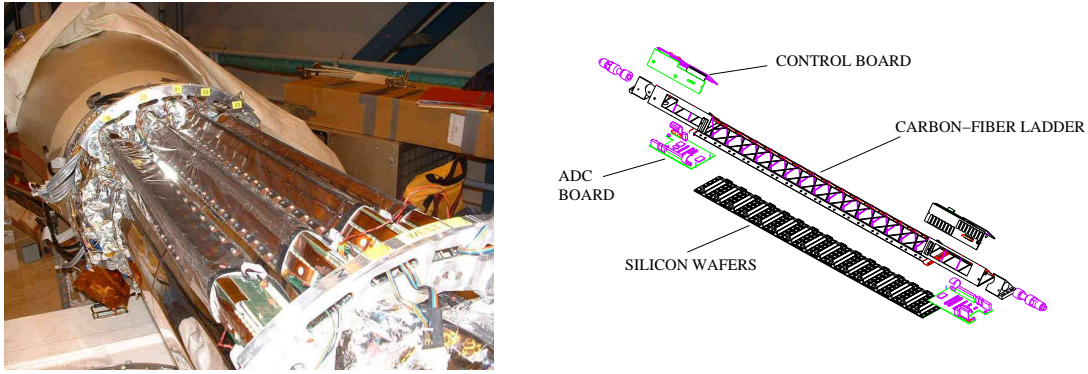


FIG. 2.16: *Left:* The SSD placed around the STAR beam cone. *Right:* Cartoon depicting one SSD ladder. Figure taken from [Arnold 03].

TAB. 2.2: SSD characteristics and operation values. Values taken from [Arnold 03].

| Summary of the SSD characteristics | |
|------------------------------------|---------------------------------------|
| Radius | 23 cm |
| Ladder length | 106 cm |
| Acceptance | $ \eta \leq 1.2$ |
| Numbers of ladders | 20 |
| Numbers of wafers per ladder | 16 |
| Total silicon surface | 0.98 m^2 |
| Total number of wafers | 320 |
| Number of strips per side | 768 |
| Number of sides per wafer | 2 |
| Wafer dimensions [L × W × H] | $73 \times 40 \times 15 \text{ [mm]}$ |
| $r-\phi$ resolution | $20 \mu\text{m}$ |
| z resolution | $740 \mu\text{m}$ |
| Operating voltage | 20–50 V |

2.10.1 The SSD Module

As mentioned above, the SSD is composed of 20 frame carbon structures as shown in Figure 2.16. Each one, supports 16 detection modules. A module is the basic element of the SSD and integrates a silicon wafer and its front-end electronics. The Si detector module is composed of:

- i. A double sided silicon strip detector;
- ii. 768 micro-strips per side of the detector;
- iii. 95 mm pitch;
- iv. 35 mrad stereo angle between p and n side;
- v. 4 cm of strip length; and
- vi. two hybrid circuits.

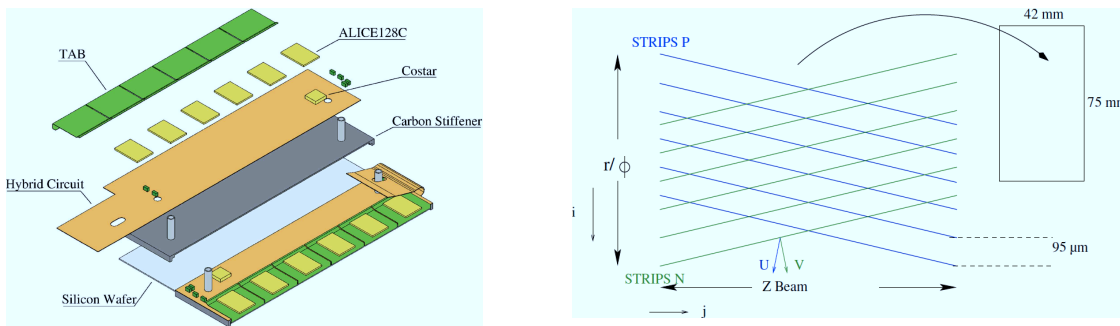


FIG. 2.17: *Left:* Sketch of the SSD module. *Right:* Stereoscopic view of the p and n strip orientation inside a SSD module. The beam axis (z), along with the local coordinate system in $r\phi$ as well as the dimensions and the pitch of the module, are clearly shown. Figures taken from [Martin 02].

In addition, each hybrid circuit, is composed of:

- i. One flexible circuit (made of kapton and copper) glued on a carbon fiber stiffener;
- ii. 6 analog readout chips: A128C; and
- iii. 1 multi-purpose control chip dedicated to temperature measurements, low and high voltage monitoring called COSTAR.

The connection between the strips on the detector and the analog inputs of the A128C chips, is ensured by a tape automated bonding (TAB). This bumpless technology is based on a kapton microcable onto which the copper strips are printed. The flexibility

of the cable allowing the folding of the hybrids circuits on top of the detector in order to make the detection module very compact. Furthermore, this cable plays the role of pitch adaptor between the 95 mm pitch of the detector and the 44 mm pitch of the chips on the hybrid circuit. The tape is also used to connect the A128C chips to the hybrid circuit.

SSD Pulsters

For calibration purposes of the read out electronics, a pulser generator for every A128C circuit is being used [Germain 02]. This generator allows the injection of a signal to every pre-amplifier allowing the simulation of a modifiable charge signal.

2.11 Energy Loss by Ionization

Charged particles when passing through a medium, will lose energy by ionization, that will be transferred to the knock-on electrons. Namely the *stopping power* $-\frac{dE}{dx}$ as predicted by the (2.1).

$$-\frac{dE}{dx} = Kz^2 \frac{Z}{A} \frac{1}{\beta^2} \left[\frac{1}{2} \ln \frac{2m_e c^2 \beta^2 \gamma^2 T_{max}}{I} - \beta^2 - \frac{\delta^2}{2} \right] \quad (2.1)$$

where:

z is the charge of the particle (expressed in units of q_e);

Z and A are the atomic number and atomic mass of the absorber;

m_e is the mass of the electron;

c is the speed of light *in vacuo*;

I is the average ionization energy of the material;

T_{max} is the maximum kinetic energy that a free electron can obtain within an interaction;

δ is a correction based on the electric density; and

$\beta\gamma = p/mc$, where p is the momentum of the particle and m its mass.

Let us also note that (2.1) is valid for charged particles heavier than electrons, and lighter than atomic nuclei (valid until α particles), because of the presence of the supplementary energy loss mechanisms. The electron case present the *bremsstrahlung*, emission of electromagnetic radiation arising from scattering in the electric field of the

nucleus. It is considerable for the case of electrons and positrons, since the emission probability varies as the inverse square of the particle mass [Leo 92]. The case of the atomic nuclei, exhibits additional difficulty, since the effective charge has to be taken into account.

2.12 The Time Projection Chamber

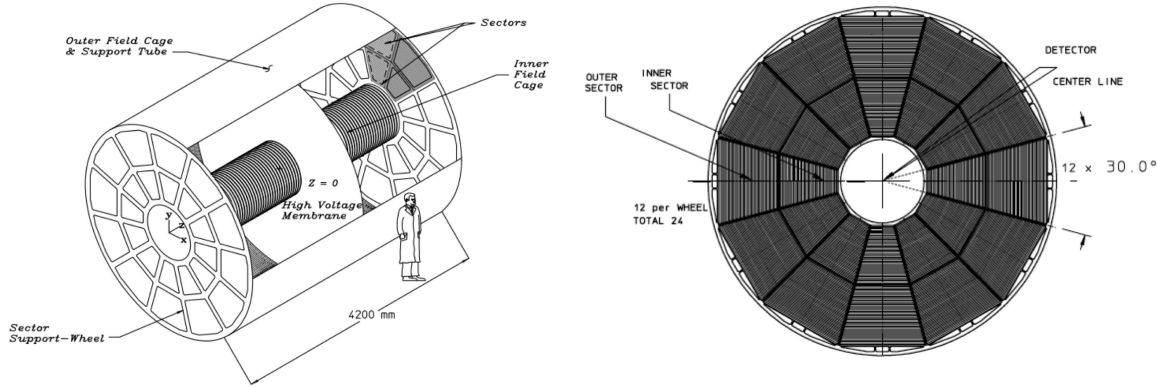


FIG. 2.18: The STAR Time Projection Chamber. *Left:* The dimensions are 4.2 m in length (z direction) and inner and outer sectors are situated at 0.5 m and 2 m respectively. *Right:* TPC Endcap. Figures taken from [Anderson 03].

The main tracking device at STAR is the Time Projection Chamber as it is sketched on the left of Figure 2.18, covering a full azimuth (2π) and $|\eta| < 1.8$. It serves to measure the track momentum by energy loss, due to the ionization of the gas. Surrounded by a uniform magnetic field along the z direction, the latter can be tuned to either *Reverse* or *Forward* field depending on the orientation ($-z$ or $+z$ respectively) and to *Half* or *Full* Field depending on the magnitude of the magnetic field, 0.25 T or 0.5 T respectively. The dimensions of the TPC are 4 m in diameter, 4.2 m in length cylinder. At distances $z = \pm 210$ cm the read-out pads cover a radial distance r of (50, 200) [cm] from the center of the beam pipe. Also the inner TPC field cage is located at 50 cm.

The electrons' drift speed is relatively slow (5.45 cm/ μ s) and for high luminosities this can lead to *pile-up* events cf. Section 2.12.1, since the rate of STAR is 0.1 kHz. The central membrane acting as a cathode is held at -28 kV when at the same time the outer field cages are grounded thus generating an electric field of 135 V/cm in the z direction. Each side, is divided into 12 sectors, as shown on the right side of Figure 2.18, that are equivalently divided into 45 padrows, 13 on the inner subsector, equipped with smaller pads (2.85×11.5 [mm]) and 32 rows of larger (6.20×19.5 [mm]) pads on the outer subsector.

As the charged particles emerging from the collision point, are passing through the gas, the *knock-on* electrons are accelerated towards the anodes (endcaps). Before actually hitting the read-out board (RDO), there are Multi-Wire Proportional Chambers (MWPC) where the *avalanche* takes place. In particular one drift electron is able to produce some thousands of *avalanche* electrons, and the latter ones finally are detected from the RDO's, as an enhanced signal.

For a given track (represented by a *helix*, cf. Appendix D.1) of a charged particle in a uniform magnetic field \mathbf{B} along z -axis, the magnitude of the transverse momentum p_T is given by the following *handy* formula (cf. Appendix D.3):

$$p_T = 0.3BRq \quad [\text{GeV}/c] \quad (2.2)$$

where q_e is the absolute particle's charge value (expressed in units of the electron charge) and R it's radius of curvature in m. The magnitude of magnetic field, B , is expressed in T. The total momentum is calculated using this radius of curvature and the angle that the track makes with respect to the z -axis of the TPC. This procedure works for all primary particles coming from the vertex, but for secondary decays, such as Λ or K_s the circle fit must be done without reference to the primary vertex. Energy loss in the TPC gas is a valuable tool for identifying particle species. It works especially well for low momentum particles but as the particle energy rises, the energy loss becomes less mass dependent and it is hard to separate particles with velocities $v > 0.7c$. STAR is designed to be able to separate pions and protons up to 1.2 GeV/c, Figure 2.19. This requires a relative $\frac{dE}{dx}$ resolution of 7%. The gas that is contained in the TPC, is a mixture of Ar and CH₄ in a 90 : 10 proportion, called *P10*, kept under pressure of 2 mbar over the atmospheric in order to prevent the possibility of contamination of the gas ingredients [Anderson 03]. The principle of detection that TPC is using is described in detail in Section 2.11. Finally let us also mention the spatial resolutions for the r - ϕ and z components

- i. $\sigma_{\text{DCA}_{xy}} = 600 \mu\text{m}$ and $\sigma_{\text{DCA}_z} = 1200 \mu\text{m}$ for the inner sectors; and
- ii. $\sigma_{\text{DCA}_{xy}} = 1200 \mu\text{m}$ and $\sigma_{\text{DCA}_z} = 1600 \mu\text{m}$ for the outer sector.

2.12.1 The TPC Cluster Reconstruction

After the collision takes place, the ionization clusters are found, separately in x , y and z coordinate space [Anderson 03]. The x and y positions of a hit are found by fitting a Gaussian to the distribution of the pixel clusters located at a given pad. In order to measure the z position of a hit, one needs to know the distance traversed by the electron cloud and the drift velocity at the time of drift. The drift velocity is calculated using calibration data available from daily laser runs (cf. Section 2.12.2), while the distance

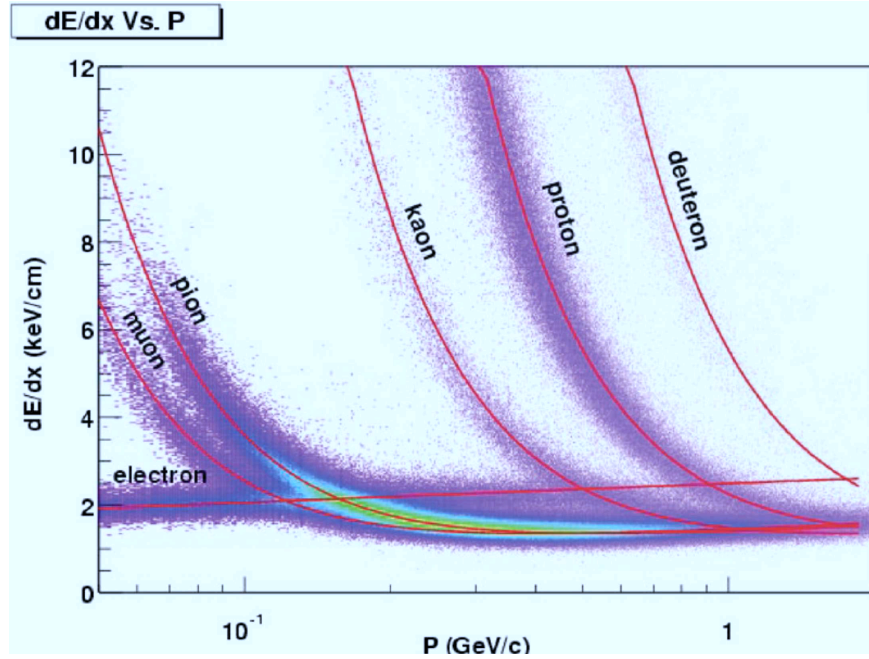


FIG. 2.19: Energy loss distribution for primary and secondary particles in the STAR TPC as a function of the momentum p of the particle track. Figure taken from [Anderson 03].

drifted by the electron cloud is calculated by measuring the time of arrival of the electrons on the pad in time buckets and then weighting the average of these by the number of electrons collected in each bucket. The drift velocity is monitored by laser system with precision $2 \cdot 10^{-4}$ providing systematic error in z direction of $400 \mu\text{m}$ at the maximum drift length (2 m) [Fisyak 07]. Once the track is found, the total $\frac{dE}{dx}$ of the particle can be calculated by using all padrows that were affected by the particle's passage. The length over which the energy loss occurred is calculated after taking into account the *dip* and the *crossing angle* which are the angle between particle momentum and the direction of the electron drift, and the angle between particle momentum and the read-out plane, respectively. Let us also note that the reconstructed tracks are classified into *primaries* and *globals* (cf. Appendix E) depending on whether the point of the primary vertex was taken into account concerning the reconstruction of the track [Pruneau 03].

Pile-Up

The slow drift speed in the TPC, leads to a low event rate 0.1 kHz for STAR as compared to 10 kHz for PHENIX [Franz 08]. Pile-up occurs when the collision rate starts to become comparable with the electrons drift time in the TPC. This effect

leads to events from previous bunch crossings being recorded with the event from the triggered bunch crossing. In Figure 2.20 it is shown a different set of cases of pile-up.

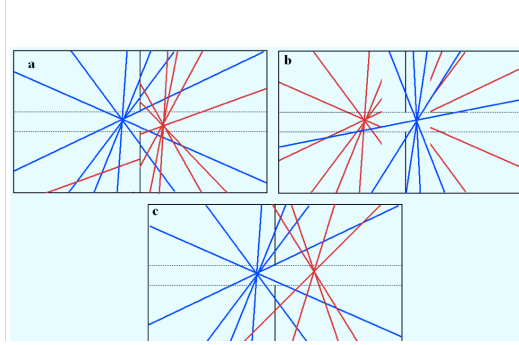


FIG. 2.20: Cartoon depicting Pile-Up events, with the vertex in blue is constructed from the collision that fired the trigger, while the vertex in red is a pile-up vertex. (a): after, (b): before and (c): same bunch crossing. Figure taken from [Reed 09].

The pile-up collision for (a) occurred after the triggered collision (post-crossing), which means that the tracks associated with the triggered collision had already drifted away from the TPC Central Membrane. In (b) the pile-up collision happened before the triggered collision, so the tracks from that collision had already started to drift down the TPC when the trigger was fired, and in (c) shows within bucket pile-up, where both collisions happen within the same bunch crossing. Finally, let us mention that the pile-up conditions are manageable for high-multiplicity events, where the primary vertex can be reconstructed and the tracks sorted out. However, in low-multiplicity collisions such as in p+p, pile-up can become a problem.

2.12.2 The TPC Laser System

The STAR Physics program demands a 10% momentum resolution for $p_T = 10 \text{ GeV}/c$, which is translated in a resolution of $\sim 200 \mu\text{m}$ and an error in the z direction not more than $1000 \mu\text{m}$. The UV laser system of the TPC, serves in order to have an updated image of the TPC concerning the value of the drift velocity and the morphology of the detector [Abele 03]. There are many factors that can interfere, such as:

- i. Variation in drift velocity caused by gas mixture, temperature, pressure and electric field variation;
- ii. detector misalignment in the magnet;
- iii. radial inhomogeneities of magnetic and electric field;

- iv. space charge build-up due to high multiplicity, especially in Au+Au collisions; and
- v. TPC endcap displacement and inclination.

The Nd-YAG laser[†] of wavelength $\lambda = 266\text{ nm}$ allows to simulate the passage of a *MIP* track, by ionizing the gas' organic substances, (abundance in $\sim p.p.b$) via the *two photon* process.

2.13 The Forward TPC Modules

Situated at $162.75 < |z| < 256.75\text{ cm}$ position from the interaction point $z_0 = 0$, the two Forward Time Projection Chambers (FTPC) [Ackermann 03] provide an extension of STAR tracking ability in the region of $2.5 < |\eta| < 4.0$. As it can be seen in Figure 2.21 each module presents a cylindrical symmetry around the z axis. The length of each detector is 120 cm and its diameter is 75 cm. The drift region is extended up to 23 cm.

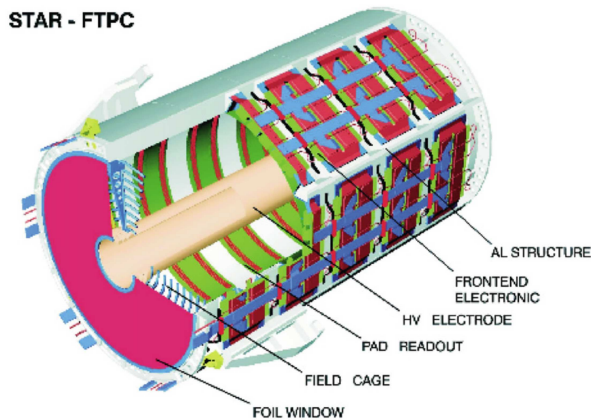


FIG. 2.21: Perspective of STAR FTPC. Figure taken from [Ackermann 03].

Although the principle of detection is similar to the TPC, as described in Section 2.11, there is a difference between the two detectors. In particular the drift velocity of the electrons in the FTPC is perpendicular to the STAR magnetic field, since in FTPC $\vec{E} \perp \vec{B}$, where in TPC $\vec{E} \parallel \vec{B}$. The radial drift configuration was chosen to improve the two-track separation in the region close to the beam pipe where the particle density is highest. The radial drift field as well as the readout chambers are mounted on the outer cylindrical surface. The FTPC is capable to reconstruct all charged tracks (~ 1000) traversing the detector in a central Au+Au collision. The

[†]neodymium-doped yttrium aluminium garnet Nd: Y₃Al₅O₁₂

selection of the FTPC gas was done taking under consideration the low coefficient of diffusion for the electrons. The mixture of Ar/CO₂ was finally chosen [Ackermann 03] in 50:50 proportion.

2.14 The STAR Calorimetry

The ensemble of the Barrel (BEMC) along with the Endcap Electromagnetic Calorimeter (EEMC), consist the main system that perform the calorimetry in STAR. The BEMC is effectively used to identify electrons, including single electrons as a result from heavy quark decay, neutral pions π^0 and photons γ [van Buren 08].

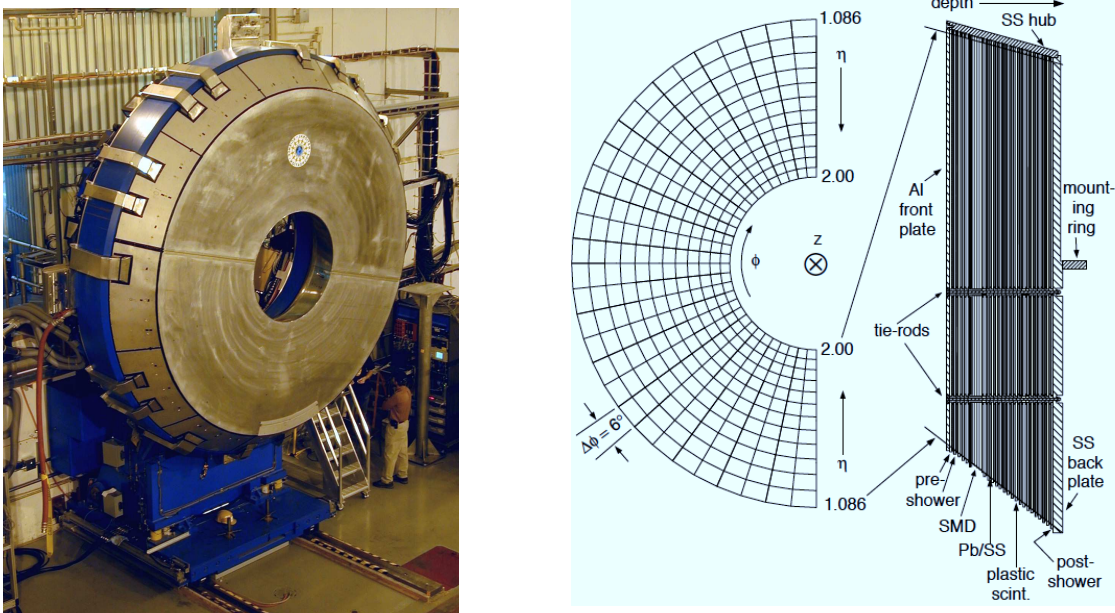


FIG. 2.22: *Left:* Photo of STAR Endcap Electromagnetic Calorimeter inside the STAR experimental hall. *Right:* The half part of the total 720 towers. The towers are projective, with edges aligned with the center of the beam intersection region, 2.7 m distant along the z -axis from the EEMC front face. Towers span $\Delta\phi = 0.1$ in azimuthal angle, and varying size in pseudorapidity $\Delta\eta = [0.057, 0.099]$. Each tower has 23 layers of lead/stainless steel absorber interleaved with 24 layers of plastic scintillator. Figures taken from [Allgower 03].

2.15 The Endcap Electromagnetic Calorimeter

The greatest demand for such forward calorimetry arises from the program of experiments to be carried out with colliding polarized proton beams at RHIC. One of the

most important goals of this program is to determine the helicity preference for gluons $\Delta g(x)$ inside the polarized proton, as a function of the fraction x_g of the proton's momentum carried by the gluon, and to constrain strongly the net gluon contribution to the proton's spin, given by the integral of this quantity over x_g [Allgower 03]. The gluon polarization can be probed in quark-gluon Compton scattering, by the longitudinal spin correlations, the difference divided by the sum of cross sections for equal versus opposite beam helicities—for direct photon production at transverse momentum transfers $p_T \geq 10 \text{ GeV}/c$. The Endcap Electromagnetic Calorimeter [Allgower 03] covers $1 < \eta < 2$, as can be also seen in Figure 2.5. It includes a scintillating-strip shower maximum detector in order to provide π^0/γ discrimination and preshower and postshower layers in order to provide the separation between electrons and charged hadrons. At the energies of interest, the most probable lab-frame opening angle between the two photons $\phi_{min}^{\gamma\gamma} = 2 \sin^{-1} \frac{m_{\pi^0}}{E_{\pi^0}}$ can be as small as 10 mrad [Bland 99].

The choice of a traditional Pb/plastic scintillator for the EEMC towers shares the same technology with the ones of the BEMC. Let us also note that due to the focus on p+p analyses rather than A+A, the demand on tower segmentation is less constrained when compared to the STAR BEMC (Section 2.16). The mesons are produced via significantly larger cross sections than the direct photons, as a part of the fragmentation of hard-scattered quarks and gluons. It is therefore essential for the EEMC to have a Shower Maximum Detector (ESMD), to further distinguish single photons from photon pairs. Placed at about 5 radiation lengths (X_0) inside the EEMC, the SMD is a specially configured layer designed to provide the fine granularity crucial to distinguishing the transverse shower profiles characteristic of single photons vs. the close-lying photon pairs, organized into orthogonal u and v planes. The active material of the ESMD is the plastic scintillator. Such a design and similar techniques have been developed by the DØ collaboration [Adams 96] for use as a tracking preshower detector. The SMD is made of extruded polystyrene based scintillator strips. Finally the energy resolution is given by (2.3).

$$\frac{\sigma_E}{E} \leq \frac{12}{\sqrt{E \text{ [GeV]}}} + 2 [\%] \quad (2.3)$$

2.15.1 The Endcap Pre Shower Detector

There are two preshower and one postshower readouts from the layers of the endcap towers. The calibration is achieved by using the MIP signals.

2.16 The Barrel Electromagnetic Calorimeter

The Barrel Electromagnetic Calorimeter [Beddo 03] is located inside the magnet and covers a full azimuth and $|\eta| \leq 1$ matching the TPC acceptance. The calorimeter is

divided into two barrels covering $-1 \leq \eta \leq 0$ (East) and $0 \leq \eta \leq +1$ (West). Inner and outer radii are 223 cm and 263 cm, respectively. The length of the detector is 293 cm along the z -axis. Every barrel is segmented in azimuth, in 60 modules, each module is of approximately 26 cm wide and covers 6° , as shown in Figure 2.23.

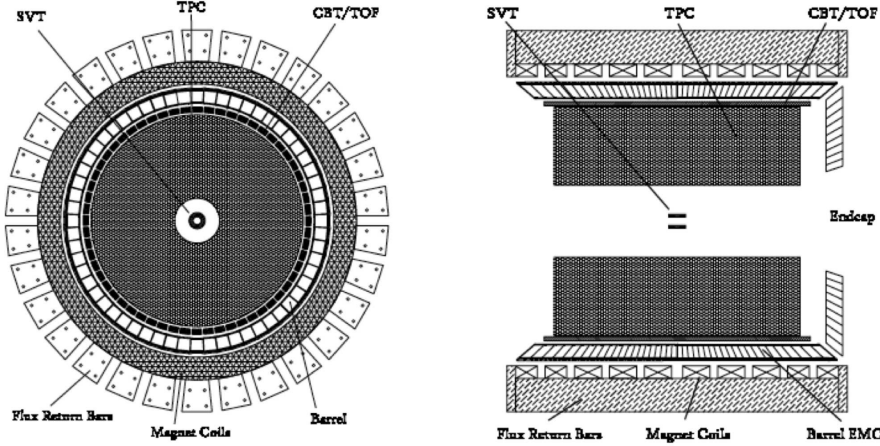


FIG. 2.23: STAR Barrel Electromagnetic Calorimeter. *Left:* Transverse view. *Right:* z view. Figures taken from [Beddo 03].

The modules are grouped then into 40 projective towers of Pb-scintillator modules. A detail of the BEMC module can be shown in Figure 2.24. Each tower is covering an area of $\Delta\eta \times \Delta\phi = 0.05 \times 0.05$, yielding a total number of 2400 towers for each half barrel. The tower is constructed of two stacks, inner and outer. The inner consists of a 5 layers of lead (Pb) and 5 layers of scintillator, sandwiched together and the outer stack of 15 layers of lead and 16 layers of scintillator. Each layer is 5 mm in thickness. Finally, the energy resolution of the detector is given by (2.4).

$$\frac{\sigma_E}{E} = \frac{16\%}{\sqrt{E \text{ [GeV]}}} \quad (2.4)$$

Additionally, between the inner and the outer sector the Shower Maximum Detector (SMD), is being placed at a $5 X_0$ depth. The latter detector is discussed thoroughly in Section 2.16.2.

2.16.1 The Barrel Pre Shower Detector

The Pre Shower Detector (PSD) contains the first and second scintillating layers of each calorimeter module. A separate read-out is being used, with the use of two Wave

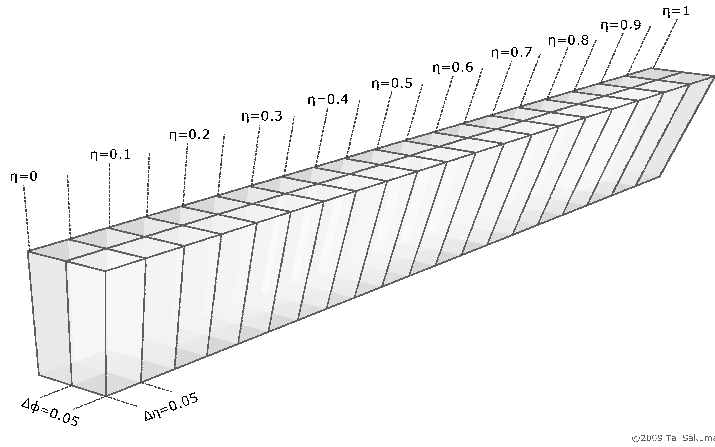


FIG. 2.24: Detail of the BEMC detection module. Figure taken from [Sakuma 10].

Length Shifting (WLS) fibers, illuminating a single pixel of the multi-anode PMT. In total of 300 16-pixel multi-anode PMT's are used to provide the 4800 tower preshower signals. The main purpose of this detector is to provide a photon versus electron versus hadron shower identification.

2.16.2 The Barrel Shower Maximum Detector

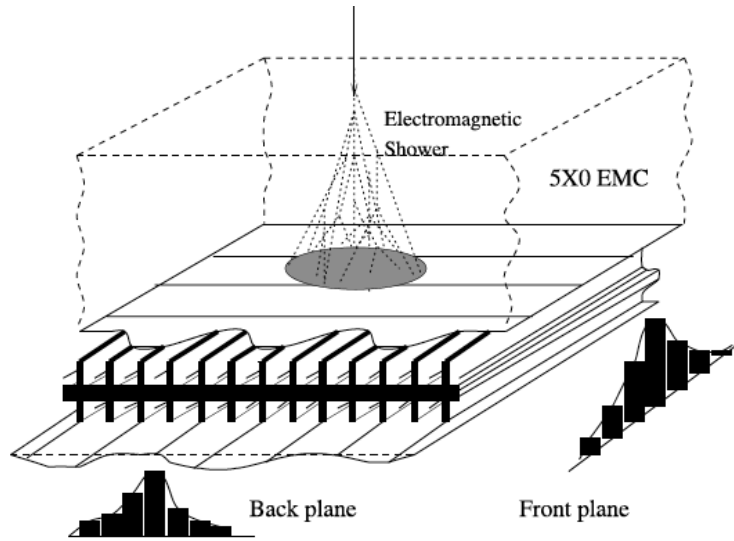


FIG. 2.25: The STAR Shower Maximum Detector. Figure taken from [Beddo 03].

The Shower Maximum Detector (SMD) is a multi-wire proportional counter with strip readout. Located after the BEMC, it covers $|\eta| \leq 1$ and has $5.6 X_0$ at $\eta = 0$ and increases to $7.9 X_0$ near the edges, $\eta \rightarrow 1$, as can be seen in Figure 2.24. It serves to improve the spatial resolution of the calorimeter, and to separate the γ showers coming from high- p_T neutral meson decays such as π^0 and η . The energy resolution of the detector is given by (2.5).

$$\frac{\sigma_E}{E} \Big|_{\eta} = 12 + \frac{86}{\sqrt{E \text{ [GeV]}}} [\%] \quad (2.5)$$

In the ϕ plane the energy resolution is worsened by 3–4%. The detector consists of two planes: η (front plane) and ϕ (back plane), with spatial resolutions stated in (2.6) and (2.7).

$$\sigma_{r-\phi} = 2.4 + \frac{5.6}{\sqrt{E \text{ [GeV]}}} \text{ [mm]} \quad (2.6)$$

$$\sigma_z = 3.2 + \frac{5.8}{\sqrt{E \text{ [GeV]}}} \text{ [mm]} \quad (2.7)$$

All values in (2.5)–(2.7) are taken from [Beddo 03], and a sketch of the SMD layer behind the EMC, can be seen in Figure 2.25.

2.17 The Forward Meson Spectrometer

In the context of the upgraded forward instrumentation in STAR, the FMS serves to measure in large η (forward rapidity) the neutral pions π^0 . The ultimate goal is the measurement of the gluon distribution $xg(x)$, in nuclei in the range of $0.001 < x < 0.1$. Let us also note that the function $g(x)$ describes the differential probability to find gluons with a fraction x of the longitudinal momentum of the parent nucleon.

The FMS detector is a $2\text{m} \times 2\text{m}$ wall of 1264 lead glass detectors, as shown in Figure 2.26, penetrated through its center by the vacuum pipe traversed by the beams before they collide at the center of STAR. In order to maximize the ability to distinguish single photons from pairs of photons produced by π^0 or η decay, the FMS detector is located as far from the interaction point as possible, ultimately limited by the location of the DX magnet cf. Section 2.3.4, west of the STAR interaction point.

The FMS faces the blue beam (cf. Section 2.1), and reconstructs particles produced at small angles ($\sim 2.5 < \eta < 4.0$) via the detection of their decay photons. The latter ones are viewed through the large holes in the poletips of the STAR magnet. Let us also underline the importance of the construction of the FMS at STAR being a partial realization of the long-sought *full-acceptance* collider detector. In particular the STAR barrel EMC spans $|\eta| < 1.0$, the Endcap EMC spans $1.08 < \eta < 2.0$ and finally the FMS spans $2.5 < \eta < 4.0$, all with full azimuthal acceptance, albeit with small acceptance gaps [Bland 05].

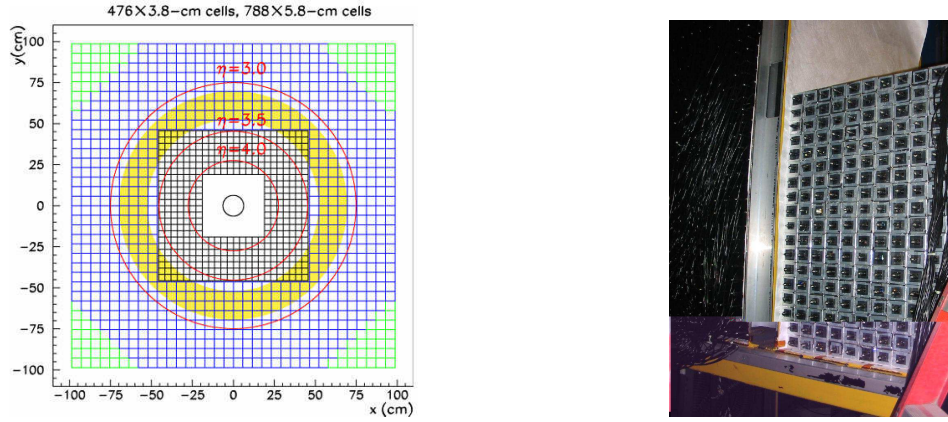


FIG. 2.26: *Left:* Schematic view of STAR forward meson spectrometer as seen from the interaction point. The *blue* beam penetrates into the page at the center of the matrices. *Right:* The north half of the FMS after stacking was completed, before the monitoring panels were put in place and before the calorimeter was sealed. Figures taken from [Jacobs 09].

2.18 The Forward GEM Tracker

The STAR collaboration is preparing a tracking detector upgrade to further investigate fundamental properties of the new state of strongly interacting matter produced in relativistic heavy ion collisions at RHIC and to provide fundamental studies of the proton spin structure and dynamics in high energy polarized p+p collisions at RHIC. In this context, the current proposal is one component of the upgrade program, called the Forward GEM (*Gas Electron Multiplier*) Tracker (FGT). The goal of the detector, is to focus on the novel spin physics measurements in high-energy polarized proton-proton collisions [Surrow 07]. The discrimination of $\bar{u} + d(\bar{d} + u)$ quark combinations requires the ability to discriminate between high- p_T e^\pm through their opposite charge sign, which in turn requires precise tracking information.

An upgrade of the STAR forward tracking system is needed to provide the required tracking precision for charge sign discrimination, shown in Figure 2.27. This upgrade will consist of six triple-GEM detectors with two dimensional readout arranged in disks along the beam axis z , referred to as the Forward GEM Tracker. The charge-sign discrimination of high- p_T e^\pm to distinguish W^\pm bosons in the range $1 < \eta < 2$ will be based on the use of a beam line constraint, precise hit information from the six triple-GEM disks, hits from the TPC, and the electromagnetic cluster data from the shower-maximum detector of the STAR EEMC. Information from the already installed detectors (in the absence of FGT) is insufficient.

The principle of detection is that charged particles ionize gas in the top detector volume of a triple-GEM detector and some of the primary ions generate secondary ionization. Diffusion smears the charge cloud transversely until it reaches the first

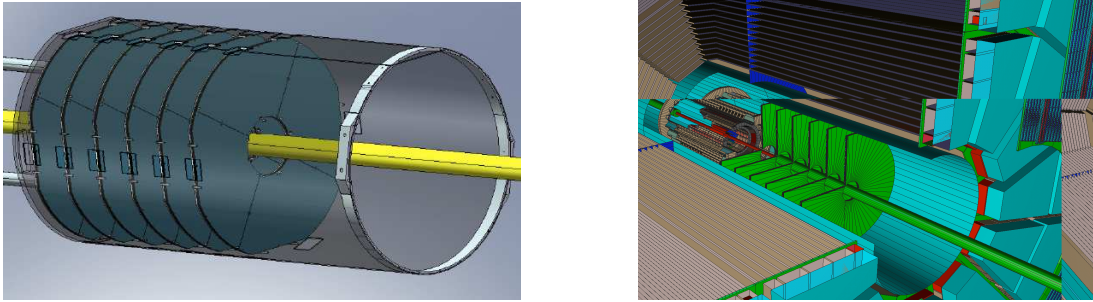


FIG. 2.27: *Left:* 3D-view of the FGT as modeled by the mechanical engineering design tool called SolidWorks. *Right:* 3D-view of the STAR inner and forward tracking region as implemented in the GEANT model of the STAR detector (STARSIM). Figures taken from [Surrow 07].

GEM foil. As a consequence, the charge cloud follows the electric field lines and its position gets quantized on the hexagonal grid holes in the GEM foil and further diffused. As a final step, the amplified charge cloud passes the third GEM foil and is collected by a handful of strips in each plane.

2.19 The Time of Flight Detector

The particle identification at mid-rapidity is accomplished by several techniques but one of the most powerful is the measurement of the particles' energy loss ($\frac{dE}{dx}$) in the TPC gas. This technique works extremely well at momenta below the 1 GeV/c but is subject to ambiguous identification of pions, kaons, and protons above this value. These ambiguities can be resolved by measuring the time of flight (TOF) of the particles from the vertex to the outer radius of the TPC. The new TOF modules will be located at the outer radius of the TPC. The technology for the upgrade is relatively new [Bonner 03] since each module will use multi-resistive plate chambers (MRPC).

The TOF system will perform measurements with a time precision of 85 ps, or in other words, it will double the momentum range over which particles can be directly identified in STAR. In particular by combining the momentum p as measured in the TPC and the velocity β (measured by TOF).

$$m = p \sqrt{\frac{1}{\beta^2} - 1} \quad (2.8)$$

The β in the TOF is measured according to (2.9), by measuring the time interval Δt the time the particle crosses the space interval ΔL . For this reason, the p-VPD (Section 2.21) is used to trigger the initial time measurement.

$$\beta = \frac{\Delta L}{c \Delta t} \quad (2.9)$$

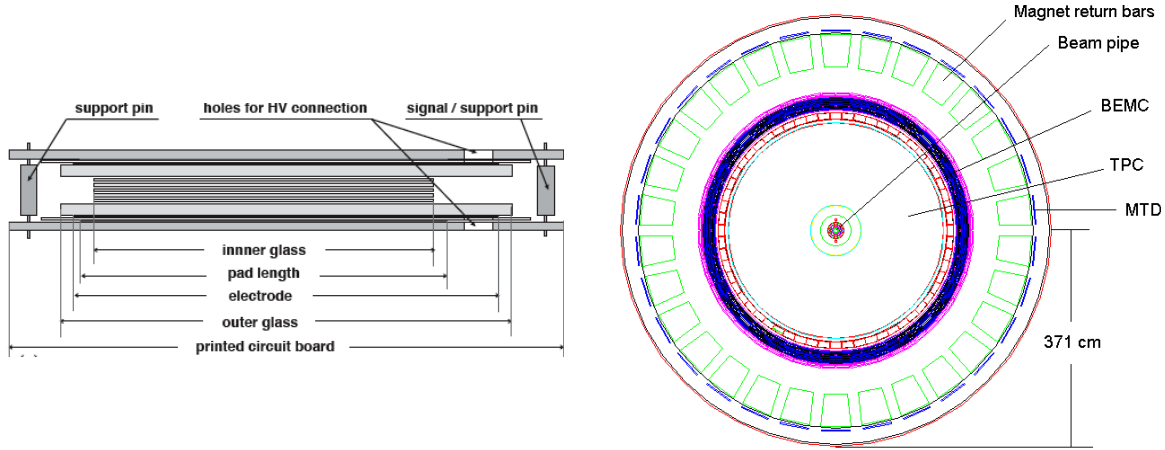


FIG. 2.28: *Left:* Detail of the MRPC that are used in the STAR Time of Flight detector. Figure taken from [Bonner 03]. *Right:* Sketch of the STAR Muon Telescope Detector. Figures taken from [Lin 09].

Concerning the D meson production, at moderate p_T , particle identification of the daughter K and π is possible, although these are separated by large gaps in rapidity and azimuthal angle (ϕ). As a consequence, the large acceptance of the proposed barrel TOF is essential to measure the $D^0 \rightarrow K^-\pi^+$ decay, since the decay kinematics of the D meson, can be fully reconstructed. The combinatorial background for the $K^-\pi^+$ candidates can be reduced, by a factor of 3 because of the identification of the decay daughters. It is calculated that in central Au+Au collisions the error is approximately 15% [Bonner 04].

The MRPC is basically a stack of resistive plates arranged in parallel. The use of the resistive plates is applied in order to quench the streamers so that they do not initiate a spark breakdown [Bonner 03]. The intermediate plates create a series of gas gaps. Electrodes are applied to the outer surfaces of the two outer plates and a strong electric field is generated in each subgap by applying a high voltage across these external electrodes. All the internal plates are electrically floating; they initially take the voltage as defined by electrostatics, but are kept at the correct voltage by the flow of electrons and ions produced in the gas by avalanches. When a charged particle passes through the chamber, it generates avalanches in the gas gaps. Since the plates are resistive they are transparent to the signal induced by avalanches, thus a signal induced in the pickup pad is the sum of signals from all the gas gaps.

The series of chambers have glass resistive plates with a resistivity of $5 \times 10^{12} [\Omega \cdot \text{cm}]$. The dimensions of the current module are $94 \text{ mm} \times 212 \text{ mm} \times 12 \text{ mm}$ and the active area is $61 \text{ mm} \times 200 \text{ mm}$. The devices are operated in avalanche mode, with a non-flammable gas mixture which contains 90 % of tetra-fluoroethane ($\text{C}_2\text{H}_2\text{F}_4$), 5 % of iso-butane (C_4H_{10}) and 5% of sulfur hexafluoride (SF_6). Each module is placed into

trays, (cf. Figure 2.28) and one tray can hold up to 32 modules. The dimensions of the tray are $241 \times 21.6 \times 8.9$ ($L \times W \times H$ [cm]). Around 120 trays are needed in order for the full azimuthal coverage to be attained.

2.20 The Muon Telescope Detector

At almost twice the radius of the new TOF system, it will be installed a new muon identification system that will allow the tracking and the identification of the decay of heavy flavor vector mesons at mid-rapidity. The proposed large-area MTD covers more than 50% azimuthal and $|\eta| < 0.8$ coverage behind the return iron bars for the magnetic field, as shown in Figure 2.28 (*left* side). This capability will be new and unique at RHIC. The essential technology will be the placement of double-stacked MRPC modules outside of the magnet iron that surrounds the TPC.

The signal from these detectors will be used to tag muons primarily coming from the collision vertex. Muons can easily penetrate the magnet iron, whereas the more abundant pions from the collision will either be stopped or create showers in the iron. Only at high transverse momentum ($p_T \geq 10$ GeV/c) can a significant fraction of pions penetrate the steel or create a shower that reaches the MRPC modules. The showers due to pions, can be rejected by precise timing measurements and good position resolution determined by the MRPC strips. In order to achieve even greater discrimination between the μ and π sample, a correlation of the particle's track in the TPC will be performed as well.

The shape of the track (perhaps including a decay *kink*) along with the energy loss ($\frac{dE}{dx}$) (in the TPC) of the track provide precious information about the track identity. In particular, the Monte Carlo simulations have suggested that muons and pions can be identified with a high reliability using the $\frac{dE}{dx}$ information. The latter statement can be interpreted that by performing a simple analysis procedure, it can be achieved a μ/π separation by a factor of 200. Along with the TOF detector (cf. Section 2.19), the rejection of all kaons and protons can be also performed. With this kind of discrimination, a very active program of the muon measurement in order to reconstruct the J/ψ and Υ at mid-rapidity can be pursued. Since muons, due to their mass, are less affected than electrons—by the Bremsstrahlung radiation energy loss in the detector materials—they can provide excellent mass resolution of the vector mesons ($J^P = 1^-$) and quarkonia. The latter is essential for the separation of the ground state ($1S$) of Υ from its excited ones: ($2S + 3S$) [Ruan 08].

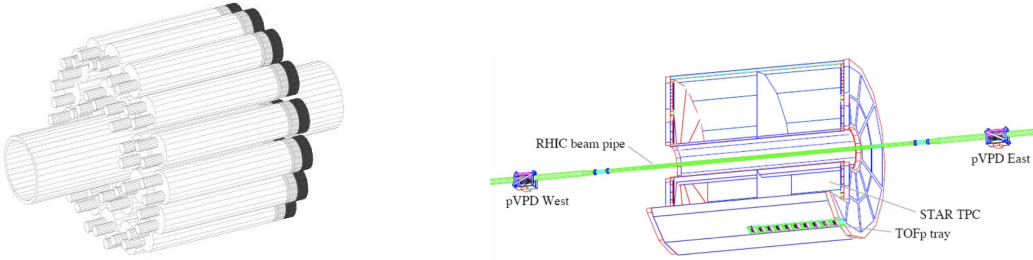


FIG. 2.29: *Left:* Detail of the STAR Vertex Position Detector *Right:* Position of TOFр in STAR detector and pV р along the beam axis. Figures taken from [Bonner 03].

2.21 The Pseudo-Vertex Position Detectors

The pV р consists of the two identical detector assemblies shown in Figure 2.29 one on each side of STAR very close to the beam pipe at a distance of $|z| = 5.6$ m from the center of STAR (z_0). The pseudorapidity coverage is $4.43 < |\eta| < 4.94$. The mounting structure consists of an aluminum base plate, two 1-thick machined Delrin face plates, and three welded aluminum rails, onto which detector elements are attached using pipe clamps. The base plate of the mounting structure clamps onto the aluminum. The on-detector electronics for the pV р are the same as those used in the TOFр tray (Section 2.19). Finally, the pV р signals travel over a similar signal path as for TOFр, and are digitized in the same CAMAC crate.

The specific detector is able to detect photons, generated during the collision and establish a t_0 (initial time measurement for the TOF. In particular, photons create electromagnetic showers in the Pb, that develop in the scintillator creating photons. The latter ones are finally gathered in the PMT's where via the *photoelectric effect*, electrons are being created. Due to the presence of the electric field, the electrons are focused by electrodes and oriented towards the dynodes, where the population of electrons is enhanced by the process of *secondary emission*.

2.22 The Heavy Flavor Tracker

In order to extend STAR's particle identification capabilities further into the heavy flavor domain, there will be installed several layers of high resolution silicon trackers starting with a *pixel* detector at 2.5 cm radius from the collision point. The full suite of detectors will be called the Heavy Flavor Tracker (HFT) [Xu 08b]. The proposed

configuration starts with two tracking layers of comprised monolithic CMOS (Complementary Metal Oxide Semiconductor) pixel arrays using 30×30 [mm] square pixels. The pixel layers will be situated at radii of 2.5 cm and 7.0 cm, respectively. They provide 135 pixels of information for every event studied.

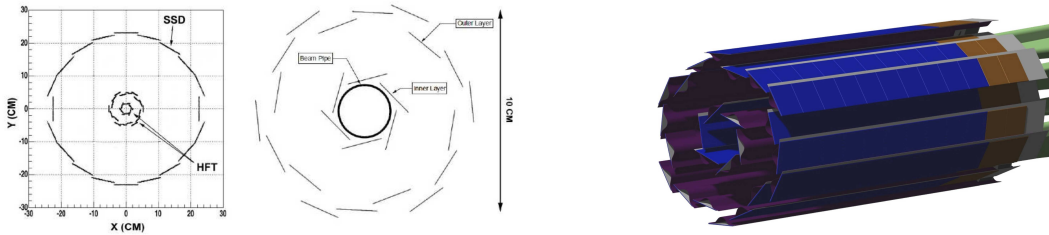


FIG. 2.30: The STAR Heavy Flavor Tracker. The first layer is the pixel detector and the second is the IST. The third is the SSD. *Left:* Beam view. *Right:* 3D view. Figures taken from [Xu 08b].

In order to provide graded resolution between the TPC and the pixel layers, two additional high rate conventional silicon barrel layers are proposed at intermediate radii of 12 cm and 17 cm. These Intermediate Strip Tracker (IST) layers provide space-points with high accuracy in $r-\phi$ and in the z direction between the Pixel layers and the existing Silicon Strip Detector (SSD) cf. Section 2.10, reducing the number of possible track combinations that can connect with hits on the outer layer of the pixel detectors. This is particularly crucial to enable accurate measurements in high multiplicity environments. The HFT can provide tracking information for short lived particle decays displaced by $100 \mu\text{m}$, or less, from the interaction point.

As an example, the neutral meson decay $D^0 \rightarrow K^- \pi^+$ can be identified directly by using the pixel detector to select the daughter tracks: K^- and π^+ tracks while the fast moving D^0 cannot be seen because it is a neutral particle, leaving no track in the detector. When combined with the existing STAR TPC and SSD, the HFT constitutes an integrated state-of-the-art at mid-rapidity inner tracking system which is unique at RHIC. This tracking system will significantly extend the reach of the STAR scientific program. In particular it will afford efficient topological reconstruction of D and B mesons down to low transverse momenta (e.g. for D 's at 500 MeV/c) illuminating their in-medium interactions and the properties of the strongly interacting quark-gluon plasma.

2.23 The DAQ1000

The STAR data acquisition is a fast and flexible system, receiving data from multiple sub-detectors having a wide range of readout rates. Currently the events are recorded at input rates up to 100 Hz. In order to acquire data at even higher rates, there has

to be designed a new set of electronics for the TPC. The new system, was inaugurated in 2008 and is called DAQ1000, will acquire data at rates up to 1000 Hz. The new technology that makes this upgrade possible are the front-end chips and associated readout electronics being developed for the ALICE TPC [Musa 03]. The CERN chips are truly the next-generation of TPC front-end chips and were designed based on our experience with the STAR electronics and built using specifications that are nearly identical to the STAR requirements. Thus, the replacement of the existing STAR electronics with a derivative of the newer CERN electronics will mean an order of magnitude increase in performance.

2.24 The PPV and the MinuitVF Method

The Proton-Proton Vertex (PPV) finds the z position of a vertex, by requiring a beam line constraint in order to determine the x and y values of the vertex. The beam line constraint is calculated by fitting all the events with the MinuitVF without any constraints on the vertex position [Reed 09]. A straight line fit is performed to the vertex distributions obtaining a relationship between x, y and z components.

Although many of the vertices found in this method will not be the correct ones for the event, the number that are the correct vertices will have enough statistics so that the beam line is a valid representation of the beam path. In particular, from each event, the tracks are selected based on their quality in the TPC. The tracks should extrapolate to within < 3 cm of the beam line and to a point within the volume of the TPC. In addition they should have a minimum momentum of 0.2 GeV/c.

Concerning the quality assurance of the tracks, the fraction of TPC hit points over the number of possible TPC hit points should comply with (2.10).

$$\frac{n\text{HitsFit}}{n\text{HitsPoss}} = 0.7 \quad (2.10)$$

Also (2.10) allows many tracks from post crossing events to be removed, (cf. Section 2.12.1). In addition, the post crossing pile-up is harder to remove than pre-crossing pile-up as the tracks will be reconstructed so that they appear to cross the TPC central membrane. Each track that meets the track quality cuts is given a weight based on whether it extrapolates to a deposit of energy in a fast detector or it crosses the TPC central membrane. Tracks that perform so, are likely to be tracks from the triggered vertex as these detectors can be reset between bunch crossings. However, this does not allow the vertex finder to remove pile-up (cf. Section 2.12.1) from within bucket collisions.

A track which extrapolates to a fast detector without energy deposited is given a *veto* factor. The track is not completely removed from the analysis, however it is more probable that this track is not from the triggered event so it is not given much weight.

In the case where the track does not extrapolate to a fast detector—or the part of the detector it extrapolates to is unable to be read out—the track gets a *dunno* factor. The latter is set to 1 as there is no knowledge about whether this track belongs to the triggered vertex. The total weight for the track is the product of the three weights from the various detectors.

As with the PPV algorithm, similar track quality cuts are applied to the collection of tracks used for the vertex finder. Vertex candidates are any point with at least 5 tracks pointing to within 6 cm in z direction, and within < 2 cm of the beam line. Let us also note that any two candidates cannot be within 6 cm from each other. Finally, the 3D position of this vertex is found by using the MINUIT [James 06a] minimization routine in order to minimize the mean distance of closest approach (DCA) of the collection of associated tracks.

As a final step, each vertex candidate is given a rank based on the average dip angle cf. Section 2.12 of the associated tracks versus z , the number of tracks which are matched to the BEMC and the number of tracks that finally cross the TPC central membrane.

Chapter 3

Data Analysis

The analysis methodology of the D^0 reconstruction is the main focus of this chapter. The event selection along with the track quality assurance cuts, as well as the electron and hadron identification is discussed. In addition, the various methods for the generation of the background as well as the consecutive subtraction and scaling approaches are also presented. The chapter concludes by mentioning the calculation of the significance for the extracted signal.

3.1 Introduction

The $D^0(c\bar{u})$ meson belongs to the SU(4) (flavor) pseudoscalar ($J^P = 0^-$) 16-plet of u, d, s, c quarks. A representation in the I, C and Y space can be seen in Figure 3.1. The $D^0 \rightarrow K^-\pi^+$ hadronic decay that the analysis will be focused on, has a branching ratio B.R. = 3.89%. The D^0 particle has a nominal mass value $m = (1864.84 \pm 0.17)$ MeV/c² and lifetime of $\tau = (410.1 \pm 1.5) \cdot 10^{-15}$ sec. The mean decay length is $c\tau = 122.9 \mu\text{m}$ [Amsler 08]. Finally, the weak interaction being responsible for the D^0 hadronic decay transmutes the charm quark to a strange quark via the emission of a W^+ particle, as shown in Figure 3.1. In order to study the charm decay topology, we need not only to identify the daughter particles into K^\pm and π^\pm , but also it is needed to combine the probe side ($K^-\pi^+/K^+\pi^-$) with the trigger side (e^\pm) in order to apply the novel method of the e - D^0 azimuthal correlation. As a last step, and in order to be able to reconstruct the secondary vertex, the point that the D^0 decay takes place, the microvertexing technique will be applied.

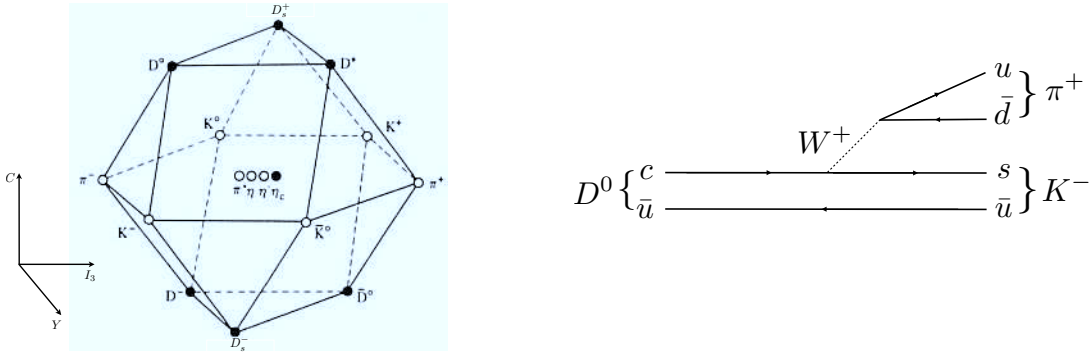


FIG. 3.1: *Left:* Graphical representation of the pseudoscalar meson 16-plet of SU(4) flavor u, d, s, c as a function of isospin I , charm C and hypercharge $Y = S + B - \frac{C}{3}$. The SU(3) nonet flavor, K^0 , lays in the middle $C = 0$ plane. *Right:* Feynman diagram of a $D^0 \rightarrow K^- \pi^+$ hadronic decay. The weak force is responsible for the particle's decay, transmuting the charm quark (c) into a strange quark (s) via the emission of the W^+ boson.

3.2 The Event Selection

The events are categorized by a trigger name and trigger setup. We are interested in events that triggered the Barrel Electromagnetic Calorimeter (BEMC) and there is a large probability that they contain a high- p_T particle, that we are interested in. For the case of the Cu+Cu we selected the *High Tower*, events. In the Au+Au case there are the *Btag* triggered events. Finally for the p+p (2006), p+p (2008) as well as d+Au (2008), we also consider the *Minimum Biased* events.

3.2.1 Minimum Bias Triggered Events

The Minimum Bias trigger (MinBias), in p+p collisions, demands a coincidence of the signals from two BBC (cf. Section 2.3.4) on the opposite sides of the interaction point.

3.2.2 High Tower Triggered Events

A brief description of the BEMC detector, can be found at Section 2.16. The BEMC offers the ability to select events that contain at least one high- p_T particle. This condition required, in addition to the Minimum Bias (Section 3.2.1), an energy deposit above a predefined threshold in at least one calorimeter tower. Two different thresholds were applied yielding the HighTower-1 and HighTower-2. The purpose of the specific trigger is to enrich the sample with events that contain particles with a large transverse energy deposit.

3.2.3 The Primary z -vertex Selection

A preliminary cut is being imposed on the vertex and in particular in the z component. Events that contain $(V_x, V_y, V_z) = (0, 0, 0)$ concerning the vertex components, are excluded since—by convention—these are cases that the primary vertex was not reconstructed. In Table 3.1, we summarize the cuts for various datasets on the z component of the primary vertex for the events that are taken under consideration in the current analysis. The reason for cutting on the z -vertex is in order to have tracks that do not cross a lot of detector material and are constrained in a region around the $z_0 = 0$.

TAB. 3.1: Cut on the z - primary vertex component for various datasets used in the current analysis. All runs are at $\sqrt{s_{\text{NN}}} = 200 \text{ GeV}$.

| Run | Dataset | $ z\text{-vertex} [\text{cm}]$ |
|------|---------|---------------------------------|
| V | Cu+Cu | ≤ 30 |
| VI | p+p | |
| VII | Au+Au | |
| VIII | d+Au | ≤ 20 |
| | p+p | |

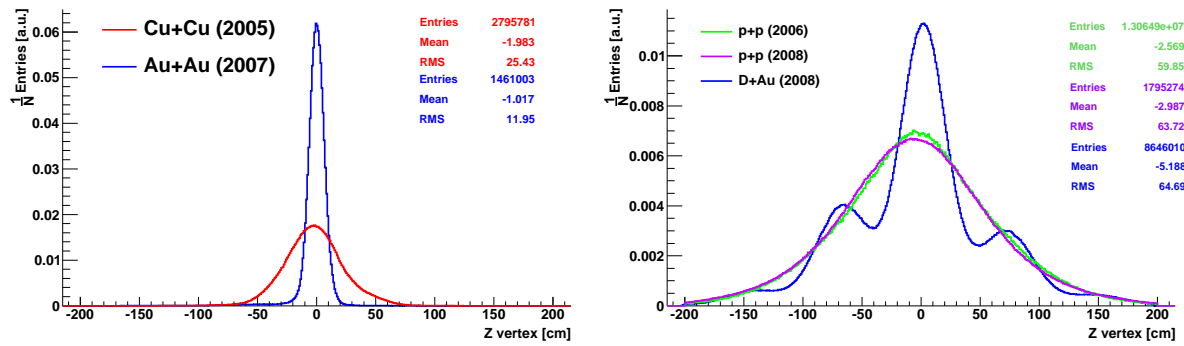


FIG. 3.2: Distribution of z vertex (normalized to the total number of events). *Left:* Cu+Cu (*High Tower*) (run V) (red) and Au+Au (*Btag*) (run VII) (blue). *Right:* p+p (run VI) (green), p+p (run VIII) (purple) and d+Au (run VIII) (blue). All datasets are at $\sqrt{s_{\text{NN}}} = 200 \text{ GeV}$.

3.2.4 The Charged Particle Event Multiplicity

The charged multiplicity is a useful tool in order to classify the events via their centrality. It performs so by utilizing the Glauber Model, as described in Section 1.10.

It is possible to perform a cut on the event multiplicity on datasets, usually selecting events that comply with the cut stated in (3.1).

$$0 < \text{multiplicity} < A \quad (3.1)$$

Let also note that (3.1) allows to select more peripheral (smaller multiplicity values) or central events (towards larger values), allowing to perform the analysis in different centrality bins. Additionally, in Table 3.2 it is presented the equivalence between the charged multiplicity and the different centrality bins in Cu+Cu and Au+Au datasets at $\sqrt{s_{\text{NN}}} = 200$ GeV datasets.

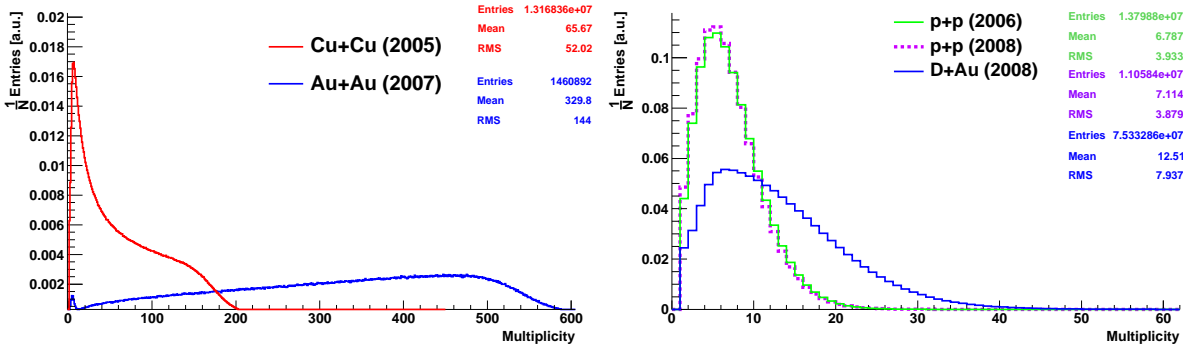


FIG. 3.3: Event multiplicity distributions (normalised to the total number of events) *Left*: Cu+Cu (*High Tower*) (run V) (red) and Au+Au (*Btag*) (run VII) (blue). *Right*: p+p (run VI) (red) and p+p (run VIII) (green) and d+Au (run VIII) (blue). All datasets are at $\sqrt{s_{\text{NN}}} = 200$ GeV.

3.2.5 Trigger Event Selection

We are mostly interested in events that contain a high- p_{T} trigger particle that will hit the BEMC. In Table 3.3 it is presented the BEMC energy thresholds for various datasets and triggers. For the case of Cu+Cu (run V) and Au+Au (run VII) there was explicitly a trigger Id., *High Tower* or *Btag* signifying a different BEMC tower energy threshold.

3.3 The Track Quality Assurance Selection

A preliminary set of cuts is being imposed on the track selection, affecting both the electron and hadron candidates' selection. In particular, we consider tracks spanning in the region $|\eta| < 1$ in the TPC volume, in order to take into account the acceptance

TAB. 3.2: Centrality definition and multiplicity values. *Left*: for the Cu+Cu (run V) *Right*: for the Au+Au (run VII). Minimum Bias events. Both runs at $\sqrt{s_{\text{NN}}} = 200 \text{ GeV}$. Values are taken from [Timmins 06, Timmins 09b].

| Centrality [%] | Multiplicity [\geq] | Centrality [%] | Multiplicity [\geq] |
|----------------|-------------------------|----------------|-------------------------|
| <u>Cu+Cu</u> | | <u>Au+Au</u> | |
| | | 0–5 | 485 |
| 0–10 | 140 | 0–10 | 399 |
| 0–20 | 103 | 0–20 | 269 |
| 0–30 | 74 | 0–30 | 178 |
| 0–40 | 53 | 0–40 | 114 |
| 0–50 | 37 | 0–50 | 69 |
| 0–60 | 25 | 0–60 | 39 |
| | | 0–70 | 21 |
| | | 0–80 | 10 |

of the TPC. In addition, tracks with TPC hits that comply with (3.2). This cut is shown in Figure 3.4.

$$\text{nHitsTPC} > 20 \quad (3.2)$$

$$\frac{\text{nHitsFit}}{\text{nHitsPoss}} > 0.15$$

The upper part of (3.2) is used in order to obtain a better quality concerning the momentum measurement of the track, since it is proportional to the track length, as will be presented and discussed in Section 4.3, and in particular (4.13). The maximum number of the TPC hits that one track can have is 45. The lower part of (3.2) serves in order to avoid the *split* tracks. The latter situation occurs, when the reconstruction software takes into account hits from one track, generating two separate ones.

3.4 The Role of the BEMC

The BEMC plays a crucial role in our study, allowing us to determine the high- p_{T} events. It offers the fast triggering on events at the *L0* level, deciding which ones are selected to contain a high- p_{T} particle hitting the BEMC towers (*High Tower, Btag* events). The

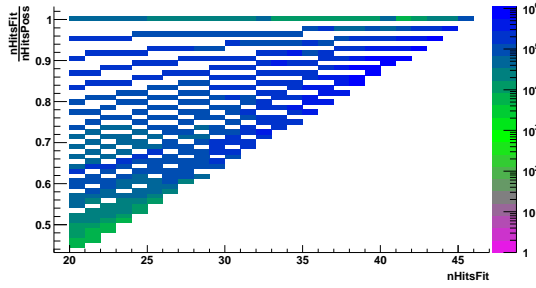


FIG. 3.4: 2D plot of the ratio $\frac{n\text{HitsFit}}{n\text{HitsPoss}}$ as a function of the $n\text{HitsFit}$ for the selected tracks used in the current analysis.

detector was partially instrumented in 2005 (covering only the west side: $0 < \eta < 1$), and fully after the p+p at $\sqrt{s} = 200$ GeV (run VI). In Figure 3.5, it can be seen the acceptance of the detector, in $\eta\phi$, for the two different runs (partial and full instrumentation).

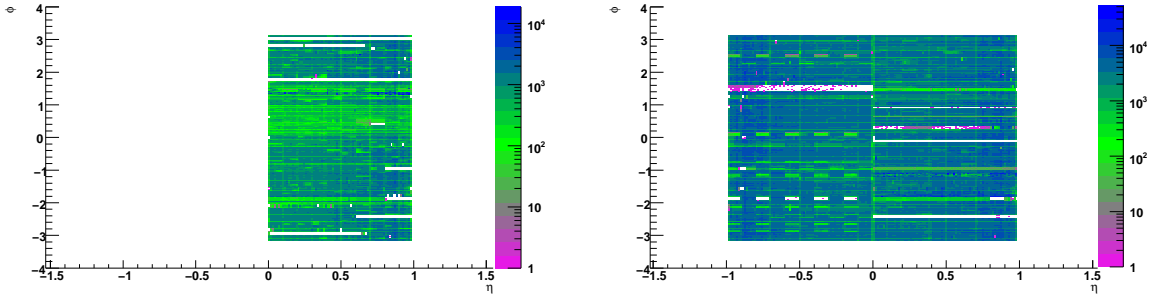


FIG. 3.5: BEMC $\eta\phi$ acceptance. *Left:* partially instrumented during the Cu+Cu (run V). *Right:* fully instrumented during the Au+Au (run VII). Both runs are at $\sqrt{s_{\text{NN}}} = 200$ GeV.

3.5 The Electron Identification

The identification of the electrons in the current analysis, plays a major role in order to accept the events that contain at least one high- p_T electron candidate. Additionally it is needed to create a pure electron sample that will allow the application of the $e-D^0$ correlation analysis. In order to perform this selection for the electron track candidates, we apply the following set of cuts.

- i. The event must contain at least one hit in the BEMC (tower) that satisfies the E or E_T threshold: *High Tower* (for the Cu+Cu) or *Btag* (for the Au+Au), as stated in Table 3.3;

TAB. 3.3: BEMC Tower energy threshold for various datasets and triggers. Calorimeter η acceptance: East $[-1, 0]$ and West $[0, +1]$. For the years 2007–2008 the *transverse energy* E_{t} was considered as the calorimeter threshold. All runs are at $\sqrt{s_{\text{NN}}} = 200 \text{ GeV}$. Values are taken from [Dunlop 08a].

| YEAR | COLLIDING SPECIES | TRIGGER ID. | THRESHOLD E [GeV] | BEMC η ACCEPTANCE |
|------|-------------------|-------------|---------------------|------------------------|
| 2005 | Cu+Cu | 66201 | 2.40 | $[0, +1]$ |
| | | 66203 | 3.75 | |
| 2006 | p+p | 117211 | 5.0 | $[0, +1]$ |
| | | 117212 | | |
| | | 127212 | 5 (W), 5.4 (E) | |
| | | 127213 | 5.4 | |
| 2007 | Au+Au | 137213 | 4.3* | $[-1, +1]$ |
| | | 200212 | | |
| | | 200213 | | |
| 2008 | d+Au | 200214 | 4.3* | $[-1, +1]$ |
| | | 210501 | | |
| | | 210511 | | |
| | | 210521 | | |
| | p+p | 210541 | 8.4 | |
| | | 220500 | 2.6* | |
| | | 220510 | 3.6 | |
| | | 220520 | 3.6 | |

- ii. a cut on the energy loss of the tracks in the TPC is performed between the values $\frac{dE}{dx} \in [3.5, 5.0]$ [keV/cm] along with a track momentum cut, accepting only the tracks with momentum greater than $p \geq 1.5$ GeV/c;
- iii. a cut on the shower profile of the particle, by imposing on the SMD strips both in η and ϕ plane of the detector to have at least one strip hit. Hence the following cut: $SMD_\eta > 1$ and $SMD_\phi > 1$;
- iv. a cut on the ratio of $0 < \frac{p}{E_{\text{TOWER}}} < 2$, p measured by the TPC and E_{TOWER} by the BEMC;
- v. the extrapolated track that matches the point on the BEMC surface of the tower, is considered as the electron track; and
- vi. in order to extract the portion of non photonic electrons from the overall electron sample, a cut on the di-electron invariant mass is applied both of like sign ($e^\pm e^\pm$) and unlike sign ($e^\pm e^\mp$). The sample of the electron candidates is rejected if at least one of the particles belongs to a pair with invariant mass value $m_{e^+e^-} \leq 150$ MeV/c², as shown in Figure 3.9. The latter cut is described in detail in Section 3.5.5.

3.5.1 The Role of the SMD

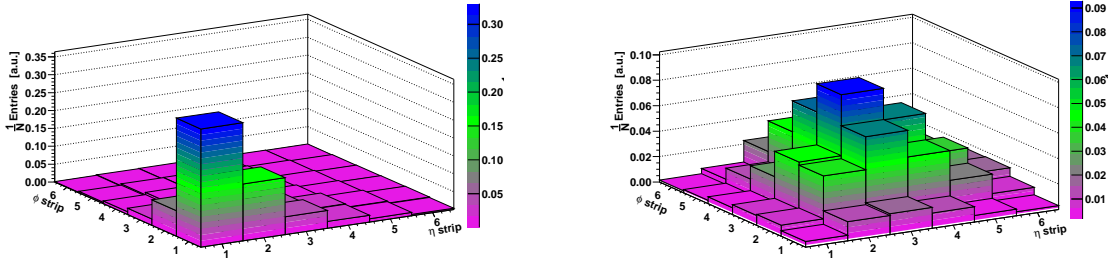


FIG. 3.6: SMD strips occupancy in η and ϕ plane, for showers. *Left:* for the hadrons. *Right:* for the electrons. Both plots are normalized to unity. Figures taken from [Kurnadi 10].

Both hadrons and electrons create showers in the BEMC. The former having a very constraint geometrical profile of the shower and the latter presenting a broader shower distribution. It is of great importance the cut on the SMD strips in η and ϕ plane (for the detector description cf. Section 2.16.2) allowing to perform a cut in the (η, ϕ) plane by cutting on the profile of the shower. The detector is consisted of proportional gas chambers with a strip read-out at a depth of $5 X_0$ in order to measure shower shapes

and position. For our current study, we select the *towers* that comply with the cut (3.3).

$$\begin{aligned} \text{SMD}_\eta &> 1 \\ \text{SMD}_\phi &> 1 \end{aligned} \quad (3.3)$$

The electromagnetic showers from electrons have their maximum intensity at $5 X_0$ where the SMD is located, while hadronic showers are incompletely developed, remaining restrained in η and ϕ strip occupancy. Based on calibrations of the SMD response to electrons and hadrons, tracks whose shower projection occupies more than 1 strip in both η and ϕ SMD planes were selected as electron candidates. In particular in Figure 3.6, it is shown such a distribution in the η - ϕ strips of the SMD for hadronic and electromagnetic shower shape.

3.5.2 The Energy Loss for the Electron Candidates

As stated in Section 2.11, a charged particle traveling inside a medium loses energy by ionizing the constituents of the matter. On the left side of Figure 3.7 it is shown the track energy loss $\frac{dE}{dx}$ versus its rigidity ($p \cdot q$), measured by STAR TPC for different particle species. The electrons are expected to span in the area: $3.5 < \frac{dE}{dx} < 5.0$ [keV/cm], which is also shown on the right side of Figure 3.7. Above the 1 GeV/c all the particles seem to lose the same amount of energy, imposing a difficulty in the particle identification above this momentum limit.

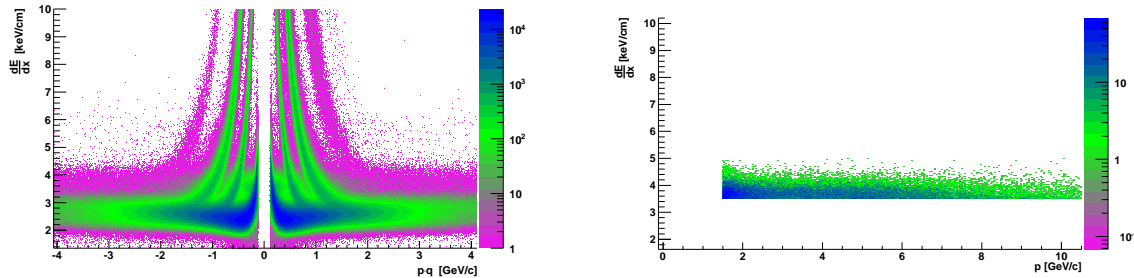


FIG. 3.7: *Left:* The energy loss $\frac{dE}{dx}$ in the TPC vs the rigidity for all tracks. *Right:* The energy loss $\frac{dE}{dx}$ versus momentum p for the electron candidates after the cuts $0 < \frac{p}{E_{\text{TOWER}}} < 2$, $p > 1.5 \text{ GeV}/c$, $\frac{dE}{dx} \in (3.5, 5.0)$ [keV/cm] and SMD strips cut: $\text{SMD}_\eta + \text{SMD}_\phi \geq 2$. Both plots are created from d+Au run(VIII) data.

3.5.3 The Ratio $\frac{p}{E_{\text{TOWER}}}$

The momentum of the track (p) is calculated in the TPC (cf. Section 2.12) and the energy of the tower measurement (E_{TOWER}) is given by the BEMC towers, as described in Section 2.16. The high- p_{T} electrons transfer almost all of their energy in the calorimeter cells, generating electromagnetic showers. For the latter case, it can be considered that $E_{\text{TOWER}} \simeq p$, or in other words $p/E_{\text{TOWER}} \sim 1$, whereas for the case of hadrons, the $\frac{p}{E_{\text{TOWER}}}$ distribution is broader, since hadrons lose only a portion of their energy for the creation of (hadronic) showers, $E_{\text{TOWER}} \ll p$, thus the ratio $p/E_{\text{TOWER}} \gg 1$ can extend to a large range of values above unity. In Figure 3.8 the distribution of the ratio both for the electron and the hadron is being presented for tracks with momenta $p > 2 \text{ GeV}/c$. A gaussian fit is also performed for the electron case yielding a mean value as in (3.4) and with a standard deviation of $\sigma = 0.19$.

$$\langle \left. \frac{p}{E_{\text{TOWER}}} \right|_{e^{\pm}} \rangle = 0.996 \pm 0.049 \quad (3.4)$$

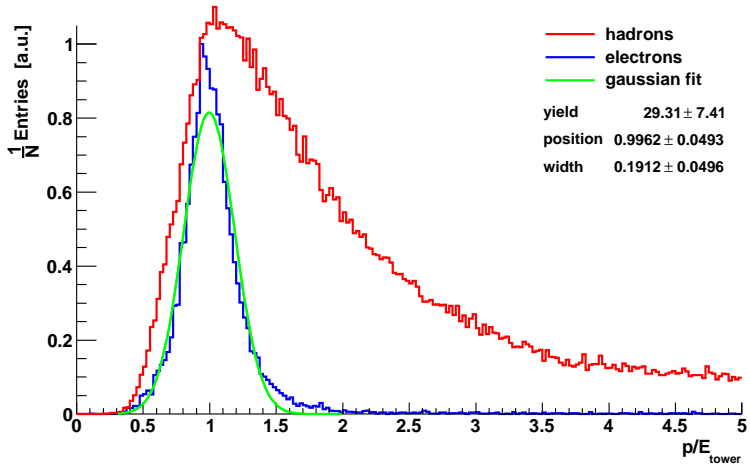


FIG. 3.8: p/E_{TOWER} distributions for hadrons (red line) and electrons (blue line) for tracks with $p > 2 \text{ GeV}/c$. A fit (green line) is performed on the electrons distribution yielding a mean value $\mu = 0.99$ and $\sigma = 0.19$. Both distributions are normalised to their total number of entries. Data used from [Kurnadi 10].

3.5.4 The Distance Between the Extrapolated Track and the Tower

On the BEMC surface we can identify with a resolution of $(\Delta\eta \times \Delta\phi) = (0.001 \times 0.001)$ [Beddo 03] the position of tower. In order to identify the electron, the track that

passes the previous cuts described in Sections 3.5.1–3.5.3 needs to be extrapolated to the BEMC surface. The distance between the tower and the projection of the track is calculated as

$$r_{Ti} = \sqrt{(x_T - x_i)^2 + (y_T - y_i)^2 + (z_T - z_i)^2} \quad (3.5)$$

where (x_T, y_T, z_T) are the tower coordinates and (x_i, y_i, z_i) refer to the coordinates of the extrapolated track to the BEMC surface.

3.5.5 The Selection of the Non Photonic Electrons

The main contamination for the non-photonic electrons originates from the neutral mesons' decay $\pi^0 \rightarrow 2\gamma$, $\eta \rightarrow 3\pi^0$. Also the material, such as the silicon detectors, the beam pipe made of Be and the TPC inner field cage contribute to the photon conversion, $\gamma \rightarrow e^-e^+$, as shown in the left part of Figure 3.9. In particular, it is shown the distance (from the origin) of the vertex that the gamma conversion takes place in STAR detector. In order to separate the non-photonic electrons from the photonic

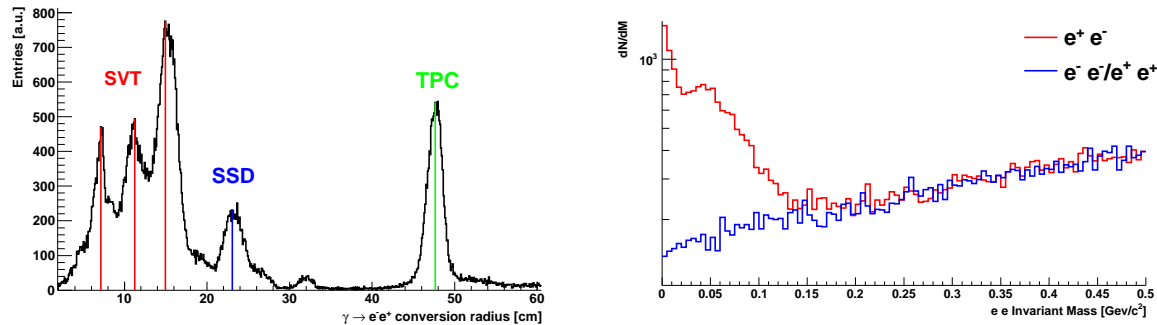


FIG. 3.9: *Left:* Distance (radius) of the photon conversion ($\gamma \rightarrow e^+e^-$) vertex interaction point to the x_0, y_0, z_0 center point of STAR detector. The 3 layers of SVT (red) along with the one SSD layer (blue), the kapton foil (~ 32 cm) and the inner TPC field cage (green) can be clearly seen. Figure taken from [Choi 09]. *Right:* Same-sign (blue) and opposite sign (red) invariant mass yields for electron candidates. A cut at $150 \text{ MeV}/c^2$ is imposed in order to separate the non-photonic electrons. Plot created from the p+p at $\sqrt{s} = 200 \text{ GeV}$ (run VI).

electrons the invariant mass method is used. In specific every electron candidate is combined with all the tracks in the TPC passing the loose $\frac{dE}{dx}$ for the electron candidates (cf. Section 3.5.2). This method yields an invariant mass spectrum, as shown on the right part of Figure 3.9 for *like* sign ($e^\pm e^\pm$) and *unlike* sign ($e^\pm e^\mp$) pairs. By superimposing both invariant mass spectra, we seek the common point of the two plots. In particular it is clearly shown the cut at $150 \text{ MeV}/c^2$. Finally, let us note that the invariant mass calculation is being considered with the tracks' momenta calculated at the DCA of each two tracks.

3.6 The Particle Identification for the Daughter Tracks

The daughter tracks need to be classified into kaons and pions. For this reason we apply the following method that includes a selection cut between the charge of the hadron and the trigger electron, and a second cut based on the $\frac{dE}{dx}$ energy loss of the track in the TPC.

3.6.1 The Charge Correlation Between the Electron and the Hadron

As stated in Section 1.13, the charge of the trigger particle, is considered to play an important role in the deduction of the species of the hadron. In particular, we can distinguish two cases:

- i. D^0 as a product of a $c\bar{c}$ decay–dominant source. If the sign of the charge of the trigger particle (e) is equal to the sign of the charge of the hadron (h) and an azimuthal angular cut at $\Delta\phi = \pi$ between the two particles momenta is imposed. Hence the hadron is a kaon candidate inheriting the charge of the trigger.
- ii. D^0 produced by a $b\bar{b}$ decay–dominant source. We consider the sign of the charge of the e to be opposite to the charge of the h and a cut at $\Delta\phi = \pi$ is imposed. The hadron is considered to be a kaon candidate with a charge opposite to the trigger's.

The second and final decision on the species of the hadron will be taken after the additional $\frac{dE}{dx}$ cut, as explained in Section 3.6.2.

3.6.2 The nSigmaKaon and nSigmaPion Distributions

A supplementary cut that is applied in order to identify the hadrons, is related to the energy loss $\frac{dE}{dx}$ due to the passage of the charged particle through the gas of the TPC, cf. Section 2.11. The energy loss of a track is expressed in terms of standard deviations (σ) with a prior mass hypothesis [Bichsel 06]. In Figure 3.10 it is shown such a distribution for the $n\sigma_\pi$ for a predetermined p_T window at $3.75 < p_T < 4.0 \text{ GeV}/c$.

3.7 The Role of the Silicon Detectors

In datasets such as Cu+Cu (run V) and Au+Au (run VII) at $\sqrt{s_{nn}} = 200 \text{ GeV}$, the silicon detectors (SVT and SSD) were present in the data acquisition and subsequently used in the offline track reconstruction. A supplementary cut on the total number of Silicon Hits of each track can be applied, in the form $\text{SVT} + \text{SSD} > a$, with a be an

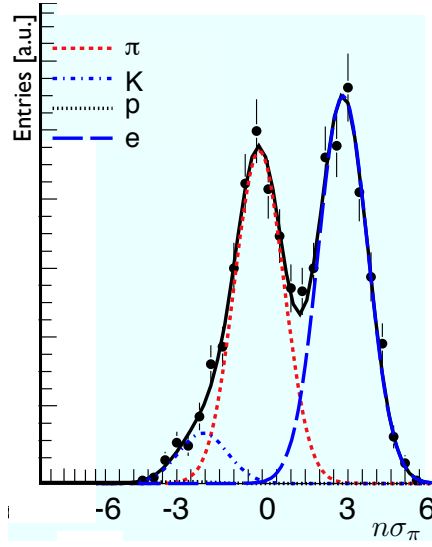


FIG. 3.10: $n\sigma_\pi$ distribution for different particle species at $3.75 < p_T < 4.0 \text{ GeV}/c$. Also shown the result from a 4-Gaussian fit. Figure taken from [Xu 08a].

integer. This cut offers better resolution concerning the DCA of tracks with respect to the primary vertex, as will be discussed in Section 4.3. The demand on the silicon cuts, allows the possibility to select tracks that are more likely to emerge from the primary vertex.

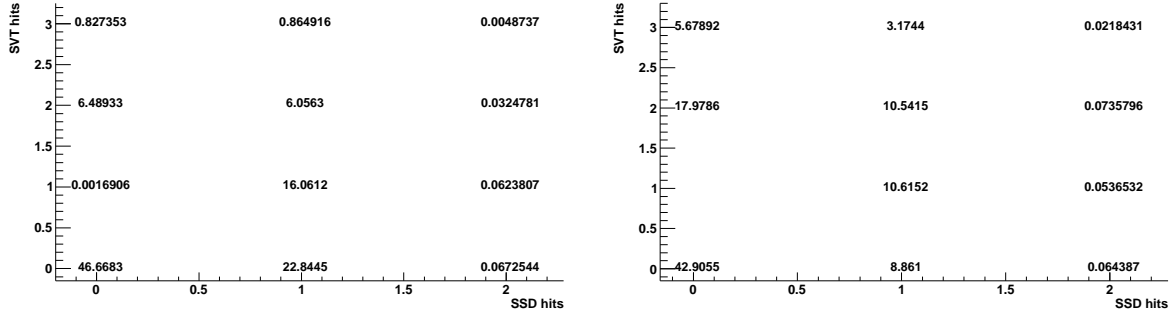


FIG. 3.11: 2D distribution of SVT vs. SSD hits for Cu+Cu (*High Tower*) (*left*) and Au+Au (*Btag*) (*right*) at $\sqrt{s_{NN}} = 200 \text{ GeV}$. All values are normalized to the total number of entries and given in [%].

Let us also make a note for the particular case of $\text{SVT} + \text{SSD} = 0$. The convention for this case is that when the sum of silicon hits for a given track is $\text{SVT} + \text{SSD} = 1$, then the hits for the two detectors is distributed as follows: $\text{SVT} = 0$ and $\text{SSD} = 1$. Practically that means that the percentage of tracks with only 1 silicon hit and of which this hit

does not belong to the SSD is zero. Finally, in Figure 3.11 it is shown the distribution of SVT and SSD hits of tracks, for Cu+Cu and Au+Au at $\sqrt{s_{\text{nn}}} = 200 \text{ GeV}$ datasets.

3.8 The D^0 Invariant Mass Reconstruction

After applying all cuts concerning the selection of electrons , the tracks, and the event selection, we can proceed in reconstructing the D^0 invariant mass. For a hadron pair the invariant mass M_{12} is given by (3.6).

$$M_{12} = \sqrt{E_1 E_2 - \vec{p}_1 \cdot \vec{p}_2} \quad (3.6)$$

where E_i and \vec{p}_i are the energy and momentum of each i -particle. The energy of each daughter particle is calculated using the nominal mass value as stated in Appendix A.3.

3.8.1 The Ambiguity in the Daughters Mass Attribution

At this point let us make a note concerning the calculation of the D^0 invariant mass. Especially let us consider the hadron pairs. Initially there exists no prior knowledge concerning the nature of each particle (either K^\pm or π^\pm) composing the hadron pair. For each hadron track, we perform an exclusive $\frac{dE}{dx}$ cut in the form of standard deviations, keeping the tracks that comply by (Section 3.6.2).

$$\begin{aligned} |\text{nSigmaKaon}| &< a \\ \text{and} \\ |\text{nSigmaPion}| &< b \end{aligned} \quad (3.7)$$

Let us note that the cuts concerning one species of a particle are not exclusive to each other. In other words the demand for a hadron to belong to species A does not exclude the possibility that the same track can belong to species B . As a result the track can be considered *twice* (both K and π) and it will be taken under consideration in both cases for the calculation of the D^0 invariant mass as in (3.6). From an algorithm point of view, since we are using a double loop over the hadrons, in order to create pairs, let us consider the case of a hadron pair for the $(i, j) = (K^-, \pi^+)$ whose tracks fulfill both cuts in (3.7). Therefore (3.6) becomes (3.8).

$$M_{ij} = \sqrt{E_{K_i} E_{\pi_j} - \vec{p}_{K_i} \cdot \vec{p}_{\pi_j}} \quad (3.8)$$

If both tracks pass the $\frac{dE}{dx}$ cuts in (3.7), then the pair, can also be considered—as a different pair of course—and can be written $(i, j) = (\pi^+, K^-)$, yielding (3.9).

$$M_{ji} = \sqrt{E_{K_j} E_{\pi_i} - \vec{p}_{K_j} \cdot \vec{p}_{\pi_i}} \quad (3.9)$$

3.9 The Background Reconstruction

The reconstruction of the background yield has the same importance as the generation of the invariant mass yield. One of the main aspects of a proper background consists of simulating the D^0 invariant mass yield. In other words it is required the *smooth* behavior beneath the D^0 mass region. In order to successfully simulate the background, the following different methods are used for the extraction of the D^0 signal from the invariant mass yield.

- i. Samesign, using the yield of $\sqrt{K^-\pi^- \otimes K^+\pi^+}$, described in Section 3.9.1;
- ii. rotational, rotating the momentum of one daughter track, by a fixed angle, as described in Section 3.9.2; and
- iii. polynomial, where a fit with a polynomial function of n^{th} degree, $\text{pol}[n]$, is performed *around* the D^0 mass region, as stated in Section 3.9.3.

In the following paragraphs, we present the method that was used for the creation of every background yield, and the various aspects for each case.

3.9.1 The Same-Sign Background

For a given $K^-\pi^+$ pair, the *samesign* background $K^+\pi^+$, cf. Figure 3.12, can be selected in order to be subtracted from the $S + B$ yield. In order to construct a high statistics yield the total samesign is constructed by combining the negative and positive pairs, following (3.10).

$$\sqrt{K^-\pi^- \otimes K^+\pi^+} \tag{3.10}$$

For the high p_{T} triggered events (*High Tower* or *Btag*), it is important to note that since the sign of the trigger particle determines the sign of the K candidate, as explained in Section 1.13, it is not possible to have in the same event both species $K^-\pi^-$ and $K^+\pi^+$ in the same event. Nevertheless both the invariant mass and the background yields since they are constructed over the total number of events and not examined on an event by event basis, the overall charged samesign is not affected (Figure 3.12). Of course in the *Minimum Bias* events, since there is no high p_{T} particle there is no such a restriction concerning the reconstruction of both samesign species.

3.9.2 The Rotational Invariant Mass Background

We refer to the *rotational* background as the invariant mass yield, calculated via (3.6), but this time one of the daughter tracks' momentum is being rotated in space by an angle θ_{rot} with respect to the initial track direction, cf. Figure 3.13. In particular, we

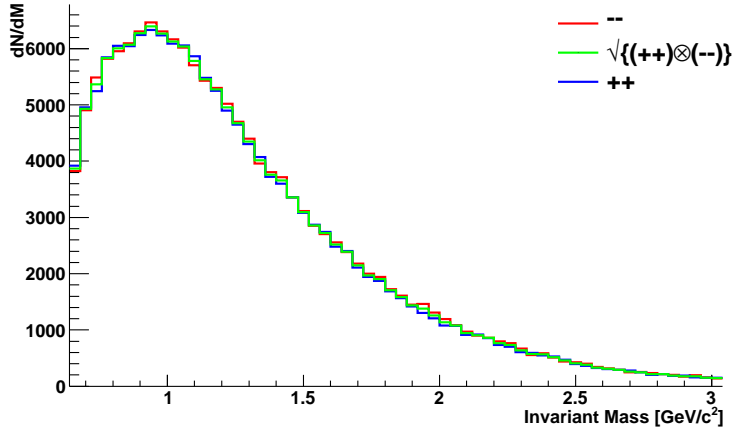


FIG. 3.12: Distribution of the same-sign invariant mass yields for $K^-\pi^-$ (red), $K^+\pi^+$ (blue) and total $\sqrt{K^-\pi^- \otimes K^+\pi^+}$ (green).

choose this track to be the one corresponding to the kaon. In mathematical form it is expressed by (3.11).

$$M_{12} = \sqrt{E_1 E_2 - |\vec{p}_1| |\vec{p}_2| \cos(\theta + \theta_{\text{rot}})} \quad (3.11)$$

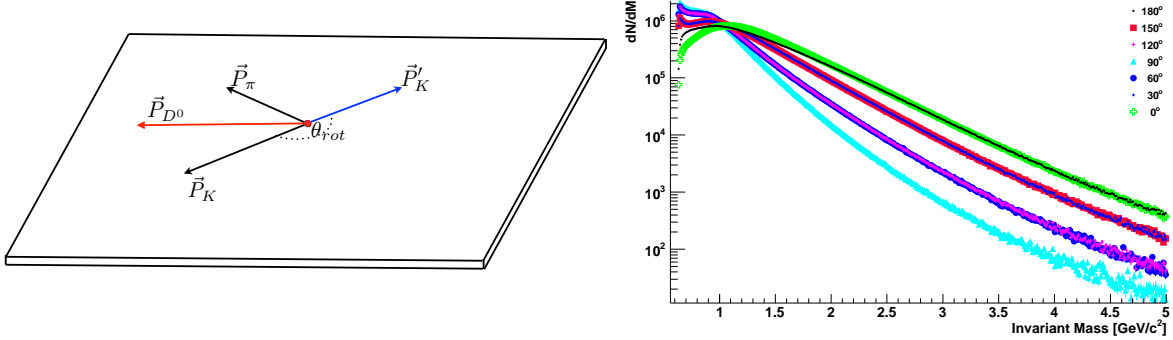


FIG. 3.13: *Left:* Schematic depiction of the rotation of a kaon's momentum in space by an angle θ_{rot} . Let us note that the decay plane before and after the rotation, remains the same. *Right:* Rotational $K^-\pi^+/K^+\pi^-$ invariant mass yields for various θ_{rot} angles of rotation. Supplementary rotational angles exhibit similar invariant mass yield in the region close to the D^0 mass region ($1.865 \text{ GeV}/c^2$). The D^0 invariant mass before any rotation is plotted by the green empty cross.

In (3.11), let θ be the initial angle between the two particles' momenta. Also we denote by θ_{rot} the angle of rotation. Let us mention that the initial reaction plane of the decay is being respected prior and after the rotation. In particular, this means that the particle's momentum components are found on the same plane, before and after the rotation takes place. In Figure 3.13, it is presented the rotational invariant mass yields for the various rotational angles θ_{rot} .

The Rotational Background and the Silicon Hits

Due to the non isotropic azimuthal acceptance (cf. Figure 3.14) in the silicon detectors: SVT+SSD, it is observed that the rotational invariant mass subtraction is not applicable, when a cut on the silicon hits of the tracks is applied in the form of $\text{SVT+SSD}=a$. In particular the subtraction of the rotational mass does not scale as expected, yielding a non-properly background residual invariant mass yield around the D^0 mass region.

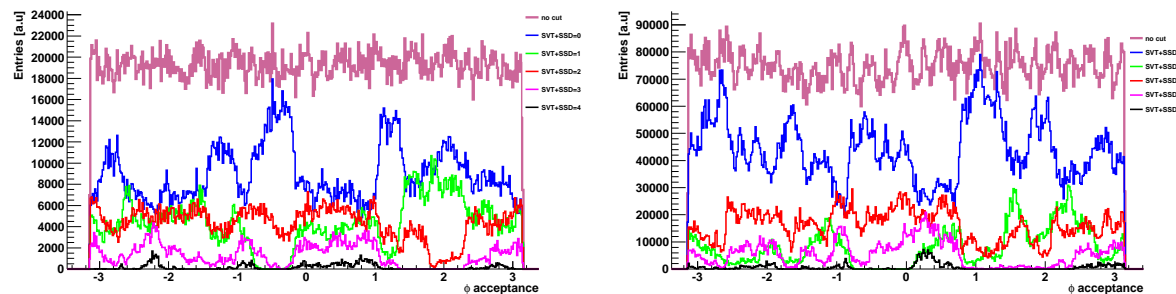


FIG. 3.14: Azimuthal acceptance for tracks with $\text{SVT+SSD}=a$ hits: no cuts (pink), 0 (blue), 1 (green), 2 (red), 3 (magenta) and 4 (black). *Left:* for the Cu+Cu dataset. *Right:* for the Au+Au. Both runs are at $\sqrt{s_{\text{NN}}} = 200 \text{ GeV}$.

3.9.3 The Polynomial Background

A third method that can be applied for the background subtraction, is the use of a polynomial in order to simulate the background, usually in the form of (3.12).

$$P_n(x) = a_0x^0 + a_1x^1 + a_2x^2 + \dots + a_nx^n = \sum_n a_nx^n \quad (3.12)$$

The values of the coefficients a_n are calculated by fitting the invariant mass yield with the function $P_n(x)$. The fit is being performed between the region $[1.7, 2.1] (\text{GeV}/c^2)$, and the order of the polynomial is considered to be between $n = 1-7$. In Figure 3.16 it is shown the invariant mass of the $K^-\pi^+$ pairs along with the polynomial fit for various

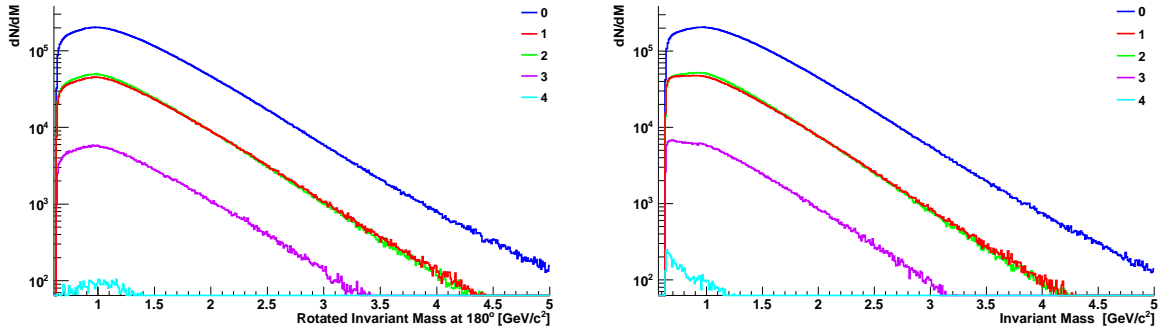


FIG. 3.15: Background D^0 invariant mass plots for different SVT+SSD cases. *Left:* Rotational (at 180°) invariant mass yield. *Right:* Invariant Mass yield of $K^- \pi^+ / K^+ \pi^-$. Plots created with the dataset Cu+Cu at $\sqrt{s_{\text{NN}}} = 200$ GeV (*High Tower*) data.

degrees n . In order to estimate the goodness of fit we are using the $\chi^2/\text{n.d.f.}$, where n.d.f. is the number of degrees of freedom, the number of points of the curve that the fit was performed minus the number of the free parameter [James 06b]. In addition, the values of $\chi^2/\text{n.d.f.}$ are summarized for the various cases of polynomial fit functions and such a fit is presented along with the D^0 invariant mass yield.

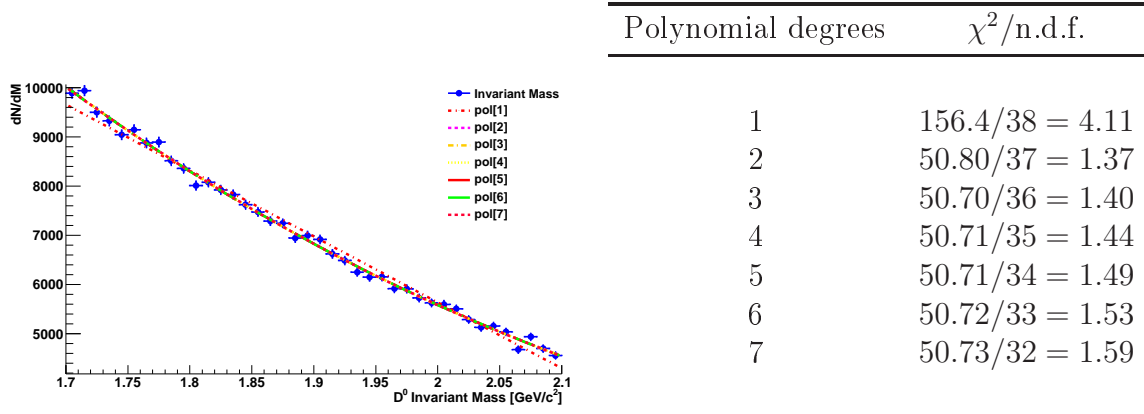


FIG. 3.16: *Left:* The D^0 Invariant Mass along with the fit for polynomial degrees $n=1-7$. *Right:* $\chi^2/\text{n.d.f.}$ values for the corresponding fit polynomial degrees. Plots and values are created from the Cu+Cu at $\sqrt{s_{\text{NN}}} = 200$ GeV run.

3.10 The Scaling of the Background

The goal of creating the background is to perform the subtraction afterwards, in order to extract the D^0 signal. Both rotational and samesign need to be scaled before

the subtraction as shown in Figure 3.19. The scaling of the background is achieved by calculating the *scaling factor* (c) in the following way. Let us consider the invariant mass distributions $\frac{dN}{dM}$ both for the *signal+background* yield (N_{S+B}) and *pure background* yield (N_B). The integral over an area away from the D^0 nominal mass (1.865 GeV/c²) is then considered, both for the D^0 invariant mass yield and the corresponding background (samesign or rotational) yield. In particular we consider the area both for the $K^-\pi^+/K^+\pi^-$ and the corresponding background between the invariant mass regions $[M_A, M_B]$.

$$c \equiv \frac{\int_{M_A}^{M_B} \frac{dN_{S+B}}{dm} dm}{\int_{M_A}^{M_B} \frac{dN_B}{dm} dm} \quad (3.13)$$

The normalization factor c is used for the background yield N_B is hence scaled to N'_B according to the following formula:

$$\int \frac{dN'_B}{dm} dm = c \int \frac{dN_B}{dm} dm \quad (3.14)$$

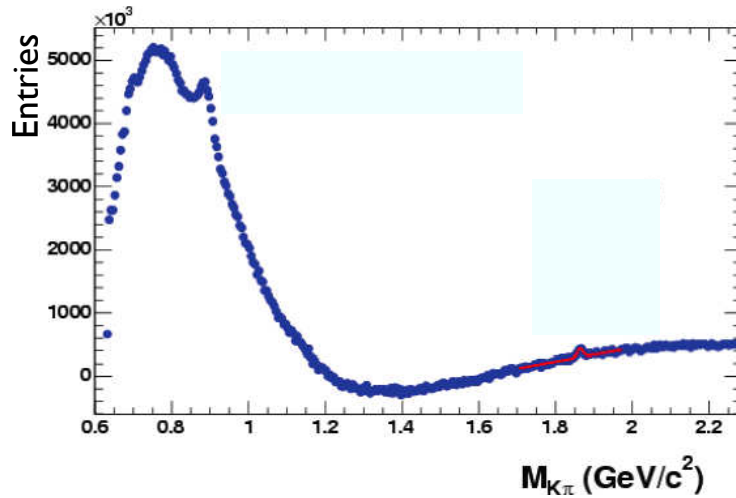


FIG. 3.17: Invariant mass of $K\pi$. Both peaks of $K^0(892)$ and $D^0(1865)$ (red area) can be clearly seen. Figure taken from [Zhang 03].

3.10.1 The Region above 2.1 GeV/c²

In order to calculate the normalization factor c , we consider the first case to be the region above $M_A = 2.1$ GeV/c², as shown in Figure 3.18. The reason behind the

selection of this region is the contribution of the $K^0(892) \rightarrow K\pi$ decay channel (B.R. = 0.01) [Amsler 08], into the D^0 invariant mass spectrum. The latter situation is shown in Figure 3.17.

3.10.2 The Regions $[1.7, 1.8] \cup [1.9, 2.0]$ [GeV/c^2]

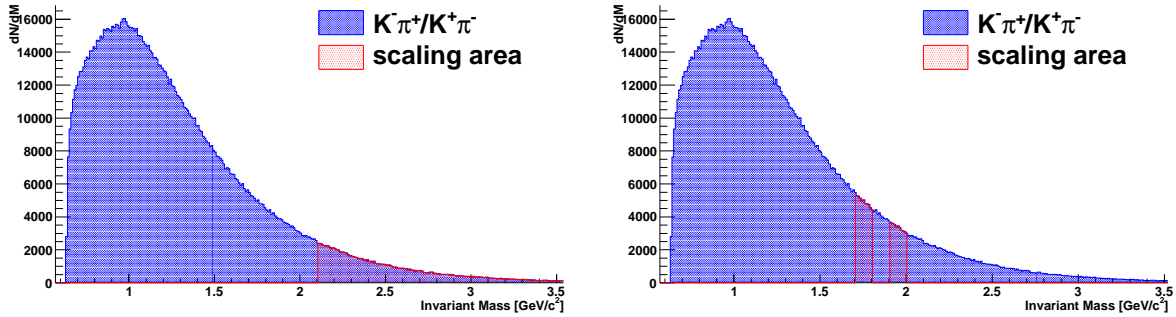


FIG. 3.18: Cartoon depicting the scaling of the background for the case $(2.1, \infty)$ (*left*) and the $[1.7, 1.8] \cup [1.9, 2.0]$ (*right*).

An alternative method for the deduction of the factor c is to consider the following steps. Instead of integrating over only area $[M_A, M_B]$, we also consider a second area $[M_C, M_D]$. Therefore the factor is calculated in the latter case by exploiting (3.15).

$$c = \frac{\int_{M_A}^{M_B} \frac{dN_{S+B}}{dm} dm + \int_{M_C}^{M_D} \frac{dN_{S+B}}{dm} dm}{\int_{M_A}^{M_B} \frac{dN_B}{dm} dm + \int_{M_C}^{M_D} \frac{dN_B}{dm} dm} \quad (3.15)$$

The values of the integrating areas are considered to be $[1.7, 1.8] \cup [1.9, 2.0]$ [GeV/c^2], excluding the region around the D^0 mass peak, as shown in Figure 3.18. The choice of the mass area that is used in order to scale the background, depends strongly on the form of the subtracted invariant mass yield. In particular, it is expected that the subtracted spectrum to fluctuate around 0, near the D^0 mass region. In the contrary case, a double background subtraction can also be performed. Namely, after the rotational or the same sign background subtraction, the polynomial fit is also subtracted from the residual spectrum.

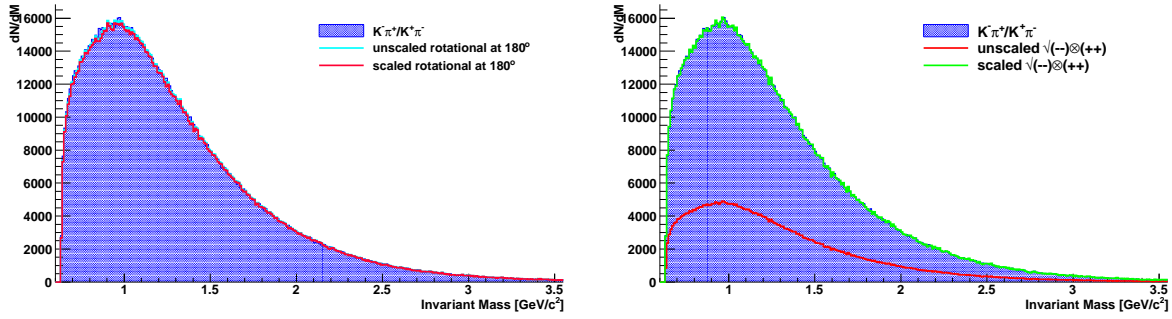


FIG. 3.19: Invariant mass yield of $K^-\pi^+/K^+\pi^-$ (blue). *Left:* along with unscaled (cyan) and scaled (red) samesign $\sqrt{K^-\pi^- \otimes K^+\pi^+}$ background yields. *Right:* along with unscaled (red) and scaled (green) rotational background (at 180°) yields. The scaling area is considered to be: $[1.7, 1.8] \cup [1.9, 2.0]$ [GeV/c²] for both cases.

3.11 The Significance of a Signal

When treating with the signal extraction, often it is useful to present the *significance* given by the general formula (3.16).

$$\sigma = \frac{S}{\sqrt{S + nB}} \quad (3.16)$$

The factor n expresses the uncertainty on the form of the B distribution. After fitting the signal with a gaussian peak, the parameters such as the mean value \bar{x} and the standard deviation σ acquired by the fit, are recorded. In (3.16) the S , B are the signal and background yields (3.17) inside a given region $[\bar{x} - \kappa\sigma, \bar{x} + \kappa\sigma]$ around the value \bar{x} . The factor κ can vary between the values 1–3. In particular, we consider the set in (3.17).

$$\begin{aligned} S &= \int_{-\kappa\sigma}^{+\kappa\sigma} \frac{dN_S}{dm} dm \\ S + B &= \int_{-\kappa\sigma}^{+\kappa\sigma} \frac{dN_{S+B}}{dm} dm \end{aligned} \quad (3.17)$$

If $S + B$ and B are uncorrelated quantities, then a simple calculation yields for the errors:

$\sqrt{S + B}$ is the error is δ_{S+B} for the signal and background, e.g. opposite sign; and

\sqrt{B} is the error is δ_B for the background, e.g. samesign.

The error of the signal S , therefore is

$$\delta_S = \sqrt{\delta_{S+B}^2 + \delta_B^2} = \sqrt{S + 2B} \quad (3.18)$$

Chapter 4

Microvertexing Technique

The main focus of the current chapter, is the secondary vertex reconstruction method; namely the microvertexing technique. The methodology followed for the calculation of the microvertexing variables is also presented. In the chapter conclusion it is also presented a study on the improvement of the resolution of tracking and the improvement on the calculation of the microvertexing variables, by including the silicon hits (SVT+SSD) for every track.

4.1 Introduction

A charged track in the magnetic field, is considered as a helix whose parameterization is described thoroughly in Appendix D.1. In order to describe the trajectory of the charged particle's track, one can use the following set of equations that describe the helix coordinates, described by (4.1).

$$\begin{aligned}x(s) &= x_0 + \frac{1}{\kappa}[\cos(\Phi_0 + hs\kappa \cos \lambda) - \cos \Phi_0] \\y(s) &= y_0 + \frac{1}{\kappa}[\sin(\Phi_0 + hs\kappa \cos \lambda) - \sin \Phi_0] \\z(s) &= z_0 + s \sin \lambda\end{aligned}\tag{4.1}$$

In (4.1) the following values are used.

s is the path length along the helix;

x_0 , y_0 and z_0 is the starting point at $s = s_0 = 0$;

λ is the dip angle;

κ is the curvature, i.e. $\kappa = \frac{1}{R}$, and R let be the radius of the helix in the xy plane;

B is the z component of the homogeneous magnetic field $\vec{B} = (0, 0, B_z)$;

q is charge of the particle in units of positron charge; and

h is the sense of rotation of the projected helix in the xy (bending) plane.

The notion of helix is of great importance, since it is used in order to calculate the distance of closest approach between two tracks and therefore deduce the point of the secondary vertex. The method is explained in detail in Section 4.2. In the following paragraphs, the method of microvertexing will be presented. It consists of the method that was developed in order to deduce the parameters needed for the reconstruction of the D^0 decay. The most fundamental parameters are listed below.

- i. The distance of closest approach, denoted by DCA, between the two daughter particles' tracks;
- ii. the secondary vertex coordinates, defined as the point where the D^0 decay takes place;
- iii. the decay length of D^0 , defined as the distance between the primary and the secondary vertices;
- iv. the distance of closest approach of the D^0 to the primary vertex; and
- v. the distance of closest approach of daughter particles (K, π) to the primary vertex.

As it will be later shown, these variables will be used as a powerful tool in performing the adequate cuts needed for the topological reconstruction of the D^0 decay. In addition, we refer that there exists a set of subsequent variables, that are derived from the above ones. The description of these variables, along with the reconstruction method is the main topic of the discussion of Section 4.2. Let us also mention that for the microvertexing calculation, the *global* tracks are used as opposed to the *primary* stated in Appendix E.

4.2 The Calculation of the Microvertexing Variables

In the microvertexing algorithm, the most crucial step is the determination of the distance of the closest approach (DCA) between the daughter particles. A detailed description of the method for the analytical calculation of the DCA between two tracks t_1, t_2 (helices) can be found in Appendix D.4. We also consider *a priori* the geometrical middle of the DCA between the two tracks to be the point of the secondary vertex, which is defined as the point when the D^0 decay takes place. Once the specific point is localized, and with the prior knowledge of the primary vertex coordinates, on an

event-by-event basis, we can proceed with the calculation of the decay length of the D^0 candidate. In Figure 4.1 it is shown a schematic depiction of a D^0 decay along with the trajectories of the daughter tracks (t_1 and t_2) in the transverse plane ($r-\phi$). In the same Figure 4.1, it is marked also the primary and the secondary vertex, as well as the DCA of daughter tracks to the primary vertex.

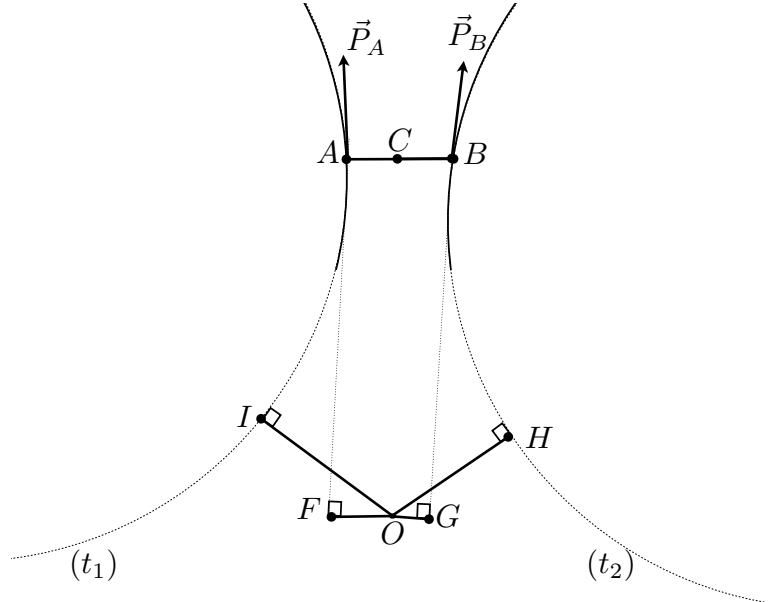


FIG. 4.1: Cartoon depicting the detail of the D^0 decay along with the microvertexing parameters.

In particular, let us consider:

O to be the point of the primary vertex;

C to be the point of the secondary vertex;

\vec{OC} to be the vectorial decay length of the $K\pi$ pair;

$|\vec{AB}|$ to be the DCA between the daughters;

$|\vec{OF}|, (|\vec{OG}|)$ to be the DCA of the $t_1, (t_2)$ track to the primary vertex, d_0^1 , using a straight line approximation (in the absence of magnetic field);

$|\vec{OI}|, (|\vec{OH}|)$ to be the DCA of the $t_1, (t_2)$ track to the primary vertex, extrapolating the helix $t_1, (t_2)$ in the magnetic field;

$\vec{P}_A, (\vec{P}_B)$ to be the momentum of the $t_1, (t_2)$, tangent to the point $A, (B)$;

\vec{AF} to be the vector pointing towards the primary vertex, opposite in direction to the \vec{P}_A and with magnitude the distance of the decay point A and the point of closest approach F (to the primary vertex);

\vec{BG} to be the vector pointing towards the primary vertex, opposite in direction to the \vec{P}_B and with magnitude the distance of the decay point B and the point of closest approach G (to the primary vertex);

$\cos \theta_{\text{POINTING}}$ with θ_{POINTING} let be the angle between the D^0 flight line (\vec{OC}) and its reconstructed momentum \vec{P}_{D^0} as calculated by (4.2), a sketch of this variable combining the momentum and the decay length, is shown in Figure 4.4; and

DCA_{D^0} to be the DCA of the D^0 reconstructed parent particle to the primary vertex, whose calculation is given by (4.3).

Furthermore, let us mention that the momentum of each track that is used both in the microvertexing technique and in the calculation of the invariant mass, is being calculated by propagating the track using the helix method in the DCA between tracks as stated in Appendix D.2. In addition, concerning the calculation of the θ_{POINTING} , since the D^0 is a neutral particle, its momentum is not affected by the presence of the magnetic field, hence a straight line extrapolation of the parent momentum $\vec{P}_{D^0} = \vec{P}_A + \vec{P}_B$ to the primary vertex is considered.

$$\cos \theta_{\text{POINTING}} = \frac{\vec{OC} \cdot (\vec{P}_A + \vec{P}_B)}{|\vec{OC}| \cdot |\vec{P}_A + \vec{P}_B|} \quad (4.2)$$

Therefore the distance of closest approach of the parent is given by (4.3).

$$\text{DCA}_{D^0} = |\vec{OC}| \cdot \sin \theta_{\text{POINTING}} \quad (4.3)$$

Finally, let us also make a note that the position vectors \vec{OA} and \vec{OB} with respect to the primary vertex can be calculated simply by subtracting from each position vector—with respect to the origin of the axis (x_0, y_0, z_0) —the vector of the primary vertex: \vec{KO} . In particular by considering \vec{KO} , \vec{KA} and \vec{KB} , the vector of primary vertex, of the first (t_1) and the second track (t_2)—with respect to the (x_0, y_0, z_0) —the relations between the two reference frames become:

$$\vec{OA} = \vec{KA} - \vec{KO} \quad (4.4)$$

$$\vec{OB} = \vec{KB} - \vec{KO} \quad (4.5)$$

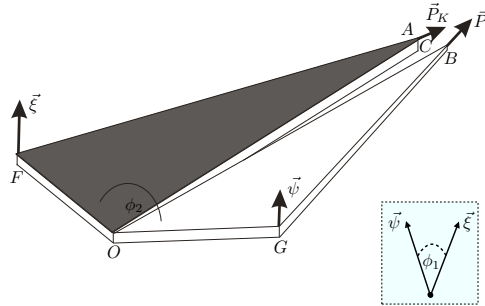


FIG. 4.2: Cartoon depicting the angle ϕ_2 between the planes of the decay daughters and the angle ϕ_1 between the normal vectors.

4.2.1 The Coplanarity of the Decay Daughters

Let us consider the triangles OAF for the t_1 track and OGB for the track t_2 , as shown in Figure 4.1. Each triangle, corresponds to the plane that the momentum \vec{p} and the $D\bar{C}A$ lay on, for each daughter.

A cut that allows to determine a possible D^0 candidate, is the demand whether the momentum of the $K\pi$ pair *points back* to the primary vertex. In particular, we can examine the relative positions of the points F, G of closest approach of the two daughter particles, with respect to the primary vertex. By introducing the following cross products

$$\vec{\psi} \equiv \vec{OF} \times \vec{AF} \quad (4.6)$$

$$\vec{\xi} \equiv \vec{OG} \times \vec{BG} \quad (4.7)$$

we define the normal vectors of the planes OFA and OGB . Let us also define the angle between these two planes as ϕ_2 and the angle between the normal vectors as ϕ_1 , as can be seen in Figure 4.2. It is clearly seen that ϕ_1 and ϕ_2 are supplementary angles. Also:

$$\phi_1 \equiv \arccos \frac{\vec{\psi} \cdot \vec{\xi}}{|\vec{\psi}| \cdot |\vec{\xi}|} \quad (4.8)$$

The angle between the planes therefore is given by the relation $\phi_2 = \pi - \phi_1$. It is important to note that this angle is not the angle between the vectors \vec{OF} and \vec{OG} . We can distinguish which $K\pi$ pair is likely to emerge from a D^0 decay, by introducing a cut on the angle ϕ_2 .

The Angle Between the Daughter Planes

The demand for this angle to be $0 < \phi_2 < \pi/2$, explaining that daughter particles emerging from a D^0 decay, need to lay in separate spaces separated by the \vec{OC} (flight

line of the D^0). We can discriminate the possible D^0 candidate pairs, by imposing such a cut as it will be later discussed. In particular, two cases are distinguishable:

- i. When the points of closest approach F, G lay on opposite sides with respect to the flight line \vec{OC} as it is shown in Figure 4.3(a); and
- ii. when the points of closest approach F, G for both daughter tracks, lay on the same side of the \vec{OC} (the pair flight line) as can be seen in Figure 4.3(b).

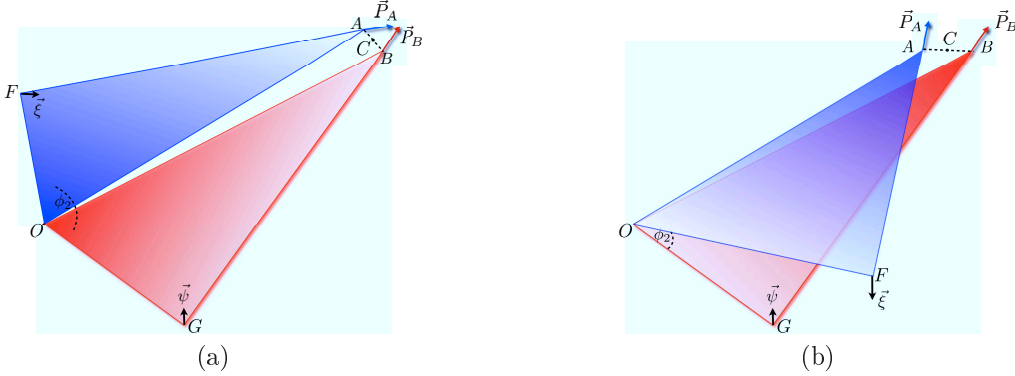


FIG. 4.3: Cartoon of $K\pi$ daughters plane. The angle between the two planes is $\phi_2 > \frac{\pi}{2}$ (a) and $\phi_2 < \frac{\pi}{2}$ (b).

4.2.2 The Angle θ_{POINTING}

After the reconstruction of the parent momentum \vec{P}_{D^0} as well as the parent flight line \vec{OC} , the θ_{POINTING} is defined as the angle between \vec{OC}, \vec{P}_{D^0} , as can be seen in Figure 4.4. A cut on the $\cos \theta_{\text{POINTING}}$ can be imposed, having in mind that for a the D^0 signal, the momentum is collinear with the flight line \vec{OC} , yielding $\cos \theta_{\text{POINTING}} \sim 1$, as it will be presented from the MC study, (cf. Section 5.5.5).

4.2.3 The Angle θ^*

Let us consider the decay of the D^0 both in the lab frame and the D^0 rest frame. In the latter frame, the two daughters are emitted in a back-to-back correlation, because of the conservation of the 4-momenta. The momentum of one of the daughters is \vec{p}' in the D^0 rest frame. Let also denote by \vec{v} the direction of emission of the D^0 in the laboratory frame. Therefore the angle between \vec{p}' and \vec{v} is the θ^* of that particle as seen in Figure 4.4. In Appendix A.3 it is explained the exact procedure of the calculation of the angle θ^* .

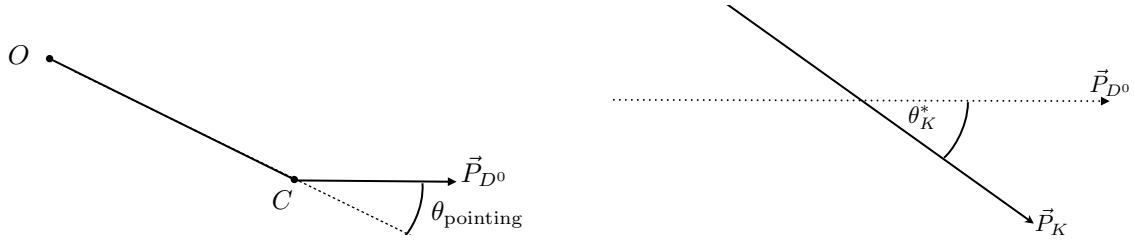


FIG. 4.4: *Left:* Cartoon depicting the angle θ_{POINTING} for the reconstructed D^0 defined as the angle between the reconstructed parent momentum and the flight line. *Right:* Cartoon of the θ^* for the kaon track. In the dotted line the parent momentum in the laboratory reference frame is denoted. In the center of mass, both daughter particles are emitted in back to back orientation.

4.2.4 The Calculation of DCA_{xy} and DCA_z

During the event reconstruction, each track is propagated towards the primary vertex and a consecutive fit is performed. The distance of the closest approach of the track trajectory and the event's primary vertex, is denoted by DCA_{xy} (in the transverse plane) and in a similar manner the DCA_z is calculated along the z -axis. For each value of the DCA_{xy} , DCA_z the adequate error is being given, denoted by σDCA_{xy} and σDCA_z . The total (*global*) DCA_G of the track in 3– D is given by (4.10). The reason for this cut to be applied that in order to select the tracks that have a large probability to have been generated at the primary vertex.

$$\text{DCA}_G = \sqrt{\text{DCA}_{xy}^2 + \text{DCA}_z^2} \quad (4.9)$$

It is of extreme importance to carefully perform a cut on a maximum value of the global DCA. In particular we consider

$$\text{DCA}_G < 1.5 \text{ cm} \quad (4.10)$$

The distributions of the DCA along with the resolutions σDCA (both in r – ϕ) as well as the ratio $\frac{\text{DCA}}{\sigma\text{DCA}}$ are plotted in Figures 4.5 (a)–(f) for the Cu+Cu (2005) run and in Figures 4.6 (a)–(f) for the Au+Au (2007) run.

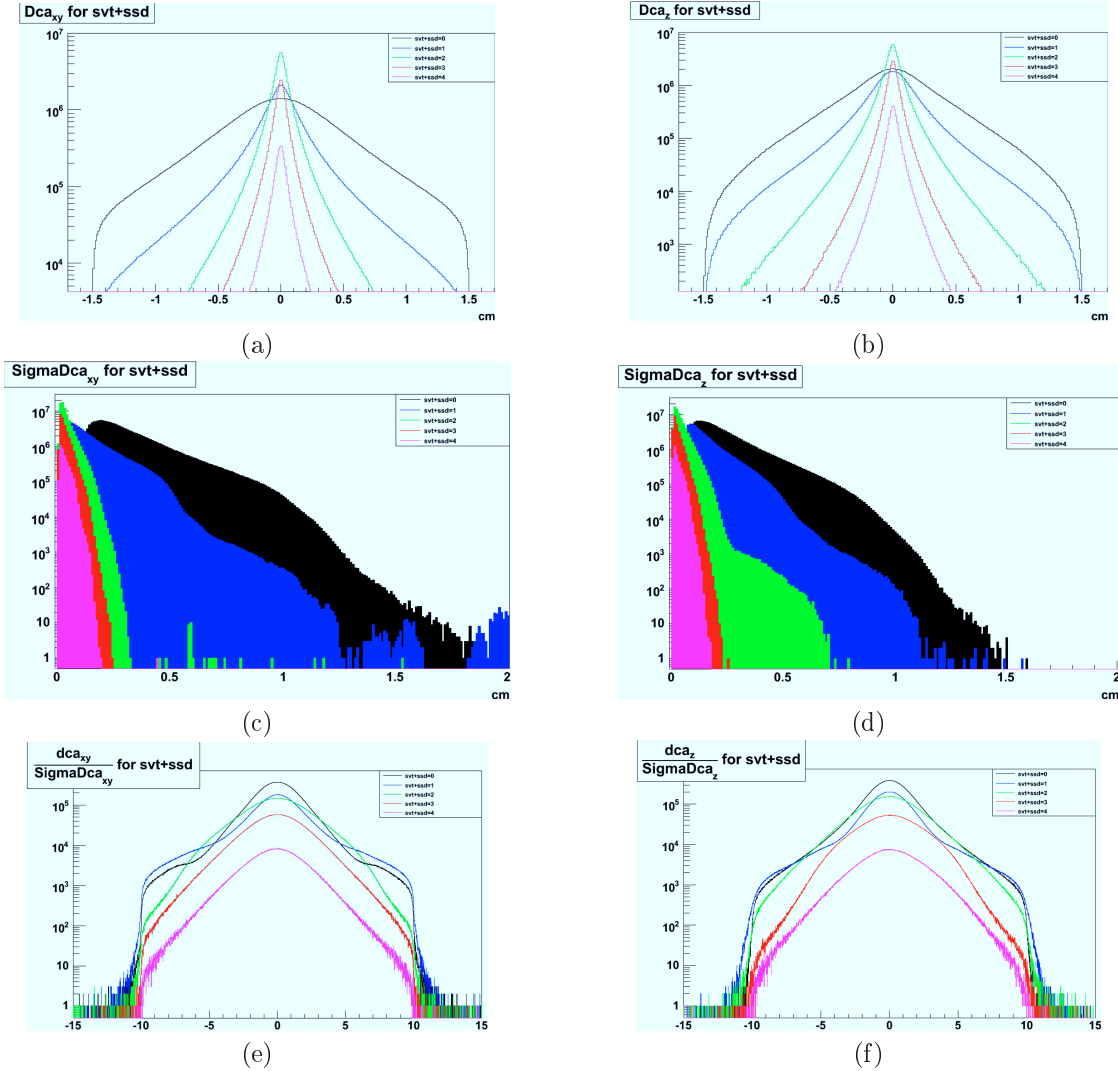


FIG. 4.5: Distributions of DCA_{xy} (a), DCA_z (b), σDCA_{xy} (c), σDCA_z (d), $\frac{DCA_{xy}}{\sigma DCA_{xy}}$ (e) and $\frac{DCA_z}{\sigma DCA_z}$ (f). All plots correspond to tracks for various SVT+SSD=0 (black), 1 (blue), 2 (green), 3 (red) and 4 (magenta) hits. Taken from the Cu+Cu at $\sqrt{s_{NN}} = 200$ GeV (High Tower) (run V).

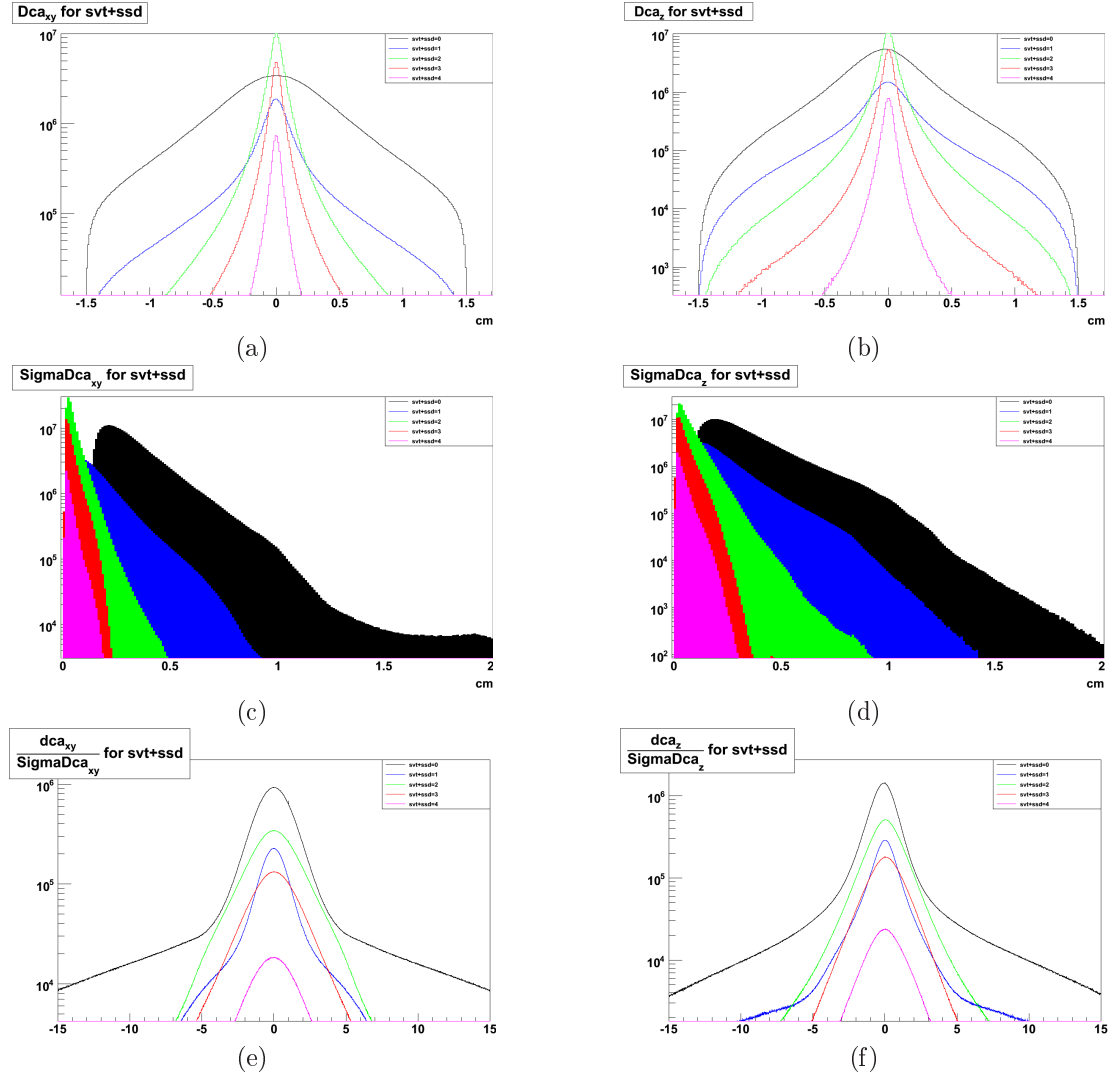


FIG. 4.6: Distributions of DCA_{xy} (a), DCA_z (b), σDCA_{xy} (c), σDCA_z (d), $\frac{DCA_{xy}}{\sigma DCA_{xy}}$ (e) and $\frac{DCA_z}{\sigma DCA_z}$ (f). All plots correspond to tracks for various SVT+SSD=0 (black), 1 (blue), 2 (green), 3 (red) and 4 (magenta) hits. Taken from the Au+Au at $\sqrt{s_{NN}} = 200$ GeV (*Btag*) (run VII).

4.2.5 The Products $\text{DCA}_{\text{xy}}^1 \cdot \text{DCA}_{\text{xy}}^2$ and $d_0^{xy,1} \cdot d_0^{xy,2}$

The calculation of the DCA is performed by extrapolating the momentum of the track e.g. \vec{P}_A , calculated at point A to the primary vertex and calculating at that point the DCA. As shown in Figure 4.1, the calculation of the \vec{OI} and \vec{OH} is being performed taking into account the magnetic field and propagating the helix till the point of closest approach to the primary vertex. From now on, we shall refer to the \vec{OH} by the DCA_{xy} and DCA_z , the *transverse* and *z*-component of the DCA.

However, for the \vec{OG} we consider a rather *straight line* propagation to the primary vertex. The latter parameter will be denoted from now on, as the *impact parameter* d_0 . It is clear that for high- p_{T} particles, the length of the *sagitta* approaches the null value, (Appendix B.2) therefore both DCA_{xy} and d_0^{xy} for each track tend to coincide. We select the transverse profile of the DCA to primary vertex for each track, creating a useful variable that will be used as a cut. The products Π_1 and Π_2 are defined as the inner product of the transverse DCA of the tracks to the primary vertex of each $K\pi$ pair.

$$\Pi_1 \equiv \text{DCA}_{\text{xy}}^K \cdot \text{DCA}_{\text{xy}}^\pi \quad (4.11)$$

$$\Pi_2 \equiv d_0^{xy,K} \cdot d_0^{xy,\pi} \quad (4.12)$$

4.3 The Resolution of the DCA in Tracking

In cylindrical coordinates, given the error on the measurement in the r, ϕ plane is $\sigma_{r\phi}$ the error for the tracking with momentum p_{T} [Ferbel 87] is given by (4.13).

$$\frac{\sigma_{p_{\text{T}}}}{p_{\text{T}}} = \frac{p_{\text{T}} \cdot \sigma_{r\phi}}{0.3 \cdot B \cdot L^2} \sqrt{\frac{720}{N+4}} \quad (4.13)$$

In (4.13), B is the magnetic field measured in [T], L is the range of the track in [m] and by N is denoted the number of points that were used to measure the track, in a uniform spacing among them. The error on the angle θ given the error σ_z , is calculated by (4.14).

$$\sigma_\theta = \frac{\sigma_z}{L} \sqrt{\frac{12(N-1)}{N(N+1)}} \quad (4.14)$$

4.3.1 The Multiple Coulomb Scattering

When a charged particle traverses a *thin* medium, then it is deflected by many *small angle* scatters. The Coulomb force from the nuclei is mainly responsible for such a deflection, therefore the name *Multiple Coulomb scattering* (MCS). However for hadronic projectiles, the strong interaction contributes to the total multiple scattering, as well.

In particular we can consider that the deflection angle θ_0 [Amsler 08] is related to the momentum p of the particle via (4.15).

$$\theta_0 = \frac{13.6 \text{ [MeV]}}{\beta c p} z \sqrt{x/X_0} \left(1 + 0.038 \ln \frac{x}{X_0} \right) \quad (4.15)$$

In (4.15) the z in the charge of the incident particle and $\frac{x}{X_0}$ refer to the target medium thickness expressed in radiation lengths X_0 . Let us also note that (4.15) is valid up to 11% for $10^{-3} < \frac{x}{X_0} < 10^2$ and single charged incident particle (with $\beta = 1$) and all Z of target material. Taking the MCS under consideration and for a given material, it is only proportional to the p^{-1} of the track. In addition to the measurement error (4.13)–(4.14), there exists also error due to the MCS effect [Ferbel 87]. Taking into account, for the transverse plane is:

$$\frac{\sigma_{p_T}^{\text{MCS}}}{p_T} = \frac{0.05}{BL} \sqrt{1.43 \frac{L}{X_0}} \quad (4.16)$$

and for the θ component resolution due to the same effect, is:

$$\sigma_\theta^{\text{MCS}} = \frac{0.015}{\sqrt{3} p} \sqrt{\frac{L}{X_0}} \quad (4.17)$$

It is clear from (4.13)–(4.17) that the momentum resolution improves with L^2 and B , whereas with the increase of N it only improves by \sqrt{N} . For a total resolution we can consider that the σ of tracking for a track with momentum p is given by the following formula

$$\sigma(p) = \sqrt{a^2 + \frac{b^2}{p^2}} \quad (4.18)$$

with the first term incorporates the measurement error, and the second term reflects the MCS. In STAR experiment, it is expected that in r - ϕ plane, the tracking to have a better resolution [Fisyak 07] than in the z dimension. In Figures 4.7: (a)–(d) the resolution in both in r - ϕ and z is plotted as a function of p^{-1} for the two datasets: Cu+Cu (run V) and Au+Au (run VII) at $\sqrt{s_{\text{NN}}} = 200 \text{ GeV}$. In order to construct the current 2-D distributions, we consider or a given p interval and fixed number of hits of the tracks, $\text{SVT+SSD} = \mathcal{C}$ where $\mathcal{C} < 5$, $\mathcal{C} \in \mathbb{Z}$, the distributions of the $\sigma_{\text{DCA}_{xy}}$ and σ_{DCA_z} are being plotted in 1-D distributions. The mean value \bar{x} (4.19) of each distribution, along with the adequate error (4.20), are correlated for the corresponding Δp^{-1} bin and for a fixed \mathcal{C} .

$$\bar{x} = \frac{1}{N} \sum_i^N x_i \quad (4.19)$$

$$\sigma = \sqrt{\frac{1}{N-1} \sum_i^N (x_i - \bar{x})^2} \quad (4.20)$$

The typical values for the resolution both in $r-\phi$ and z cylindrical components, for tracks with momentum of $p = 1 \text{ GeV}/c$ are summarized in Table 4.1. The overall resolution distributions (both transverse and z components), as a function of the inverse momentum p^{-1} , are shown in Figure 4.7 both for the Cu+Cu (run V) and the Au+Au (run VII) at $\sqrt{s_{\text{NN}}} = 200 \text{ GeV}$ datasets.

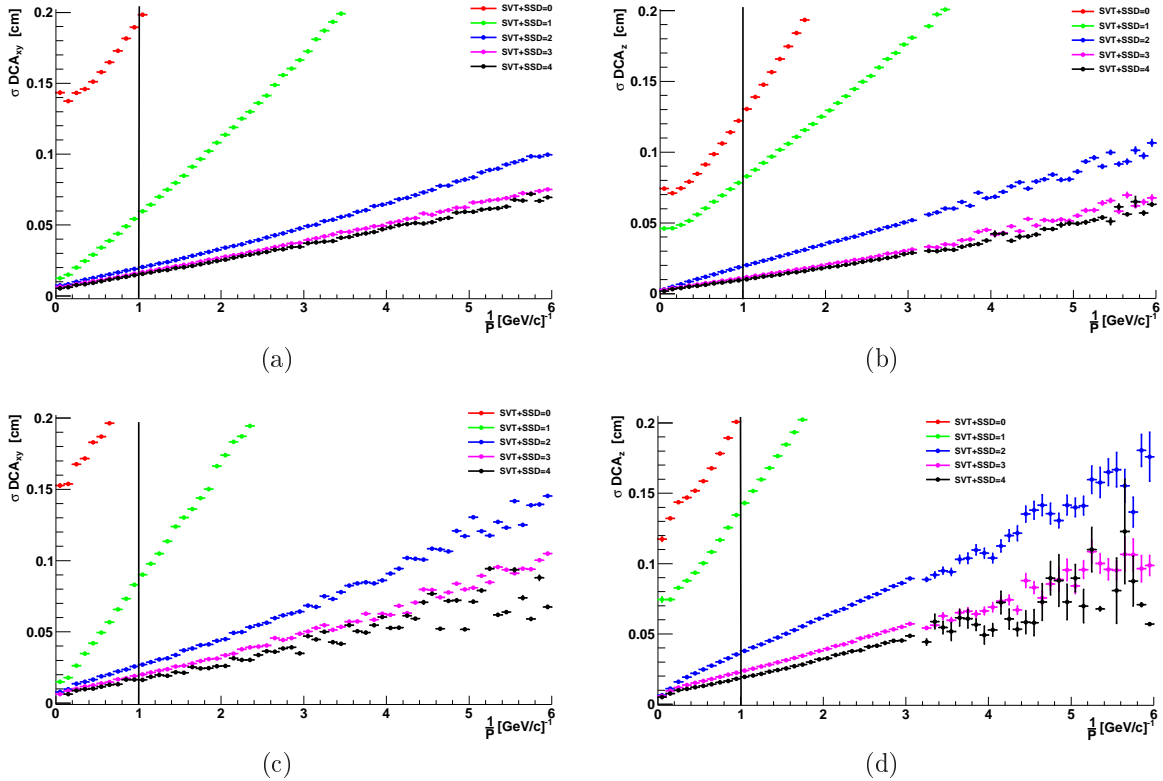


FIG. 4.7: Tracking resolution in $r-\phi$ (a) and z (b) as a function of p^{-1} for tracks with SVT+SSD=0 (red), 1(green), 2(blue), 3(magenta) and 4(black) hits. Plots (a) and (b) created with Cu+Cu at $\sqrt{s_{\text{NN}}} = 200 \text{ GeV}$ (*High Tower*) data, (c) and (d) created with Au+Au at $\sqrt{s_{\text{NN}}} = 200 \text{ GeV}$ (*Btag*) data. The black line indicates the $p = 1 \text{ GeV}/c$. Vertical error bars reflect the statistical error.

TAB. 4.1: Resolution of DCA_{XY} and DCA_z values calculated at $p = 1 \text{ GeV}/c$ for various SVT+SSD cases, shown in Figure 4.7. Taken from Cu+Cu at $\sqrt{s_{NN}} = 200 \text{ GeV}$ (run V), (*High Tower*) and Au+Au at $\sqrt{s_{NN}} = 200 \text{ GeV}$ (run VII) (*Btag*) data. All errors are statistical.

| SVT+SSD hits | $\sigma DCA_{XY} [\mu\text{m}]$ | $\sigma DCA_z [\mu\text{m}]$ |
|--------------|---------------------------------|------------------------------|
| Cu+Cu | | |
| 0 | 1983.92 ± 0.27 | 1304.3 ± 0.13 |
| 1 | 596.48 ± 0.15 | 830.13 ± 0.09 |
| 2 | 203.03 ± 0.05 | 201.80 ± 0.07 |
| 3 | 167.64 ± 0.07 | 116.73 ± 0.06 |
| 4 | 156.04 ± 0.14 | 101.89 ± 0.07 |
| Au+Au | | |
| 0 | 2248.93 ± 0.96 | 2117.61 ± 0.68 |
| 1 | 900.66 ± 0.54 | 1430.63 ± 0.86 |
| 2 | 272.00 ± 0.16 | 379.71 ± 0.32 |
| 3 | 201.25 ± 0.16 | 240.00 ± 0.27 |
| 4 | 163.52 ± 0.38 | 195.11 ± 0.58 |

Chapter 5

Simulation Study

The main subject of the current chapter, is the simulation study of the decay properties of $D^0 \rightarrow K^-\pi^+$. The goal is to obtain a study on the decay topological properties. The microvertexing code is applied on the simulation sample allowing the comparison between reconstructed and initial values. Also a comparison of the simulation and the data is performed, in the final sections allowing a cut study on the microvertexing variables. The latter study allows the extraction of the optimized values of the cuts that will be applied on the data sample, concerning the D^0 analysis.

5.1 Introduction

The STARSIM [Potekhin 06, Perevoztchikov 10] simulation interface is a framework designed for the STAR detector using the GEANT [Apostolakis 93] simulation package. It can simulate the geometry of different subsystems of the STAR detector, as well as particle generation. Using the STARSIM simulation package a pure D^0 signal is generated with the following properties. A total of approximately 400000 events, with each event containing 1 D^0 that decays only in the hadronic channel $K^-\pi^+$. The daughter particles are then propagated through the ensemble of the material of STAR detector for the year 2005, denoted by the geometry tag: y2005g [Didenko 10]. Each event is generated within $30 \leq z - \text{vertex} \leq 30$ [cm], as shown in Figure 5.1. The daughter tracks span within the $\eta \in [-1, 1]$ area in pseudorapidity, and full azimuth coverage $\phi \in [-\pi, \pi]$ as can be seen in Figure 5.2. The tracks' distance of closest approach to the primary vertex both in the bending plane and in z direction: DCA_{xy} and DCA_z, can be seen in Figure 5.2. Finally the invariant mass of D^0 with the adequate gaussian fit can be seen in Figure 5.5. No further background subtraction was needed to be performed.

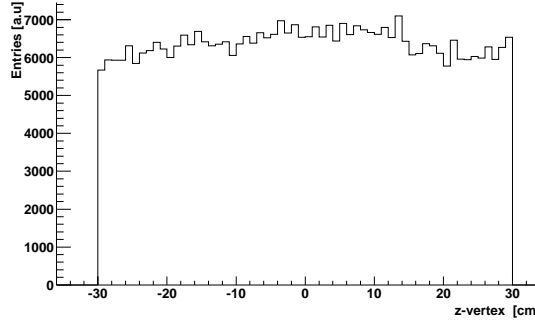


FIG. 5.1: Primary z -vertex component of the generated MC events, including the cut of the $|\text{vertex}| < 30 \text{ cm}$.

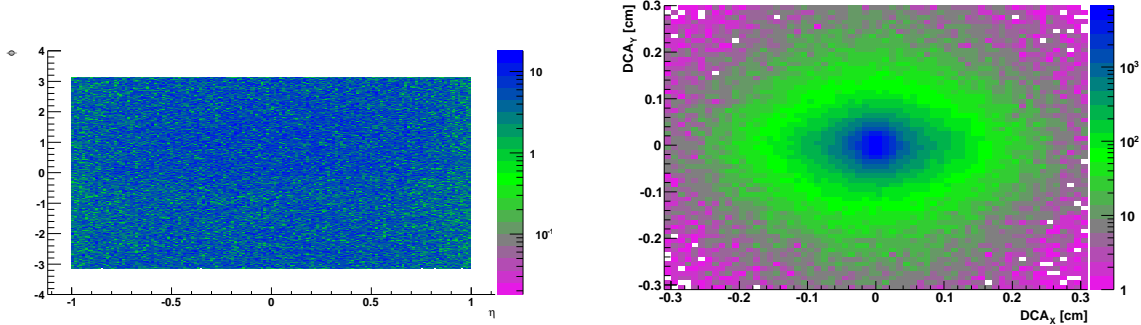


FIG. 5.2: *Left:* $\eta-\phi$ coverage of the daughter particles in the TPC space, emerging from the simulation of $D^0 \rightarrow K^-\pi^+$ case. *Right:* Correlation of distances of closest approach DCA_{xy} vs. DCA_z with respect to the primary vertex for the daughter particles. Plots created from simulation data.

5.2 The STARSIM initial values

The initial values of the decay particles were also introduced in the STARSIM. In particular we present the initial decay length in Figure 5.3 (left side), as well as the initial p_T distribution as shown in Figure 5.3 (right side) for the η of the D^0 (Figure 5.4).

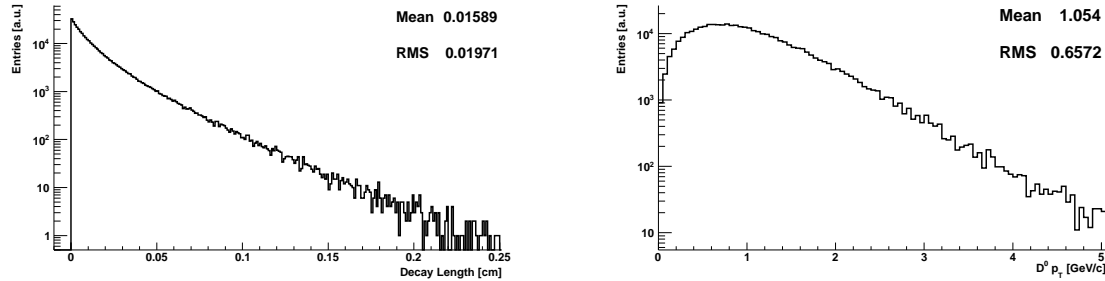


FIG. 5.3: Pure D^0 signal created with STARSIM. *Left*: D^0 decay length distribution. The mean value of the distribution is $L = 158 \mu\text{m}$. *Right*: D^0 initial p_T spectrum.

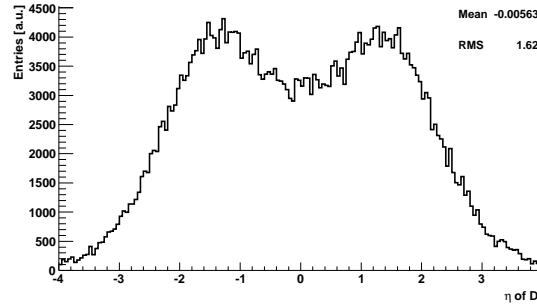


FIG. 5.4: Pseudorapidity distribution of a pure D^0 signal created with STARSIM simulation package.

5.3 The Tracking Resolution

The daughter tracks coming from the $D^0 \rightarrow K^- \pi^+$ are extrapolated to the primary vertex and the distances: DCA_{xy} and DCA_z are calculated, along with their errors ($\sigma_{\text{DCA}_{xy}}$ and σ_{DCA_z}). In Figure 5.6 it is presented the resolution of the tracking in the transverse plane ($\sigma_{\text{DCA}_{xy}}$) and z -component (σ_{DCA_z}). The method that is applied in order to perform the study, is identical to the one applied on the

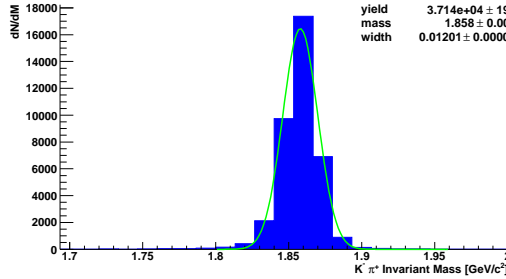


FIG. 5.5: Simulation of $D^0 \rightarrow K^- \pi^+$ invariant mass yield along with gaussian fit (green line) yielding the mean value of $1.858 \text{ GeV}/c^2$ and $\sigma = 12 \text{ MeV}/c^2$.

Cu+Cu and Au+Au datasets, as described in Section 4.3. Finally the values of both the tracking resolutions σDCA_{xy} and σDCA_z for tracks with $p = 1 \text{ GeV}/c$ and for various SVT+SSD hits are shown in Table 5.1. The distributions of the resolutions as a function of the inverse momentum, p^{-1} of tracks and for various SVT+SSD cases, respecting (4.15), is presented in Figure 5.6.

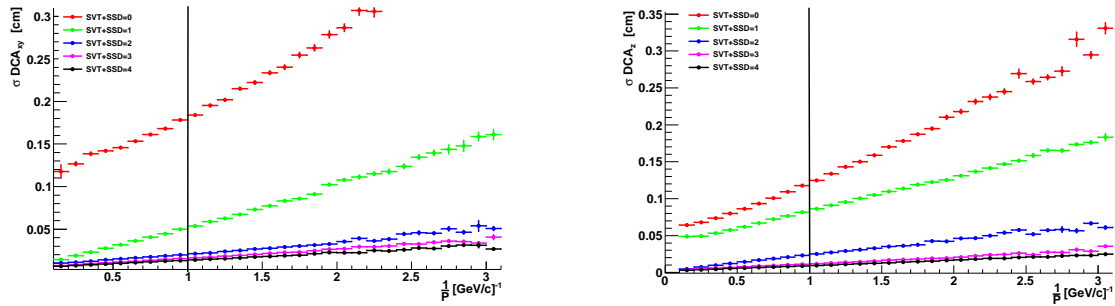


FIG. 5.6: Tracking resolution as a function of p^{-1} in $r-\phi$ (left) and z (right) components. Taken from simulation with geometry y2005g. The black line indicates the $p = 1 \text{ GeV}/c$. Vertical error bars reflect the statistical error.

5.4 The Microvertexing Method Application on Monte Carlo

In order to compare the results of the microvertexing method on data and Monte Carlo, we can plot the relative difference of the value of each variable reconstructed (denoted by the tag RECO) by the microvertexing technique and the initial values of the simulation (denoted by the tag GEANT). After generating the pure D^0 signal and forcing it to decay only in the hadronic channel $D^0 \rightarrow K^- \pi^+$ we can extract

TAB. 5.1: Resolution of DCA_{xy} and DCA_z values calculated at $p = 1 \text{ GeV}/c$ for various SVT+SSD cases. Taken from simulation with geometry y2005g. All errors are statistical.

| SVT+SSD hits | $\sigma DCA_{xy} [\mu\text{m}]$ | $\sigma DCA_z [\mu\text{m}]$ |
|--------------|---------------------------------|------------------------------|
| 0 | 1839.64 ± 10.34 | 1247.61 ± 4.03 |
| 1 | 535.64 ± 2.88 | 861.27 ± 1.68 |
| 2 | 210.33 ± 1.48 | 249.98 ± 1.69 |
| 3 | 162.36 ± 0.83 | 119.26 ± 0.67 |
| 4 | 139.15 ± 0.71 | 95.87 ± 0.36 |

the information of the kinematics of daughter particles, such as the momentum. By propagating the daughter particles through the STAR detector material, we apply the reconstruction code, that contains the microvertexing technique. For every pair of negative and positive tracks, the secondary vertex (the point that the D^0 decay takes place), as well as the decay length are being calculated using the method described in Section 4.2. The information is stored on an event by event basis and the values obtained are compared to the *initial* GEANT values. We present this comparison for the following microvertexing variables as a difference between the reconstructed and initial values: $\Delta L \equiv \text{GEANT} - \text{RECO}$. Let also note that the primary vertex is not calculated but rather extracted from the event information and plotted in order to guarantee that the values obtained belong to the same event.

- i. The difference between the values of primary vertex in x , y and z , as shown in Figure 5.7. Let us note that the only reason the comparison for the primary vertex is performed is to make sure that the variables corresponding to the same events are compared each time;
- ii. the difference between the values of secondary vertex in x , y and z , shown in Figure 5.9; and
- iii. the difference between the values of decay length vertex in x , y and z , shown in Figure 5.11.

In addition a correlation of RECO-GEANT as a two dimensional plot is also presented:

- i. The values of the primary vertex in x , y and z , obtained by GEANT vs. the reconstructed (RECO) ones, as shown in Figure 5.8;
- ii. the secondary vertex in x , y and z shown in Figure 5.10; and
- iii. the decay length in x , y and z , shown in Figure 5.12.

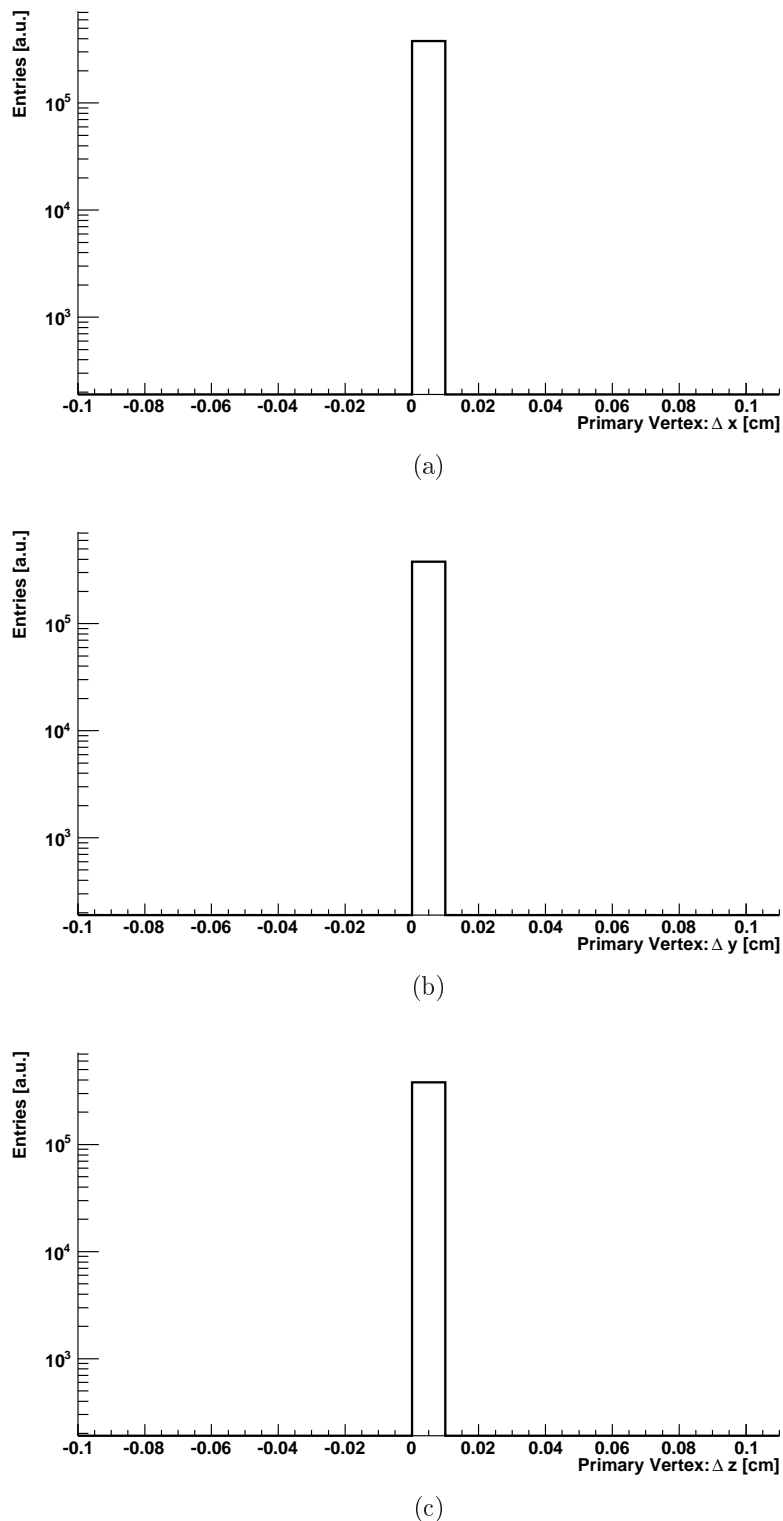


FIG. 5.7: Distribution of the difference between the reconstructed (RECO) and the initial values (GEANT) for the primary vertex position in Δx (a), Δy (b) and Δz (c) components.

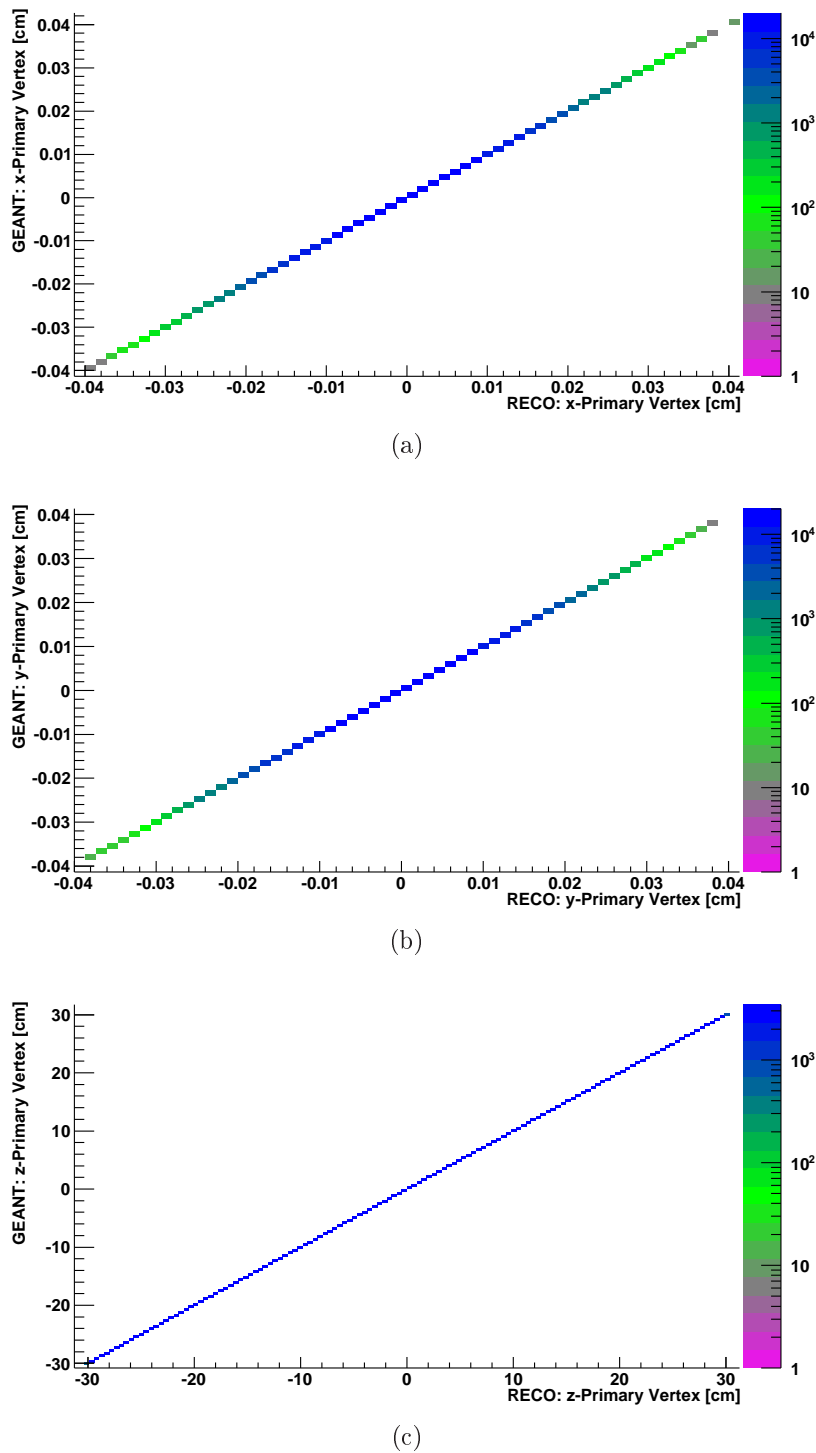


FIG. 5.8: Comparison of RECO vs. GEANT values for the primary vertex components: x (a), y (b) and z (c).

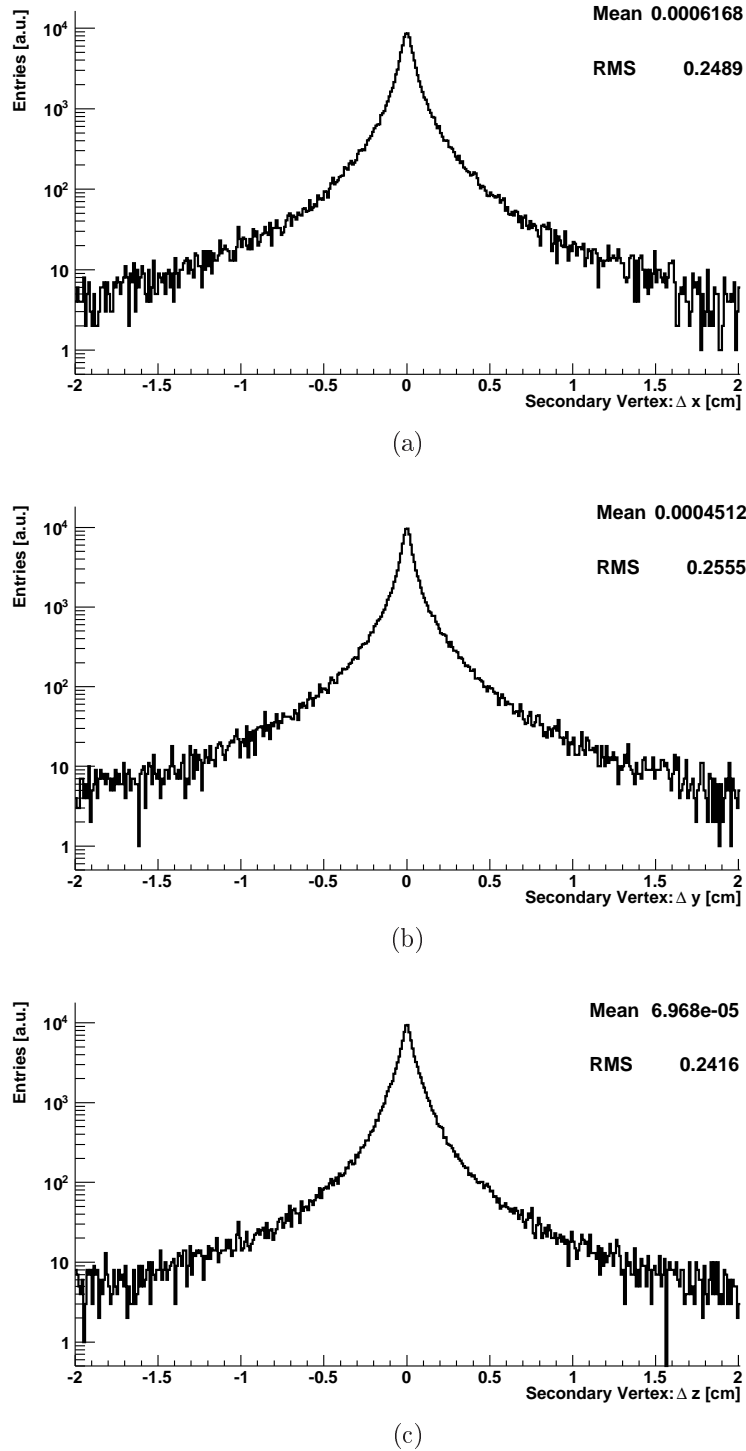


FIG. 5.9: Distribution of the difference between the reconstructed (RECO) and the initial values (GEANT) for the secondary vertex position in Δx (a), Δy (b) and Δz (c) components.

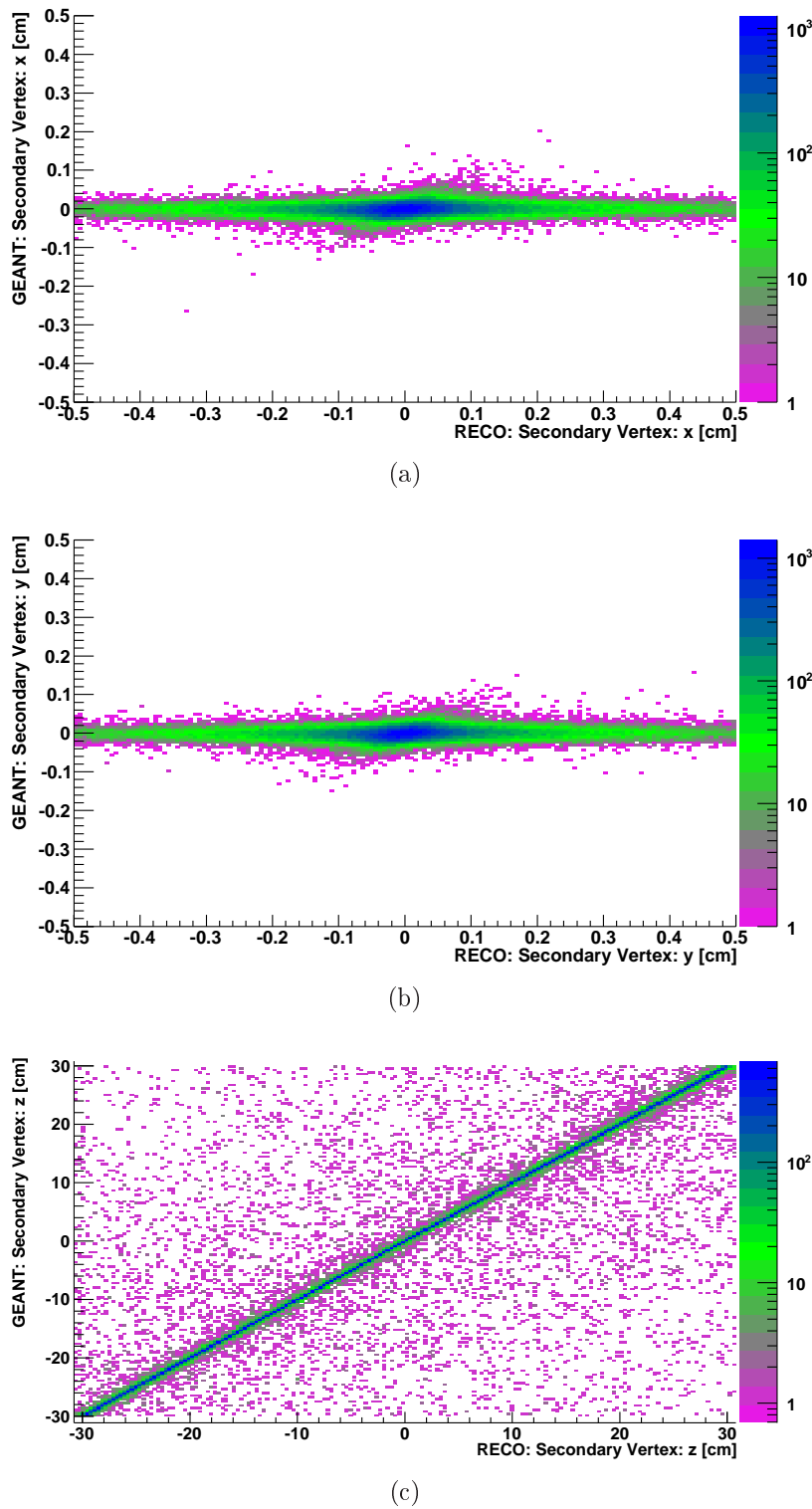


FIG. 5.10: Comparison of RECO vs. GEANT values for the secondary vertex components: x (a), y (b) and z (c).

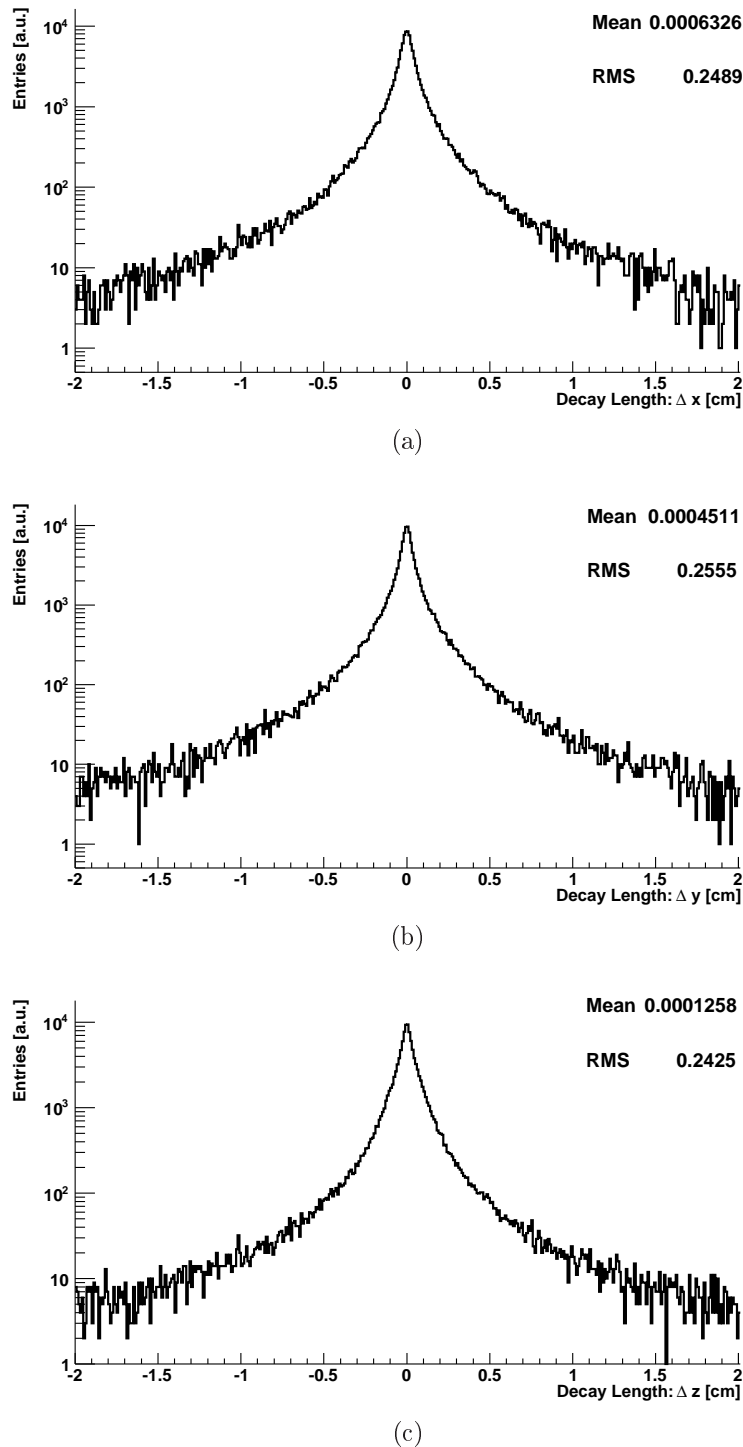


FIG. 5.11: Distribution of the difference between the reconstructed (RECO) and the initial geant values for the decay length in Δx (a), Δy (b) and Δz (c) components.

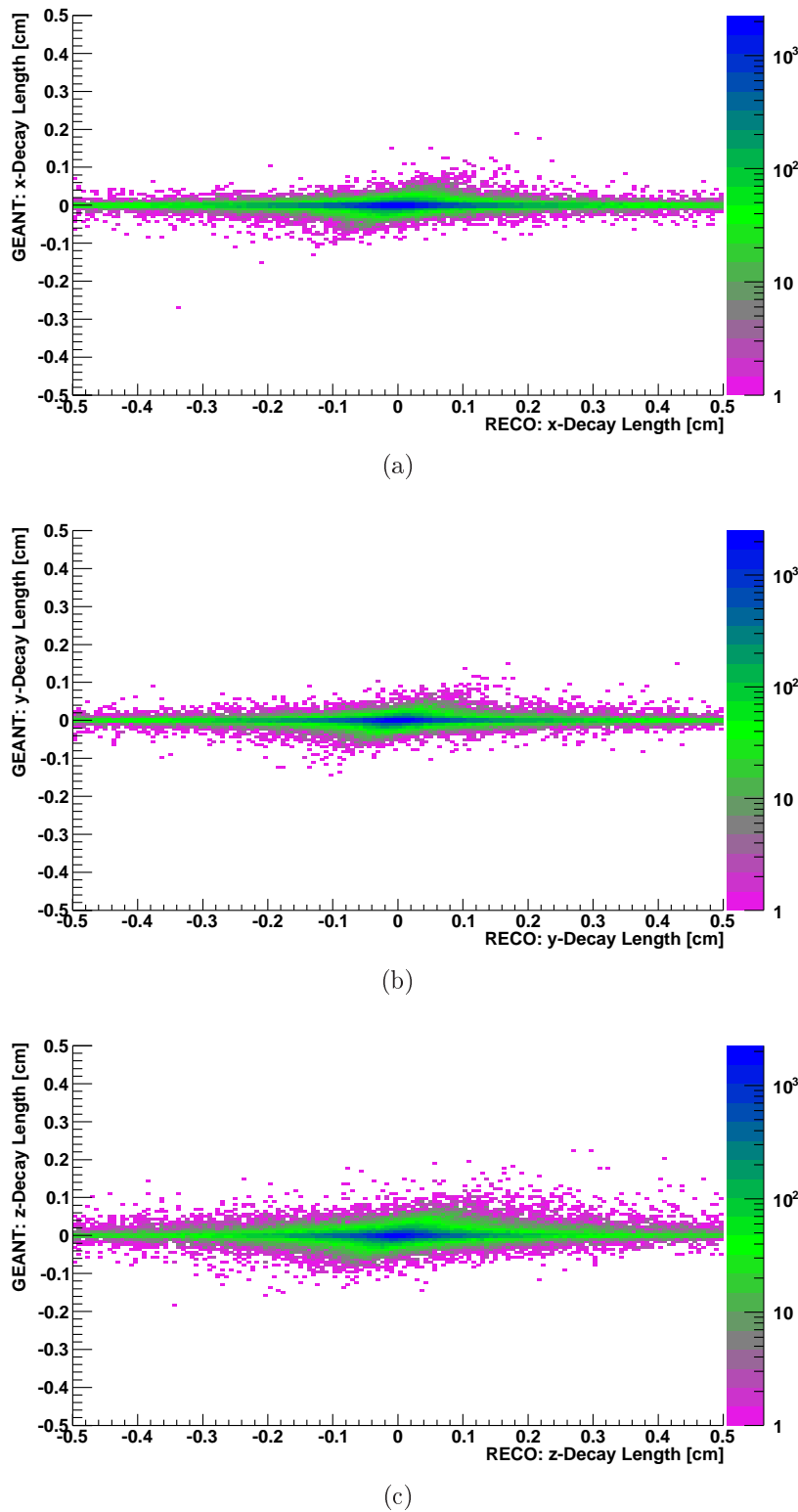


FIG. 5.12: Comparison of RECO vs. GEANT values for the decay length components: x (a), y (b) and z (c).

5.4.1 The Impact of the Silicon Hits on the Microvertexing Variables

In order to investigate the impact of the inclusion of the Si hits in the tracks, we perform the following cut. By demanding explicitly for every track to comply with the cut $\text{SVT+SSD}=n$ (where $n=0\text{--}4$), we calculate distributions of the:

- i. The DCA between the daughter tracks shown in Figure 5.13 (a);
- ii. the decay length of D^0 as seen in Figure 5.13 (b); and
- iii. the DCA of D^0 to primary vertex shown in Figure 5.13 (c).

The calculation of the D^0 DCA is performed by taking into consideration the straight line extrapolation, using (4.3). As it will be later shown in Section 5.5, the cut on the total SVT+SSD hits of a track has an impact on the reconstruction of the microvertexing variables. In Table 5.2 the mean values of the reconstructed microvertexing variables extracted from the MC dataset are summarized.

TAB. 5.2: Mean values of the microvertexing variables for various $\text{SVT+SSD}=0\text{--}4$ cases. Data is taken from simulation.

| Si hits \ variables [cm] | DCA between daughters | Decay length of D^0 | DCA of D^0 to primary vertex |
|-----------------------------|-----------------------------|--------------------------|--------------------------------------|
| 0 | 0.202 | 0.280 | 0.220 |
| 1 | 0.114 | 0.172 | 0.124 |
| 2 | 0.073 | 0.114 | 0.080 |
| 3 | 0.058 | 0.090 | 0.063 |
| 4 | 0.048 | 0.076 | 0.052 |

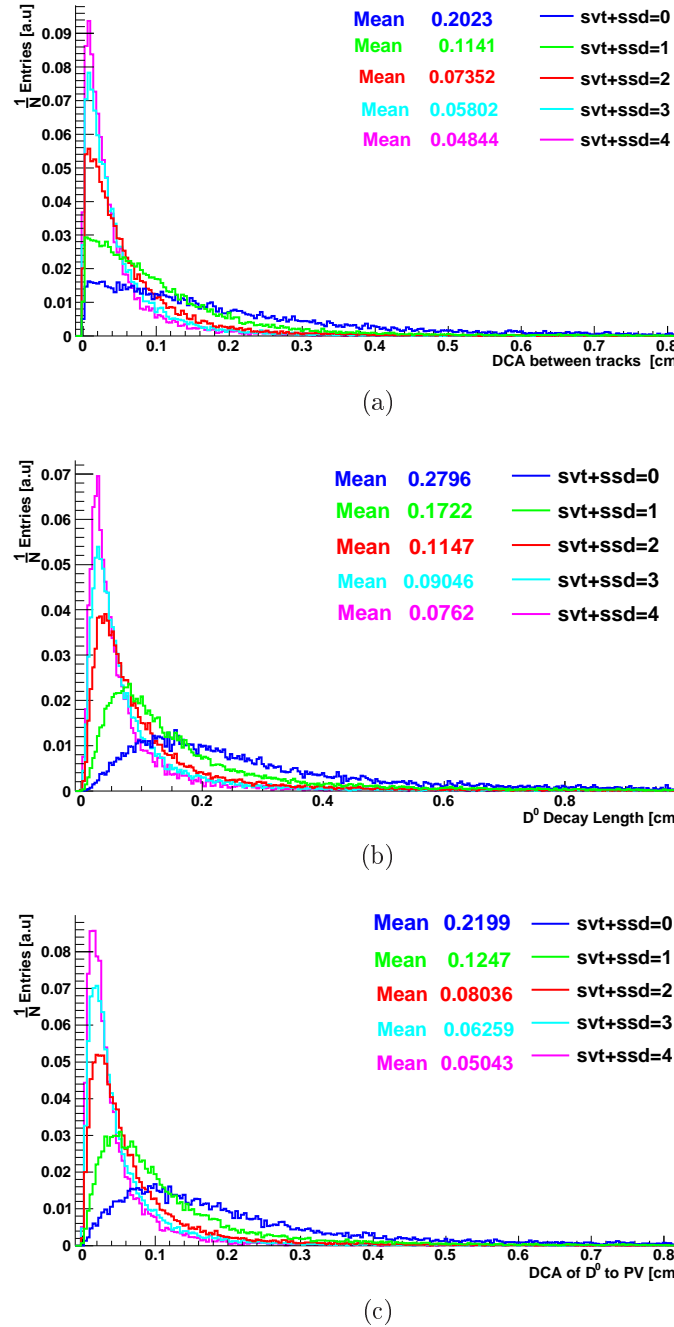


FIG. 5.13: The microvertexing variables distribution along with the mean values for various SVT+SSD cases=0,1,2,3 and 4. DCA between tracks (a), D^0 decay length (b) and DCA of D^0 to primary vertex (c). All plots are normalized to their total number of entries. Data is taken from simulation.

5.5 The Reconstructed Microvertexing Values Cut Study

In order to tune up the cuts that will be later used for the analysis and find the optimal cuts for the reconstruction of the D^0 , a cut study is being performed on the simulation sample, and in particular examining the microvertexing variables, cf. Section 4.2. Let us consider the distribution of the variable a both in the MC and data. The MC values of that variable (denoted by a_{mc}) can be considered as the *signal* (S) and the Cu+Cu data values (denoted by a_{data}) can also be considered as the *background* (B). Both variables are presented in one dimensional $\frac{da}{dN}$ distributions, with their integral normalized to unity (e.g. Figure 5.14 (a) for the DCA between tracks). The goal of the current study is to investigate the impact of an inclusive cut (keeping the region of $\Delta a \equiv [a_1, a_2]$) on the S and B distributions. For this reason, we investigate the variation of the (5.1) in the pre-determined interval Δa . In addition we examine the variation of both the $\frac{S}{B}$ and the $\frac{S}{\sqrt{B}}$ in the predetermined interval. Finally, the *survival percentage* (denoted by SP); ergo the percentage contained of the variable for each data sample (MC and data) in the range Δa is also presented for every microvertexing variable.

$$\begin{aligned} S &\equiv \int_{a_1}^{a_2} \frac{da_{mc}}{dN} dN \\ B &\equiv \int_{a_1}^{a_2} \frac{da_{data}}{dN} dN \end{aligned} \tag{5.1}$$

In addition, the inclusion of the Si hits of each track in the calculation of the microvertexing variables, is investigated by repeating the study for the various SVT+SSD cases. The MC dataset that is used for the current described in Section 5.1. For the data comparison we used the Cu+Cu at $\sqrt{s_{nn}} = 200$ GeV, *High Tower* trigger setup dataset, (cf. Chapter 6). The calculation of the variables both for MC and real data is done using the same technique as described in Section 4.2. Additionally, two regions will be considered: $[0, 1]$ (cm) and $[0, 0.1]$ (cm). The following variables are used to perform this cut study.

- i. The distance of closest approach (DCA) between the daughters;
- ii. the decay length of the $K\pi$ pair; and
- iii. the reconstructed DCA of the D^0 (parent particle) with respect to the primary vertex.

5.5.1 The S/B Study for $\text{SVT}+\text{SSD}>0$ hits

We begin the S/B variation study by considering the case where all the tracks used for this study have a total number of silicon hits $\text{SVT}+\text{SSD}>0$. We select the region $[0, 1]$ (cm) and the variation of the S and B is examined with a step of 0.1 cm. We will insist on the region $[0, 0.1]$ cm by varying the ratios S/B , S/\sqrt{B} , with a more fine step of 0.01 cm.

The Range of Study $[0, 1]$ cm

In Table 5.3 the values of S and B along with the ratios S/B and S/\sqrt{B} for each microvertexing variable are summarized for the $\Delta a = [0, 1]$ (cm) range. Also the *survival percentage* (SP) in the range Δa is also presented for every microvertexing variable in (b), as well as the ratios S/B (c) and S/\sqrt{B} (d). In particular, the DCA between daughter tracks is plotted in Figures 5.14, the D^0 decay length in Figures 5.15 and the D^0 DCA to the primary vertex in Figures 5.16.

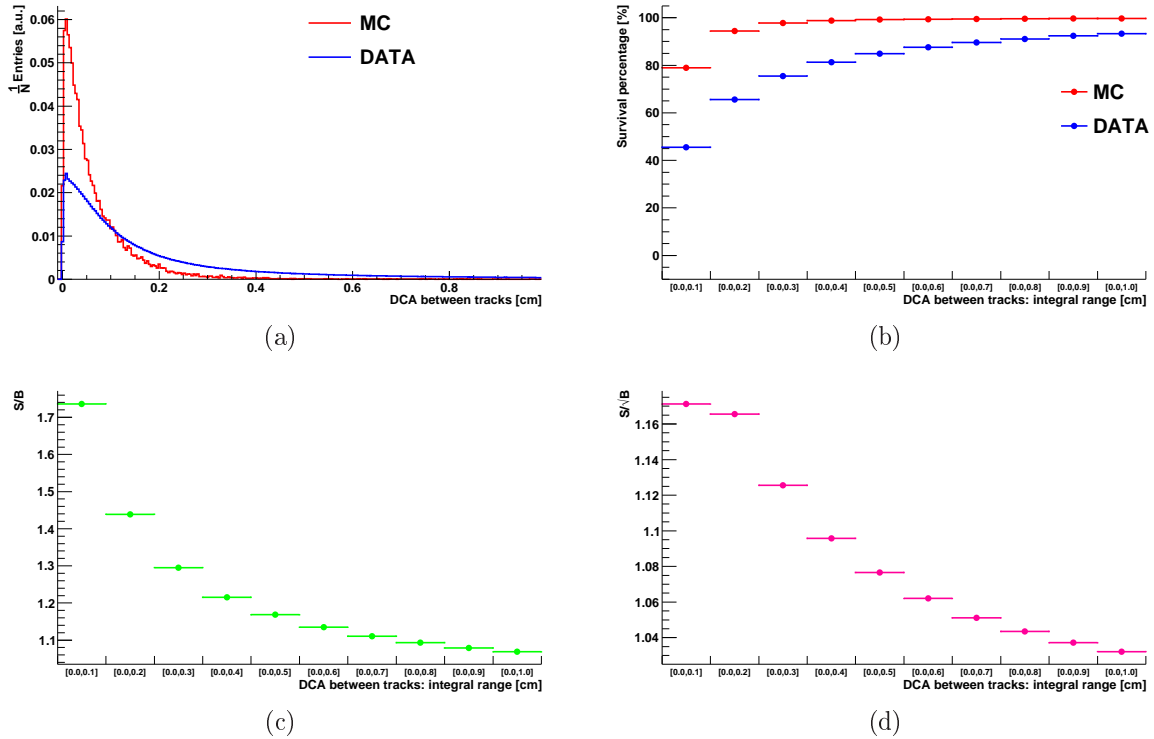


FIG. 5.14: DCA between tracks S/B variation study for $\text{SVT}+\text{SSD}>0$, in the range $[0, 1]$ (cm). Normalized distribution of S and B (a), survival percentage per value range (b), ratio S/B (c) and S/\sqrt{B} (d).

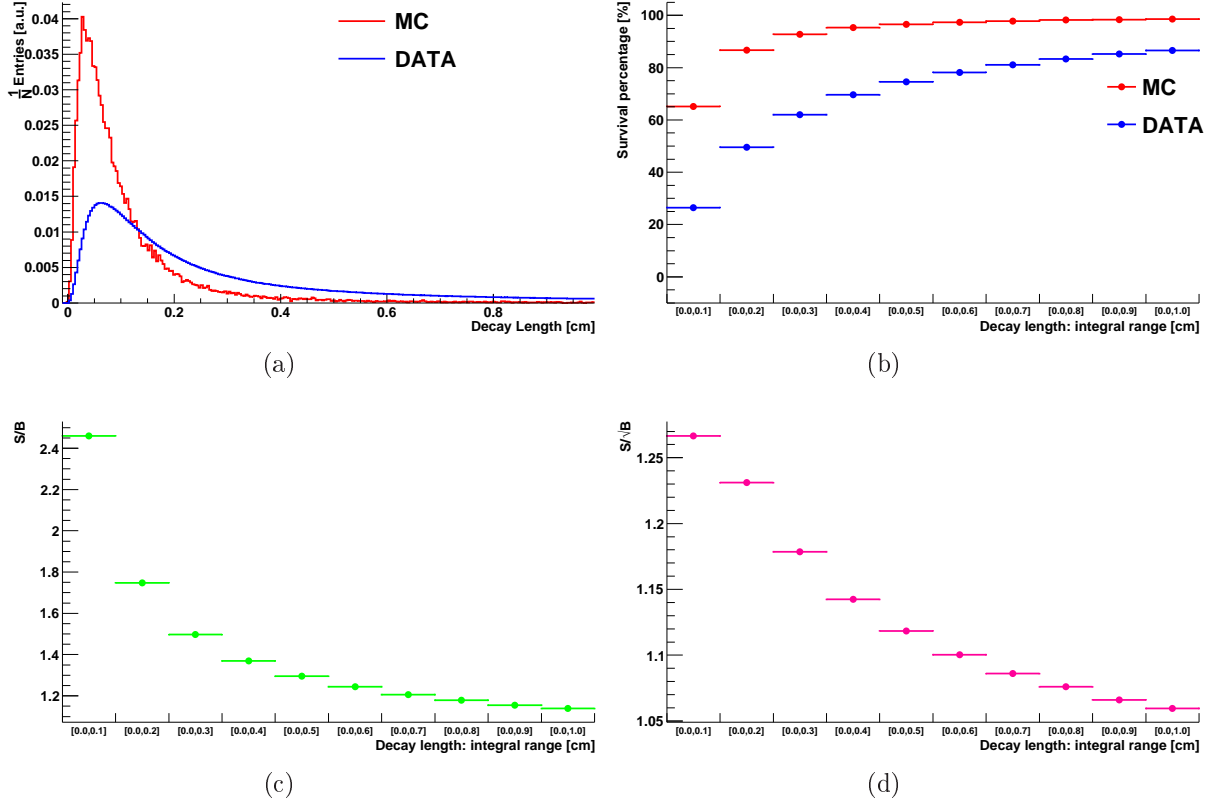


FIG. 5.15: D^0 decay length S/B variation study for $\text{SVT}+\text{SSD}>0$, in the range $[0, 1]$ (cm). Normalized distribution of S and B (a), survival percentage per value range (b), ratio S/B (c) and S/\sqrt{B} (d).

TAB. 5.3: S/B variation of microvertexing variables in the $[0, 1]$ (cm) range, for $\text{SVT} + \text{SSD} > 0$ hits of each track.

| variables \ range (cm) | | [0, 0.1] | [0, 0.2] | [0, 0.3] | [0, 0.4] | [0, 0.5] | [0, 0.6] | [0, 0.7] | [0, 0.8] | [0, 0.9] | [0, 1.0] |
|-----------------------------|--------------|----------|----------|----------|----------|----------|----------|----------|----------|----------|----------|
| DCA between tracks | S | 0.790 | 0.944 | 0.978 | 0.988 | 0.992 | 0.994 | 0.995 | 0.996 | 0.997 | 0.997 |
| | B | 0.455 | 0.656 | 0.755 | 0.813 | 0.849 | 0.876 | 0.896 | 0.911 | 0.924 | 0.933 |
| | S/B | 1.737 | 1.437 | 1.294 | 1.216 | 1.167 | 1.134 | 1.110 | 1.092 | 1.078 | 1.068 |
| | S/\sqrt{B} | 1.171 | 1.166 | 1.126 | 1.096 | 1.077 | 1.062 | 1.051 | 1.044 | 1.037 | 1.032 |
| D^0 decay length | S | 0.652 | 0.867 | 0.928 | 0.953 | 0.966 | 0.973 | 0.978 | 0.982 | 0.984 | 0.986 |
| | B | 0.265 | 0.496 | 0.620 | 0.696 | 0.746 | 0.782 | 0.811 | 0.833 | 0.852 | 0.866 |
| | S/B | 2.466 | 1.748 | 1.495 | 1.369 | 1.295 | 1.243 | 1.206 | 1.177 | 1.155 | 1.138 |
| | S/\sqrt{B} | 1.267 | 1.231 | 1.179 | 1.142 | 1.118 | 1.100 | 1.086 | 1.076 | 1.066 | 1.060 |
| D^0 DCA to primary vertex | S | 0.797 | 0.943 | 0.973 | 0.984 | 0.989 | 0.992 | 0.994 | 0.995 | 0.995 | 0.996 |
| | B | 0.459 | 0.682 | 0.779 | 0.833 | 0.869 | 0.894 | 0.913 | 0.929 | 0.941 | 0.950 |
| | S/B | 1.736 | 1.382 | 1.248 | 1.180 | 1.139 | 1.109 | 1.087 | 1.071 | 1.057 | 1.048 |
| | S/\sqrt{B} | 1.176 | 1.142 | 1.102 | 1.078 | 1.061 | 1.049 | 1.040 | 1.032 | 1.026 | 1.022 |

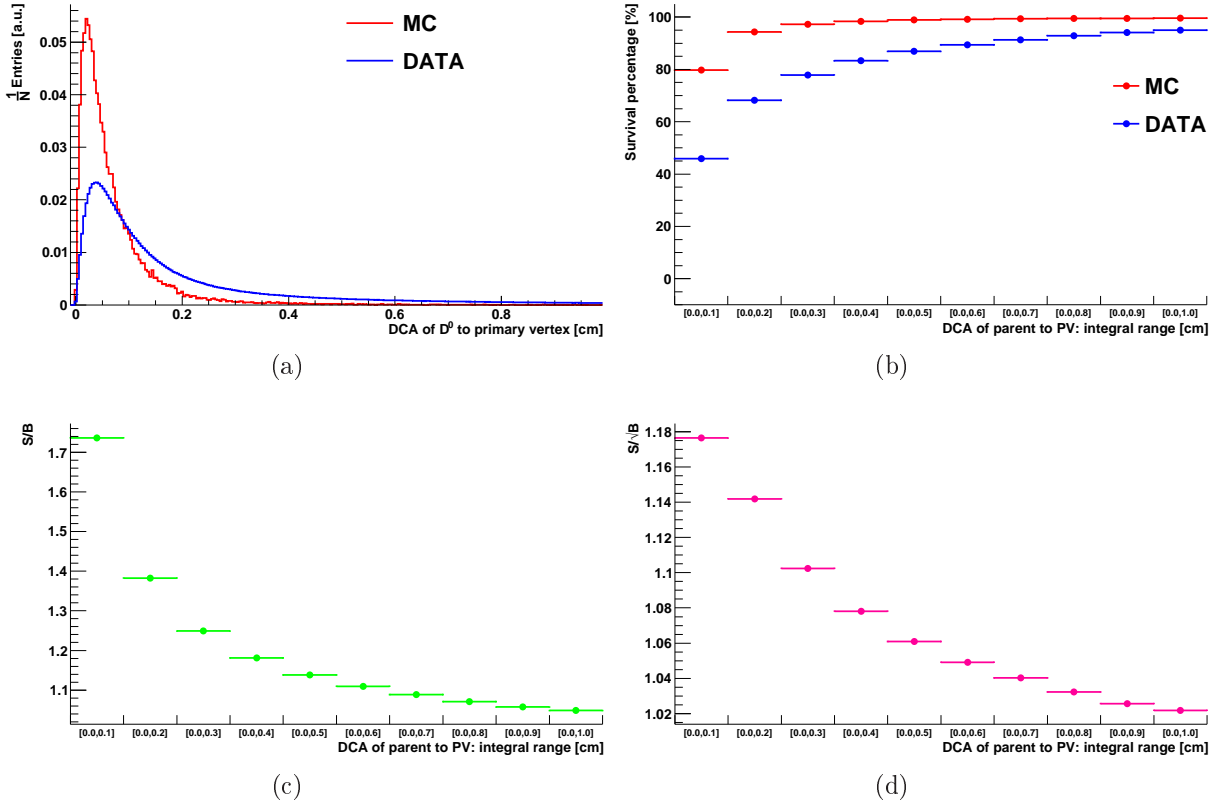


FIG. 5.16: D^0 DCA to primary vertex S/B variation study for $SVT+SSD>0$, in the range $[0, 1]$ cm. Normalized distribution of S and B (a), survival percentage per value range (b), ratio S/B (c) and S/\sqrt{B} (d).

Range of Study $[0, 0.1]$ cm

For the specific range interval, the values of S and B along with the ratios S/B and S/\sqrt{B} for each microvertexing variable are summarized for the $\Delta a = [0, 0.1]$ (cm) range in Table 5.4. Concerning the graphical part, for every Figure the raw distributions are given in (a), the SP in (b), along with both S/B in (c) and S/\sqrt{B} in (d). In Figures 5.17 the plots referring to the DCA between daughter tracks are presented. For the D^0 decay length the plots are given in Figures 5.18. Finally for the D^0 DCA to the primary vertex the plots are found in Figures 5.19.

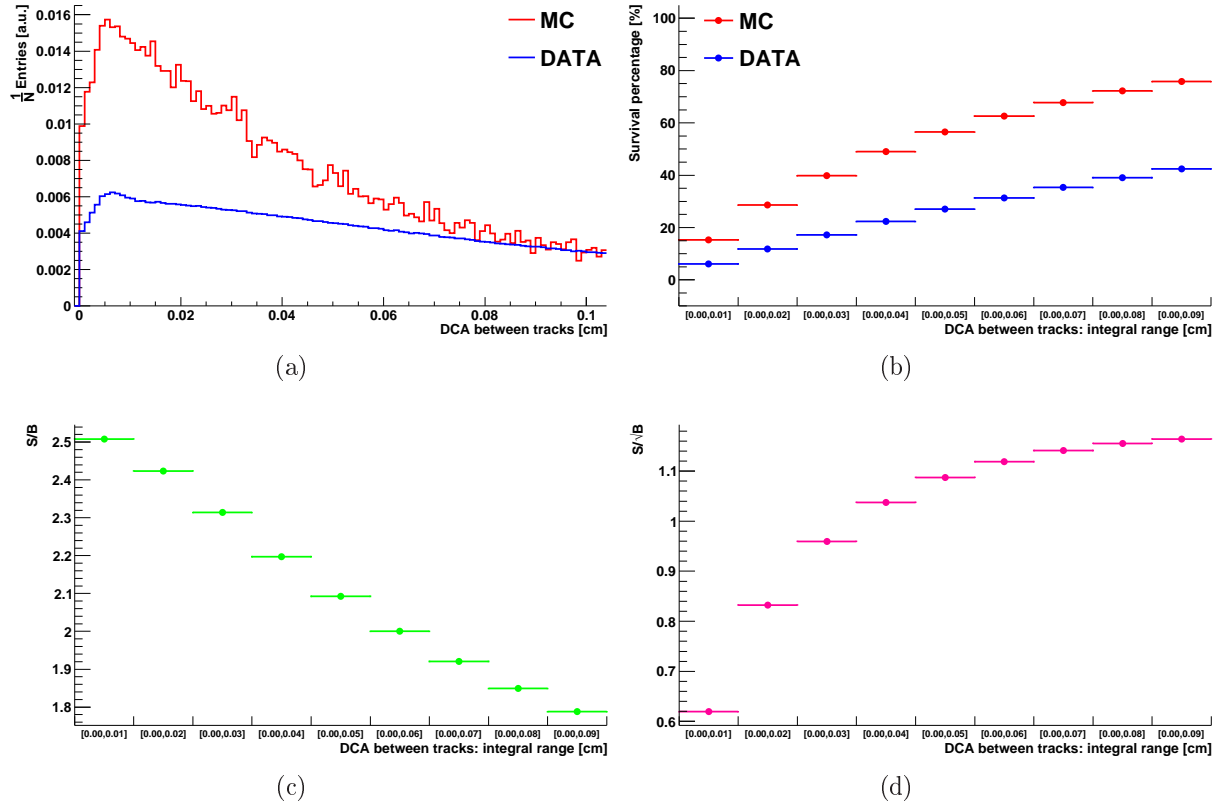


FIG. 5.17: DCA between tracks S/B variation study for $SVT+SSD>0$, in the range $[0, 0.1]$ (cm). Normalized distributions of S and B (a), survival percentage per value range (b), ratio S/B (c) and S/\sqrt{B} (d).

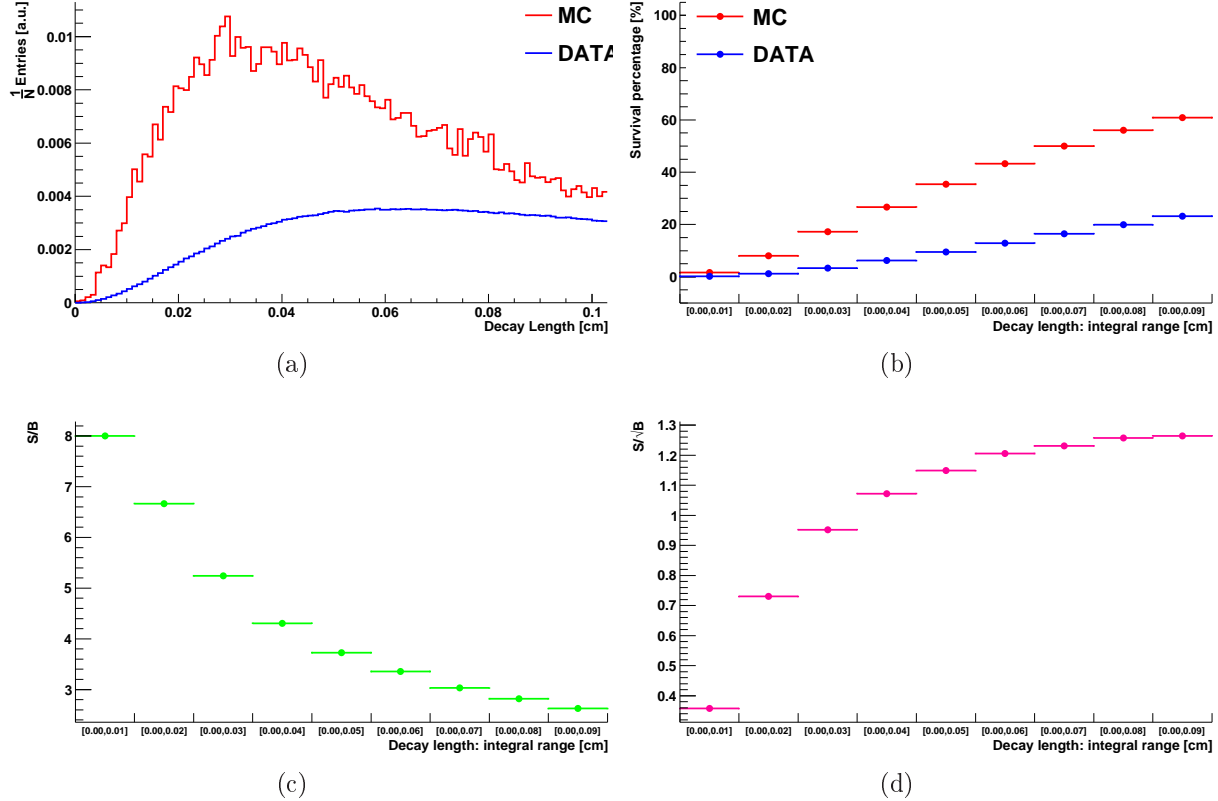


FIG. 5.18: D^0 Decay length S/B variation study for $SVT+SSD>0$ in the range $[0, 0.1]$ (cm). Normalized distribution of S and B (a), survival percentage per value range (b), ratio S/B (c) and S/\sqrt{B} (d).

TAB. 5.4: S/B variation of microvertexing variables for different ranges in the $[0, 0.09]$ (cm) and SVT+SSD>0 hits of each track.

| variables \ range (cm) | | [0, 0.01] | [0, 0.02] | [0, 0.03] | [0, 0.04] | [0, 0.05] | [0, 0.06] | [0, 0.07] | [0, 0.08] | [0, 0.09] |
|--------------------------------|--------------|-----------|-----------|-----------|-----------|-----------|-----------|-----------|-----------|-----------|
| DCA between tracks | S | 0.153 | 0.286 | 0.398 | 0.490 | 0.565 | 0.626 | 0.678 | 0.722 | 0.758 |
| | B | 0.061 | 0.118 | 0.172 | 0.223 | 0.270 | 0.313 | 0.353 | 0.391 | 0.424 |
| | S/B | 2.508 | 2.419 | 2.310 | 2.196 | 2.091 | 1.990 | 1.918 | 1.848 | 1.788 |
| | S/\sqrt{B} | 0.619 | 0.832 | 0.959 | 1.037 | 1.087 | 1.118 | 1.141 | 1.155 | 1.164 |
| D^0 decay length | S | 0.016 | 0.080 | 0.173 | 0.267 | 0.354 | 0.433 | 0.500 | 0.561 | 0.609 |
| | B | 0.002 | 0.012 | 0.033 | 0.062 | 0.095 | 0.129 | 0.165 | 0.199 | 0.232 |
| | S/B | 8.000 | 6.666 | 5.242 | 4.300 | 3.732 | 3.355 | 3.030 | 2.811 | 2.618 |
| | S/\sqrt{B} | 0.357 | 0.730 | 0.952 | 1.072 | 1.148 | 1.205 | 1.230 | 1.258 | 1.264 |
| D^0 DCA to primary vertex | S | 0.074 | 0.204 | 0.333 | 0.442 | 0.533 | 0.607 | 0.669 | 0.719 | 0.760 |
| | B | 0.018 | 0.059 | 0.114 | 0.172 | 0.229 | 0.283 | 0.332 | 0.378 | 0.419 |
| | S/B | 4.111 | 3.413 | 2.925 | 2.568 | 2.326 | 2.145 | 2.010 | 1.902 | 1.813 |
| | S/\sqrt{B} | 0.551 | 0.839 | 0.986 | 1.065 | 1.113 | 1.141 | 1.161 | 1.169 | 1.174 |

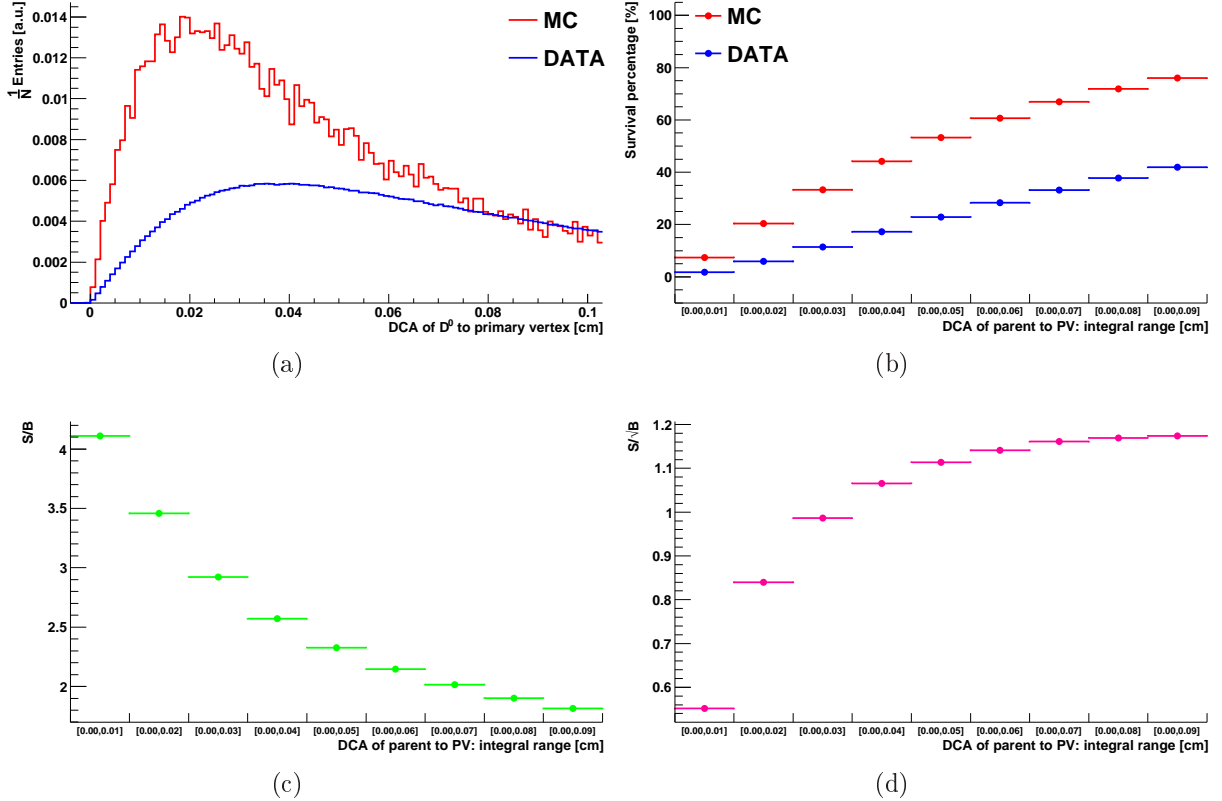


FIG. 5.19: D^0 DCA to primary vertex S/B variation study for $SVT+SSD>0$, in the range $[0, 0.1]$ (cm). Normalized distribution of S and B (a), survival percentage per value range (b), ratio S/B (c) and S/\sqrt{B} (d).

5.5.2 The S/B Study for $\text{SVT}+\text{SSD}>1$ hits

The Range of Study $[0, 1]$ cm

In Table 5.5 the values are summarized in the interval $\Delta a = [0, 1]$ (cm) and B along with the variation of S/B and S/\sqrt{B} in a given range. Concerning the graphical part, for every Figure the raw distributions are given in (a), the SP in (b), along with both S/B in (c) and S/\sqrt{B} in (d). The DCA between tracks is shown in Figure 5.20, the D^0 decay length in Figure 5.21 and finally the D^0 DCA to the primary vertex in Figure 5.22.

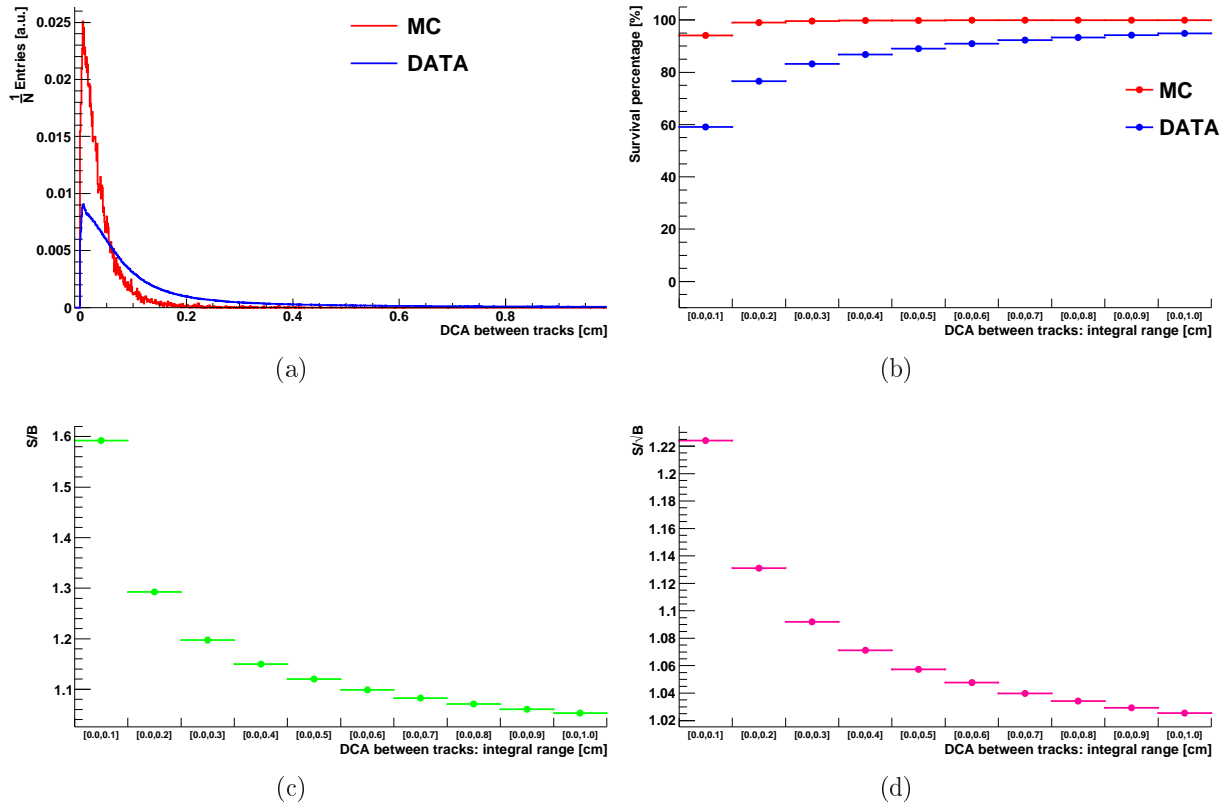


FIG. 5.20: DCA between tracks S/B variation study for $\text{SVT}+\text{SSD}>1$, in the range $[0, 1]$ (cm). Normalized distribution of S and B (a), survival percentage per value range (b), ratio S/B (c) and S/\sqrt{B} (d).

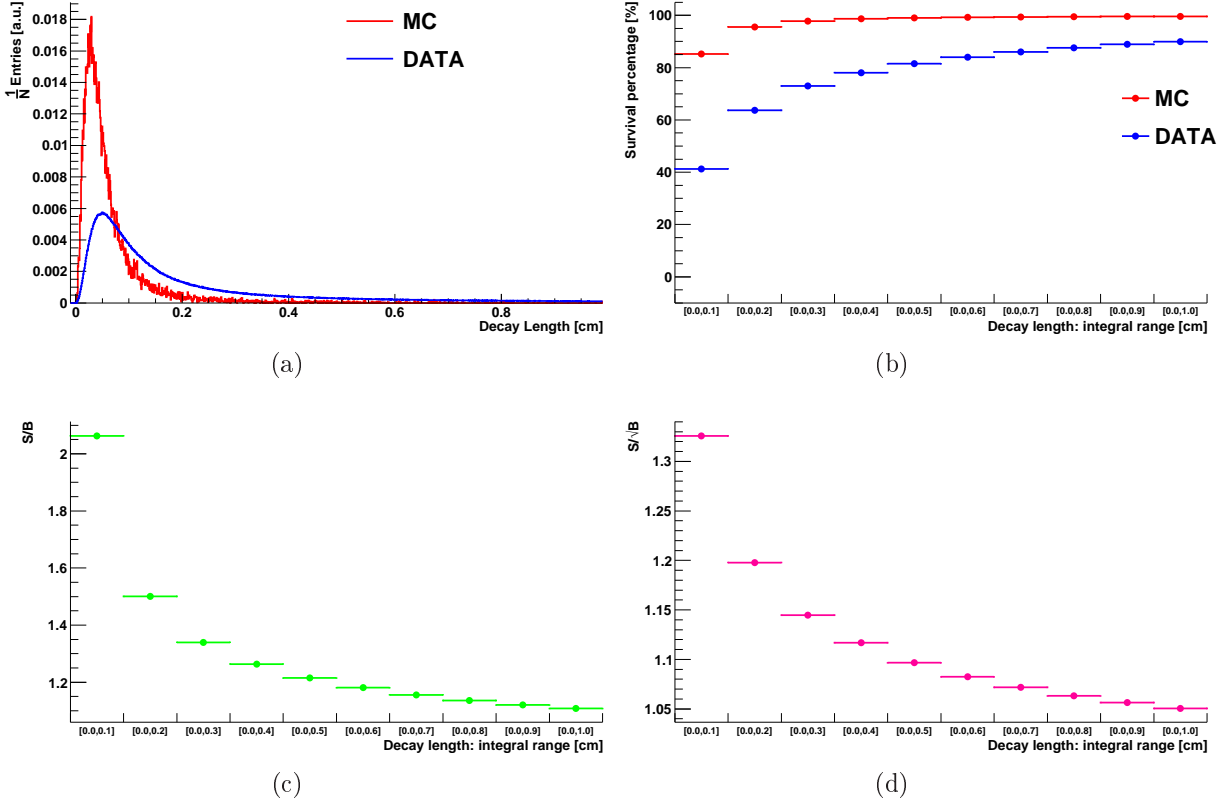


FIG. 5.21: D^0 decay length S/B variation study for $\text{SVT}+\text{SSD}>1$, in the range $[0, 1]$ (cm). Normalized distribution of S and B (a), survival percentage per value range (b), ratio S/B (c) and S/\sqrt{B} (d).

TAB. 5.5: S/B variation of microvertexing variables in the $[0, 1]$ (cm) range, for $\text{SVT+SSD}>1$ hits for each track.

| variables \ range (cm) | | [0, 0.1] | [0, 0.2] | [0, 0.3] | [0, 0.4] | [0, 0.5] | [0, 0.6] | [0, 0.7] | [0, 0.8] | [0, 0.9] | [0, 1.0] |
|--------------------------------|--------------|----------|----------|----------|----------|----------|----------|----------|----------|----------|----------|
| DCA between tracks | S | 0.941 | 0.990 | 0.996 | 0.998 | 0.998 | 0.999 | 0.999 | 0.999 | 0.999 | 0.999 |
| | B | 0.591 | 0.766 | 0.832 | 0.868 | 0.891 | 0.909 | 0.923 | 0.933 | 0.942 | 0.949 |
| | S/B | 1.591 | 1.293 | 1.197 | 1.150 | 1.120 | 1.098 | 1.082 | 1.070 | 1.059 | 1.052 |
| | S/\sqrt{B} | 1.224 | 1.131 | 1.091 | 1.071 | 1.057 | 1.047 | 1.039 | 1.034 | 1.029 | 1.025 |
| D^0 decay length | S | 0.852 | 0.956 | 0.978 | 0.987 | 0.990 | 0.992 | 0.994 | 0.995 | 0.996 | 0.996 |
| | B | 0.413 | 0.637 | 0.730 | 0.781 | 0.815 | 0.840 | 0.860 | 0.876 | 0.889 | 0.899 |
| | S/B | 2.061 | 1.500 | 1.340 | 1.261 | 1.210 | 1.180 | 1.155 | 1.135 | 1.120 | 1.108 |
| | S/\sqrt{B} | 1.326 | 1.197 | 1.145 | 1.116 | 1.096 | 1.082 | 1.071 | 1.063 | 1.056 | 1.050 |
| D^0 DCA to primary vertex | S | 0.944 | 0.990 | 0.995 | 0.997 | 0.998 | 0.998 | 0.998 | 0.998 | 0.998 | 0.998 |
| | B | 0.628 | 0.790 | 0.849 | 0.882 | 0.906 | 0.924 | 0.939 | 0.950 | 0.959 | 0.966 |
| | S/B | 1.502 | 1.253 | 1.173 | 1.129 | 1.100 | 1.079 | 1.063 | 1.050 | 1.040 | 1.033 |
| | S/\sqrt{B} | 1.191 | 1.114 | 1.079 | 1.061 | 1.049 | 1.038 | 1.029 | 1.024 | 1.019 | 1.015 |

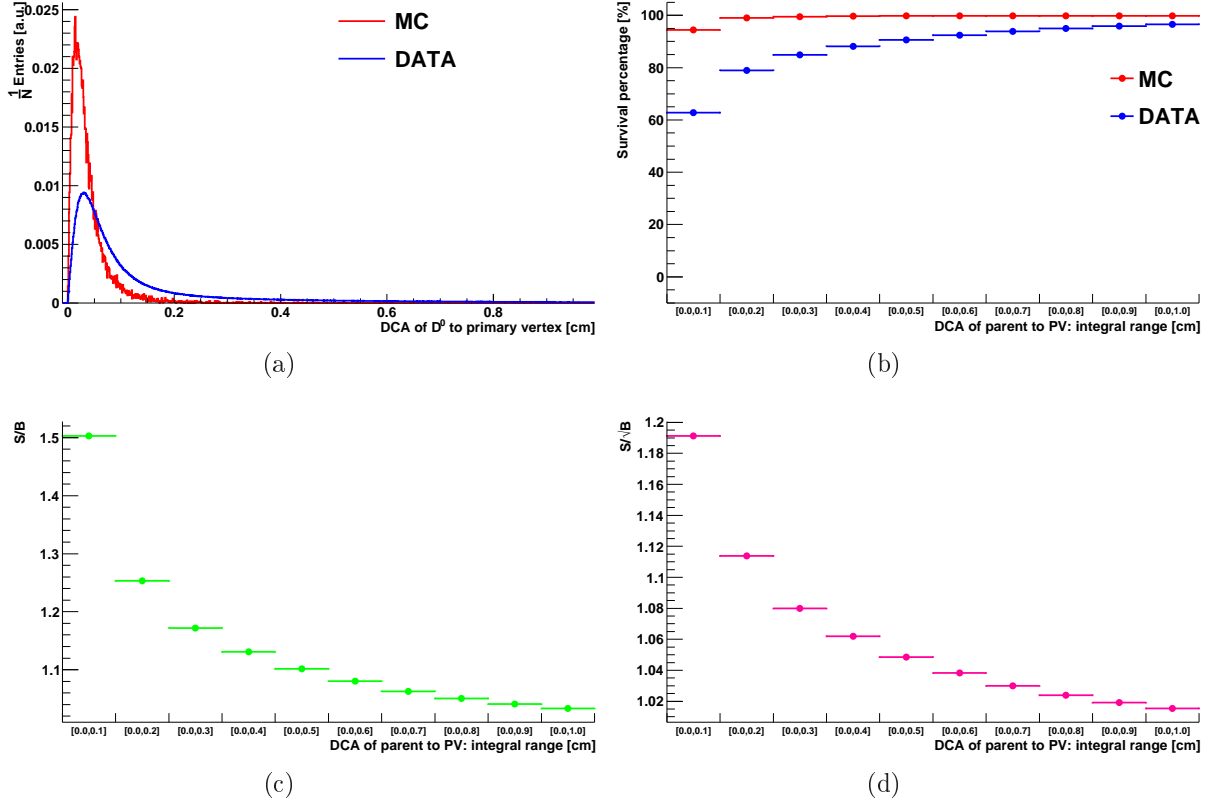


FIG. 5.22: D^0 DCA to primary vertex S/B variation study for $SVT+SSD>1$, in the range $[0, 0.1]$ cm. Normalized distribution of S and B (a), survival percentage per value range (b), ratio S/B (c) and S/\sqrt{B} (d).

Range of Study $[0, 0.1]$ cm

For the specific range interval, the values of S and B along with the ratios S/B and S/\sqrt{B} for each microvertexing variable are summarized for the $\Delta a = [0, 0.1]$ (cm) range in Table 5.6. Concerning the graphical part, for every Figure the raw distributions are given in (a), the SP in (b), along with both S/B in (c) and S/\sqrt{B} in (d). In Figures 5.23 the plots referring to the DCA between daughter tracks are presented. For the D^0 decay length the plots are given in Figures 5.24. Finally for the D^0 DCA to the primary vertex the plots are found in Figures 5.25.

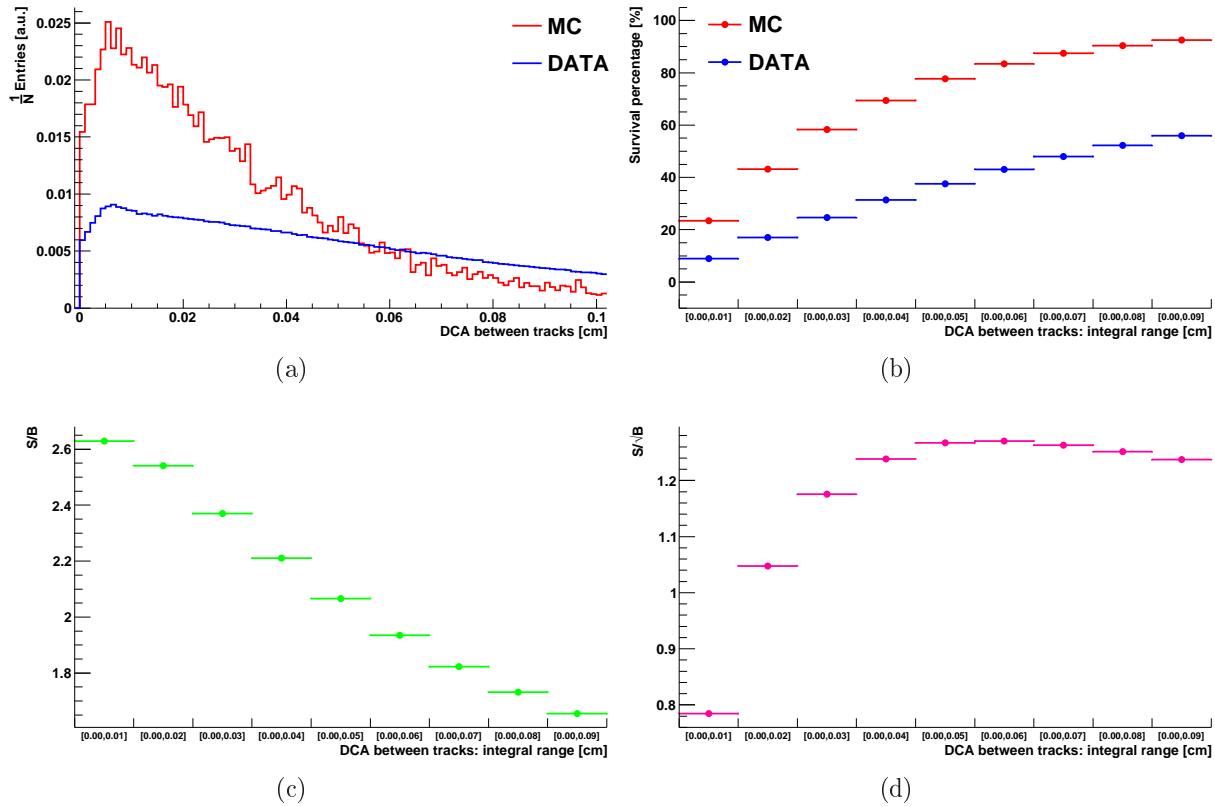


FIG. 5.23: DCA between tracks S/B variation study for $SVT+SSD>1$, in the range $[0, 0.1]$ (cm). Normalized distributions of S and B (a), survival percentage per value range (b), ratio S/B (c) and S/\sqrt{B} (d).

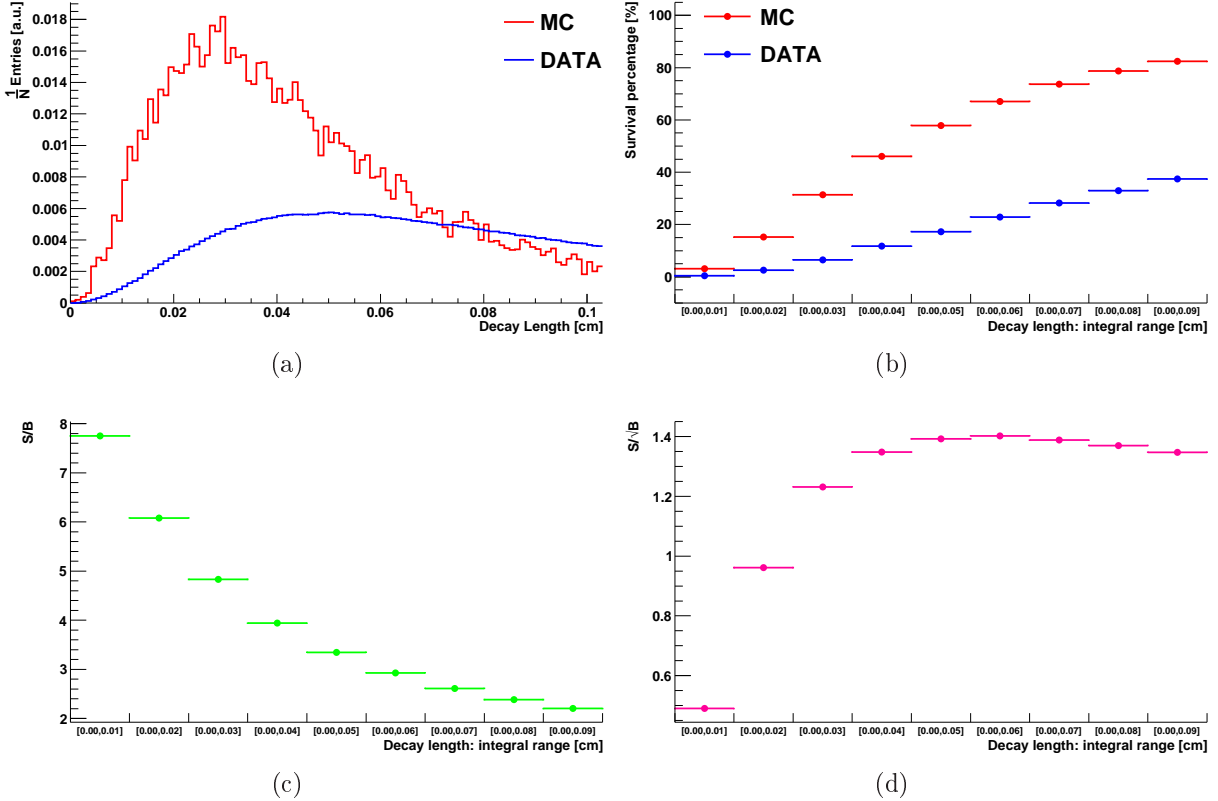


FIG. 5.24: D^0 Decay length S/B variation study for $\text{SVT}+\text{SSD}>1$ in the range $[0, 0.1]$ (cm). Normalized distribution of S and B (a), survival percentage per value range (b), ratio S/B (c) and S/\sqrt{B} (d).

TAB. 5.6: S/B variation of microvertexing variables for different ranges in the $[0, 0.09]$ (cm) and SVT+SSD>1 hits for each track.

| variables \ range (cm) | | [0, 0.01] | [0, 0.02] | [0, 0.03] | [0, 0.04] | [0, 0.05] | [0, 0.06] | [0, 0.07] | [0, 0.08] | [0, 0.09] |
|--------------------------------|--------------|-----------|-----------|-----------|-----------|-----------|-----------|-----------|-----------|-----------|
| DCA between tracks | S | 0.234 | 0.432 | 0.583 | 0.694 | 0.777 | 0.834 | 0.875 | 0.904 | 0.925 |
| | B | 0.089 | 0.170 | 0.246 | 0.314 | 0.376 | 0.431 | 0.480 | 0.522 | 0.559 |
| | S/B | 2.604 | 2.530 | 2.373 | 2.205 | 2.062 | 1.932 | 1.821 | 1.730 | 1.653 |
| | S/\sqrt{B} | 0.784 | 1.047 | 1.175 | 1.239 | 1.267 | 1.270 | 1.262 | 1.251 | 1.237 |
| D^0 decay length | S | 0.031 | 0.152 | 0.314 | 0.461 | 0.579 | 0.671 | 0.737 | 0.787 | 0.824 |
| | B | 0.004 | 0.025 | 0.065 | 0.117 | 0.173 | 0.229 | 0.282 | 0.330 | 0.374 |
| | S/B | 7.750 | 5.929 | 4.798 | 3.920 | 3.333 | 2.920 | 2.609 | 2.380 | 2.201 |
| | S/\sqrt{B} | 0.490 | 0.961 | 1.231 | 1.348 | 1.392 | 1.402 | 1.388 | 1.370 | 1.347 |
| D^0 DCA to primary vertex | S | 0.137 | 0.358 | 0.550 | 0.682 | 0.775 | 0.837 | 0.880 | 0.908 | 0.928 |
| | B | 0.033 | 0.108 | 0.200 | 0.291 | 0.374 | 0.444 | 0.504 | 0.553 | 0.594 |
| | S/B | 4.058 | 3.295 | 2.742 | 2.338 | 2.072 | 1.883 | 1.746 | 1.641 | 1.560 |
| | S/\sqrt{B} | 0.754 | 1.089 | 1.229 | 2.343 | 1.267 | 1.256 | 1.240 | 1.221 | 1.204 |

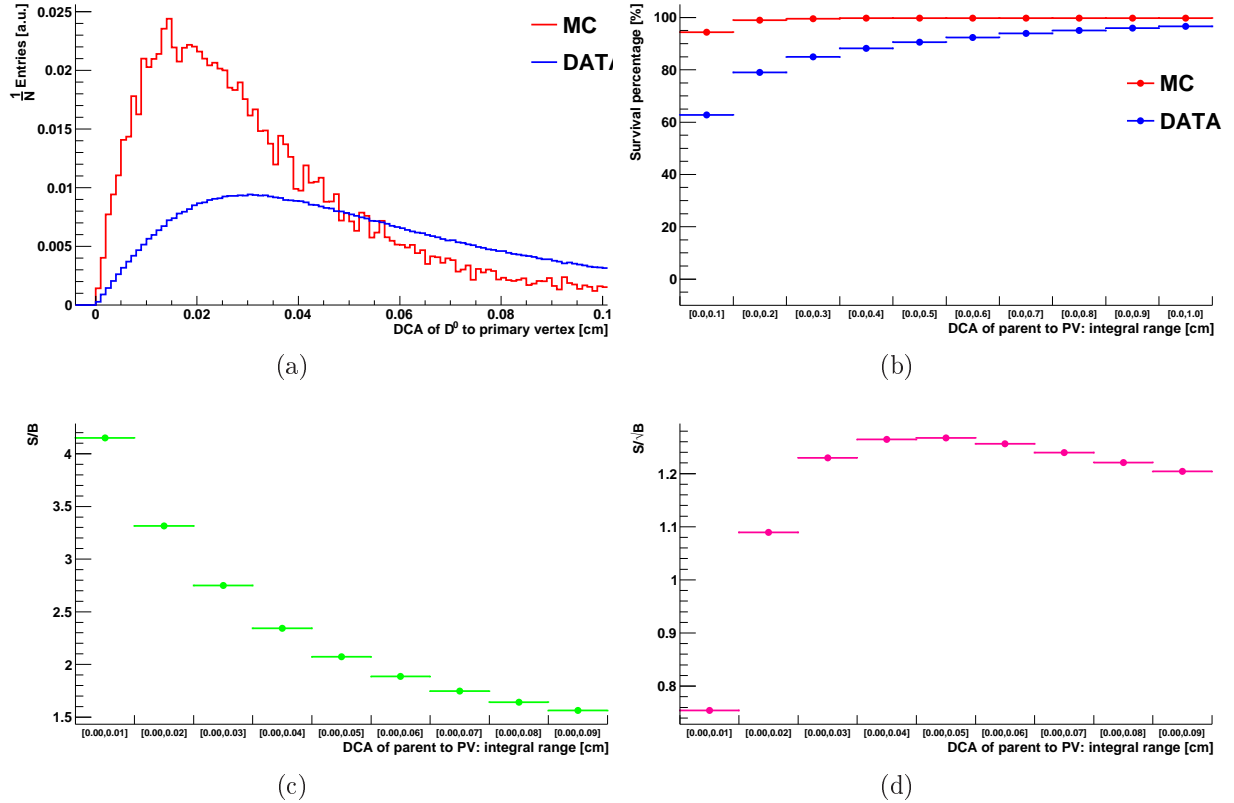


FIG. 5.25: D^0 DCA to primary vertex S/B variation study for $SVT+SSD>1$, in the range $[0, 0.1]$ (cm). Normalized distribution of S and B (a), survival percentage per value range (b), ratio S/B (c) and S/\sqrt{B} (d).

5.5.3 The S/B Study for SVT+SSD>2 hits

The Range of Study $[0, 1]$ cm

In Table 5.7 it is summarized the variation of S , B as well as S/B , S/\sqrt{B} for the $\Delta a = [0, 1]$ (cm) range, for tracks with SVT+SSD>2. In addition all tracks comply with the SVT+SSD>2 silicon hits track. The DCA between tracks is shown in Figure 5.26, the D^0 decay length in Figure 5.27 and finally the D^0 DCA to the primary vertex in Figure 5.28.

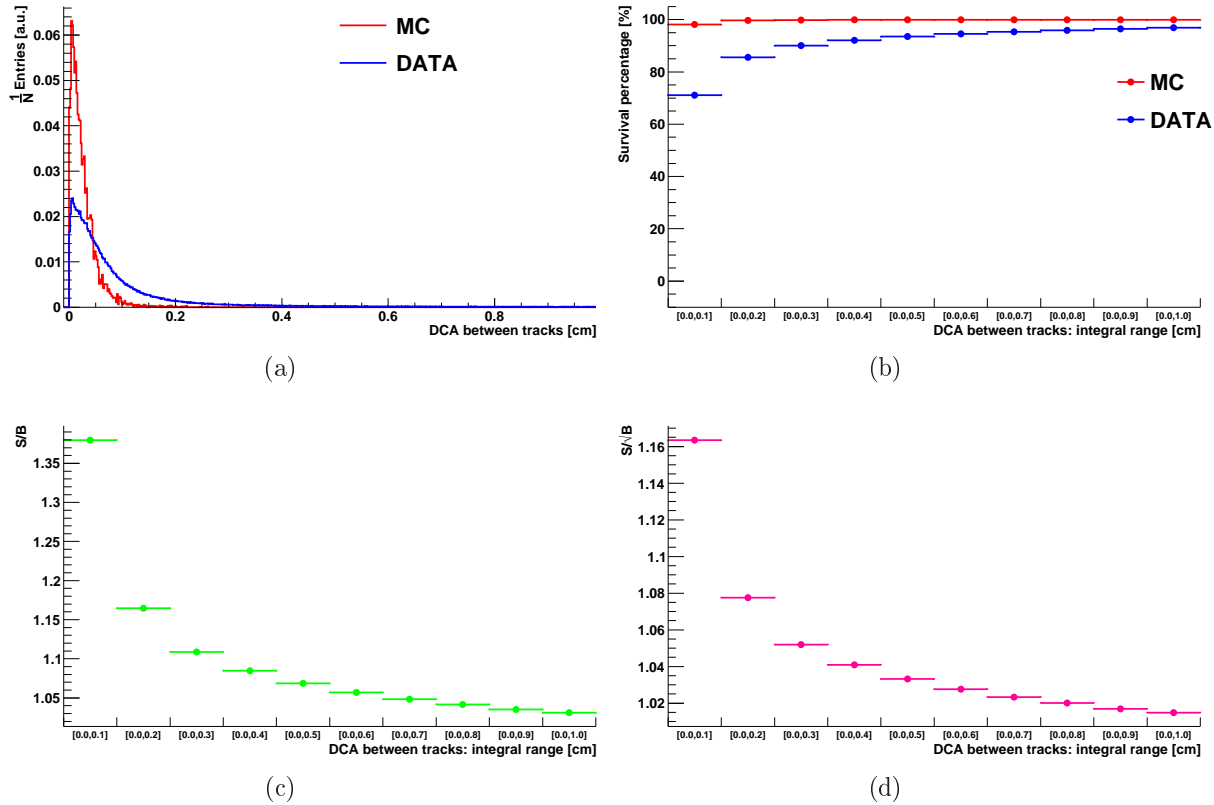


FIG. 5.26: DCA between tracks S/B variation study for SVT+SSD>2, in the range $[0, 1]$ (cm). Normalized distribution of S and B (a), survival percentage per value range (b), ratio S/B (c) and S/\sqrt{B} (d).

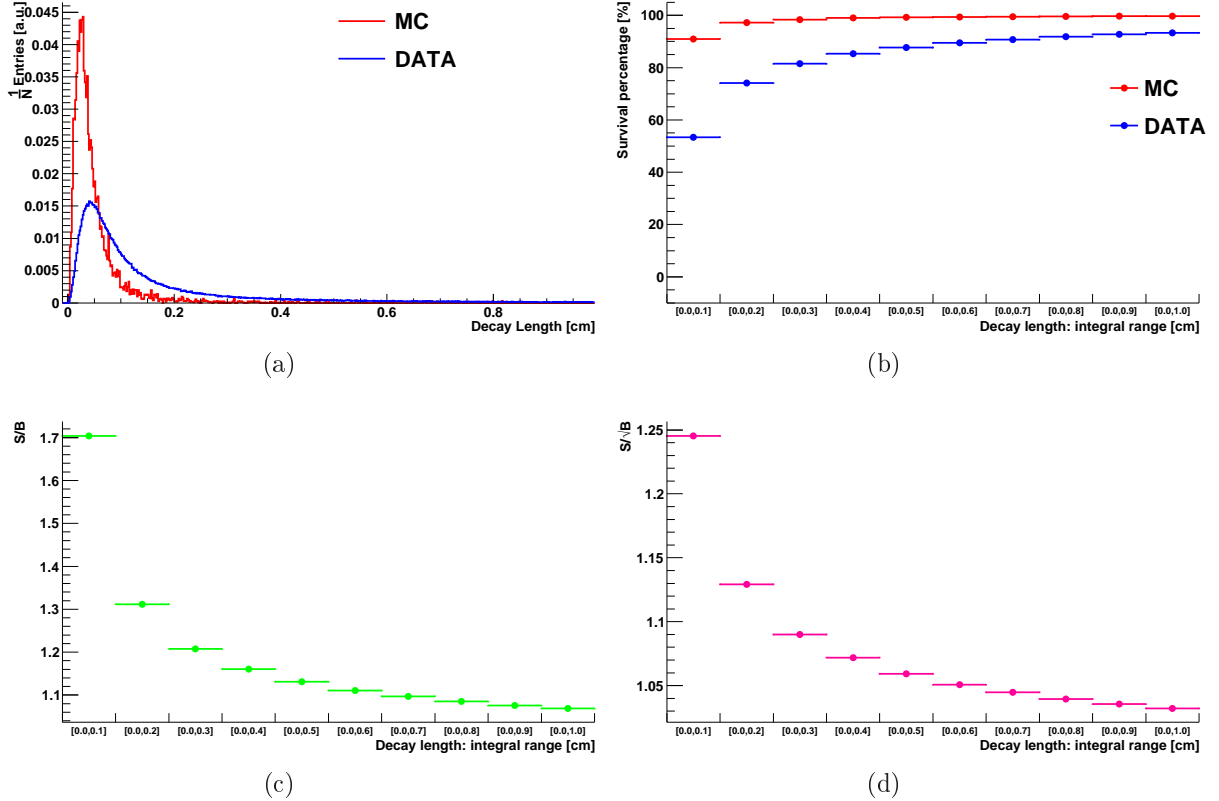


FIG. 5.27: D^0 decay length S/B variation study for $\text{SVT}+\text{SSD}>2$, in the range $[0, 1]$ (cm). Normalized distribution of S and B (a), survival percentage per value range (b), ratio S/B (c) and S/\sqrt{B} (d).

TAB. 5.7: S/B variation of microvertexing variables in the $[0, 1]$ (cm) range, for SVT+SSD>2 hits for each track.

| variables \ range (cm) | | [0, 0.1] | [0, 0.2] | [0, 0.3] | [0, 0.4] | [0, 0.5] | [0, 0.6] | [0, 0.7] | [0, 0.8] | [0, 0.9] | [0, 1.0] |
|-----------------------------|--------------|----------|----------|----------|----------|----------|----------|----------|----------|----------|----------|
| DCA between tracks | S | 0.981 | 0.997 | 0.998 | 0.999 | 0.999 | 0.999 | 0.999 | 0.999 | 0.999 | 0.999 |
| | B | 0.711 | 0.856 | 0.900 | 0.921 | 0.935 | 0.945 | 0.953 | 0.959 | 0.965 | 0.969 |
| | S/B | 1.378 | 1.165 | 1.100 | 1.083 | 1.067 | 1.056 | 1.047 | 1.040 | 1.035 | 1.030 |
| | S/\sqrt{B} | 1.163 | 1.077 | 1.051 | 1.040 | 1.033 | 1.027 | 1.023 | 1.020 | 1.016 | 1.015 |
| D^0 decay length | S | 0.910 | 0.972 | 0.984 | 0.990 | 0.992 | 0.994 | 0.995 | 0.996 | 0.997 | 0.997 |
| | B | 0.534 | 0.741 | 0.815 | 0.853 | 0.877 | 0.895 | 0.907 | 0.918 | 0.927 | 0.933 |
| | S/B | 1.703 | 1.311 | 1.208 | 1.159 | 1.130 | 1.110 | 1.096 | 1.080 | 1.075 | 1.068 |
| | S/\sqrt{B} | 1.245 | 1.129 | 1.089 | 1.072 | 1.059 | 1.050 | 1.045 | 1.040 | 1.036 | 1.032 |
| D^0 DCA to primary vertex | S | 0.973 | 0.995 | 0.997 | 0.998 | 0.999 | 0.998 | 0.999 | 0.998 | 0.999 | 0.998 |
| | B | 0.763 | 0.874 | 0.907 | 0.927 | 0.942 | 0.953 | 0.961 | 0.968 | 0.974 | 0.979 |
| | S/B | 1.280 | 1.138 | 1.098 | 1.076 | 1.060 | 1.048 | 1.039 | 1.031 | 1.024 | 1.020 |
| | S/\sqrt{B} | 1.114 | 1.064 | 1.046 | 1.037 | 1.029 | 1.022 | 1.019 | 1.014 | 1.012 | 1.008 |

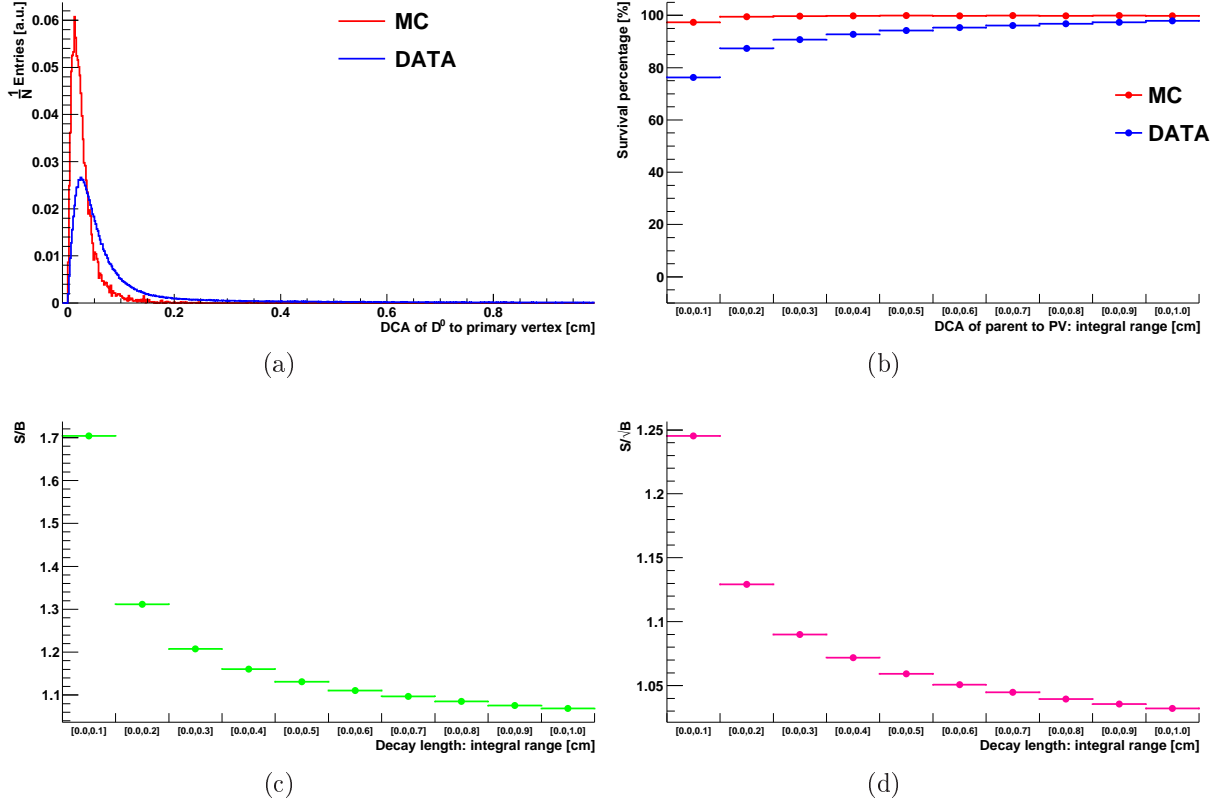


FIG. 5.28: D^0 DCA to primary vertex S/B variation study for $\text{SVT}+\text{SSD}>2$, in the range $[0, 1]$ (cm). Normalized distribution of S and B (a), survival percentage per value range (b), ratio S/B (c) and S/\sqrt{B} (d).

Range of Study $[0, 0.1]$ cm

For the specific range interval, the values of S and B along with the ratios S/B and S/\sqrt{B} for each microvertexing variable are summarized for the $\Delta a = [0, 0.1]$ (cm) range in Table 5.8. Concerning the graphical part, for every Figure the raw distributions are given in (a), the SP in (b), along with both S/B in (c) and S/\sqrt{B} in (d). In Figures 5.29 the plots referring to the DCA between daughter tracks are presented. For the D^0 decay length the plots are given in Figures 5.30. Finally for the D^0 DCA to the primary vertex the plots are found in Figures 5.31.

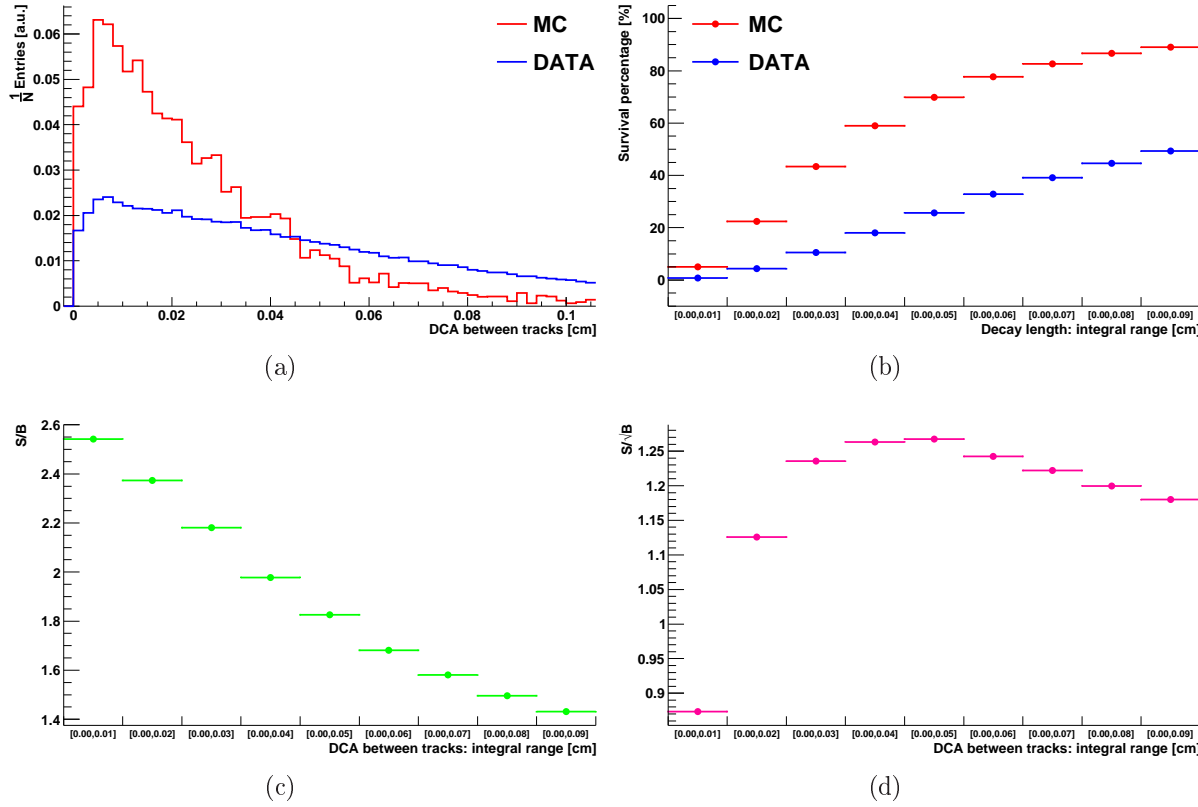


FIG. 5.29: DCA between tracks S/B variation study for $SVT+SSD>2$, in the range $[0, 0.1]$ (cm). Normalized distributions of S and B (a), survival percentage per value range (b), ratio S/B (c) and S/\sqrt{B} (d).

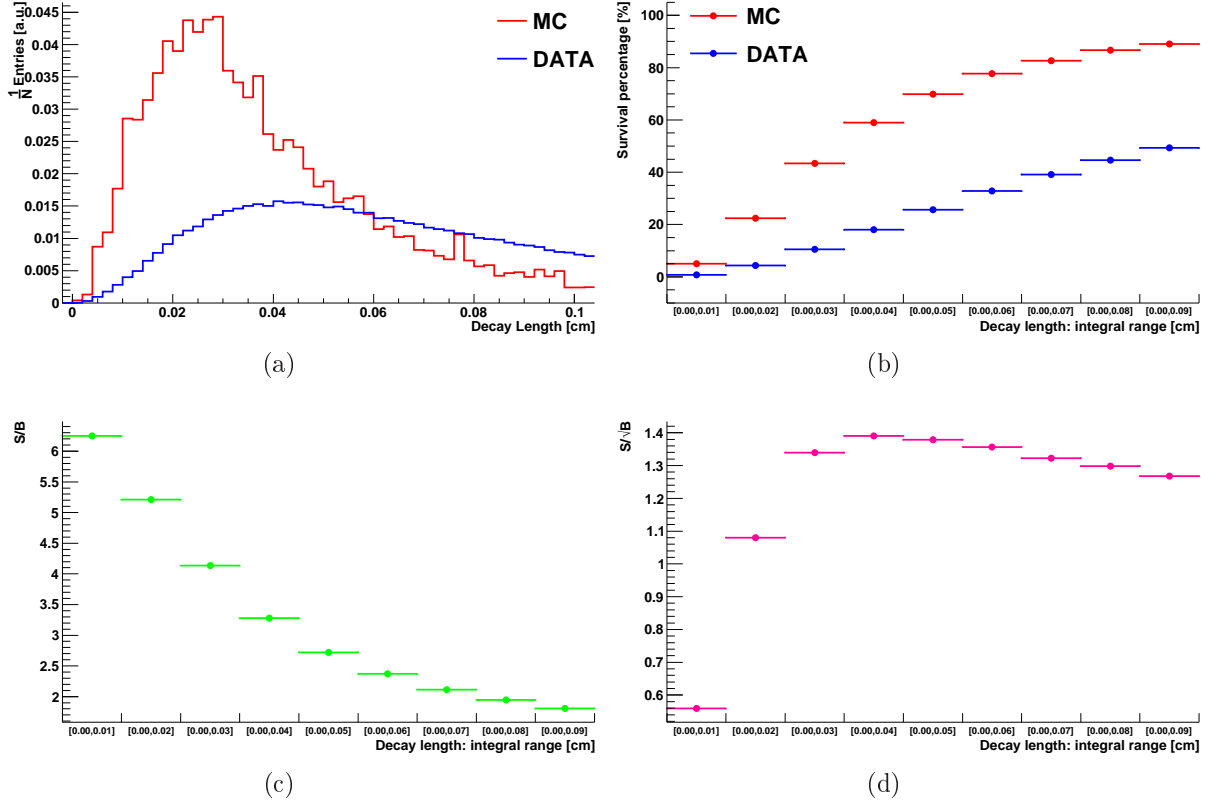


FIG. 5.30: D^0 Decay length S/B variation study for $\text{SVT+SSD}>2$ in the range $[0, 0.1]$ (cm). Normalized distribution of S and B (a), survival percentage per value range (b), ratio S/B (c) and S/\sqrt{B} (d).

TAB. 5.8: S/B variation of microvertexing variables for different ranges in the $[0, 0.09]$ (cm) and SVT+SSD>2 hits for each track.

| variables \ range (cm) | | [0, 0.01] | [0, 0.02] | [0, 0.03] | [0, 0.04] | [0, 0.05] | [0, 0.06] | [0, 0.07] | [0, 0.08] | [0, 0.09] |
|--------------------------------|--------------|-----------|-----------|-----------|-----------|-----------|-----------|-----------|-----------|-----------|
| DCA between tracks | S | 0.300 | 0.534 | 0.700 | 0.807 | 0.880 | 0.918 | 0.945 | 0.962 | 0.973 |
| | B | 0.118 | 0.225 | 0.321 | 0.408 | 0.482 | 0.546 | 0.598 | 0.643 | 0.680 |
| | S/B | 2.520 | 2.372 | 2.177 | 1.978 | 1.825 | 1.683 | 1.578 | 1.490 | 1.429 |
| | S/\sqrt{B} | 0.873 | 1.125 | 1.235 | 1.263 | 1.267 | 1.242 | 1.222 | 1.199 | 1.179 |
| D^0 decay length | S | 0.050 | 0.224 | 0.434 | 0.590 | 0.699 | 0.777 | 0.827 | 0.867 | 0.890 |
| | B | 0.008 | 0.043 | 0.105 | 0.180 | 0.257 | 0.328 | 0.391 | 0.446 | 0.493 |
| | S/B | 6.589 | 5.167 | 4.100 | 3.270 | 2.722 | 2.367 | 2.115 | 1.943 | 1.803 |
| | S/\sqrt{B} | 0.559 | 1.080 | 1.339 | 1.390 | 1.378 | 1.356 | 1.322 | 1.298 | 1.268 |
| D^0 DCA to primary vertex | S | 0.196 | 0.471 | 0.678 | 0.799 | 0.870 | 0.912 | 0.936 | 0.955 | 0.964 |
| | B | 0.054 | 0.169 | 0.300 | 0.418 | 0.516 | 0.593 | 0.653 | 0.698 | 0.734 |
| | S/B | 3.603 | 2.783 | 2.256 | 1.908 | 1.686 | 1.537 | 1.434 | 1.360 | 1.312 |
| | S/\sqrt{B} | 0.843 | 1.145 | 1.237 | 1.235 | 1.211 | 1.184 | 1.158 | 1.143 | 1.125 |

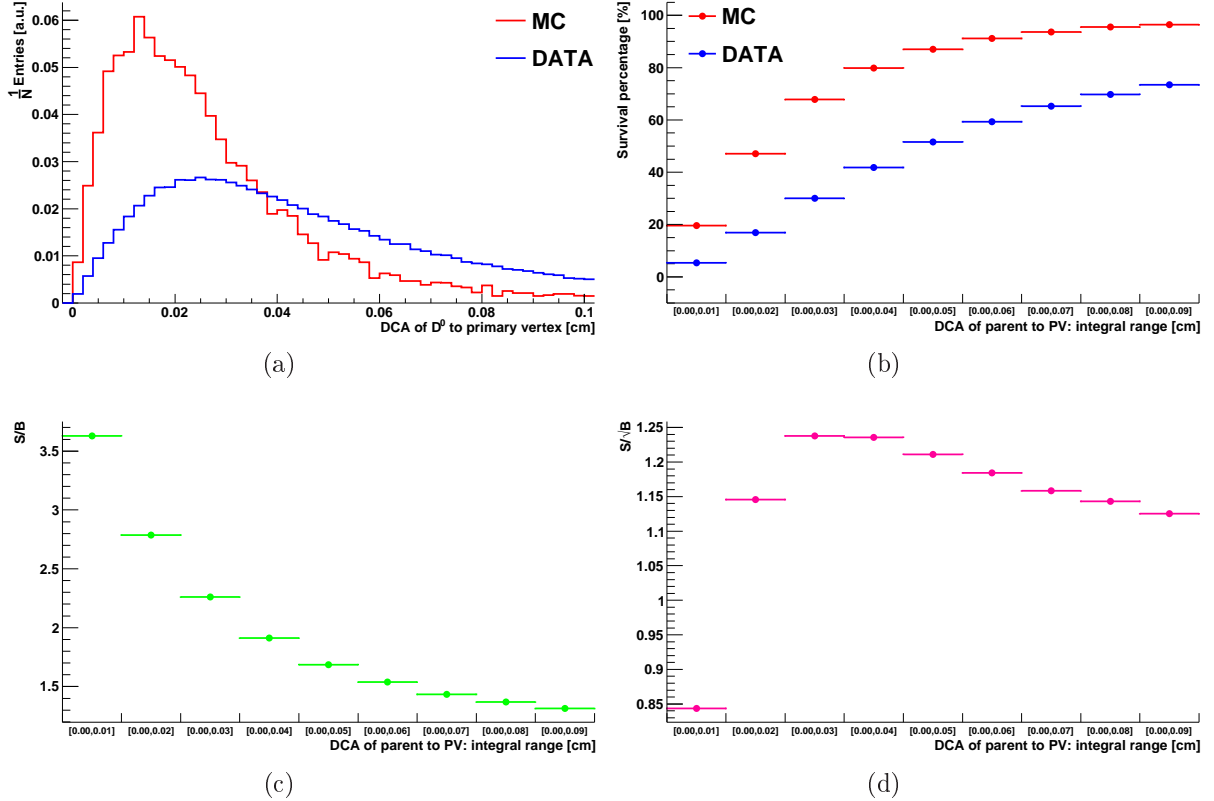


FIG. 5.31: D^0 DCA to primary vertex S/B variation study for $SVT+SSD>2$, in the range $[0, 0.1]$ (cm). Normalized distribution of S and B (a), survival percentage per value range (b), ratio S/B (c) and S/\sqrt{B} (d).

5.5.4 The S/B Study for $\text{SVT}+\text{SSD}>3$ hits

The Range of Study $[0, 1]$ cm

In Table 5.9 it is summarized the variation of S , B , as well as S/B and S/\sqrt{B} in the range $[0, 1]$ (cm) for tracks with $\text{SVT}+\text{SSD}>3$. Concerning the graphical part, for every Figure the raw distributions are given in (a), the SP in (b), along with both S/B in (c) and S/\sqrt{B} in (d). The DCA between tracks is shown in Figure 5.32, the D^0 decay length in Figure 5.33 and finally the D^0 DCA to the primary vertex in Figure 5.34.

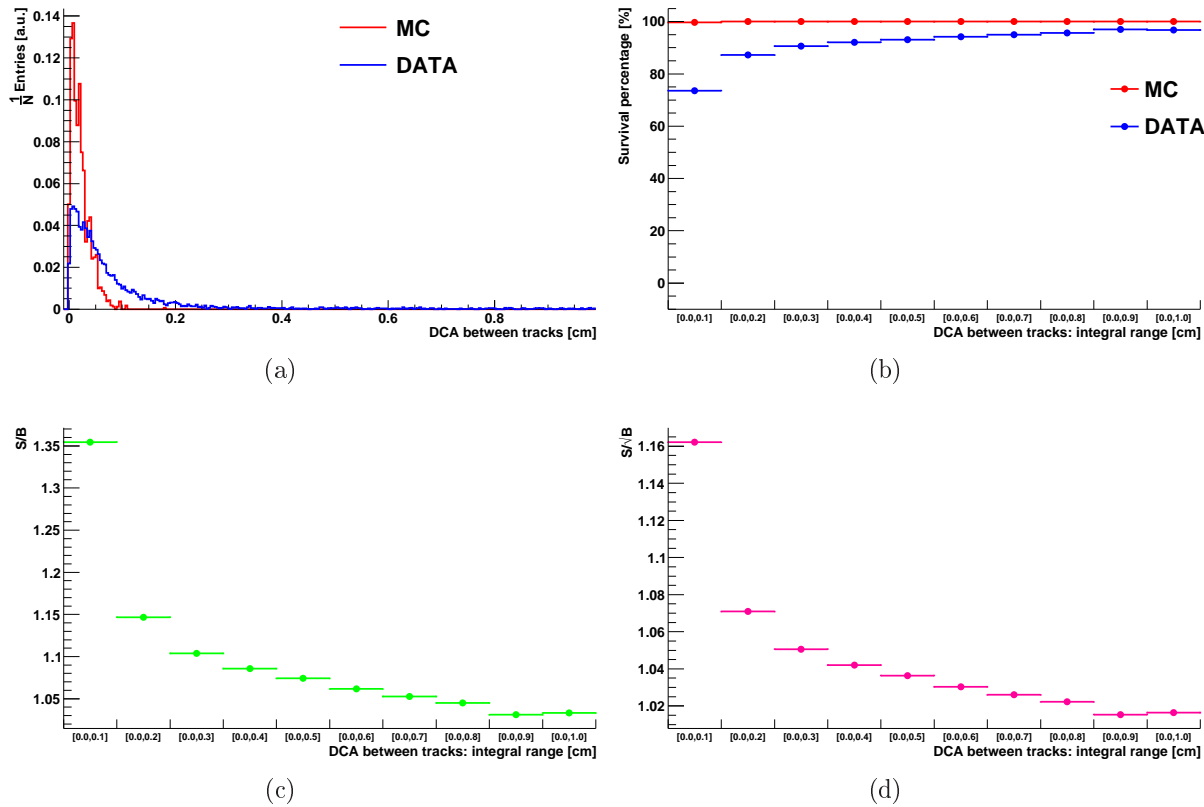


FIG. 5.32: DCA between tracks S/B variation study for $\text{SVT}+\text{SSD}>3$, in the range $[0, 1]$ (cm). Normalized distribution of S and B (a), survival percentage per value range (b), ratio S/B (c) and S/\sqrt{B} (d).

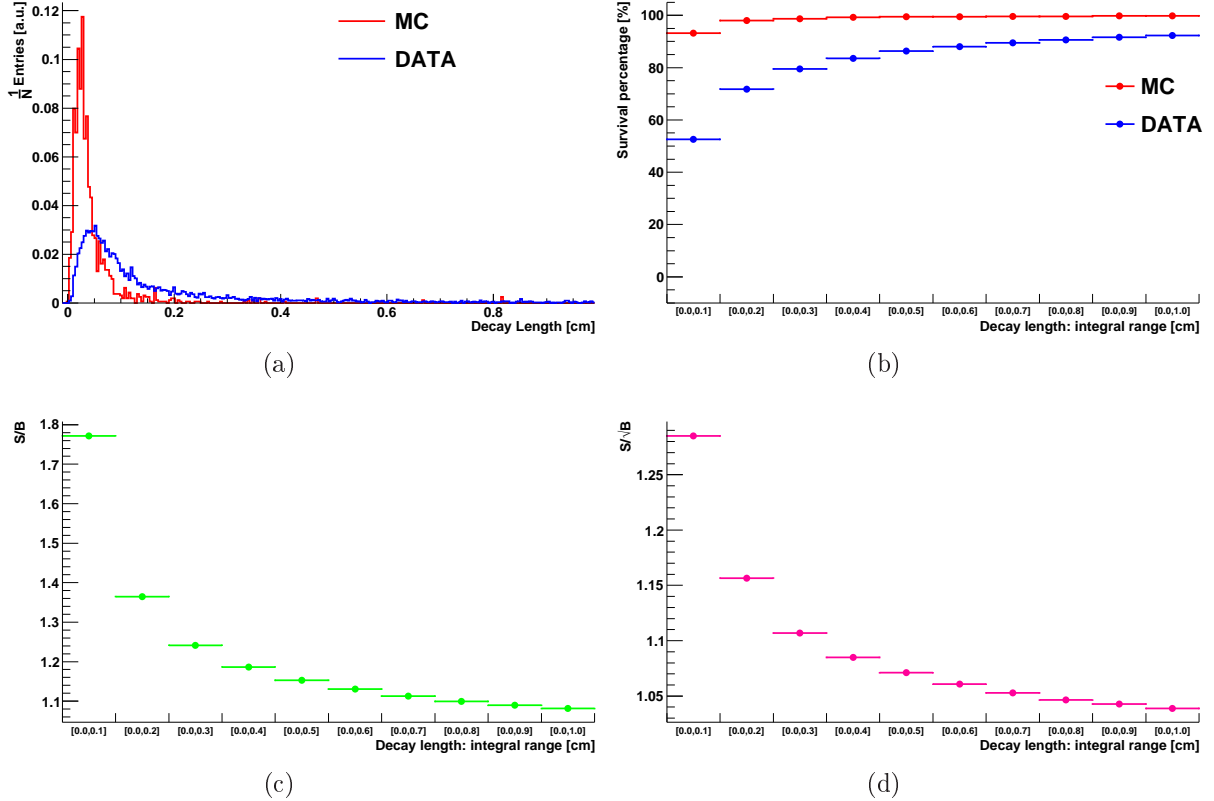


FIG. 5.33: D^0 decay length S/B variation study for $\text{SVT}+\text{SSD}>3$, in the range $[0, 1]$ (cm). Normalized distribution of S and B (a), survival percentage per value range (b), ratio S/B (c) and S/\sqrt{B} (d).

TAB. 5.9: S/B variation of microvertexing variables in the $[0, 1]$ (cm) range, for SVT+SSD >3 hits for each track.

| variables \ range (cm) | | [0, 0.1] | [0, 0.2] | [0, 0.3] | [0, 0.4] | [0, 0.5] | [0, 0.6] | [0, 0.7] | [0, 0.8] | [0, 0.9] | [0, 1.0] |
|-----------------------------|--------------|----------|----------|----------|----------|----------|----------|----------|----------|----------|----------|
| DCA between tracks | S | 0.997 | 1.000 | 1.000 | 1.000 | 1.000 | 1.000 | 1.000 | 1.000 | 1.000 | 1.000 |
| | B | 0.736 | 0.872 | 0.906 | 0.921 | 0.931 | 0.942 | 0.950 | 0.957 | 0.970 | 0.968 |
| | S/B | 1.354 | 1.145 | 1.103 | 1.084 | 1.073 | 1.061 | 1.051 | 1.044 | 1.030 | 1.032 |
| | S/\sqrt{B} | 1.086 | 1.049 | 1.036 | 1.033 | 1.031 | 1.025 | 1.021 | 1.018 | 1.013 | 1.030 |
| D^0 decay length | S | 0.932 | 0.980 | 0.987 | 0.992 | 0.995 | 0.995 | 0.996 | 0.996 | 0.998 | 0.998 |
| | B | 0.526 | 0.718 | 0.795 | 0.836 | 0.863 | 0.880 | 0.895 | 0.906 | 0.916 | 0.923 |
| | S/B | 1.770 | 1.365 | 1.240 | 1.187 | 1.152 | 1.129 | 1.112 | 1.099 | 1.089 | 1.081 |
| | S/\sqrt{B} | 0.725 | 0.847 | 0.891 | 0.914 | 0.928 | 0.938 | 0.946 | 0.951 | 0.957 | 0.957 |
| D^0 DCA to primary vertex | S | 0.977 | 0.998 | 0.999 | 1.000 | 1.000 | 1.000 | 1.000 | 1.000 | 1.000 | 1.000 |
| | B | 0.792 | 0.882 | 0.908 | 0.924 | 0.941 | 0.950 | 0.964 | 0.970 | 0.974 | 0.981 |
| | S/B | 1.234 | 1.131 | 1.100 | 1.081 | 1.062 | 1.049 | 1.037 | 1.030 | 1.025 | 1.010 |
| | S/\sqrt{B} | 1.097 | 1.062 | 1.048 | 1.082 | 1.040 | 1.025 | 1.025 | 1.015 | 1.013 | 1.009 |

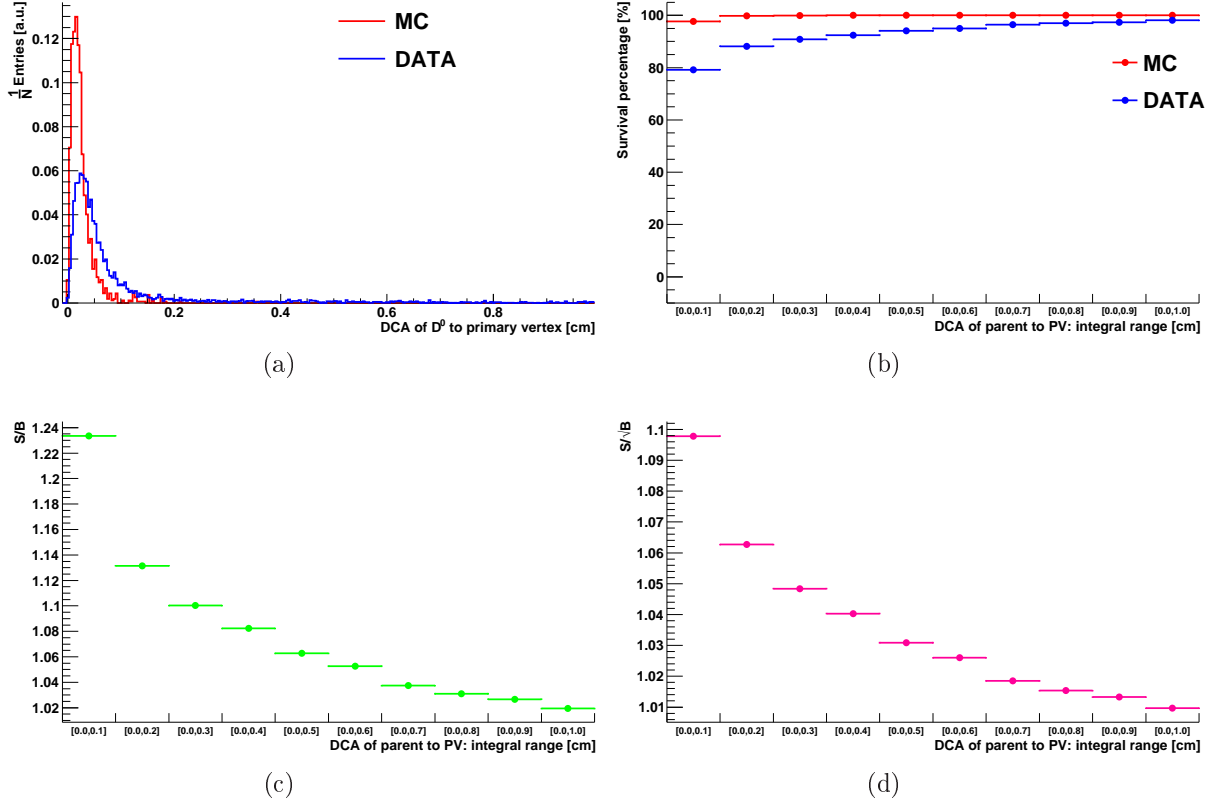


FIG. 5.34: D^0 DCA to primary vertex S/B variation study for $\text{SVT}+\text{SSD}>3$, in the range $[0, 1]$ (cm). Normalized distribution of S and B (a), survival percentage per value range (b), ratio S/B (c) and S/\sqrt{B} (d).

Range of Study $[0, 0.1]$ cm

For the specific range interval, the values of S and B along with the ratios S/B and S/\sqrt{B} for each microvertexing variable are summarized for the $\Delta a = [0, 0.1]$ (cm) in Table 5.10. Concerning the graphical part, for every Figure the raw distributions are given in (a), the SP in (b), along with both S/B in (c) and S/\sqrt{B} in (d). In Figures 5.35 the plots referring to the DCA between daughter tracks are presented. For the D^0 decay length the plots are given in Figures 5.36. Finally for the D^0 DCA to the primary vertex the plots are found in Figures 5.37.

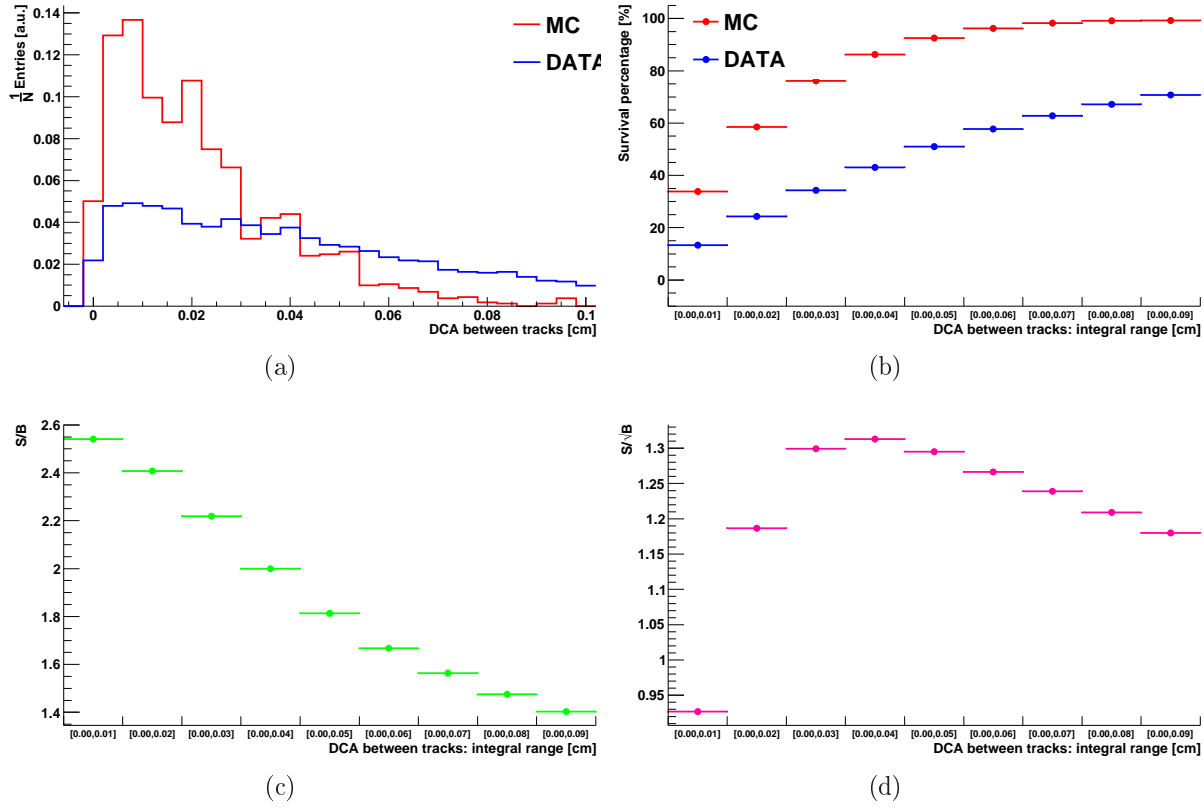


FIG. 5.35: DCA between tracks S/B variation study for $SVT+SSD>3$, in the range $[0, 0.1]$ (cm). Normalized distributions of S and B (a), survival percentage per value range (b), ratio S/B (c) and S/\sqrt{B} (d).

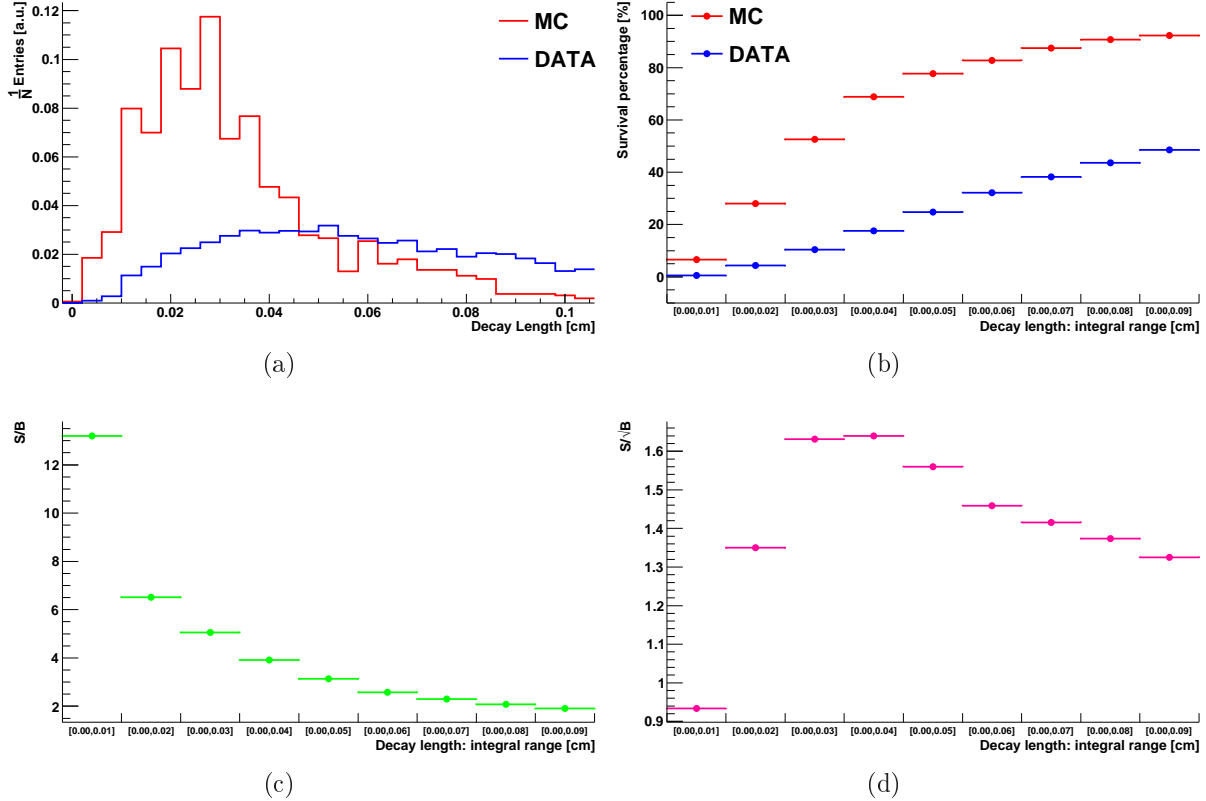


FIG. 5.36: D^0 decay length S/B variation study for $\text{SVT}+\text{SSD}>3$ in the range $[0, 0.1]$ (cm). Normalized distribution of S and B (a), survival percentage per value range (b), ratio S/B (c) and S/\sqrt{B} (d).

TAB. 5.10: S/B variation of microvertexing variables for different ranges in the $[0, 0.09]$ (cm) and SVT+SSD >3 hits for each track.

| variables \ range (cm) | | [0, 0.01] | [0, 0.02] | [0, 0.03] | [0, 0.04] | [0, 0.05] | [0, 0.06] | [0, 0.07] | [0, 0.08] | [0, 0.09] |
|-----------------------------|--------------|-----------|-----------|-----------|-----------|-----------|-----------|-----------|-----------|-----------|
| DCA between tracks | S | 0.338 | 0.585 | 0.761 | 0.862 | 0.925 | 0.962 | 0.982 | 0.991 | 0.993 |
| | B | 0.133 | 0.243 | 0.343 | 0.431 | 0.510 | 0.577 | 0.628 | 0.672 | 0.708 |
| | S/B | 2.540 | 2.407 | 2.218 | 1.995 | 1.812 | 1.667 | 1.562 | 1.474 | 1.403 |
| | S/\sqrt{B} | 0.926 | 1.187 | 1.299 | 1.313 | 1.295 | 1.266 | 1.239 | 1.239 | 1.180 |
| D^0 decay length | S | 0.066 | 0.280 | 0.526 | 0.688 | 0.777 | 0.828 | 0.875 | 0.907 | 0.923 |
| | B | 0.005 | 0.043 | 0.104 | 0.176 | 0.248 | 0.322 | 0.382 | 0.436 | 0.485 |
| | S/B | 11.511 | 6.511 | 5.030 | 3.898 | 3.122 | 2.568 | 2.288 | 2.076 | 1.901 |
| | S/\sqrt{B} | 0.934 | 1.350 | 1.631 | 1.639 | 1.560 | 1.459 | 1.415 | 1.373 | 1.325 |
| D^0 DCA to primary vertex | S | 0.225 | 0.540 | 0.751 | 0.846 | 0.905 | 0.938 | 0.961 | 0.970 | 0.974 |
| | B | 0.059 | 0.188 | 0.336 | 0.464 | 0.569 | 0.643 | 0.700 | 0.737 | 0.769 |
| | S/B | 3.818 | 2.860 | 2.235 | 1.821 | 1.588 | 1.457 | 1.372 | 1.315 | 1.265 |
| | S/\sqrt{B} | 0.926 | 1.245 | 1.295 | 1.241 | 1.199 | 1.169 | 1.148 | 1.129 | 1.110 |

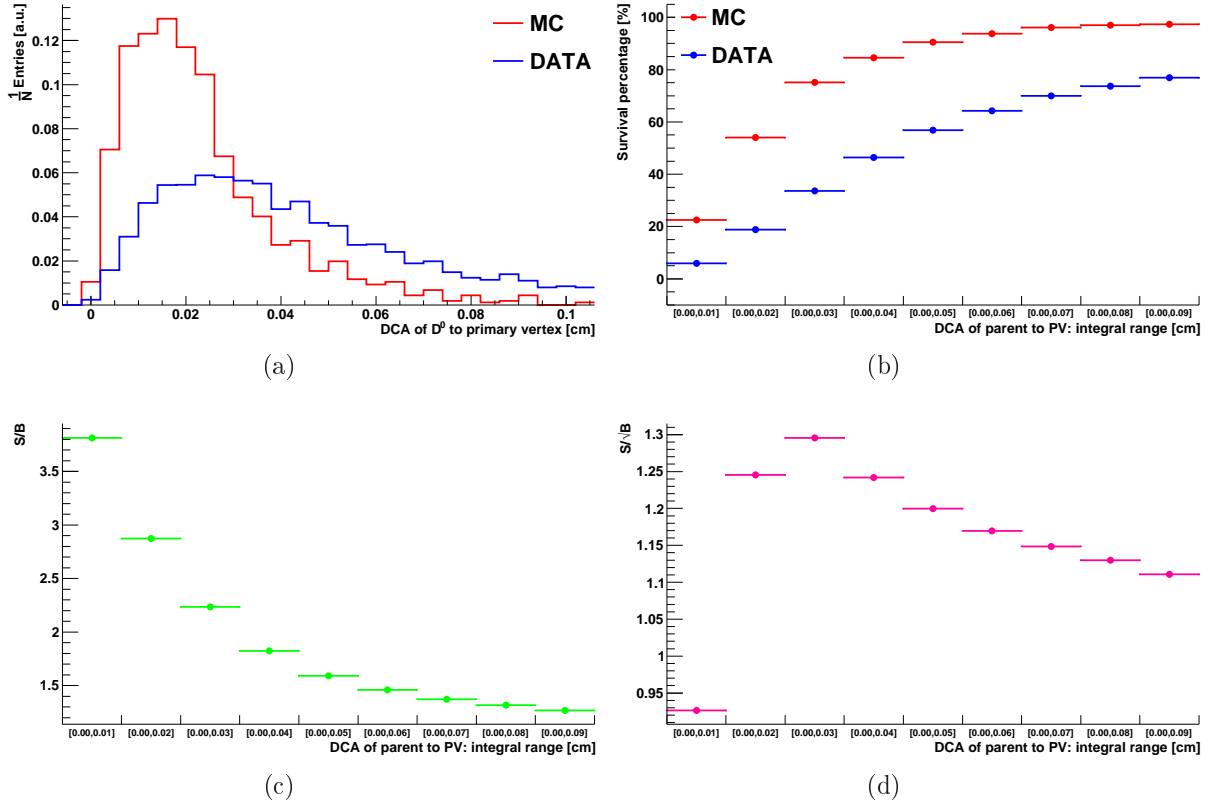


FIG. 5.37: D^0 DCA to primary vertex S/B variation study for $SVT+SSD>3$, in the range $[0, 0.1]$ (cm). Normalized distribution of S and B (a), survival percentage per value range (b), ratio S/B (c) and S/\sqrt{B} (d).

5.5.5 The S/B Study for the Rest of the Microvertexing Variables

Concerning the microvertexing variables listed below, the S/B variation study will be treated using a different range. We shall begin the study by considering the following variables:

- i. The angle ϕ_2 as presented in Section 4.2.1, defined as the angle between the two planes OAF and OBG of the daughter particles and plotted in Figure 5.38.
- ii. the variable $\cos \theta_{\text{POINTING}}$, (cf. Section 4.2.2), its distribution can be seen in Figure 5.38;
- iii. the product of $\text{DCA}_{xy}^K \cdot \text{DCA}_{xy}^\pi$ (cf. Section 4.2.5) defined as the dot product of the DCA daughter tracks in the transverse plane and shown in Figure 5.39; and
- iv. the $\cos \theta^*$ (cf. Section 4.2.1) as seen in Figures 5.40 for the K and the π candidates;

For the $\cos \theta_{\text{POINTING}}$ variable we select values in the region $[a, 1]$. For the angle ϕ_2 between the planes (as described in Section 4.2.1), we can distinguish two cases. In particular we select values within the range $\phi_2 < \pi/2$ or the range $\phi_2 > \pi/2$. Concerning the inner product of the DCA to primary vertex of the daughter tracks, $\text{DCA}_{xy}^K \cdot \text{DCA}_{xy}^\pi$ in the region $[-c, 0]$ (cm^2). In Table 5.11, we summarize the cut study of the above mentioned variables. Finally, let us also note that we select only the cases that both tracks of the $K^- \pi^+$ comply with the $\text{SVT+SSD} > 0$.

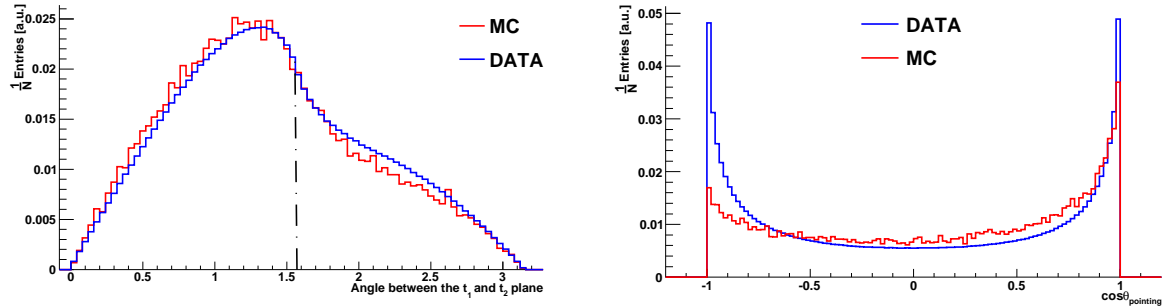


FIG. 5.38: Simulation (red) and data values (blue) *Left*: For the angle between the planes OAF and OBG of the daughter tracks (t_1 and t_2). The black line denotes the 90° . *Right*: Distribution of $e \cos \theta_{\text{POINTING}}$. Both distributions are normalized to the total number of entries.

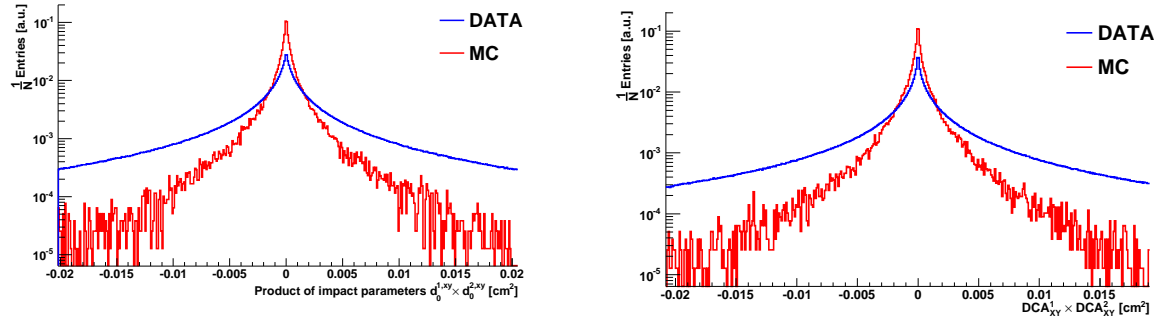


FIG. 5.39: Simulation (red) and data values (blue) for the transverse inner product $d_0^K \cdot d_0^\pi$ (left) and $\text{DCA}_{XY}^K \cdot \text{DCA}_{XY}^\pi$ (right). Both distributions are normalized to the total number of entries.

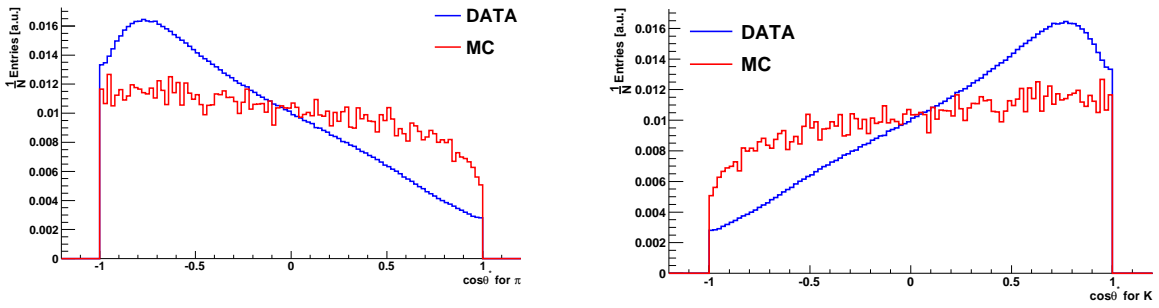


FIG. 5.40: Simulation (red) and data values (blue) for the $\cos\theta^*$ for pion (left) and kaon (right) candidates. Both distributions are normalized to the total number of entries.

TAB. 5.11: S/B variation study of the $\cos\theta_{\text{POINTING}}$, $\cos\theta_K^*$, $\cos\theta_\pi^*$ along with the $\text{DCA}_{\text{xy}}^K \cdot \text{DCA}_{\text{xy}}^\pi$ and the angle ϕ_2 between the planes of the daughter particles. All values are normalized to unity and all the tracks comply with the demand: $\text{SVT} + \text{SSD} > 0$ hits.

| variables \ range [cm ²] | | < -0.020 | < -0.010 | < 0.000 | < 0.002 |
|---|--------------|-----------------------|----------------|-------------------------|---------------|
| $\text{DCA}_{\text{xy}}^K \cdot \text{DCA}_{\text{xy}}^\pi$ | S | 0.003 | 0.008 | 0.624 | 0.929 |
| | B | 0.084 | 0.132 | 0.537 | 0.729 |
| | S/B | 0.041 | 0.065 | 1.163 | 1.275 |
| | S/\sqrt{B} | 0.012 | 0.023 | 0.851 | 1.088 |
| | | [0.80, 1.00] | [0.85, 1.00] | [0.90, 1.00] | [0.95, 1.00] |
| $\cos\theta_{\text{POINTING}}$ | S | 0.218 | 0.187 | 0.154 | 0.091 |
| | B | 0.219 | 0.193 | 0.163 | 0.105 |
| | S/B | 0.993 | 0.965 | 0.944 | 0.864 |
| | S/\sqrt{B} | 0.465 | 0.425 | 0.382 | 0.281 |
| | | [-1.00, -0.75] | [-1.00, -0.50] | [-1.00, 0.00] | [-1.00, 0.20] |
| $\cos\theta_K^*$ | S | 0.092 | 0.208 | 0.455 | 0.559 |
| | B | 0.045 | 0.116 | 0.325 | 0.435 |
| | S/B | 2.044 | 1.793 | 1.400 | 1.284 |
| | S/\sqrt{B} | 0.434 | 0.611 | 0.797 | 0.847 |
| | | [-0.20, 1.00] | [0.00, 1.00] | [0.50, 1.00] | [0.75, 1.00] |
| $\cos\theta_\pi^*$ | S | 0.559 | 0.444 | 0.199 | 0.092 |
| | B | 0.434 | 0.315 | 0.109 | 0.045 |
| | S/B | 1.284 | 1.408 | 1.812 | 2.044 |
| | S/\sqrt{B} | 0.846 | 0.791 | 0.600 | 0.434 |
| | | $(0^\circ, 90^\circ]$ | | $(90^\circ, 180^\circ]$ | |
| ϕ_2 | S | 0.669 | | 0.380 | |
| | B | 0.642 | | 0.406 | |
| | S/B | 1.042 | | 0.928 | |
| | S/\sqrt{B} | 0.835 | | 0.594 | |

Results in Cu+Cu collisions at $\sqrt{s_{\text{NN}}} = 200 \text{ GeV}$

In the current chapter, we present the results obtained by performing the analysis on the Cu+Cu dataset at $\sqrt{s_{\text{NN}}} = 200 \text{ GeV}$ and in particular the *High Tower* trigger. The various cuts along with the invariant mass plots for each separate azimuthal $\Delta\phi$ case, and the significance of the signal are presented as well.

6.1 Introduction

In the run V two different species (p+p and Cu+Cu at various energies as stated in Table 2.1) were used for collisions, as mentioned in Table 2.1. Our analysis focuses on Cu+Cu at $\sqrt{s_{\text{NN}}} = 200 \text{ GeV}$ and in particular the *High Tower* triggered dataset. Concerning the STAR detector, let us also note that the Barrel Electromagnetic Calorimeter (BEMC) as it is presented in Section 2.16, is partially instrumented covering in acceptance $\eta \in [0, 1]$. The BEMC towers are accepted in the current analysis, only in the region $[0, 0.7]$. The latter cut serves to avoid lots of material, close to the edges ($\eta = 1$), crossing when the vertex is at $z_c = \pm 30 \text{ cm}$. In run V the overall dataset of Cu+Cu at $\sqrt{s_{\text{NN}}} = 200 \text{ GeV}$ is distributed in the following data trigger setup names [Dunlop 05].

- i. $\sim 30 \cdot 10^6$ events in `cuProductionMinBias`; and
- ii. $\sim 17 \cdot 10^6$ events in `cuProductionHighTower`.

The analysis is performed on the `cuProductionHighTower` data subset.

6.2 Applied Event Cuts

6.2.1 Primary z -Vertex Cut

A primary vertex cut is performed on the z component, accepting only events that comply with $|z\text{-vertex}| < 30 \text{ cm}$. In the current analysis 2795681 events were processed, passing—after the z -vertex cut—2191462, and finally accepting 26717 events, that contain a high- p_{T} electron, as seen in Figure 6.1.

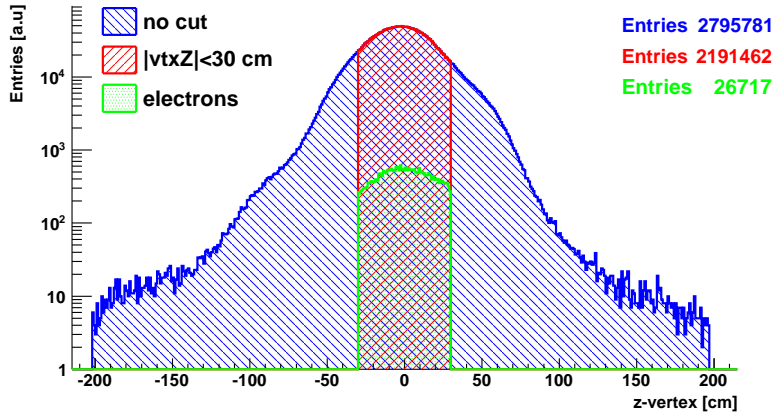


FIG. 6.1: Distribution of primary z -vertex for: all events (blue), $|z\text{-vertex}| < 30 \text{ cm}$ (red) and selected (green) events for the Cu+Cu at $\sqrt{s_{\text{NN}}} = 200 \text{ GeV}$ (*High Tower*) dataset.

6.2.2 BEMC Energy Threshold

An online cut is imposed on the energy threshold of the BEMC tower at $E > 3.75 \text{ GeV}$, complying with the values of Table 3.3, for the adequate trigger. The current trigger setup is used in order to obtain a high- p_{T} triggered events, with a large probability of containing an e^{\pm} as the trigger particle. In addition for the electron identification the cuts described in Section 3.5 are applied.

6.3 Applied Track Cuts

6.3.1 Track Quality Cuts

The track selection, includes a cut on the $|\eta| < 1$ and the number of the points in the TPC. In particular $n\text{HitsTPC} > 20$ and $\frac{n\text{HitsFit}}{n\text{HitsPoss}} > 0.15$, in agreement with (3.2). The total number of selected pairs per event, *samesign* (++ or --) and *unlike* (+-) sign

can be seen in Figure 6.2. Also in order to apply the microvertexing technique we are using the *global* tracks as stated in Appendix E.

6.3.2 Particle Identification Cuts

In order to identify the hadron into different species, we select tracks that comply with the $\frac{dE}{dx}$ cut: as described in Section 3.6 and in particular for the whole p_T spectrum, respecting (6.1).

$$|n_{\text{SigmaKaon}}| < 2 \text{ and } |n_{\text{SigmaPion}}| < 3 \quad (6.1)$$

A supplementary cut on the kaon candidates is also imposed involving the charge. In particular if the charge of the hadron is equal to the electron charge, then the hadron becomes a kaon candidate, as described in Section 1.13. In this way, we are looking for contribution mainly from the $c\bar{c}$ at $\Delta\phi = 180^\circ$ and $b\bar{b}$ at $\Delta\phi = 0^\circ$ fragmentation channel as it is summarized in Table 1.2.

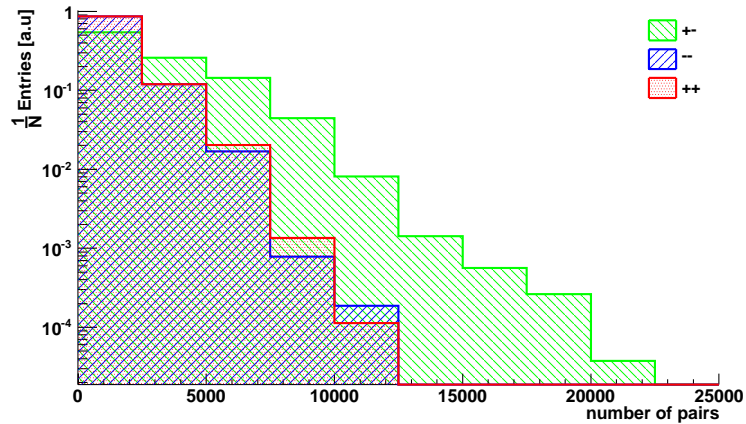


FIG. 6.2: Unlike sign (in green) hadron pairs distribution per event for the Cu+Cu dataset, along with the like sign (— in blue and ++ in red). All plots are normalized to the total number of entries.

6.4 Charged Event Multiplicity and $\Delta\phi$ Cuts

We begin the description of the analysis by mentioning the cuts that will be used later on. In order to study the invariant mass yield, we perform specific cuts on the event charged multiplicity and on the $\Delta\phi$ of the trigger particle (e^\pm) and the reconstructed $K^-\pi^+/K^+\pi^-$ pair. We summarize the $\Delta\phi$ along with the event multiplicity in the following combinations. Also let us consider the $\Delta\phi \equiv \phi_e - \phi_{\text{pair}}$ to be the azimuthal

difference between the trigger particle (e^\pm) and the reconstructed parent particle D^0 . The distribution of the multiplicity for the Cu+Cu dataset can be seen in Figure 3.3 and a correlation of the centrality bins along with the multiplicity can be found in Table 3.2.

A. No multiplicity cut

- I. $\Delta\phi = 0 \pm 1.2$
- II. $\Delta\phi = \pi \pm 1.2$
- III. No $\Delta\phi$ cut

B. Multiplicity < 74

- I. $\Delta\phi = 0 \pm 1.2$
- II. $\Delta\phi = \pi \pm 1.2$
- III. No $\Delta\phi$ cut

C. Multiplicity < 104

- I. $\Delta\phi = 0 \pm 1.2$
- II. $\Delta\phi = \pi \pm 1.2$
- III. No $\Delta\phi$ cut

6.5 Microvertexing Cuts

In addition to the event cuts described in Section 6.5, by applying the microvertexing technique described in Chapter 4, we construct the following set of cuts to be applied for every hadron pair $K^\pm\pi^\mp$.

- a. i. SVT+SSD > 0
 - ii. DCA between the daughters < 0.2 cm
 - iii. Decay length < 0.2 cm
 - iv. DCA of D^0 to primary vertex (PV) < 0.2 cm
- b. i. SVT+SSD > 0
 - ii. Decay length < 0.3 cm
 - iii. DCA of D^0 to PV < 0.2 cm
- c. i. SVT+SSD > 0

- ii. DCA between the daughters $< 0.04 \text{ cm}$
- iii. DCA of D^0 to PV $< 0.2 \text{ cm}$
- iv. $\cos \theta_K^* < 0.24$
- v.
 - 1. Decay length $< 0.30 \text{ cm}$
 - 2. $< 0.20 \text{ cm}$
 - 3. $< 0.10 \text{ cm}$
 - 4. $< 0.05 \text{ cm}$
- d. i. $\text{SVT+SSD} > 0$
 - ii. DCA between the daughters $< 0.3 \text{ cm}$
 - iii. Decay length $< 0.3 \text{ cm}$
 - iv. DCA of D^0 to PV $< 0.3 \text{ cm}$
- e. i. $\text{SVT+SSD} > 0$
 - ii. DCA between the daughters $< 0.05 \text{ cm}$
 - iii. DCA of daughters to PV $< 0.05 \text{ cm}$
 - iv. $\text{DCA}_{\text{XY}}^K \cdot \text{DCA}_{\text{XY}}^\pi < 0.5 \text{ cm}^2$
 - v. $\cos \theta_{\text{POINTING}} > 0.8$
 - vi. $p_T > 0.3 \text{ GeV}/c$ for each daughter track

6.6 Invariant Mass Plots

6.6.1 Results with Cutset c

After having implemented the previous cuts as described, a major set of invariant mass plots has been generated. In the following sections, a subset of the results for the investigated set of cuts is presented. In particular, the event cuts described in $\Delta\phi$ and charge multiplicity—described in Section 6.4—with the tracks cuts as described in Section 6.5. The results for all cuts are available in the following link <http://tinyurl.com/3yd5oob> for the STAR collaboration and are not included in the thesis as they are several hundreds of pages.

In the following plots, it is presented the case of the D^0/\bar{D}^0 invariant mass yield along with the total samesign $\sqrt{(++) \otimes (--)}$ background and the subsequent subtraction. In addition to these, a polynomial fit of 7th degree along with a gaussian fit is performed. A supplementary set of event cuts is imposed, namely for the $\Delta\phi = 0$ in Figure 6.3, for the $\Delta\phi = \pi$ shown in Figure 6.4, and without any $\Delta\phi$ cut shown in Figure 6.5.

Event Cut AI

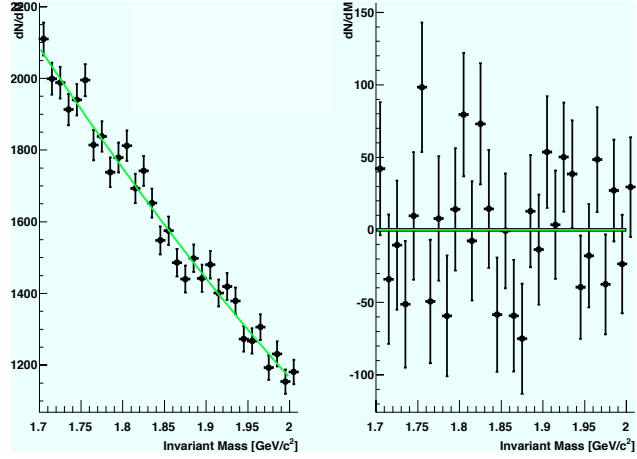


FIG. 6.3: D^0/\bar{D}^0 Invariant mass yield plots obtained with $\Delta\phi = 0$ cut and Cutset c. *Left:* Invariant mass yield (*black*) along with polynomial and gaussian fit (*green*). *Right:* Subtracted invariant mass yield.

Event Cut AII

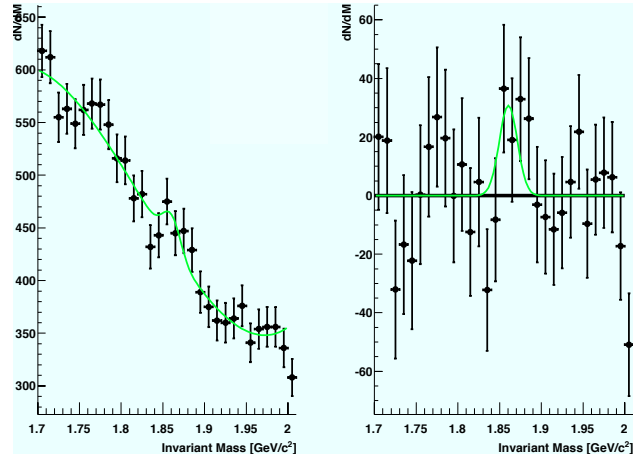


FIG. 6.4: D^0/\bar{D}^0 Invariant mass yield plots obtained with $\Delta\phi = \pi$ cut and Cutset c. *Left:* Invariant mass yield (*black*) along with polynomial and gaussian fit (*green*). *Right:* Subtracted invariant mass yield.

Event Cut AIII

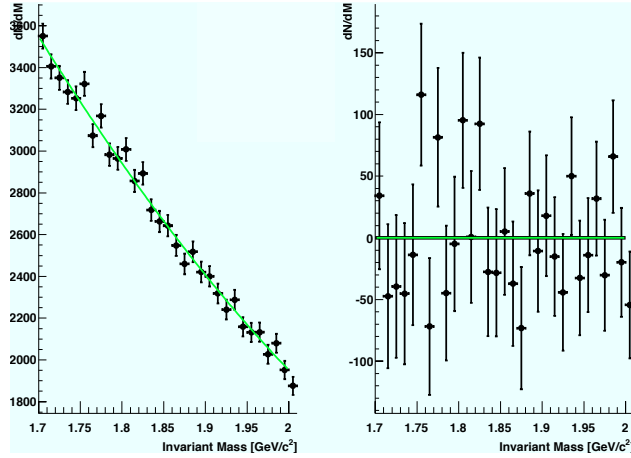


FIG. 6.5: D^0/\bar{D}^0 Invariant mass yield plots obtained with no $\Delta\phi$ cut and Cutset c. *Left:* Invariant mass yield (black) along with polynomial and gaussian fit (green). *Right:* Subtracted invariant mass yield.

6.6.2 Results with Cutset d

Event Cut AI

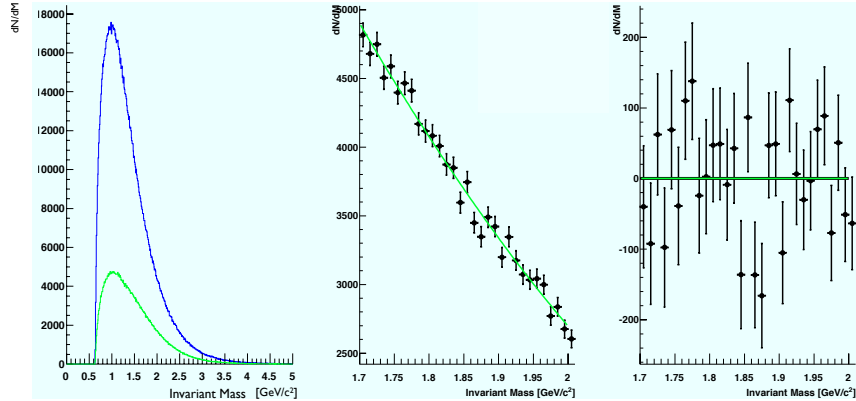


FIG. 6.6: D^0/\bar{D}^0 Invariant mass plots obtained with $\Delta\phi = 0$, and Cutset d. *Left:* Invariant mass yield (blue) along with same-sign background (green). *Center:* Primary background subtraction (black) along with polynomial and gaussian fit (green). *Right:* Secondary background subtraction of the invariant mass yield.

Event Cut AII

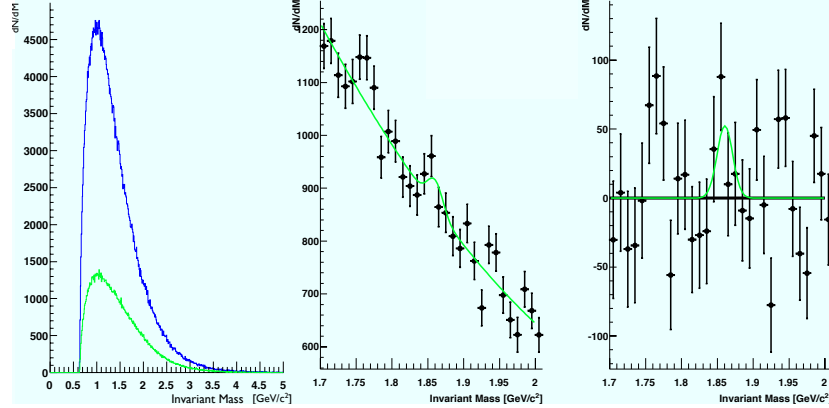


FIG. 6.7: D^0/\bar{D}^0 Invariant mass plots obtained with $\Delta\phi = \pi$, and Cutset d. *Left:* Invariant mass (blue) yield with samesign background yield (green). *Center:* Primary background subtraction (black) along with polynomial and gaussian fit (green). *Right:* Secondary background subtraction of the invariant mass yield.

Event Cut AIII

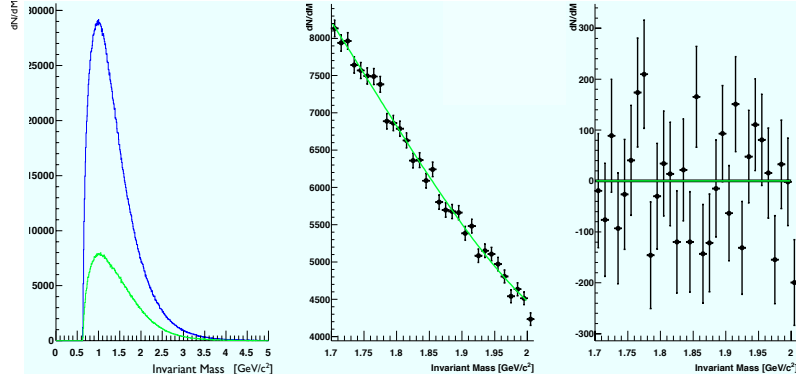


FIG. 6.8: D^0/\bar{D}^0 Invariant mass plots obtained with no $\Delta\phi$ cut and Cutset d. *Left:* Invariant mass (blue) yield with samesign background yield (green). *Center:* Primary background subtraction (black) along with polynomial and gaussian fit (green). *Right:* Secondary background subtraction of the invariant mass yield.

6.6.3 Results with Cutset e

Using the Cutset e, and by combining the event Cutset $\Delta\phi = \{0, \pi\}$ in Figures 6.9–6.10 cut as well as no $\Delta\phi$ cut in Figure 6.11, we obtain the following cases.

Event Cut AII

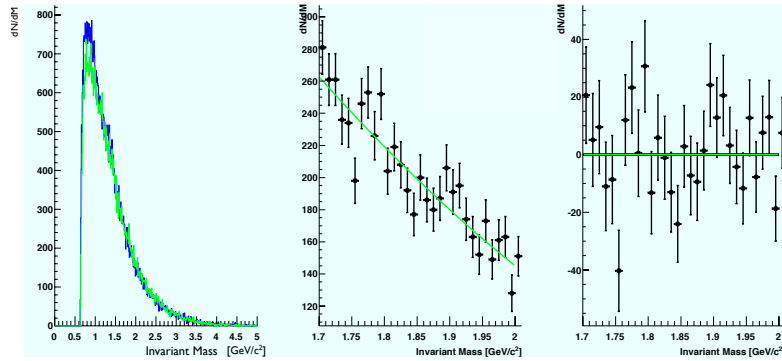


FIG. 6.9: D^0/\bar{D}^0 Invariant mass plots obtained with $\Delta\phi = 0$ cut and Cutset e. *Left:* Invariant mass (blue) yield with samesign background yield (green). *Center:* Primary background subtraction (black) along with polynomial and gaussian fit (green). *Right:* Secondary background subtraction of the invariant mass yield.

Event Cut AII

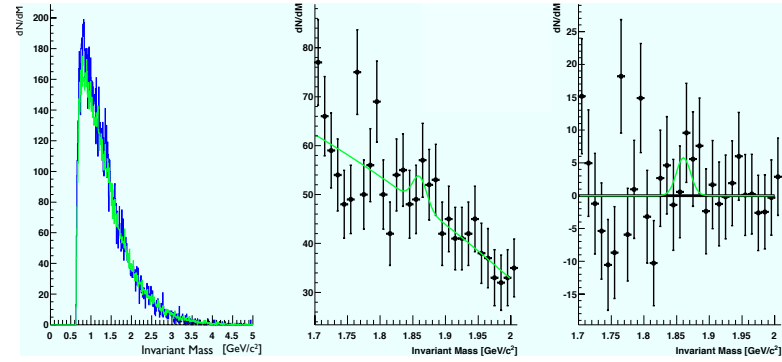


FIG. 6.10: D^0/\bar{D}^0 Invariant mass plots obtained with $\Delta\phi = \pi$ cut and Cutset e. *Left:* Invariant mass (blue) yield with samesign background yield (green). *Center:* Primary background subtraction (black) along with polynomial and gaussian fit (green). *Right:* Secondary background subtraction of the invariant mass yield.

Event Cut AIII

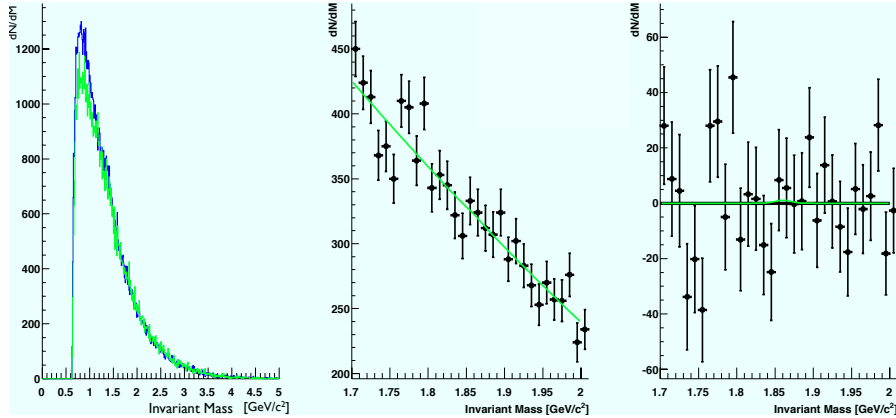


FIG. 6.11: D^0/\bar{D}^0 Invariant mass plots obtained with no $\Delta\phi$ cut and Cutset e. *Left:* Invariant mass (blue) yield with samesign background yield (green). *Center:* Primary background subtraction (black) along with polynomial and gaussian fit (green). *Right:* Secondary background subtraction of the invariant mass yield.

Event Cut BII

By implementing the Cutset e, we are continuing the analysis along with the event cuts on the charge multiplicity < 74 and the $\Delta\phi$, it is obtained the case shown in Figure 6.12.

6.7 Discussion

We have investigated the cut sets shown in Section 6.4 and Section 6.5 in the overall Cu+Cu dataset at $\sqrt{s_{\text{NN}}} = 200 \text{ GeV}$, by performing the event cuts listed below:

- i. Event charged multiplicity with no cut and multiplicity $\in \{74, 103\}$; and
- ii. azimuthal angular correlation between trigger particle and the hadron pair. In particular it is chosen no $\Delta\phi$ cut as well as $\Delta\phi = \{0, \pi\}$.

We have also presented in this chapter the results for the investigated set of cuts applied in the Cu+Cu dataset. In particular using the Cutset c we obtained the results shown in Section 6.6. The results that were obtained with Cutset d are shown in Section 6.6.2 and finally in Section 6.6.3 the plots with the results obtained with Cutset e are presented. For the like sign $e-K$ case which has been investigated for the

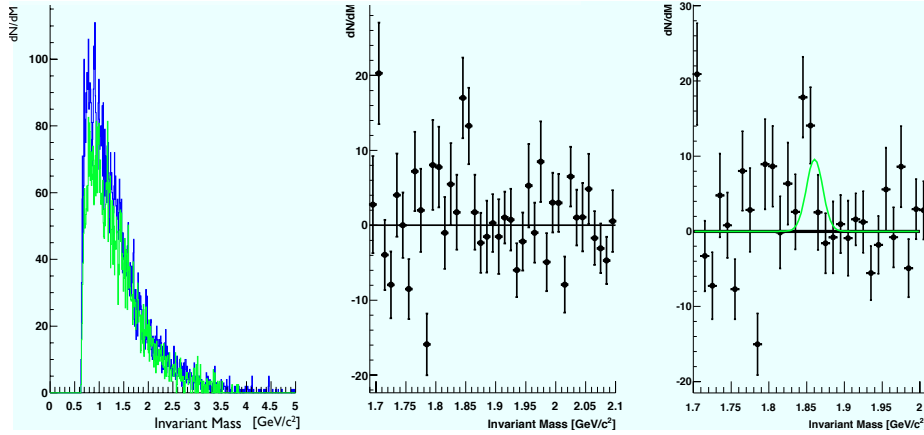


FIG. 6.12: D^0/\bar{D}^0 Invariant mass plots obtained with charge multiplicity < 74 , $\Delta\phi = \pi$ cut and Cutset e. *Left:* Invariant mass (blue) yield with same-sign background yield (green). *Center:* Primary background subtraction along with polynomial and gaussian fit. *Right:* Secondary background subtraction of the invariant mass yield.

Cu+Cu reactions, in a systematic way no signal is observed for the case of $\Delta\phi = 0$ (beauty dominant contribution), while a signal of significance of up to maximum of 2.2σ is obtained for the $\Delta\phi = \pi$ case (charm dominant contribution). This trend is followed for all the multiplicity studies. The correlation method is described in Section 1.13, and the combinations of angular correlation along with the charge sign are summarized in Table 1.2. In particular Figures 6.3, 6.6 and 6.9 show the results for $\Delta\phi = 0$ cases, while Figures 6.4, 6.7 and 6.10 show the results for the $\Delta\phi = \pi$ cases. As an example of a signal case, a signal of significance 2.1σ is obtained for the $\Delta\phi = \pi$ case and multiplicity < 74 —keeping the 0–30% in centrality, cf. Table 3.2. The current result is shown in Figure 6.12. The latter case refers to the charm contribution, that is attained by combining the like sign $e-K$ pairs and selecting the $\Delta\phi = \pi$. We summarize the results obtained in Table 6.1.

TAB. 6.1: D^0 invariant mass along with σ and significance of the signal for each $\Delta\phi$ azimuthal correlation in *High Tower*.

| $\Delta\phi$ | D^0 mass [GeV/c ²] | σ [MeV/c ²] | significance: $\frac{S}{\sqrt{S+B}}$ |
|--------------|----------------------------------|--------------------------------|--------------------------------------|
| 0° | 1.893 ± 0.006 | 10.8 ± 4.2 | 2.50 |
| 180° | 1.888 ± 0.006 | 16.0 ± 5.0 | 3.04 |
| No Cut | 1.892 ± 0.005 | 14.7 ± 4.7 | 4.85 |

Chapter 7

Results in p+p collisions at $\sqrt{s} = 200 \text{ GeV}$

The main objective of the current chapter is the results obtained by analyzing the p+p dataset at $\sqrt{s} = 200 \text{ GeV}$ (run VI). In particular we describe the various cuts that were used and present the invariant mass plots for each separate $\Delta\phi$ case and e-K pair charge demand. A conclusion is also drawn about the charm and beauty contribution for the specific dataset.

7.1 Introduction

During the run VI in the year 2006, the silicon detectors—although physically present—were not taken under consideration in the reconstruction chain of the events. Therefore, for the particular dataset since there is no information on the silicon hits, no microvertexing technique can be applied for the $e-D^0$ analysis. The total dataset consists of approximately $213 \cdot 10^6$ events, distributed in the following subsets (production trigger setup names and only *physics* stream) [Dunlop 06].

`ppProductionTrans` containing 101865945 events;

`ppProductionLong` containing 101367002 events;

`ppProduction` containing 8892171 events; and

`pp2006MinBias` containing 1074068 events.

Let us also mention that it is the first year that the BEMC (Section 2.16), is fully instrumented covering in $\eta \in [-1, +1]$ acceptance.

7.2 Applied Event Cuts

7.2.1 Primary z -Vertex Cut

Concerning the primary vertex z component, an inclusive cut is performed, keeping events that comply with the $|z\text{-vertex}| < 30 \text{ cm}$, as can be seen in Figure 7.1. After processing in total 1795274 events, and passing the z -vertex cut 480654, 19228 events are finally selected. In Figure 7.1, it shown a comparative plot of the number of the initial and final (selected) events used in our analysis. In addition we select BEMC towers that span into the region $\eta \in [-0.7, 0.7]$, avoiding the edges of the calorimeter, where tracks emerging from events with primary vertex at $z_c = \pm 30$, can cross significant quantity of material.

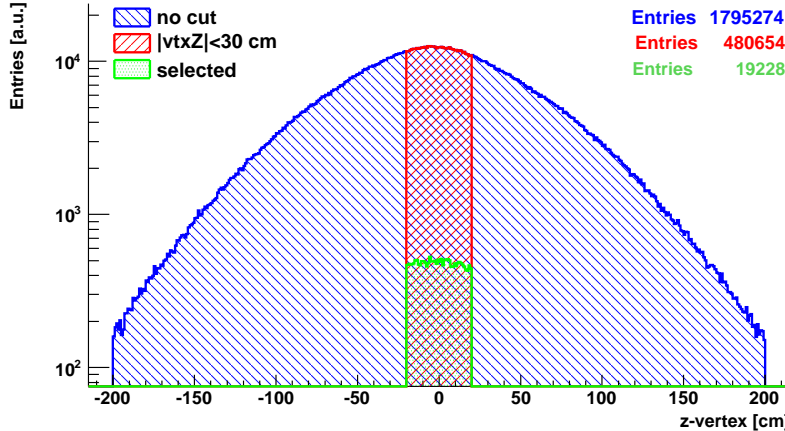


FIG. 7.1: Distribution of the z component of the primary vertex for: all events (blue), events that comply with $|z\text{-vertex}| < 30 \text{ cm}$ (red) and selected (green) events for the p+p dataset at $\sqrt{s} = 200 \text{ GeV}$.

7.2.2 BEMC Energy Threshold

An online cut on the energy of the BEMC towers is performed, complying with the values of Table 3.3, for the various trigger sets that are currently included in the analysis. The values for the energy threshold of the towers vary with the trigger selection and can take the values $E \geq \{5.0, 5.4\} \text{ GeV}$. In addition for the selection of the electrons the cuts that are applied for the tracks, are described in Section 3.5.

7.3 Applied Track Cuts

7.3.1 Track Quality Cuts

The accepted tracks span within $|\eta| < 1$ and the number of the points in the TPC comply with with (3.2), described in Section 3.3. Let us also mention that we are using the *primary* tracks, as described in Appendix E.

7.3.2 Particle Identification Cuts

The identification of hadrons is achieved by selecting tracks that comply with the cuts described in (3.8). Concerning the identification using the energy loss $\frac{dE}{dx}$, we apply the cuts described in Section 3.6. For the current dataset, we have selected the values expressed in (7.1).

$$|\text{nSigmaKaon}| < 2 \text{ and } |\text{nSigmaPion}| < 3 \quad (7.1)$$

In addition, a cut on the kaon candidates is also imposed, demanding the charge of the hadron to coincide with the electron charge, as stated in Section 1.13. The latter demand can probe the $c\bar{c}$ contribution at $\Delta\phi = \pi$ and the D^0 dominantly coming from the $b\bar{b}$ fragmentation channel at $\Delta\phi = 0$.

7.4 Invariant Mass Plots

7.4.1 Results with $\Delta\phi = \pi$

By applying a like sign demand between the e and K , as well as a $\Delta\phi = \pi \pm 1.2$, we obtain the signal of significance 3σ as shown in Figure 7.2. For the calculation of the significance it was used the (3.16) by integrating over a mass area of $[-3\sigma, 3\sigma]$ the signal obtained and the $S + B$ invariant mass yield.

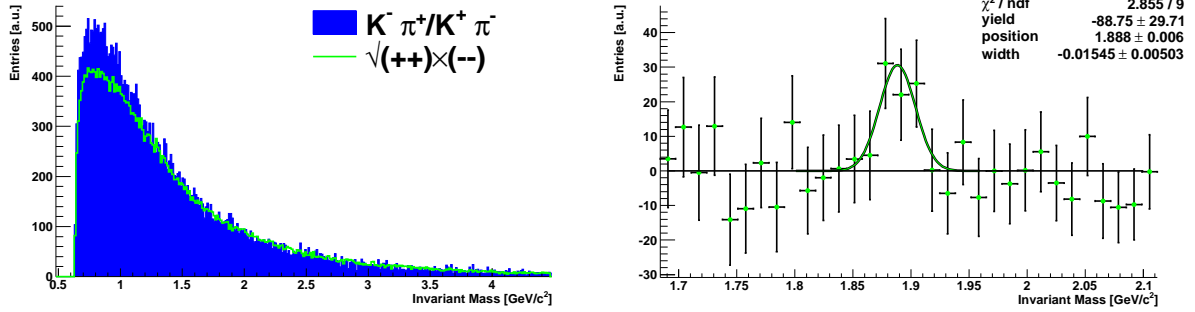


FIG. 7.2: Invariant Mass plots for the $\Delta\phi = \pi$ case for samesign $e-K$ pair. *Left:* $K^- \pi^+ / K^+ \pi^-$ invariant mass yield (blue) and samesign $\sqrt{K^- \pi^- \otimes K^+ \pi^+}$ (green). *Right:* Subtracted invariant mass along with gaussian fit (green), obtaining the value of $1.888 \text{ GeV}/c^2$ and $\sigma = 16 \text{ MeV}/c^2$. The signal significance obtained is $\frac{S}{\sqrt{S+B}} = 3.04$ ($\frac{S}{\sqrt{B}} = 3.26$).

7.4.2 Results with $\Delta\phi = 0$

By performing a $\Delta\phi = 0$ and keeping the like sign demand between trigger particle and K candidate, it is obtained Figure 7.3.

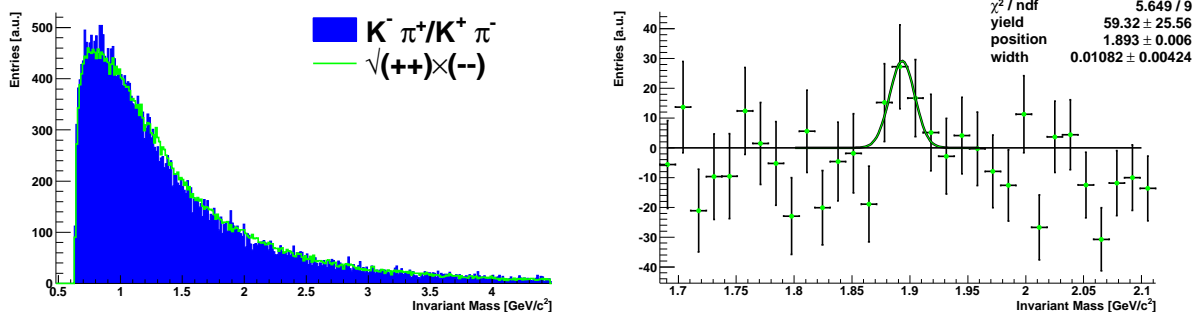


FIG. 7.3: D^0/\bar{D}^0 Invariant Mass plots for the $\Delta\phi = 0$ case for samesign $e-K$ pair. *Left:* $K^- \pi^+ / K^+ \pi^-$ invariant mass yield (blue) and samesign $\sqrt{K^- \pi^- \otimes K^+ \pi^+}$ (green). *Right:* Subtracted invariant mass yield along with the gaussian fit (green), resulting mean value $1.893 \text{ GeV}/c^2$, $\sigma = 10.8 \text{ MeV}/c^2$ and significance $\frac{S}{\sqrt{S+B}} = 2.50$ ($\frac{S}{\sqrt{B}} = 2.64$).

7.4.3 Results with no $\Delta\phi$ cut

We continue the analysis by removing the azimuthal angular cut $\Delta\phi$ and keeping the like sign demand between trigger particle and K candidate. In that way both contributions of $c\bar{c}$ and $b\bar{b}$ fragmentation are kept. The result obtained is shown in Figure 7.4.

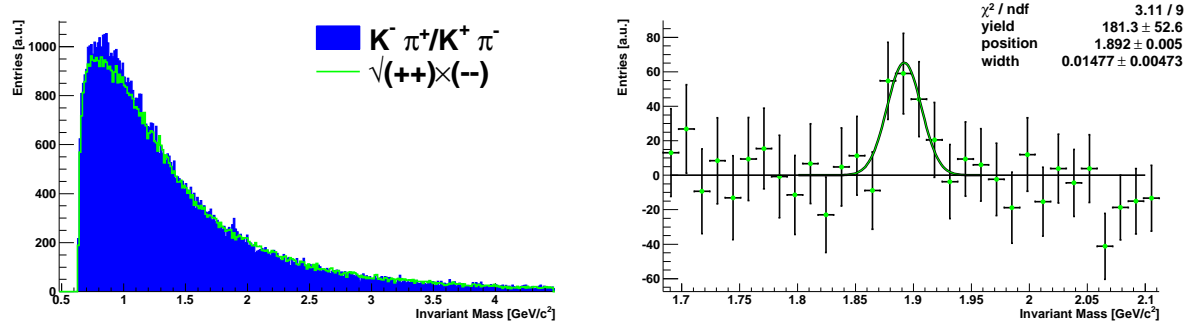


FIG. 7.4: D^0/\bar{D}^0 Invariant Mass plots with no $\Delta\phi$ cut for samesign $e-K$ pair. *Left:* $K^- \pi^+ / K^+ \pi^-$ invariant mass yield (blue) and samesign $\sqrt{K^- \pi^- \otimes K^+ \pi^+}$ (green). *Right:* Subtracted invariant mass yield along with the gaussian fit, yielding mean value $1.892 \text{ GeV}/c^2$ and $\sigma = 14.7 \text{ MeV}/c^2$ and significance $\frac{S}{\sqrt{S+B}} = 4.85$ ($\frac{S}{\sqrt{B}} = 5.21$).

7.5 Discussion

For the charm (C) contribution—the case of $\Delta\phi = \pi$ along with the like sign pairs $e-K$ as mentioned in Table 1.2—a signal was observed of significance 3.1σ as shown in Figure 7.2. For the $\Delta\phi = 0$ case and for the like sign charge demand for the $e-K$ pair, it is obtained a signal of significance 2.50σ for the beauty (B) contribution.

Using the $e-D^0$ azimuthal correlation method and the $e-h$ (electron-hadron) correlations, it is found that the beauty contribution enhances with p_T and becomes comparable to the charm contribution around $p_T \sim 5.5 \text{ GeV}/c$ in p+p collisions at $\sqrt{s} = 200 \text{ GeV}$ [Mischke 09b, Geromitsos 09]. The latter statement is shown graphically in Figure 7.5—right part. The beauty contribution is found to be compatible to FONLL calculations within the uncertainties [Aggarwal 10]. Finally in Figure 7.5 the result obtained from PYTHIA simulations fitted to the data, along with the MC@NLO calculation is shown as well.

TAB. 7.1: The D^0 invariant mass along with the σ and significance of the signal for each $\Delta\phi$ azimuthal correlation.

| $\Delta\phi$ | D^0 mass [GeV/c^2] | σ [MeV/c^2] | significance: $\frac{S}{\sqrt{S+B}}$ |
|--------------|---------------------------------|-------------------------------|--------------------------------------|
| 0° | 1.893 ± 0.006 | 10.8 ± 4.2 | 2.50 |
| 180° | 1.888 ± 0.006 | 16.0 ± 5.0 | 3.04 |
| No Cut | 1.892 ± 0.005 | 14.7 ± 4.7 | 4.85 |

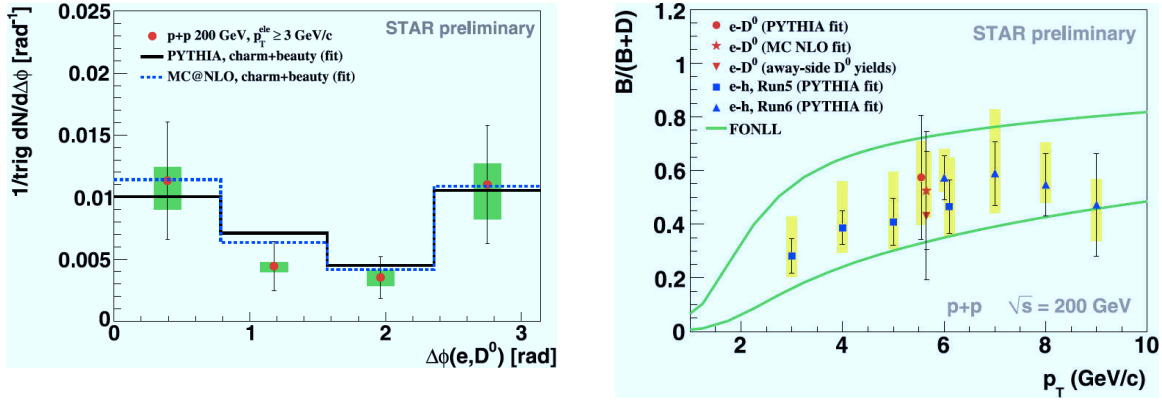


FIG. 7.5: *Left:* Azimuthal angular correlation distribution of non-photonic electrons and D^0 (for the case of like sign $e-K$ pairs) in $p+p$ collisions at $\sqrt{s} = 200 \text{ GeV}$. The systematic uncertainties are also denoted (green). The result obtained from PYTHIA simulations fitted to the data, along with the MC@NLO calculation is shown as well (black and blue-dashed lines respectively). *Right:* The relative bottom contribution to the non-photonic electron yield derived from different fits to the $e-D^0$ azimuthal correlation distribution is depicted (red points), along with a comparison to the e -hadron correlations (blue points) and to the uncertainty band from a FONLL calculation (green curves). In addition, the systematic uncertainties are presented (yellow boxes). Plots taken from [Mischke 09b].

Chapter 8

Results in Au+Au collisions at $\sqrt{s_{\text{NN}}} = 200 \text{ GeV}$

In the current chapter it is described the results obtained performing the analysis on the Au+Au dataset at $\sqrt{s_{\text{NN}}} = 200 \text{ GeV}$ and in particular the *Btag* as well as the Minimum Bias triggered events. We present the various cuts along with the invariant mass plots for each azimuthal $\Delta\phi$ correlation case.

8.1 Introduction

During the run VII the overall dataset of the Au+Au at $\sqrt{s_{\text{NN}}} = 200 \text{ GeV}$ dataset, is distributed in the following trigger setup names [Didenko 08].

- i. Approximately $62 \cdot 10^6$ events in the `2007ProductionMinBias`, (including only the *physics* datastream); and
- ii. $\sim 27.9 \cdot 10^6$ events in the `2007Production2`, all the datastreams.

In particular, in the trigger setup name `2007Production2`, the subset of events with the *Btag* stream is the portion of events that the $e-D^0$ analysis will be focused on. The high- p_{T} events belonging to this stream are $\sim 1.5 \cdot 10^6$ in total. Let us also mention that for the Minimum biased events—in the *physics* stream and in the `2007Production2`—are approximately $18 \cdot 10^6$ events are included.

8.2 Applied Event Cuts

8.2.1 Primary z -Vertex Cut

A primary vertex cut at $|z\text{-vertex}| < 20 \text{ cm}$ is performed, allowing to select tracks, that remain restrained in the STAR central tracking area. In total 1.461.003 events are

examined (belonging in the *Btag* stream and the 2007Production2). After the above primary z -vertex cut, 1415616 events are gathered. Finally the portion of the 93727 events used for the current analysis are obtained that contain a high- p_T electron, as can be seen in Figure 8.1.

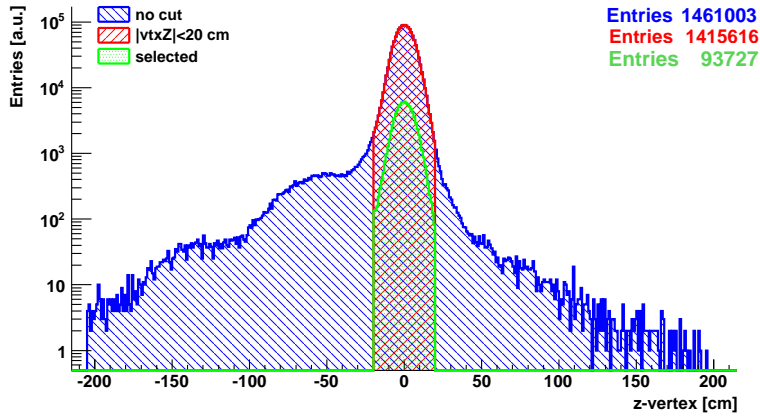


FIG. 8.1: Distribution of the z component of the primary vertex for: all events (blue), events that comply with the $|z\text{-vertex}| < 20 \text{ cm}$ (red) and the selected (green) events for the Au+Au at $\sqrt{s_{\text{NN}}} = 200 \text{ GeV}$ (*Btag*) dataset.

8.2.2 Quality of Runs

It was suggested by the Physics Working Group of STAR Collaboration, that a certain amount of runs obtained should be excluded from the analysis [Mohanty 09]. In particular, the criterion for the selection of runs it is examined the $\langle \cos \phi \rangle$ of tracks versus the run-number is plotted for several p_T bins (with a bin size of 50 MeV/c and done up to $p_T = 2 \text{ GeV}/c$). The request is whether each run has a mean value of the $\langle \cos \phi \rangle$ greater than 2σ from the overall mean value described by (8.1).

$$\begin{aligned} \langle \cos \phi_c \rangle &= -0.006 \\ \sigma_{\cos \phi} &= 0.003 \end{aligned} \tag{8.1}$$

As a result, the *Btag* sample is affected by 7.46% yielding 6847 rejected events. For the minimum biased events in 2007Production2, this demand affects 200 runs (or equivalently 675.294 events), or 3.82% of the total events.

8.2.3 BEMC Energy Threshold

The online cut implemented on the transverse energy E_T of the BEMC tower threshold is at $E_T > 4.75$ GeV, and complies with the energy threshold values stated in Table 3.3, for the adequate triggers. A tower is accepted only if it is found within the pseudorapidity area $\eta \in [-0.7, 0.7]$. The latter cut is performed in order to avoid the edges of the calorimeter where the material becomes thick, when compared to the $\eta = 0$ region.

8.3 Applied Track Cuts

8.3.1 Track Quality Cuts

The quality assurance of tracks is performed by demanding for each track to have the TPC hits that comply with (3.2). Also tracks outside the region $|\eta| < 1$ are excluded from the analysis. After the track cuts, the total number of selected pairs per event, both for the *samesign* (++) or (--) as well as for the *unlike-sign* (+-) can be seen in Figure 8.2. Also in order to perform the microvertexing technique we are using the *global* tracks as stated in Appendix E.

8.3.2 Particle Identification Cuts

The classification of hadrons into K and π is performed by selecting tracks that comply with the $\frac{dE}{dx}$ cut as described in Section 3.6. The values chosen for the current dataset, are described in (8.2).

$$|\text{nSigmaKaon}| < 2 \text{ and } |\text{nSigmaPion}| < 3 \quad (8.2)$$

Additionally, a supplementary selection on the kaon candidates is also imposed. In particular the demand of the charge of the hadron to be equal to the electron charge, yields a kaon candidate, that can probe a D^0 produced by a $c\bar{c}$ at $\Delta\phi = 180^\circ$ or a $b\bar{b}$ at $\Delta\phi = 0^\circ$. In the current dataset, we also implemented the unlike sign charge demand between the trigger particle and the hadron, that combined with the adequate $\Delta\phi$, it can probe from a $b\bar{b}$ fragmentation channel. The latter charge correlations for the $c\bar{c}$ and $b\bar{b}$ along with the azimuthal correlations, are described in Section 1.13.

8.4 Microvertexing Cuts

- a. i. $\text{SVT+SSD} > 1$
- ii. DCA of daughters to primary vertex (PV) < 0.1 cm
- iii. DCA between daughters < 0.1 cm

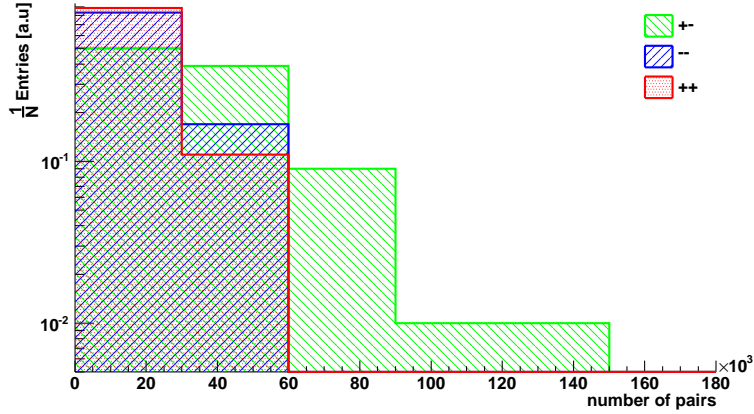


FIG. 8.2: Unlike sign hadron pairs per event (green) distribution along with samesign (positive: red and negative blue). The plot is created from the *Btag* triggered events of Au+Au at $\sqrt{s_{\text{NN}}} = 200 \text{ GeV}$. All plots are normalized to unity.

- iv. Decay Length < 0.1 cm
- b. i. SVT+SSD > 1
- ii. $\cos \theta^* < 0$
- iii. DCA between daughters < 0.06 cm
- iv. DCA of parent to PV < 0.1 cm
- v. Decay Length < 0.2 cm

8.5 Invariant Mass Plots

8.5.1 Results on Minimum Biased Events

By performing the Cutset a described in Section 8.4, on a subset of $3.71 \cdot 10^6$ minimum biased events, we obtained the results shown in Figure 8.3, where the invariant mass yield of D^0/\bar{D}^0 is presented along with the samesign background $\sqrt{K^-\pi^- \otimes K^+\pi^+}$. In addition, a polynomial fit is performed and a secondary background subtraction is performed as well. Let us mention that in the absence of a trigger particle, the charge correlation Section 1.13, cannot be applied. Therefore each hadron can belong to both species as presented in Section 3.8.1.

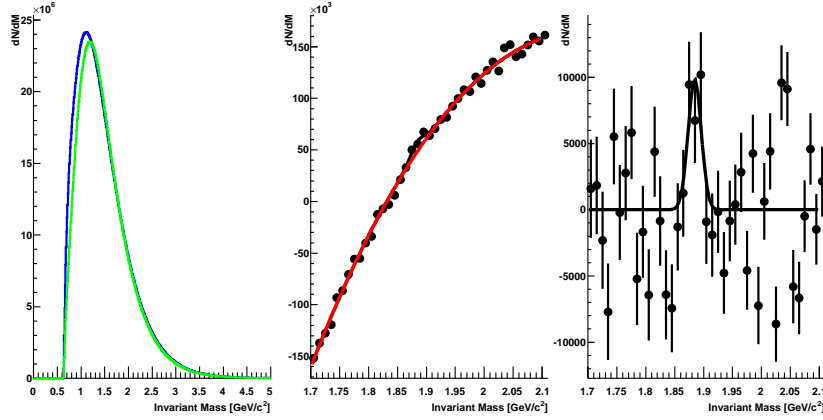


FIG. 8.3: D^0/\bar{D}^0 Invariant mass yield plots obtained with Cutset a on the minimum biased events. *Left:* Invariant mass yield (blue) along with samesign background $\sqrt{K^-\pi^- \otimes K^+\pi^+}$ (green). *Center:* Primary background subtraction along with polynomial (red) and gaussian (black) fit. *Right:* Subtracted invariant mass yield with the gaussian fit (black line). The signal observed is 3.71σ . The mean value from the fit is $1.884\text{ GeV}/c^2$ and the $\sigma = 11\text{ MeV}/c^2$.

8.5.2 Results on the *Btag* Triggered Events

In the current dataset, the demand of the charged trigger and kaon candidate, is applied, allowing to perform the $e-D^0$ correlation method. In particular, in Figure 8.4, it is seen the result for the $c\bar{c}$ fragmentation channel by selecting the samesign pairs $e-K$ and the azimuthal angular correlation at $\Delta\phi = \pi$.

8.6 Discussion

In the previous paragraphs, we have presented results obtained in the Au+Au at $\sqrt{s_{\text{NN}}} = 200\text{ GeV}$ dataset. For the *minimum biased* events a signal of significance of $\frac{S}{\sqrt{S+B}} = 3.71$ is observed by performing the microvertexing Cutset a. In addition, concerning the *Btag* data subset, the correlation method—summarized in Table 1.2—of $\Delta\phi = \pi$ along with the unlike sign charge demand for the $e-K$ was applied. The signal observed by implementing the latter method along with the microvertexing Cutset b, has a significance of $\frac{S}{\sqrt{S+B}} = 2.18$. Finally, the results are summarized in Table 8.1, obtained in the Au+Au at $\sqrt{s_{\text{NN}}} = 200\text{ GeV}$ dataset.

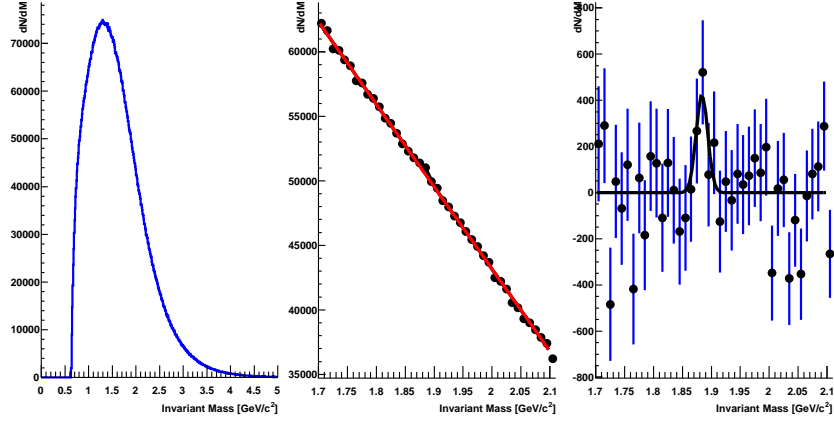


FIG. 8.4: D^0/\bar{D}^0 Invariant mass yield plots obtained with $\Delta\phi = \pi$ cut and Cutset b. *Left*: Invariant mass yield (blue). *Center*: Primary background subtraction along with polynomial (red) and gaussian fit (black). *Right*: Subtracted invariant mass yield with gaussian fit. The signal observed is 2.18σ . The mean value from the fit is $1.883\text{ GeV}/c^2$ and the $\sigma = 10\text{ MeV}/c^2$.

TAB. 8.1: D^0 invariant mass along with σ and significance of the signal for each $\Delta\phi$ azimuthal correlation in the *Btag* and the Minimum biased events for the Au+Au dataset at $\sqrt{s_{\text{NN}}} = 200\text{ GeV}$. Let us also mention that for the e - D^0 correlation method, the unlike sign pairs e - K are selected.

| $\Delta\phi$ | D^0 mass [GeV/c^2] | σ [MeV/c^2] | significance: $\frac{S}{\sqrt{S+B}}$ |
|--------------|---------------------------------|-------------------------------|--------------------------------------|
|--------------|---------------------------------|-------------------------------|--------------------------------------|

| <i>Minimum Bias</i> | | | |
|---------------------|-------------------|--------------------------|------|
| n/a | 1.884 ± 0.004 | 11.0 ± 0.4 | 3.71 |
| | | <i>Btag</i> trigger data | |
| 180° | 1.883 ± 0.002 | 10.0 ± 0.1 | 2.18 |

Chapter 9

Results in p+p and d+Au collisions at $\sqrt{s} = 200 \text{ GeV}$

The main focus of this chapter is the results obtained during run VIII, in p+p and d+Au datasets at $\sqrt{s} = 200 \text{ GeV}$. We describe the various cuts that are implemented and present the invariant mass plots for each azimuthal $\Delta\phi$ case.

9.1 Introduction

For the year 2008, the ensemble of the silicon detectors was removed, allowing the *low mass* run to be performed. In the absence of Silicon detectors, let us mention that no microvertexing technique will be used in the analysis for the current dataset. For the p+p around $27.6 \cdot 10^6$ event were taken. In particular the *physics* datastream dispatched into the following trigger setup names [Dunlop 08b]:

$\sim 24.4 \cdot 10^6$ events in `ppProduction2008`; and

$\sim 0.8 \cdot 10^6$ events in `ppProduction2008-2`.

For the d+Au case, the total number of events is $\sim 99 \cdot 10^6$. The *physics* datastream is divided accordingly into:

$\sim 62.9 \cdot 10^6$ events in `production_dAu2008`; and

$\sim 0.68 \cdot 10^6$ events in `production_mb2008`.

9.2 Applied Event Cuts

9.2.1 Primary z -Vertex Cut

Concerning the z component of the primary vertex of the event, a cut keeping the events that comply with the $|z\text{-vertex}| < 20 \text{ cm}$ is applied, as can be seen in Figures 9.1. For the p+p dataset, 8646010 events were analyzed, with only 2243256 passing the z -vertex cut and finally 81129 were kept. Concerning the d+Au dataset, a portion of 196334 events were selected, after processing in total $\sim 13 \cdot 10^6$ and only 196334 passing the z -vertex cut.

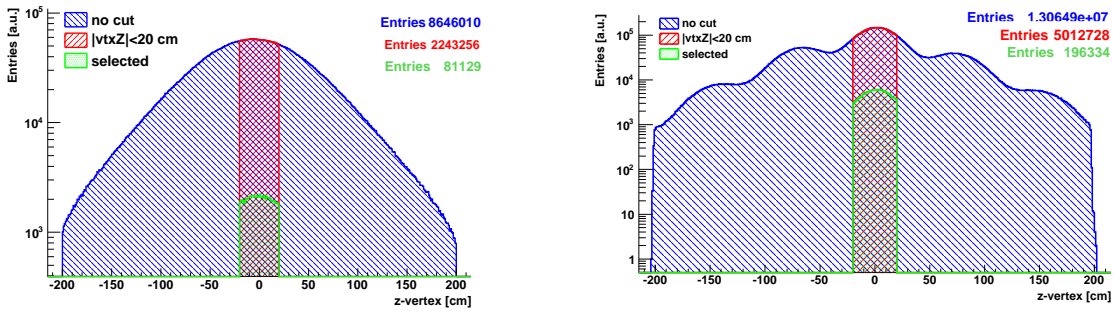


FIG. 9.1: Distribution of the primary vertex z component for the run VIII at $\sqrt{s} = 200 \text{ GeV}$. All events (blue), $|z\text{-vertex}| < 20 \text{ cm}$ (red) and selected (green) events. *Left:* For the p+p run. *Right:* For the d+Au run.

9.2.2 BEMC Energy Threshold

The cut on the transverse energy E_{T} of the BEMC towers is applied, complying with the values of Table 3.3. In specific for the p+p run the values of the energy threshold are $E_{\text{T}} \geq \{2.6, 3.6\} \text{ GeV}$, whereas for the d+Au the values are $E_{\text{T}} \geq \{2.6, 3.6, 4.3, 8.4\} \text{ GeV}$ depending on the specific trigger demand. Concerning the track cuts applied for the electron identification, the latter are mentioned in Section 3.5.

9.3 Applied Track Cuts

9.3.1 Track Quality Cuts

In order to ensure good quality of tracks, we select tracks are within $|\eta| < 1$, and concerning the number of the points in the TPC for each (3.2) is respected. Let us also note that we are using the *global* tracks as stated in Appendix E.

9.3.2 Particle Identification Cuts

The identification of hadron into K and π , is performed by selecting tracks that comply with the $\frac{dE}{dx}$ cut described in Section 3.6. For the kaon candidate, a supplementary cut on is also imposed, based on the charge demand of the hadron to be equal to the electron charge. The latter method is presented in Section 1.13. The values for the $\frac{dE}{dx}$ comply with (9.1).

$$|nSigmaKaon| < 2 \text{ and } |nSigmaPion| < 3 \quad (9.1)$$

9.4 Invariant Mass Plots

9.4.1 Results in p+p

Using the $\Delta\phi = 0$ (Figure 9.2), $\Delta\phi = \pi$ (Figure 9.3) and no $\Delta\phi$ cut as shown in Figure 9.4, we obtained the results presented in the following paragraphs.

Event Cut with $\Delta\phi = 0$ cut

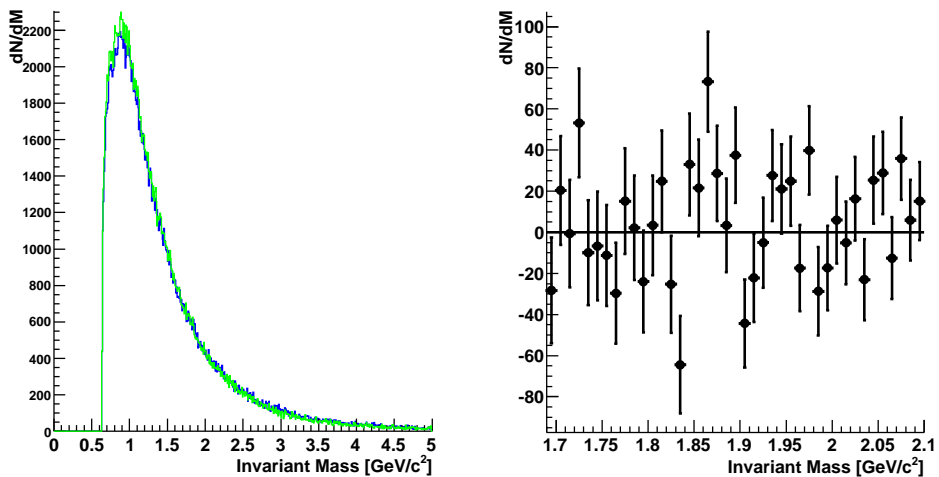


FIG. 9.2: D^0/\bar{D}^0 Invariant mass yield plots obtained with $\Delta\phi = 0$ cut. *Left:* $K^-\pi^+ / K^+\pi^-$ invariant mass yield (blue) and same-sign $\sqrt{K^-\pi^- \otimes K^+\pi^+}$ yield (green). *Right:* Subtracted invariant mass yield.

Event Cut with $\Delta\phi = \pi$ cut

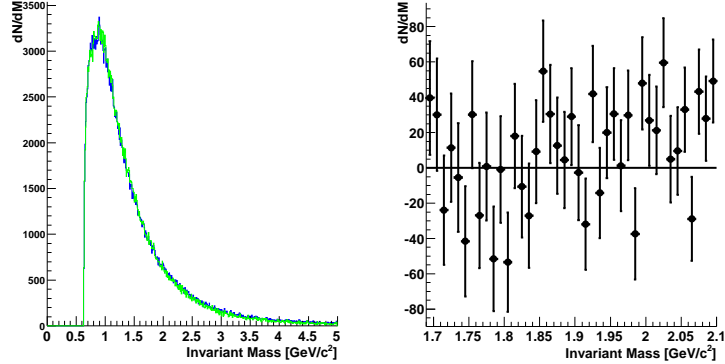


FIG. 9.3: D^0/\bar{D}^0 Invariant mass yield plots obtained with $\Delta\phi = \pi$ cut. *Left:* $K^-\pi^+/K^+\pi^-$ invariant mass yield yield (blue) and samesign $\sqrt{K^-\pi^- \otimes K^+\pi^+}$ (green). *Right:* Subtracted invariant mass yield.

Event Cut with no $\Delta\phi$ cut

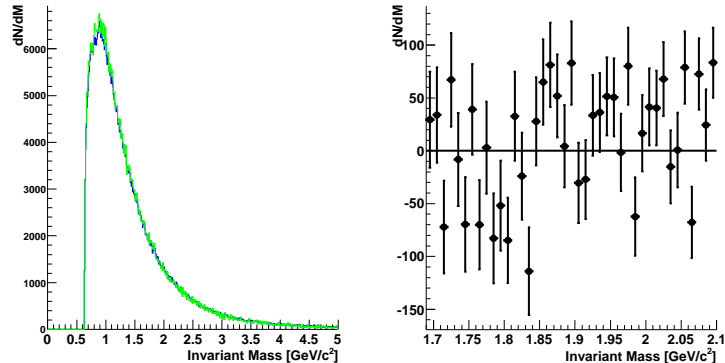


FIG. 9.4: D^0/\bar{D}^0 Invariant mass yield plots obtained and no $\Delta\phi$ cut. *Left:* $K^-\pi^+/K^+\pi^-$ invariant mass yield yield (blue) and samesign $\sqrt{K^-\pi^- \otimes K^+\pi^+}$ (green). *Right:* Subtracted invariant mass yield.

9.4.2 Results in d+Au

Using the $\Delta\phi = 0$ (Figure 9.5), $\Delta\phi = \pi$ (Figure 9.6) and no $\Delta\phi$ cut (Figure 9.7), we obtained the results shown in the following paragraphs. The samesign background that was used is $\sqrt{K^-\pi^- \otimes K^+\pi^+}$. Additionally the rotational background (at 180°) is presented as well in Figure 9.7.

Event Cut with $\Delta\phi = 0$ cut

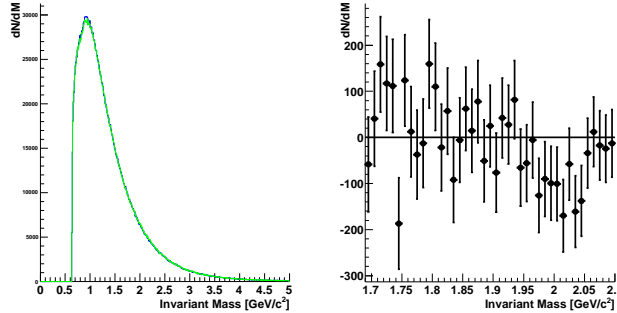


FIG. 9.5: D^0/\bar{D}^0 Invariant mass yield plots obtained with $\Delta\phi = 0$ cut. *Left:* $K^-\pi^+/K^+\pi^-$ invariant mass yield (blue) and samesign $\sqrt{K^-\pi^- \otimes K^+\pi^+}$ yield (green). *Right:* Subtracted invariant mass yield.

Event Cut with $\Delta\phi = \pi$ cut

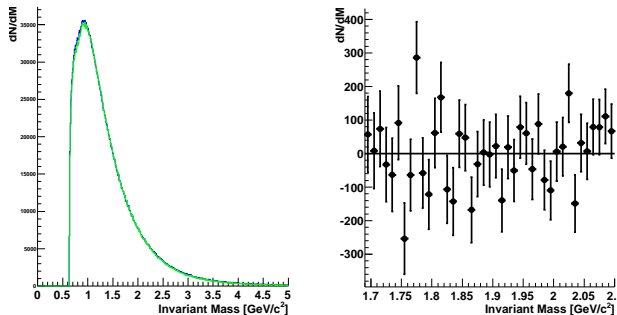


FIG. 9.6: D^0/\bar{D}^0 Invariant mass yield plots obtained with $\Delta\phi = \pi$ cut. *Left:* $K^-\pi^+/K^+\pi^-$ invariant mass yield (blue) and samesign $\sqrt{K^-\pi^- \otimes K^+\pi^+}$ yield (green). *Right:* Subtracted invariant mass yield.

Event Cut with no $\Delta\phi$ cut

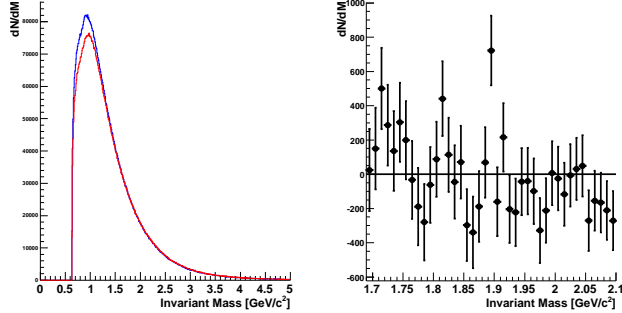


FIG. 9.7: D^0/\bar{D}^0 Invariant mass yield plots obtained and no $\Delta\phi$ cut. *Left:* $K^-\pi^+/K^+\pi^-$ invariant mass yield (blue) and rotational yield at 180° (red). *Right:* Subtracted invariant mass yield.

9.5 Discussion

The results obtained with the p+p at $\sqrt{s} = 200 \text{ GeV}$ case of year VIII did not contain the microvertexing technique, since the silicon detectors were taken out of the run. Concerning the case of the $\Delta\phi = 0$ and like sign charge demand (cf. Table 1.2) between the trigger particle and the kaon candidate, ($e-K$), it is obtained a signal of $\frac{S}{\sqrt{S+B}} = 1.18$. The mean value is $(1.873 \pm 0.005) \text{ GeV}/c^2$ and the $\sigma = (10.0 \pm 0.1) \text{ MeV}/c^2$.

For the second colliding species of year VIII (Table 2.1), namely the d+Au at $\sqrt{s} = 200 \text{ GeV}$, it was obtained by using a rotational background subtraction (as described in Section 3.9.2), a signal is with significance $\frac{S}{\sqrt{S+B}} = 2.10$. In the latter case the same sign charge demand was imposed on the $e-K$ pair, for the kaon candidate selection. Additionally no cut on the $\Delta\phi$ angular correlation was implemented. The above cuts result into the mean value of $(1.896 \pm 0.003) \text{ GeV}/c^2$ and the $\sigma = (11.0 \pm 0.2) \text{ MeV}/c^2$. The above results are summarized in Table 9.1.

TAB. 9.1: The D^0 invariant mass along with σ and the significance of the signal for each $\Delta\phi$ azimuthal correlation and for like sign charge demand for the $e-K$ pairs for the p+p and d+Au at $\sqrt{s} = 200$ GeV.

| $\Delta\phi$ | D^0 mass [GeV/c ²] | σ [MeV/c ²] | significance: $\frac{S}{\sqrt{S+B}}$ |
|--------------|----------------------------------|--------------------------------|--------------------------------------|
| n/a | 1.896 ± 0.003 | 11.0 ± 0.2 | 2.10 |
| 0° | 1.873 ± 0.005 | 10.0 ± 0.1 | 1.18 |

Chapter 10

Novel SSD Cluster Finder

In this chapter it is presented a new Cluster Finder for the Silicon Strip Detector, utilizing the Au+Au dataset at $\sqrt{s_{\text{NN}}} = 200 \text{ GeV}$ (run VII) data. A short description of the definitions of the pedestals and the subtraction of the noise for the ladders is also presented as well. The current Cluster Finder along with the novel cluster finding method are presented. Finally a comparison of the results obtained with the two methods, is performed as well.

10.1 Introduction

The Silicon Strip Detector was physically present in run V, run VI and run VII (Cu+Cu, p+p and Au+Au at $\sqrt{s_{\text{NN}}} = 200 \text{ GeV}$, respectively). The detector was taken under consideration for the production of data, only in the Cu+Cu and Au+Au case. Concerning the principle of the particle detection via semi-conductivity, the latter is presented in Section 2.8 and a thorough description of the detector can be found in Section 2.10. It is reported [Bouchet 07] that the number of charge clusters in p and n side exhibit an asymmetry. In specific, in the n side the the number of clusters is lower than the one recorded from the p side. This is due to the high noise that the n side presents. Since the standard cluster finder combines the information from both sides in order to deduce a cluster, there is an impact on the overall efficiency of the detector.

10.2 Calculation of the Noise

During a RHIC period of data acquisition, and in the absence of the beam, a dedicated run on the SSD noise is being performed, registering the values of all the strips, over N events (usually $N=10^3$). The calculation of the pedestal hence is being performed as the mean value $p_i = \langle x_i \rangle$ of the distribution of the signal of the i strip over these N events and expressed in (10.1). Let us consider the signal value of the i strip for the k

event: x_i^k (in ADC).

$$p_i = \frac{1}{N} \sum_{k=1}^N x_i^k \quad (10.1)$$

Furthermore, the noise n_i for the i strip is calculated as the standard deviation of the distribution of the ADC signals over the sample of the N events. In mathematical form the latter statement is expressed by (10.2).

$$n_i = \sqrt{\frac{1}{N-1} \sum_{k=1}^N (x_i^k - p_i)^2} \quad (10.2)$$

During the STAR data acquisition period, the values of the pedestal are stored until the next SSD dedicated run (*SSD pedestal run*) and an *online* pedestal subtraction is being performed, according to (10.3). Let x'_i be the value of the i strip signal after the subtraction.

$$x'_i = x_i - p_i > 0 \quad (10.3)$$

The values of the noise n_i are stored for each strip separately in order to be used *offline*. Also let us note that the *zero suppression* takes place for each raw ADC value.

$$x'_i > \xi \quad (10.4)$$

In (10.4), the value of ξ differs depending on the dataset. In particular for the Cu+Cu—run V—it was used $\xi = 6$ ADC whether for the Au+Au—run VII—the value was raised to $\xi = 7$ ADC.

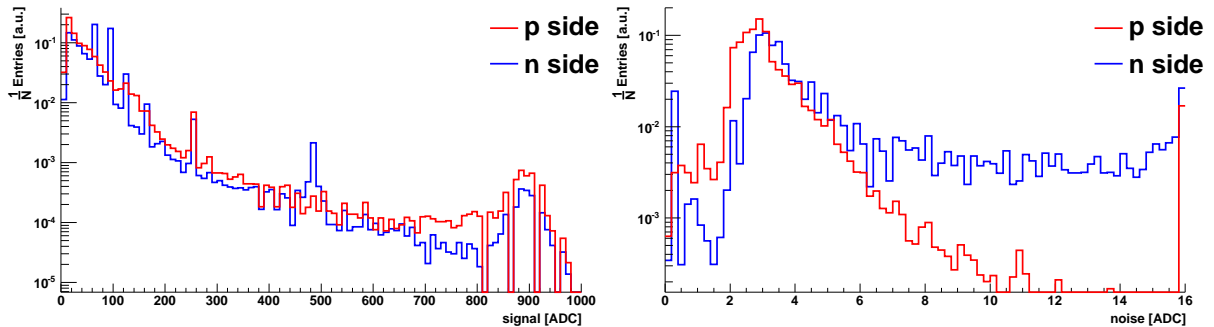


FIG. 10.1: Cumulative distributions of signal (*left*) and noise (*right*) values for the p (red) and n (blue) side of the SSD, normalised to unity. Data is taken from $N = 10000$ events of run 8105011 of the Au+Au at $\sqrt{s_{\text{NN}}} = 200$ GeV dataset.

10.3 Standard Cluster Finder

We refer to the Standard Cluster Finder, as the method that the current STAR Software is using in order to look for clusters in both sides of the detector. In particular the algorithm consists of the following steps.

- i. The method is applied first on each wafer by seeking on both sides (p and n);
- ii. only strips that satisfy $\frac{S}{N} \geq 5$, with S and N be the signal and noise for each strip;
- iii. let us consider i_c a fired strip. Then the i_{c-1} and i_{c+1} neighboring strips are also checked with a demand on the ratio of *signal to noise* comply with the $\frac{S_{i_c \pm 1}}{N_{i_c \pm 1}} < \frac{S_{i_c}}{N_{i_c}}$; and
- iv. the clusters are combined in both sides of the wafer, and accepted only if the clusters in the opposite sides (p and n) are associated.

Let us also make a final note concerning the last argument. In particular, the association of the clusters in both sides of the detector, is performed taking into account not only the topological hits (on p and n sides), but also a supplementary cut on the *charge matching* $Q_n \simeq Q_p$ is performed. It is expected that the particle passing through the SSD detection module, will deposit approximately the same amount of energy creating the same amount of electron-holes on both sides. By using this method it is also ensured the rejection of the ambiguous associated clusters, called *ghosts*.

10.4 TSpectrum ROOT Class

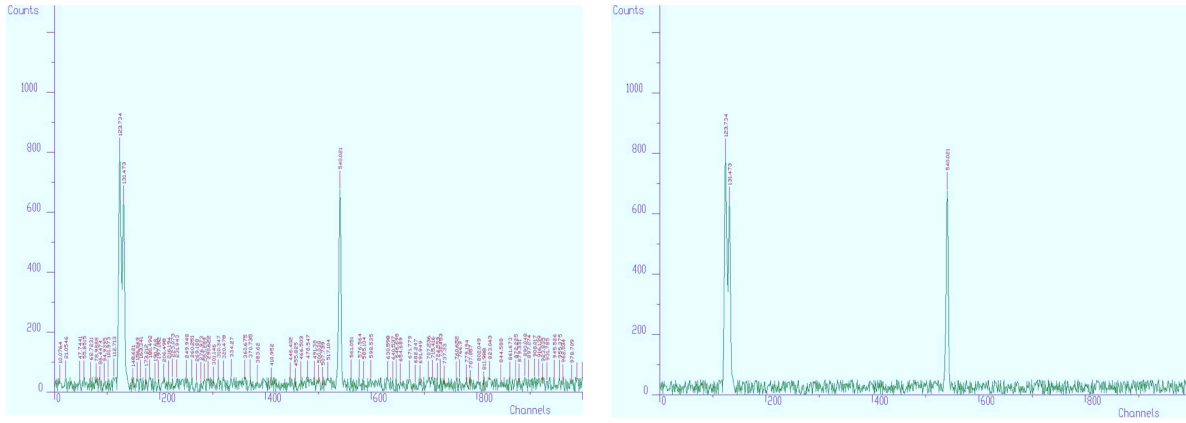
The main core of the novel cluster finding method is the algorithm implemented in the **TSpectrum** ROOT Class [Brun 06]. In particular, given a specific spectrum, the algorithm utilizes the Markov chain and seeks for peaks within a predetermined sigma and threshold [Morháč 97b] interval. A Markov chain is a collection of Markov processes $\xi_n(t)$, where $n = 1, 2, \dots, \infty$ with the property that for a given present condition, the future is conditionally independent of its past [Papoulis 02]. The latter statement, is expressed in terms of probability \mathcal{P} in (10.5). Therefore, if we consider for the time sequence that $t_{n-1} < t_n$:

$$\mathcal{P}[\xi(t_n) \leq \xi_n | \xi(t), t \leq t_{n-1}] = \mathcal{P}[\xi_i(t_n) \leq \xi_n | \xi(t_{n-1})] \quad (10.5)$$

However in the case where we have noisy data the number of peaks in the spectrum can be enormous—approaching the number of strips. The case of the SSD detector

and especially of the n side of the wafers, exhibits such a behavior, as described in Appendix F. In the above mentioned case, it is therefore necessary to impose a demand on the threshold value of the peak and to consider only the peaks higher than this threshold. In Figure 10.2 it is shown the case where only three peaks were identified, by imposing a threshold at 50 units. Let us consider a cluster of channels that build up the peak. Also by y_c we denote the value of the center of the peak, that is also the higher signal. The cut is then expressed by (10.6). The difference between the value in the center of the peak and the average value of the two symmetrically positioned channels must be greater than the threshold. The peak is ignored otherwise.

$$y_c - \frac{1}{2}(y_{c-1} + y_{c+1}) \geq \text{threshold} \quad (10.6)$$



- ii. the standard deviation should be inside the interval $\sigma \in (0, 1/\sqrt{12}]$ —following the constant distribution—as stated Appendix C; and
- iii. the mean value of the fit x'_c should be *close* to the position of the central strip of each cluster, meaning that $|x'_c - x_c| \simeq 1\text{--}2$ [strips].

Having imposed the above fitting parameters, the cluster is fitted and the gaussian integral A along its error δA , in the area $[x' - 3\sigma, x' + 3\sigma]$ is also being calculated. The cluster of strips is accepted only if the (10.7) demand is fulfilled.

$$\frac{A}{\delta A} \geq 5 \quad (10.7)$$

10.6 Comparison Methodology

In order to obtain statistics, we performed the analysis on the following runs, by examining the SSD hits obtained on an event-by-event basis using both methods. In particular the low luminosity run was used: 8120057 [DePhillips 07], for the current comparison study. In Figure 10.3 it shown the fired strips of the wafer 14, ladder 01, both sides (p and n side). In the same Figure it is also presented the comparison of the two methods, running on the same wafer. The *old* method Section 10.3 finds one hit when at the same time the *new* cluster finder, described in Section 10.5 finds 3 hits. Let us also mention that this result is obtained with 1 event. In order to enhance the statistics, the method is repeated over a total number of $N = 10000$ events contained in the above low luminosity run. The results obtained with both methods are discussed in the Section 10.7 and a graphical comparison can be found in Figure 10.4.

10.7 Discussion

By applying both methods, namely the Standard Cluster Finder (cf. Section 10.3) and the novel method involving the **TSpectrum** (cf. Section 10.5), we obtained the results over 10^3 events from the *low luminosity* run 8120057 during the Au+Au at $\sqrt{s_{\text{NN}}} = 200$ GeV. In Figure 10.4 it is shown the correlation between the clusters found by both methods. By performing a linear fit $y = ax$ on the scatter plot, we obtain the result that the clusters found with the novel method. Since the two SSD sides (p and n), exhibit different signal-to-noise ratio (Appendix F), we can separate the sides and perform a fit on the scatter plot of the clusters found by the two different methods. In addition the red line shows the case where the slope is equal to unity $y = x$. The result of the fit is that the new method finds approximately 43% more clusters than the old method for the n -side and 51% for the p -side. Of course the current comparison study is performed on the raw hits recorded by the detector and not by the hits that

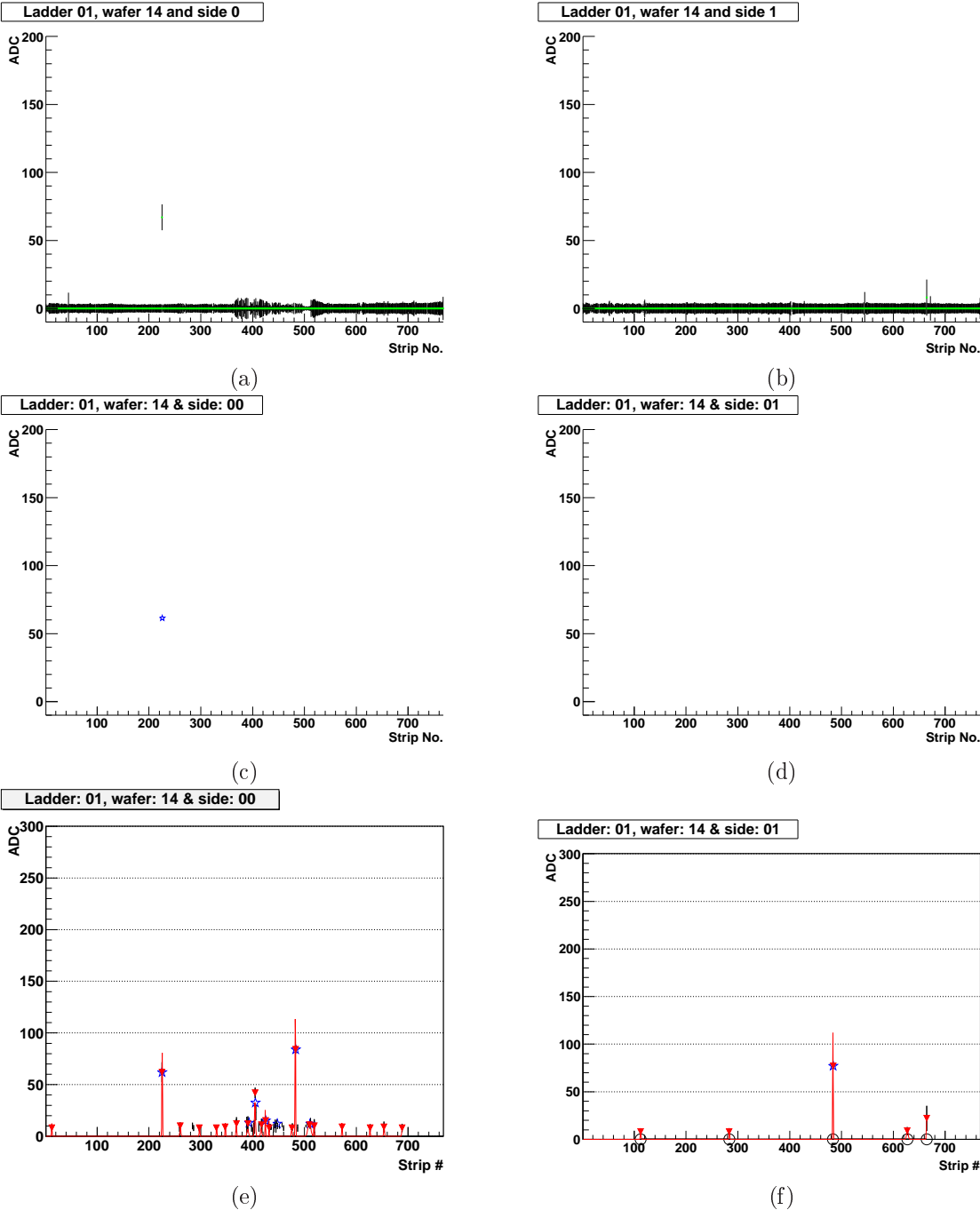


FIG. 10.3: Fired SSD strips for wafer 14, ladder 01, sides p and n . for 1 event taken from the run 8120057. *Left:* p -side. *Right:* n -side. *Upper:* The signal of each strip (green) along with the noise (black) error bars, are drawn. *Middle:* Cluster found by SCF (c)–(d), marked in blue star. *Bottom:* Plots (e)–(f), Novel Cluster Finder results, depicting the peaks found with TSpectrum (red), passing partial requirements (blue) and the selected ones (black circles along the x axis).

are combined with the rest of the detector tracking, such as the TPC and SVT. In the future plans it is included the analysis with the Monte Carlo and the re-production of a portion of the Au+Au (run VII) dataset with the Novel Cluster Finder.

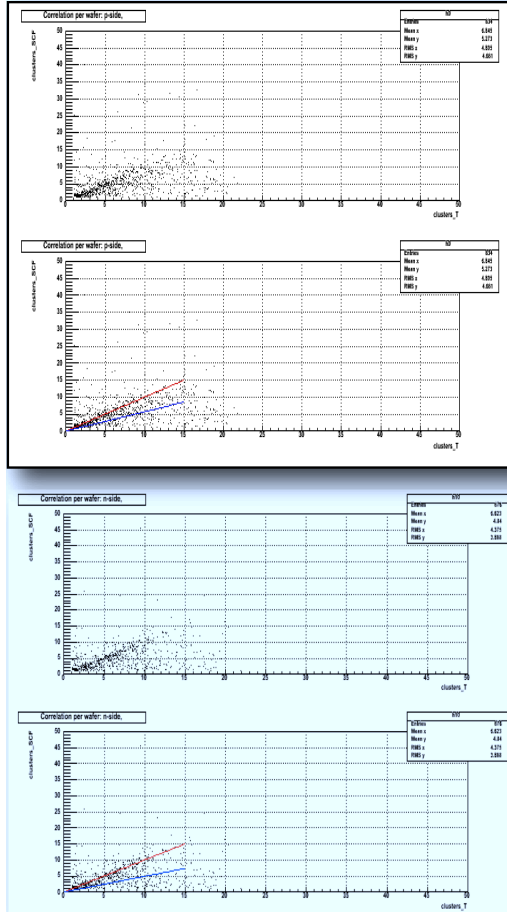


FIG. 10.4: Correlation of the number of the clusters obtained by both methods. Along with a linear fit (*blue*). The *red* line indicates the linear function with slope=1. *Upper*: *p*-side. *Lower*: *n*-side. The fitting result yields approximately 43% more clusters than the old method for the *n*-side and 51% for the *p*-side.

Conclusion

One of the most important findings of the experiments at RHIC is the discovery of anomalous quenching of jets when passing through the dense and hot matter build in nucleus nucleus collisions. This quenching is expected indeed from the theory to depend on the mass of the quark that pass through the medium, and in particular it is expected less quenching for heavier masses. The jet quenching can offer a measure for the gluon density of the partonic medium traversed by the quark. In order to extract this density the model expectation must be well understood and to be compared to different data leading to a coherent picture. An important way to compare model and data is to investigate the dependence of the jet quenching on the quark masses in the data and perform a comparison to the theory.

The heavy quarks (charm and beauty together) when measured through the non-photonic electron yields in heavy ion reactions at $\sqrt{s_{\text{NN}}} = 200 \text{ GeV}$ at RHIC, exhibit a larger suppression than the one expected from the theoretical considerations [Dokshitzer 01, Djordjevic 05]. In order to comprehend this puzzle and to understand better the flavor dependence of the jet quenching, the separation of charm and beauty contributions as well as the measurement of their quenching is necessary. Next to the direct measurement of the charm, the STAR experiment is currently utilizing two methods that can allow the disentanglement of charm and beauty. In particular:

- i. The electron-hadron ($e-h$); and
- ii. the $e-D^0$ azimuthal angular correlations.

In the current work the microvertexing techniques have been developed and have been applied to the datasets from Cu+Cu and Au+Au collisions at $\sqrt{s_{\text{NN}}} = 200 \text{ GeV}$, in order to extract the D^0 signal through the reconstruction of its secondary decay vertex. Furthermore, an analysis of the $e-D^0$ azimuthal angular correlations in the datasets such as Cu+Cu and Au+Au collisions at $\sqrt{s_{\text{NN}}} = 200 \text{ GeV}$ has been performed

using the above mentioned microvertexing techniques. Concerning the secondary vertex reconstruction of the hadronic decay $D^0 \rightarrow K^-\pi^+$, the microvertexing techniques have been tested and *quality assured* by performing a Monte Carlo (MC) comparison with real data (Au+Au at $\sqrt{s_{\text{NN}}} = 200 \text{ GeV}$). In particular, the study of the significance of the D^0 signal as a function of several cuts on microvertexing variables, has been performed utilizing the signal extracted from the MC data sample and the background from the real data. The study on the MC sample, leads to the optimization of the cuts and the definition of several cut sets which are applied to the data.

The resolution of the STAR detector including all silicon detectors (SVT+SSD), is approximately $250\text{--}300 \mu\text{m}$ for the distance of closest approach to the primary vertex (DCA) of the tracks, and therefore larger than the mean decay length—in the lab frame: $\beta\gamma c\tau$ —of the D^0 of $\sim 70 \mu\text{m}$ for the mean momentum of the D^0 in the examined collisions (while $c\tau = 120 \mu\text{m}$). Despite the above statement, it has been shown that the signal to background ratio for the $D^0 \rightarrow K^-\pi^+$ decay, is increased without losing significant portion of the signal for the particular cuts. For example cuts on the D^0 decay length, the DCA of the D^0 to the primary vertex as well as the DCA of the decay daughters to the primary vertex, both in the transverse (DCA_{xy}) and longitudinal (DCA_z) components.

As a result, we observe a D^0 signal of significance $\frac{S}{\sqrt{S+B}} = 3.71$ in a data sample of $2.5 \cdot 10^6$ Au+Au events that were collected after passing the minimum bias trigger, demanding at least one hit in the silicon detectors (SVT+SSD) and implementing the microvertexing cuts in order to reduce the background. The significance is found to increase as expected for the real signal with the number of events. Let us also note that in the minimum biased events, no electron (trigger particle) has been required to be present.

On the other hand, in datasets such as the Cu+Cu and Au+Au, events with a high transverse momentum (p_T) trigger particle (e^\pm) have been selected by the online Barrel Electromagnetic Calorimeter (BEMC) trigger (namely *High Tower* and *Btag* triggers for the Cu+Cu and Au+Au datasets, respectively). We have used the electromagnetic calorimeter of STAR to identify the electrons and to reject a large part of the *photonic* background coming from the neutral meson decays (such as π^0 and η) as well as photon conversion $\gamma \rightarrow e^-e^+$ in the material (hence the term *photonic*). The D^0 invariant mass peak is then reconstructed by the implementation of the secondary vertex reconstruction and by the application of the cuts that were mentioned above. After the identification of the electron e and the D^0 candidate (in the form of a $K\pi$ pair), we apply cuts on the relative azimuthal angle ($\Delta\phi$) of the electron and the D^0 candidates found. In particular, for the electrons with the same sign as the daughter K coming from the decay of the D^0 a relative azimuthal angle difference of $\Delta\phi \simeq 0$ is expected mainly from the beauty ($b\bar{b}$) direct production; whence a relative azimuthal angle difference around $\Delta\phi \simeq \pi$ is expected from the charm ($c\bar{c}$) direct production.

As a result we have observed the D^0 signals correlated with a high- p_T electron found in these events which exhibit a significance up to $\frac{S}{\sqrt{S+B}} = 2.2$. The number of the *Btag* events in the Au+Au collisions at $\sqrt{s_{NN}} = 200$ GeV examined is about $1.5 \cdot 10^6$ events. After the applied event cuts, the number of the events analyzed in the Au+Au collisions (*Btag* trigger) is ~ 90000 , while the same number is ~ 26000 for the Cu+Cu collisions (*High Tower* triggered dataset). As a consequence, the sample with the tagged electrons is much smaller than the Au+Au events collected with the minimum bias trigger. In addition to this, the Au+Au minimum bias data sample is superior when compared to the Cu+Cu data sample as far as the acceptance of the BEMC is concerned. In particular, during the Cu+Cu data, only half of the BEMC was installed, (pseudorapidity acceptance: $0 < \eta < 1$), as opposed to the Au+Au full acceptance ($-1 \leq \eta \leq +1$).

Several sets of cuts have been investigated and we have observed the D^0 signals which are candidates for the direct charm and beauty production. For example the observed D^0 signal appears for the relative azimuthal angles of the $\Delta\phi = \pi$ between the e and the D^0 for the like sign (LS) electron and kaon, in which the direct charm production ($c\bar{c}$) is expected to be the main source as shown in the Cu+Cu analysis dataset. For the Au+Au dataset sample, we have presented results exhibiting a D^0 signal appearing for the relative azimuthal angles of $\Delta\phi = 0$ between e^\pm and D^0/\bar{D}^0 . In the latter case for the unlike sign (ULS) electron and kaon, the direct beauty production ($b\bar{b}$) is considered to be responsible. Further analysis on those signals is needed with the use of corrections estimated with Monte Carlo D^0 embedded in real Au+Au events, which are at the moment* under quality assurance in STAR and will be very soon ready to use. The embedding will allow the D^0 signals observed in the Au+Au events to be corrected for the acceptance and efficiency losses and an estimation of the cross sections to be performed as well.

The results obtained in the current analysis of Cu+Cu and Au+Au collisions with the microvertexing methods were possible due to the excellent performance of the Silicon Strip Detector (SSD) of STAR, without which no reliable Silicon Vertex Tracker hit reconstruction is possible, due to the large number of *ghosts*. In the current work, we have furthermore analyzed the $e-D^0$ azimuthal angular distributions in p+p collisions at $\sqrt{s} = 200$ GeV. We have observed the D^0 signal for both the charm and the beauty, as it was expected in the azimuthal correlations with the electrons. These results contribute to earlier analyses of the $e-D^0$ azimuthal angular distributions in p+p collisions at $\sqrt{s} = 200$ GeV in which it has been found that the beauty contribution increases with the p_T and becomes comparable to the charm contribution around $p_T \sim 5.5$ GeV/c. The beauty contribution is found to be compatible to FONLL calculations within the uncertainties. This is an important feature for the comprehension of the jet quenching in heavy ion collisions and in particular it demonstrates that the jet quenching puzzle

*As of October 22, 2010.

in heavy ion data, cannot be linked to an absence of a large beauty contribution in p+p data in that transverse momentum (p_T) range.

Concerning the technical part of the current work, it is dedicated to a new peak finding method for the Silicon Strip Detector (SSD) including the TSpectrum ROOT Class. In particular the novel method, seeks for clusters in both sides (p and n) of the detector without the demand for charge correlation and is using a different peak finder method than previously. A preliminary result of this new method is that about 40% more signal peaks are found with this method as compared to the previous one. This study is performed using data from run Au+Au at $\sqrt{s_{NN}} = 200 \text{ GeV}$ (run VII). The new method can be used to reproduce the already taken data and is of great relevance for the future Heavy Flavor Tracker, in which the third layer will be the SSD.

From the 2009–2010 run of STAR the full TOF detector installation was achieved first time in STAR and will allow the better particle identification from which charm and beauty searches will be benefited considerably. In addition to this, the future STAR Heavy Flavor Tracker (HFT) [Bouchet 09], currently under development is going to improve significantly the momentum resolution and will lead to a much better secondary vertex reconstruction resolution as compared to the current silicon detector of STAR used in the present thesis, which was not initially conceived and optimized for heavy flavor studies.

The excellent capabilities of the SSD detector proven in the present and other STAR analyses [Bouchet 07], lead to the inclusion of the silicon strip detector of STAR in the future HFT. The future silicon tracker is conceived especially in order to perform the application of the microvertexing techniques for the charm and the beauty identification. The new developments achieved in this thesis, namely the successful application of the microvertexing techniques in heavy ion environment, the extraction of the D^0 signal in heavy ion collisions using such methods and the developments on a new peak finder for the SSD detector, demonstrate that charm and beauty measurements can be performed in heavy ion collisions despite the high track density pushing to the limits of the present silicon detector of STAR to successfully perform physics beyond its initial design, and which are of great relevance for the future HFT detector.

Résumé

12.1 Soupçon de théorie de physique des noyaux

Les collisions d’ions lourds ultra-relativistes permettent d’élargir nos connaissances sur la matière dans des domaines d’énergie et de densité très élevés. Selon la théorie du *Big Bang*, ces conditions ont été celles de l’Univers peu de temps après sa formation, alors que son âge était inférieur à 10^{-5} seconde. Il est très intéressant de pouvoir étudier ces premiers instants de l’Univers. Les réponses à des questions fondamentales sur l’interaction forte, la nature du vide, la brisure de symétrie chirale et l’origine de masse pourraient venir de cette recherche. Elle permet en particulier de confronter les résultats de la théorie actuelle qui décrit l’interaction forte, la Chromodynamique Quantique (QCD: *Quantum Chromodynamics*), avec des observations expérimentales. L’interaction forte—une des quatres forces fondamentales (cf. Tableau 1.1)—est décrite par cette théorie. C’est une théorie de jauge non-abélienne, selon laquelle le champ d’un fermion est essentiellement basé sur le groupe de symétrie de couleur $SU(3)$. Un nouveau degré de liberté des quarks, la charge de couleur, a été introduit après la découverte expérimentale du baryon Δ^{++} . Ce baryon, étant composé de 3 quarks up, possède un spin totale de $J = 3/2$. Comme conséquence la fonction d’onde était symétrique. Pour établir les lois imposées par la statistique de Fermi-Dirac, la fonction d’onde doit être antisymétrique. Pour récupérer la propriété d’antisymétrie de la fonction d’onde de ce baryon il a été nécessaire l’introduction d’un nouveau degré de liberté, la couleur. La densité lagrangienne de Dirac permet de décrire la dynamique des champs de quarks libres avec l’équation (1.1). Les termes de couplages dans ce lagrangien permettent les interactions entre le quark-gluon et même entre le gluon-gluon. Le dernier couplage explique le caractère non-abélien. En effet, ce type d’interaction est autorisé puisque les gluons possèdent une charge de couleur. Cette propriété se manifeste par l’existence de couplages de trois ou quatre gluons. L’interaction forte présente une comportement non-linéaire décrite par (1.3) et permet d’expliquer des

phénomènes tels que le confinement et la *liberté asymptotique* à courte distance et le confinement des quarks à grande distance. La constante de couplage α_s de l'interaction forte est introduite dans le potentiel entre deux quarks cf. (1.3). A nos jours, la valeur de la constante de couplage est prédictive à partir de sa valeur mesurée à la masse du Z^0 $\alpha_s(M_Z) = 0.1183 \pm 0.0027$ [Bethke 03].

L'étude de la QCD élargit donc par cet intermédiaire notre compréhension de la théorie dans des conditions de températures et de densités élevées. Cependant, on peut donner les éléments qui permettent de supposer l'existence d'un état déconfiné de la matière, le plasma de quarks et de gluons (PQG)*. La liberté asymptotique a conduit à supposer l'existence d'un état de la matière dans lequel les partons (quarks et gluons) sont déconfinés, c'est à dire qu'ils peuvent se déplacer librement, cet état est appelé le PQG. Comme déjà mentionné, la matière nucléaire dans les conditions habituelles (e.g. à l'intérieur d'un proton) est confinée—est constituée de partons (quarks et gluons) restreintes à l'intérieur de hadrons—and est caractérisée par une valeur importante de la constante de couplage α_s . Le libre parcours moyen des partons est toujours inférieur à la taille typique d'un hadron (de quelques fm). Dans des conditions extrêmes de température et de densité, la matière hadronique est susceptible de subir une transition de phase vers un état déconfiné. De fait, l'étude du plasma de quarks et de gluons est liée à l'étude des collisions d'ions lourds ultra-relativistes et a fortement motivé celles-ci. Ces collisions seraient en effet le seul moyen permettant de reproduire et d'observer cet état.

Le modèle standard englobe la théorie décrivant l'interaction forte qui lie les quarks entre eux, la QCD. La QCD tire son nom de l'existence d'une charge de couleur rouge, verte ou bleue dans chaque quark. De la même manière que les charges électriques de signes opposés s'attirent, cette charge de couleur attire les quarks de couleurs différentes. La QCD explique ainsi notamment la formation des hadrons. Ce terme désigne l'ensemble des particules qui sont formées par des quarks. Deux types de hadrons sont observés dans la nature. Les mésons formés par un quark lié à un anti-quark, un état lié $q\bar{q}$ et les baryons composés de trois quarks liés, cependant un état qqq . La QCD traite directement des quarks et des gluons, les constituants élémentaires, et de leurs interactions.

L'étude d'un système formé par ces composants élémentaires nécessite l'utilisation de la méthode de mécanique statistique. Elle permet de définir l'état macroscopique du système sans être obligé de connaître son état microscopique, fait qui est dans la plupart des cas difficile ou impossible à faire avec la QCD. La description statistique met à disposition des variables globales telles que le volume V et l'énergie E du système ainsi que certaines autres quantités conservées. Un système relativiste de quarks et de gluons engendre la production et l'annihilation constante de particules. L'ensemble grand canonique est donc utilisé pour la description du système, en permettant au

*ou bien *Quark Gluon Plasma* (QGP) en anglais.

nombre de particules de varier. Les paramètres de contrôle sont alors le volume V , la température T et le potentiel chimique μ . Ce dernier représente l'énergie qu'il faut apporter au système pour lui ajouter une particule. L'ensemble des états de la matière peut désormais être répertorié grâce à un diagramme de phases (T, μ) . Ce diagramme de phase (cf. Figure 1.3) définit les différentes phases de la matière et les transitions, de manière analogue au diagramme de phases de l'eau, qui donne ses trois phases: notamment la solide, la liquide et la gazeuse en fonction de la température (T) et de la pression (P). L'évolution de l'Univers peut être retracée à partir de ses premiers instants, où la température était très supérieure à T_c et où le potentiel chimique était assez faible. Durant son refroidissement, l'Univers serait sorti de la phase de QGP par une transition continue. Les noyaux des atomes, finalement formés, ont ensuite regroupé la matière nucléaire (nucléosynthèse). En dehors de cette matière nucléaire, pour des températures assez faibles et pour des potentiels chimiques supérieurs à la densité nucléaire, la matière atteindrait un état de qui on croit d'exister dans les étoiles à neutrons.

12.1.1 Le plasma des Quarks et des Gluons

Nous sommes concentrés sur la phase de plasma de quarks et de gluons. Dans cette phase, les quarks et les anti-quarks ne sont plus confinés à l'intérieur de hadrons. Ils acquièrent la possibilité de se déplacer au sein d'un champ de gluons sur des distances délimitées par la taille du système. Ce déconfinement des quarks aurait lieu dans les conditions (T, μ) délimitées. Les partons contenus dans le système doivent subir de nombreuses interactions mutuelles. Le plasma de quarks et de gluons est ainsi supposé être en équilibre thermodynamique, au moins local, justifiant la description statistique du système.

Au moment de la transition de phase hadronique vers le plasma de quarks et de gluons, le nombre de degrés de liberté du système change considérablement. Dans le même diagramme, la phase hadronique est située vers la région $T \rightarrow 0$. La libération du nombre de degrés de liberté du milieu conduit à une variation soudaine de ses caractéristiques thermodynamiques. La pression (P) et l'entropie (S) du système augmentent avec la température. Comme conséquence, lorsque la température s'approche du point critique T_c une augmentation soudaine et importante (1.4) de la densité d'énergie ε doit avoir lieu. Dans la Figure 1.4, c'est démontré l'évolution de la densité d'énergie ε du système en fonction de la température à potentiel chimique baryonique $\mu_B = 0$. Ce dernier diagramme est obtenue par les calculs de la LQCD (*lattice QCD*). Sur cette figure il y a trois scénarios différents (en fonction du nombre de saveurs: 0,2 et 3 saveurs) pour le PQG. Nous constatons, qu'autour de T_c , la densité d'énergie sous forme $\frac{\varepsilon}{T^4}$ augmente d'un ordre de grandeur en température. D'après les calculs sur réseau (*LQCD*) à potentiel chimique baryonique nul et pour 2 saveurs de quarks légers

(u et d) il été prévu que la transition de phase a lieu pour une température critique de $T_c \simeq 173$ MeV et pour une densité critique de 0.7 GeV/fm 3 . Pour une température T supérieure à la température critique $T \geq T_c$ de déconfinement, le potentiel inter-quarks est modifié par la présence de la matière déconfinée qui porte les charges de couleur. La charge de couleur de ces partons libres s'interpose entre les deux quarks et agit comme un écran. Par conséquent, le potentiel d'interaction entre les quarks est atténué, c'est l'écrantage de couleur. Les calculs obtenus par la *LQCD* ont permis d'établir le diagramme de phase de la matière hadronique pour lequel les paramètres de contrôle utilisés sont la température T et le potentiel chimique baryonique μ_B .

Le diagramme de phase

L'origine du diagramme de phase où la température et le potentiel chimique baryonique sont nuls représente le vide de la QCD. En changeant les paramètres de contrôle la matière nucléaire passe par les différentes phases décrites ci-dessous. A basse température et à bas potentiel chimique baryonique la matière nucléaire peut être décrite par un gaz de hadrons. Dans cette phase les partons sont emprisonnés sous forme de hadrons—des états liés des quarks et des gluons. Cette matière est une phase isolante de couleur car un hadron est toujours neutre du point de vue de l'interaction forte. Autrement dit, la somme des couleurs de tous les quarks contenus dans le hadron est nul (couleur blanc).

Pendant les collisions d'ions lourds ultra-relativistes ils sont produits un grand nombre de particules. Leurs multiplicités, leurs spectres en impulsion et les distributions angulaires de ces particules sont le résultat d'une convolution de phénomènes extrêmement difficiles à être dissocier. Pour cette raison, la démarche expérimentale consiste à la comparaison des résultats obtenus par les collisions d'ions lourds avec ceux d'autres types de réactions. En particulier les collisions entre protons p+p et entre un proton et un ion lourd (p+A) peuvent constituer de bonnes références pour les collisions d'ions lourds (A+A). Elles reproduisent une partie des conditions et mécanismes inhérents aux collisions A+A. Dans les collisions p+p ou bien p+A il est tr'es peu probable qu'un plasma de quarks et de gluons y soit créé.

Selon le scénario d'évolution de Bjorken (cf. Section 1.7), une collision d'ions lourds peut être illustrée par une succession de phases dans un diagramme espace-temps (t, z) , demontré à la Figure 1.5. Les différentes étapes de l'expansion du système sont représentées par des hyperboles de temps propre $f(t, z) = \sqrt{t^2 - z^2}$. A $\tau < 0$ les noyaux sont accélérés à une vitesse proche à la vitesse de la lumière. Les deux noyaux incidents prennent la forme de disques—dans le plan perpendiculaire à la direction du boost—en raison de la contraction de Lorentz. Juste après la collision, une phase de pré-équilibre durant environ $\tau_0 = 1$ fm/c est formée. Dans cette phase les multiples collisions inélastiques entre les nucléons de chaque noyau conduisent à une augmentation en termes de température. Les partons du milieu interagissent fortement

et donc les processus d'interaction peuvent être décrits par la QCD perturbative[†]. Les quarks lourds, ainsi les jets et les photons sont créés pendant cette phase. Si la densité d'énergie est supérieure à la densité d'énergie critique ε_c , le système évolue vers un milieu où les quarks et les gluons sont déconfinés. Si les conditions extrêmes sont maintenues pendant suffisamment longtemps, un équilibre thermodynamique est alors atteint et le système se thermalise pour entrer dans une phase de PQG. Notons, que la phase de thermalisation n'est pas bien comprise dans le cadre de la QCD. La durée de vie du PQG, qui dépend essentiellement de la densité d'énergie initiale et ne devrait pas excéder quelques fm. Au-delà, le système se refroidit à cause de son expansion longitudinale de nature hydrodynamique. Progressivement, les quarks et les gluons sont reconfinés à l'intérieur des hadrons.

En se refroidissant, le système subit une transition de phase à température critique $T = T_c$. Après un certain temps, puisque tous les degrés de liberté partoniques ont été confinés, le plasma disparaît complètement pour donner place à une phase purement hadronique. Le système se refroidit et évolue comme un gaz de hadrons libres dans lequel deux étapes sont bien distinguées. Dans la première, appelée le gel chimique (*chemical freeze-out*), la densité d'énergie du système est trop petite pour permettre la création de particules via des chocs inélastiques. La composition chimique du milieu est alors fixée. L'expansion et le refroidissement du système se poursuivent jusqu'à atteindre la deuxième étape, nommée le gel cinétique (*kinetic freeze-out*). Dans cette phase les collisions élastiques cessent et par conséquent les propriétés cinématiques des hadrons sont démontrées. En particulier les spectres en impulsion sont fixées. Les hadrons sont détectées par les produits de leurs désintégrations. Le temps caractéristique de la formation du gel chimique et cinétique est un point discutable. Deux cas sont envisagés. Le gel chimique et cinétique se produisent à deux instants distincts τ_{chem} et τ_{cin} ou ces deux instants sont mélangés. Les observables globales (viz. la multiplicité, l'énergie transverse à midrapidité), permettent d'obtenir l'information sur la formation et l'expansion de la collision (le paramètre d'impact, le plan de la réaction, la densité d'énergie initiale, etc.). Ces observables peuvent fournir des indications utiles concernant la possibilité pour la création du PQG.

Les signatures du PQG

Les analyses concernant l'analyse du QGP sont premièrement focalisées sur des observables sensibles à la phase de plasma de quarks et de gluons et robustes. Envisagées depuis le début des analyses de collisions d'ions lourds de hautes énergies, ces signatures devraient marquer la transition observée dans les prédictions de la *LQCD*. Même le volume et le temps de vie de l'existence de QGP sont a priori petits. Le diamètre de la zone de production de matière ne serait que de $\sim \text{fm}$ et la durée de vie

[†]la QCD perturbative fonctionne bien dans la régime des hautes énergies. En revanche, dans les basses énergies cette méthode numérique cesse d'être applicable.

de l'état déconfiné de l'ordre d'une dizaine de $\sim \text{fm}/c$. La détermination des signatures qui laissent des traces significatives est une tâche assez importante. Une certaine liste—non-exhaustive—concernant les signatures ont été proposées. Elles peuvent être classées selon les trois types suivants.

- i. La production hadronique. Dans ce cadre, on peut mentioner l'augmentation de la production de particules étranges qui était une des premières signatures, proposée par J. Rafelski and B. Müller en 1982 [Rafelski 82]. Selon cette théorie, une phase de QGP facilite notamment l'augmentation de la production d'étrangeté. Cette production est favorisée par les processus $q\bar{q} \rightarrow s\bar{s}$ et $gg \rightarrow s\bar{s}$. Le seuil en énergie pour la création du pair $s\bar{s}$ est 300 MeV, environ la masse de deux quarks. La création d'un plasma de quarks et de gluons dans les collisions d'ions lourds ultra-relativistes pourrait donc se traduire par des taux de production des particules étranges comparativement supérieurs aux résultats obtenus pendant les collisions de type p+A (matière nucléaire froide) ou bien p+p, auprès lequelles le QGP ne semble pas d'être formé.
- ii. Le déconfinement de couleur. La présence de charges colorées constitue une propriété importante d'une phase de plasma de quarks et de gluons. Cette présence crée des conséquences mesurables sur les particules énergetiques qui traverseront le milieu dense et chaud, autrement dit le QGP. Il a été prédit en particulier que les quarkonia et les particules de haute impulsion transverse seraient supprimées lorsqu'ils traverseraient une phase déconfinée. Ce phénomène peut être expliqué par la diminution du potentiel entre les quarks des quarkonia et d'autre part la perte d'énergie par la radiation de gluons (*gluon bremsstrahlung*).
- iii. Les signatures électromagnétiques. Finalement, des réactions comme la $q\bar{q} \rightarrow \gamma g$ et la $gg \rightarrow \gamma q$ peuvent être considérés comme des signatures. L'intérêt de ces observables réside dans le fait qu'elles ne sont pas sensibles aux interactions fortes. Elles interagissent très peu avec les composants du gaz hadronique et ne sont donc pas modifiées par les étapes qui succéderaient la formation du QGP. Par exemple les paires de dileptons $q\bar{q} \rightarrow l\bar{l}$ constituent une bonne sonde électromagnétique.

Les partons de hautes énergies doivent rayonner des gluons lorsqu'ils traversent un milieu contenant des charges de couleur. Cette perte d'énergie partonique est dépendante de la densité de charges colorées et serait donc particulièrement effective à l'intérieur d'une phase de plasma de quarks et de gluons. Pour cette raison, la perte d'énergie des particules de haute p_T a été considérée comme une sonde très intéressante de la matière produite durant les collisions d'ions lourds ultra-relativistes. Les partons des particules de haute p_T sont créées pendant les processus durs. Par la suite ils peuvent, comme le J/ψ , subir la phase de QGP. Leurs observation passe par l'intermédiaire des distributions azimutales des particules—dont on va parler dans

les paragraphes suivantes—de hautes p_T et des distributions des particules en fonction de leur impulsion transverse. Pour pouvoir révéler les effets nucléaires, ces dernières doivent être normalisées par les résultats obtenus dans les collisions p+p. Cette manifestation peut être exprimée par le facteur R_{AA} (appelé *Nuclear Modification Factor*) et qui est exprimé par (1.5). A ce point, on ajoute que si l'effet nucléaire était absent, cette variable (R_{AA}) serait constante et égale à l'unité.

Pour les collisions Au+Au, il était observé que ce facteur est $R_{AA} \leq 1$ et sera diminué avec l'impulsion transverse à partir de $p_T \sim 2.5 \text{ GeV}/c$. Le dernier cas est démontré sur la Figure 1.9. Ces valeurs, mesurées dans les collisions d'ions lourds ultra-relativistes, seraient en accord avec la perte d'énergie des partons dans le QGP. Néanmoins, il a été prédict que les conditions initiales des collisions, notamment la saturation des gluons dans les noyaux incidents, pouvaient également expliquer le comportement $R_{AA} \leq 1$ à haute p_T .

Les collisions d+Au peuvent reproduire en effet les mêmes conditions initiales que les collisions Au+Au mais ne devraient pas favoriser la création d'un QGP. Le modèle de saturation prédit donc que $R_{AA} < 1$ également pour les collisions d+Au, ce qui est en contradiction avec les données expérimentales. Celles-ci indiquent que le $R_{AA} > 1$ est situé entre la région $2 < p_T < 7 \text{ GeV}/c$ pour les collisions d+Au. C'est une première hypothèse de la perte d'énergie des partons dans le milieu. En plus, l'impulsion transverse de ces particules est située dans l'intervalle $4 < p_T < 6 \text{ GeV}/c$. Les distributions sont corrigées en prenant sous compte l'efficacité du détecteur.

Finalement concernant l'étude des corrélations azimutales, l'analyse des systèmes p+p et d+Au met en évidence dans le cadre un comportement quasiment similaire. Deux pics sont distinctement placés autour de $\Delta\phi = 0^\circ$ et de $\Delta\phi = 180^\circ$ et signent respectivement la détection des jets et des paires de jets (appelées *di-jets*). Au contraire, les résultats obtenus dans les collisions Au+Au présentent une absence totale de pic dans la région autour de $\Delta\phi = 180^\circ$ pour ce système [Adams 03]. Ce dernier cas est montré dans la Figure 1.6 et peut être expliqué par la formation d'un milieu qui est créé et présent uniquement dans l'état final des collisions d'ions lourds ultra-relativistes et qui supprime systématiquement les partons des *di-jets* qui le traversent.

12.2 Notions expérimentales

Dans les lignes suivantes, on va mentionner la partie expérimentale après laquelle cette thèse a été effectuée. On commence par la description générale du collisionneur RHIC, en commençant par la description de l'expérience STAR—and les systèmes de sous-détecteurs qu'on a exploité pour notre analyse. Finalement on va souligner l'importance du détecteur SSD sur l'amélioration de la trajectographie en incluant des points du détecteur pour chaque trace et on va passer à la description du partie des méthodes utilisées.

Les quatres expériences qui se trouvent autour du collisionneur RHIC (*Relativistic Heavy Ion Collider*) ont obtenu de nouveaux résultats qui apportent d'autres indications sur la formation du QGP. C'était aupres de ce collisionneur que la suppression des particules de hauts p_T dans la phase finale des collisions d'ions lourds ultra-relativistes a été observée pour la première fois.

L'expérience STAR est situe dans la ville d'Upton (à l'état de New York, États-Unis) au laboratoire BNL (*Brookhaven National Laboratory*) auprès du collisionneur RHIC (*Relativistic Heavy Ion Collider*). D'abord on présente une description du collisionneur. RHIC est capable d'accélérer des ions allant du proton (p) jusqu'à l'or (Au). Constitué de deux accélérateurs cryogéniques indépendants de 3.8 km de circonférence, il peut aussi créer des collisions asymétriques, avec deux espéces d'ions différentes dans les deux anneaux (e.g. d+Au). Le collisionneur RHIC permet aussi d'accélérer des protons jusqu'à une impulsion de 250 GeV/c pour chaque faisceau. Pour les noyaux les plus lourds, cette impulsion est réduite par le facteur Z/A (2.5 pour le cas de Au), ceci conduit à une énergie de 200 GeV par collision nucléon-nucléon. Cette énergie est environ 10 fois supérieure à celle obtenue au SPS (*Super Proton Synchrotron* à CERN) dans le centre de masse (cf. Tableau A.1). Le collisionneur contient deux tubes côté à côté qui permettent la circulation du faisceau dans les deux sens opposés (la couleur bleue est attribuée au sens horaire alors que le sens anti-horaire est appellé jaune). Chaque tube se trouve sous vide où passe le faisceau et un aimant supra-conducteur fonctionnant à température 4.2 K [Harrison 03] et sert comme dipôles. Les aimants possèdent le système de refroidissement qui contient d'hélium liquide. L'accélération du faisceau est faite progressivement. Les ions sont d'abord injectés en provenance de la ligne ATR (*AGS[‡] to RHIC*) sous la forme de paquets. Un système d'aimants permet de choisir dans quel sens le paquet est injecté en bout de la ligne ATR. L'anneau du RHIC est rempli sur toute sa circonférence lorsqu'un maximum de 56 paquets circule dans chaque sens. La phase d'accélération utilise ensuite le principe du synchrotron et dure environ une demi heure. Les collisions sont finalement possibles aux croisements des faisceaux (plutôt des *bunches*) à six endroits différents. Parmi eux, les deux sont utilisés pour la manipulation du faisceau, et dans les quatres endroits ils existent les quatre expériences, notamment PHENIX, PHOBOS, BRAHMS et STAR. Sur la Figure 2.1, un dessin incluant ces quatres expériences autour du collisionneur RHIC est présentée. Ensuite on va passer à la description synoptique des ces quatres expériences.

Concernant l'expérience PHOBOS[§], qui a pris son nom par une de deux lunes du planète Mars, a des objectifs la mesure des spectres de particules identifiées et les corrélations entre eux. La caractérisation des collisions est également effectuée à partir d'un détecteur de multiplicité (le ZDC, *Zero Degree Calorimeter*) qui sont pareils à

[‡]Alternate Gradient Synchrotron

[§]Initialement la proposition sur l'appellation de cette collaboration était MARS: *Modular Array for RHIC spectroscopy*, mais le nom a été bientôt rejeté.

eux que l'expérience STAR utilise. Les particules chargées sont mesurées et identifiées dans le région de rapidité $0 < y < 1.5$ et l'intervalle en impulsion transverse est situe entre les valeurs $15 < p_T < 600 \text{ MeV}/c$ pour les pions et entre $45 < p_T < 1200 \text{ MeV}/c$ pour les protons. L'exérience permet d'effectuer létude les rapports de particules, les spectres en impulsion transverse, la production d'étrangeté et les corrélations entre les particules, ainsi que la mesure du flot [Back 03]. Les deux spectromètres magnétiques ainsi dévoilés sont composés chacun de 5 couches de silicium à pixels et de 6 couches de silicium à pistes. Ils permettent la trajectographie et les mesures d'impulsion. Dans la Figure 2.2, une description de l'expérience est montrée. A partir de l'année 2005, la collaboration a termine son déroulement des mesures.

La collaboration BRAHMS (*BRoad RAnge Hadron Magnetic Spectrometers*) a pour but de mesurer de manière systématique les taux de production de particules (e.g. p^\pm , K^\pm et π^\pm). Pour atteindre ce but, BRAHMS utilise le dispositif expérimental montre dans la Figure 2.3. Les deux spectromètres magnétiques de hautes résolutions sont installes. Même s'ils possèdent des petits angles solides, ils peuvent être disposés suivant des angles variables dans le plan horizontal. En combinant ces deux spectromètres, la couverture en pseudorapidité est alors $0 < \eta < 4$ (l'acceptance angulaire est de $2\text{--}90^\circ$). En ce qui concerne l'identification des particules, elle est atteinte grâce à la combinaison des détecteurs de temps de vol (*TOF*) et des détecteurs Cherenkov. La détermination des impulsions et la trajectographie sont assurées par les chambres à projection temporelle (TPC) associées aux différents aimants. La TPC sont construit selon de dessin standard avec une region de dérive de 21.8 cm et un champ électrique de 229 V/cm qui est rempli par un mélange gazeux de Ar/CO₂, (en proportion 90:10). Cette expérience utilise les memes électroniques de lecture que STAR (les FEE,*front-end-electronics*). Finalement, les chambres de dérive sont construit en x , y plans à chambre à fils en utilisant le mélange Ar/C₄H₁₀ (67 : 33) avec une chambre 9°C *alcool bubbler*.

L'expérience PHENIX (*Pioneering High Energy Nuclear Interaction eXperiment*) est orientée vers la mesure des paires de probes électromagnétiques, notamment les di-électrons, les di-muons, mais ainsi que des photons et des hadrons [Adcox 03]. Cette expérience est sensible aux processus de faibles sections efficaces tels que la production de J/ψ ou la production de particules à hautes impulsions transverses. L'expérience permet de plus un taux de déclenchement élevé pour les différents types de collisions. L'aimant central induit un champ magnétique dont l'axe est parallèle à celui du faisceau. Le système d'acquisition possede une vitesse d'enregistrement très élevée: 10 kHz. Les chambres de trajectographie et les détecteurs utilisés pour l'identification des électrons, muons, photons et hadrons sont installés en dehors du champ magnétique. L'installation inclue deux bras à mi-rapidité ayant chacun une acceptance de 1 steradian pour la mesure des di-électrons. Une image du détecteur en profil et en z est montrée dans la Figure 2.4. A propos des buts expérimentaux, les photons et hadrons peuvent également y être mesurés avec des acceptances respectives de

2 et 0.36 stéradian. Ces bras sont équipés d'un détecteur à anneaux Cherenkov, d'une chambre à projection temporelle pour les mesures de perte d'énergie, d'un détecteur à temps de vol et d'un calorimètre électromagnétique. Des spectromètres à muons sont placés à rapidité élevée ($1.1 < |\eta| < 2.2$) de chaque côté du dispositif. Ces bras peuvent reconstruire la désintégration du J/ψ dans le canal $J/\psi \rightarrow \mu^+ \mu^-$. Les bras dimuons sont installés dans un champ magnétique perpendiculaire à l'axe du faisceau (axe z). Enfin un détecteur de vertex au silicium et deux compteurs du faisceau en coïncidence (BBC, *Beam-Beam Counter*) sont placés autour du point d'interaction. Le détecteur de vertex couvre une région en pseudo-rapidité de $|\eta| < 2.7$ [Adcox 03, Franz 08]. La mesure du charme ouvert (D^0) contribue aux mesures sur le charmonium. En plus la mesure du meson ϕ peut être effectuée dans les deux canaux hadronique et leptonique. Elle peut indiquer des éventuels changements en masse (en ce qui concerne la largeur). La production de photons directs sera également déterminée grâce aux calorimètres électromagnétiques composés de PbSc (Plomb-Silicium) et PbGl (Plomb-verre). Elle permettra peut-être d'observer la radiation de photons qui suivent une phase de PQG. Finalement PHENIX peut aussi étudier des observables telles que l'impulsion transverse moyenne des hadrons ou la production de l'étrangeté dans le système.

Notre thèse apporte sur le travail effectué sur les données fournis par l'expérience STAR. Dans les lignes suivantes, on va présenter une description des sous-systèmes qui appartient au STAR et on va insister à la description du détecteur en silicium, notamment le SSD (*Silicon Strip Detector*) et son utilisation sur l'analyse effectuée.

Le détecteur STAR (*Solenoidal Tracker at RHIC*), permet notamment de détecter la plupart des particules chargées qui sont émises par une collision sur une large fenêtre en pseudo-rapidité ($|\eta| < 4$) et avec une acceptance azimutale complétée ($\Delta\phi = 2\pi$). Le détecteur permet ainsi d'effectuer l'étude des collisions à travers l'analyse des taux de production et spectres en impulsion des π , K et p ainsi des particules étranges et charmées, et des résonances. La mesure du flot des différentes genres de particules et l'étude des corrélations entre les particules identiques ou deviennent faisables. Ces analyses sont effectués grâce au détecteur central qui est constitué par la chambre à projection temporelle. L'expérience STAR est placé dans un champ magnétique de 0.5 T parallèle à l'axe du faisceau (l'axe z). Une description graphique de l'ensemble du détecteur est montrée sur la Figure 2.5.

12.2.1 La chambre à projection temporelle

Le sous-système du détecteur principal dans l'expérience STAR est la chambre à projection temporelle (TPC, *Time Projection Chamber*). Cette chambre couvre le domaine en pseudo-rapidité de $|\eta| < 1.8$ et est capable de reconstruire les trajectoires des particules chargées dont l'impulsion est supérieure à 150 MeV/c. La détermination de l'impulsion ($\frac{\sigma_p}{p} = 2\%$) associée à la mesure de la perte d'énergie ($\frac{\sigma_{dE/dx}}{dE/dx} = 8\%$)—par

l'effet d'ionisation d'atomes du gaz—permet de distinguer les pions des kaons pour des impulsions inférieures à 300 MeV/c et ces derniers des protons jusqu'à 1 GeV/c. Sa longueur suivant l'axe du faisceau est de 166 cm, et les rayons internes et externes sont de 60 et 230 cm respectivement. Avec ce volume, une particule effectuant une traversée complétée de la TPC est mesurée en maximum de 45 points. Pour prolonger la couverture de la reconstruction de particules chargées dans la région de la rapidité frontale (*forward rapidity*), des chambres à projection temporelle à l'avant (Forward TPC's) sont placées. Il s'agit de deux détecteurs pareil à la TPC mais en micrographie qui sont situées de part et d'autre du point d'interaction dans les cônes qui supportent le trajectographe interne. Leur acceptance en pseudo-rapidité est comprise entre la région $2.5 < |\eta| < 4$. La seule différence avec la TPC est que la vitesse de la dérivé des électrons primaires est perpendiculaire au champ magnétique. L'ensemble de la TPC peut être considéré comme deux chambres à dérive accolées, où les électrons primaires migrent vers les extrémités. Le disque central est une fine membrane en capton aluminé qui sépare la TPC en deux parties. Cette membrane est d'épaisseur de 70 μm et est portée à un potentiel d'environ 28 kV. Les extrémités de la TPC restent à 0 V. Une série d'anneaux conducteurs de 10 mm de largeur et espacés de 1.5 mm sont de plus placés sur les membranes interne et externe au long de leur longueur. Ils sont reliés entre eux en série par des résistances (la valeur est environ des quelques $M\Omega$) formant ainsi une cage électrique enveloppant la TPC. La membrane centrale est fixée à l'anneau central de la membrane externe et est connectée électriquement à celui de la membrane interne. De cette façon, un champ électrique uniforme est créé à partir de la membrane centrale vers les extrémités. Il est délimité par les deux grilles électriques interne et externe. Une valeur constante d'environ de 135 V/cm permet ainsi la migration des électrons dans chaque moitié de la TPC vers l'extrémité correspondante [Anderson 03]. La détection des électrons primaires est ensuite assurée aux extrémités de la TPC par des chambres proportionnelles multi-fils. Ces MWPC (*MultiWire Proportional Chambers*) sont organisées en 12 modules identiques, disposées sur une roue en aluminium comme les 12 secteurs (cf. Figure 2.18). Au dessus de chaque module trois plans de fils faisant face au volume de la TPC sont situés en position parallèle entre eux. Les électrons traversent successivement ces trois plans pendant leurs trajet. Le premier plan de fils traversé, appelé la *gated grid*, est une porte qui permet le passage aux électrons primaires. En effet le trajet de ces électrons sur une moitié de la TPC dure quelques dizaines de μs et laisse le temps nécessaire au système de déclenchement (*trigger system*) d'accepter ou de rejeter cet événement. Ainsi lorsqu'une collision satisfait les critères du système de déclenchement, cette *gated grid* laisse passer les électrons car son potentiel est fixé à celui de la cage électrique à cet endroit, typiquement de ~ 110 V. Dans le cas contraire, la tension sur cette grille alterne de ± 75 V de sa valeur nominale et bloque les électrons, en empêchant la lecture dans la TPC (pour éviter l'enregistrement du bruit dans le détecteur). Le second plan de fils traversé, s'appelle *shield grid*, et le

troisième plan, s'appelle *anode grid*. En plus, un potentiel avec la valeur de 1200 V est appliqué à la *shield grid* (la cathode) alors que l'*anode grid* est à 0 V. A partir du moment où les électrons traversent la *shield grid* sont subits à une accélération vers l'anode grâce au champ électrique. Cette accélération est responsable pour la création du phénomène d'avalanche. Comme conséquence, le nombre d'électrons est multiplié par un facteur entre 1000–3000 entre ces deux plans de fils. Ce sont alors principalement des électrons—secondaires—créés par l'avalanche, qui arrivent vers l'anode (en ayant comme but l'amplification du signal). La collecte du signal est effectuée par la lecture capacitive des cellules élémentaires de détection, appelées les *pads*, disposées à la surface du circuit imprimé placé juste après l'*anode grid*. Lors de la collecte des électrons secondaires, la position des charges incidentes dans le plan transverse (x, y) du secteur est calculée à partir du signal des pads. L'emplacement de la colonne détermine la première coordonnée et la seconde coordonnée est calculée à partir du pad où le signal est le plus important et de ses deux pads voisins. La distribution du signal est ajustée par une fonction gaussienne centralisé sur ces trois pads. Cette configuration permet une meilleure précision dans l'axe des colonnes de pads. La TPC permet pas seulement la détermination des coordonnées des traces qui le traversent, mais aussi la mesure de l'impulsion en prenant sous compte la courbure de chaque trace (cf. Annexe D.1). En plus ce détecteur permet l'identification des particules en exploitant l'information de la perte d'énergie—indisponible pour notre étude. La résolution de la TPC permet une mesure plus précise du rayon de courbure des traces. Cela améliore ainsi la détermination de l'impulsion transverse, notamment dans les cas où les trajectoires des traces tendent à être étroits à cause de leurs impulsion élevée.

Un module de la TPC est en fait divisé en deux sous-secteurs interne et externe (cf. Figure 2.18). La différence entre ces deux parties est lié à la densité de modules de lecture. En effet, même la disposition ainsi la taille des pads sur la surface du secteur. Tout en contribuant globalement aux deux tâches, ces deux parties d'un secteur se spécialisent séparément dans la détection de la trajectoire d'une particule et dans la mesure de sa perte d'énergie. Avec ses pads plus petits, le sous-secteur interne permet de mesurer plus précisément la position des charges, notamment sur l'axe perpendiculaire au rayon de la TPC. Dans la mesure où la densité de traces est plus importante vers le point d'interaction, cette disposition permet d'optimiser la résolution à deux traces du détecteur. Un autre avantage est l'amélioration de la détection de particules ayant une impulsion transverse faible qui ont donc un rayon de courbure important.

Les secteurs de la TPC donnent les coordonnées des particules chargées uniquement dans le plan transverse (x, y). Pour obtenir la troisième coordonnée spatiale (z) la connaissance du temps de dérive des électrons est nécessaire à intervalles de temps réguliers—and aussi d'où vient l'appellation (*temporelle*). Plus particulièrement, les électrons primaires arrivant au fur et à mesure aux MWPC représentent l'ionisation

qui a eu lieu de plus en plus loin dans le volume de la TPC, et jusqu'à la membrane centrale. A partir du moment où les *gated grid* ont été ouvertes par le système de déclenchement, la lecture des secteurs à chaque intervalle de temps représente donc l'ionisation sur une petite tranche du volume de la TPC. Chaque tranche se projette successivement sur les secteurs avec une vitesse égale à la vitesse de dérive (d'où vient l'appellation de chambre à projection temporelle). La discréétisation du temps a été faite en fonction de la dispersion temporelle d'arrivée des charges partant d'un point de la TPC. Celle-ci est maximale et vaut environ 320 ns pour des charges traversant toute la longueur de dérive. La fréquence d'échantillonnage de l'électronique de lecture est de 9.4 MHz et le temps de mise en forme du signal par les pré-amplificateurs connectés à chaque pads est de quelques ns

Le calcul de la coordonnée des points concernant la composante spatiale z du faisceau est effectué en effectuant la division entre la différence de temps d'arrivée entre cette tranche et la dernière tranche par la vitesse de dérive des électrons primaires. Cette vitesse est de l'ordre de $5.45 \text{ cm}/\mu\text{s}$ et doit être mesurée avec une très grande précision au début d'une prise de données et au moins une fois chaque deux-trois heures (trois fois environ par *shift*). La valeur de cette vitesse est susceptible à une grande variation à cause des conditions décrites ci-dessous.

- i. Variation de la vitesse de dérive à cause de facteurs environnementaux: température, pression atmosphérique, variation du champ électrique;
- ii. désalignement du détecteur dans un champ magnétique;
- iii. Inhomogénéités concernant la composante radiale du champ magnétique et électrique;
- iv. de charge accumulée (*space charge*) à cause de la multiplicité élevée, surtout dans des collisions Au+Au; et
- v. l'inclinaison d'extremite (*endcap displacement*) du détecteur.

Dans le cadre de la mesure de la vitesse de dérive, un système de lasers[¶] a été installé à l'intérieur de la TPC [Abele 03], émettant en direction de petites cibles en aluminium, collées à la membrane centrale. Des électrons sont alors arrachés des cibles et vont dériver dans le *P10*^{||} sur toute la longueur de la chambre à dérive. Cette longueur divisée par le temps d'arrivée de ces électrons donne avec précision la vitesse de dérive. La résolution est séparée suivant différentes valeurs du champs magnétique, selon les secteurs internes et externes et si la dérive des électrons secondaires a été longue ou courte.

[¶]Y₃Al₅O₁₂: néodymium-doped yttrium aluminium garnet Nd avec la longueur d'onde de $\lambda = 266 \text{ nm}$.

^{||}Un mélange gazeux de Ar et de CH₄ en proportion 90 : 10.

12.2.2 La calorimétrie du STAR

Une autre partie qui concerne notre analyse, est la calorimétrie du STAR, les deux détecteurs principaux sont les EMC (*Electromagnetic Calorimeter*) et le BEMC (*Barrel EMC*). Le BEMC est capable d'identifier les électrons et de distinguer les pions neutres π^0 et les photons γ [van Buren 08]. Le EEMC couvre seulement la région de la pseudorapidité en avant ($1 < \eta < 2$) [Allgower 03]. Son but principal est la physique du spin. Plus particulièrement, en utilisant de faisceaux de proton polarisés du RHIC, STAR peut extraire des résultats sur l'helicité des gluons $\Delta g(x)$ en fonction du rapport x_g qui est la fraction d'impulsion du proton transportée par le gluon. La polarisation de gluons peut être démontrée dans la diffusion Compton entre les quarks et les gluons, en utilisant les corrélations longitudinales du spin. Le détecteur EMC, est un ensemble de plomb et de scintillateur plastique. Il possède le sous-détecteur SMD (*Shower Maximum Detector*) pour la discrimination de π^0/γ ainsi que de détecteurs *Pre-et-post shower* (PSD) pour la séparation entre les électrons et les hadrons chargés. Le SMD est situé dans $5X_0$ (*radiation lengths*) en profondeur. Le SMD offre la possibilité d'enregistrer le profil du gerbe des particules (électromagnétiques ou bien hadronique) et cependant identifier la particule incidente. Le ESMD est composé de polystyrène.

Le BEMC possède une géométrie cylindrique dans un rayon de 223 cm and 263 cm par l'axe du faisceau. La longueur du détecteur est de 293 cm au long d'axe z . Les deux grandes divisions du BEMC couvrent $-1 \leq \eta \leq 0$ (Est) et $0 \leq \eta \leq +1$ (Ouest). Chaque division est construite par 60 modules de détection (scintillateur verre au plomb). Chaque module est environ 26 cm et couvre en azimuth 6° . Les mêmes modules possèdent une résolution $\Delta\eta \times \Delta\phi = 0.05 \times 0.05$. Les modules sont aussi groupés en 40 *towers* du plomb et scintillateur. Comme résultat les des 2400 *towers* est obtenue pour chaque division (la moitié du détecteur). On souligne l'importance de la calorimétrie sur STAR, puisque on va utiliser l'identification des électrons pour notre analyse sur les corrélations azimutales $e-D^0$.

12.2.3 La trajectographie interne du STAR

Concernant la trajectographie interne du STAR, il possède aussi l'ensemble des détecteurs en silicium, notamment le SVT et le SSD (*Silicon Vertex Tracker* et *Silicon Strip Detector*). L'ensemble de détecteurs est montré sur la Figure 2.14. Tout d'abord le SVT est constitué de trois cylindres concentriques de détecteurs en silicium, avec les rayons compris entre 6 et 15 cm, qui utilisent des détecteurs à dérive. La quatrième couche—la plus éloignée par le faisceau—est composée de détecteurs à micropistes, et s'appelle SSD. Dans les lignes suivantes la description du SSD sera présentée.

Dans l'expérience STAR, initialement le dispositif de la reconstruction des traces dans la région de rapidité centrale ($|\eta| < 1.2$) se composait de la TPC et d'un trajectographe interne le SVT. Dans le cadre d'augmenter la puissance de la trajectographie—

autrement dit l'amélioration l'efficacité de la reconstruction des traces—une couche supplémentaire de détecteurs en silicium à micropistes (le SSD) il était proposé. Un deuxième but était la reconstruction des vertex secondaires pour les désintégration de particules étranges: K_s^0 , Λ , Ξ et Ω . D'abord on décrit le SVT et après on va insister à la description du SSD.

Le détecteur SVT

Dans le domaine de la trajectographie dans la région de basse impulsion transverse ($p_T < 150 \text{ MeV}/c$), le SVT permet d'améliorer la trajectographie des particules et la détection des hadrons de vie court (e.g. K_S^0). L'expérience STAR est équipé avec ce *tracker* situé très près du faisceau et offre une résolution spatiale de $25 \mu\text{m}$ et environ de $500 \mu\text{m}$ entre les deux traces. Le SVT est montré sur la Figure 2.14, et est composé par trois couches co-centriques. Le module de détection—appelé *wafer*—utilise la technologie de détecteurs en silicium à dérive. Les 3 échelles sont situés à distance $r = 6.37$, 10.38 et 14.19 cm par le point de la collision. Le détecteur cependant est composé par 216 modules de détection de type p avec les dimensions $6.3 \times 6.3 \times 280$ ($[W \text{ [cm]} \times L \text{ [cm]} \times H \text{ [\mu m]}$) . Les *wafers* [Bellwied 03], suivent la distribution suivante:

1^{ère} couche: 8 échelles (dont 4 *wafers*);

2^{ème} couche: 12 échelles (dont 6 *wafers*); et

3^{ème} couche: 16 échelles (dont 7 *wafers*);

Chaque couche du détecteur SVT est relativement épais ($1.5 X_0$) La résolution intrinsèque est de $\sigma_{r-\phi} < 80 \mu\text{m}$ (pour le plan transverse) et $\sigma_z < 80 \mu\text{m}$ (concernant la composante z). Finalement chaque *wafer* est divisé dans deux parties par une cathode pour diminuer la région de dérive des électrons (Figure 2.15).

Le détecteur SSD

Concernant la description du SSD, le détecteur est placé à 23 cm de l'origine de l'axe du faisceau, et dispose de 20 échelles de support. Chaque échelle (cf. Figure 2.16) contient 16 modules de détection. Chaque module de détection (cf. Figure 2.17) est espacé de 5 mm (en axe z du faisceau), comprennent chacun un détecteur en silicium de $75 \times 42 \text{ mm}^2$ qui possèdent 768 micropistes (*strips*) sur chaque face (p et n) et deux circuits hybrides supportant l'électronique de lecture. Le SSD possède en totale de 0.5 m^2 de surface active (de détection). Les échelles sont décalées (inclinaison de 5°) les unes par rapport aux autres. Concernant la reconstruction des traces, le SSD offre la possibilité d'obtenir un point supplémentaire (par rapport à la configuration SVT et la TPC). Le SSD fournit une précision sur la position déterminée dépend en premier

ordre, de la segmentation du détecteur,i.e. la distance entre chaque piste (appelé *pitch* et qui a la valeur de $95\text{ }\mu\text{m}$ [Martin 02]). La résolution attendue est de l'ordre de $20\text{ }\mu\text{m}$ sur chaque face. Cependant, le faible angle stéréoscopique de 35 mrad (cf. Figure 2.17) implique une résolution très différente après le passage dans le repère global de STAR. Les résolutions en position attendues dans les directions x et z sont respectivement $\sigma_x = 15\text{ }\mu\text{m}$ et $\sigma_z = 850\text{ }\mu\text{m}$. Le choix de la distance entre les pistes—déjà mentionné—résulte du compromis entre la résolution en position désirée et le nombre de canaux nécessaires pour la lecture.

Chaque couche de détection du trajectographe possède des zones mortes, dues à la géométrie de la construction du détecteur (l'espace entre les modules de détection) ou à des zones défectueuses ou inactives des détecteurs. Le détecteur en silicium constitue la partie sensible, aux particules chargées, autrement dit, le module de détection. Le substrat de silicium est de $300\text{ }\mu\text{m}$ d'épaisseur. Quand une particule chargée au minimum d'ionisation (MIP:*Minimum Ionising Particle*) traverse perpendiculairement ce module, perd environ 84 keV et comme conséquence ils sont créée environ 23000 paires électrons et trous cf. Figure 2.13. Ces charges sont ensuite collectées par les pistes implantées sur chaque face (p et n). Ce détecteur fournit, en réponse au passage d'une particule chargée, un couple de coordonnées (x, z), dans son repère propre, indiquant la position de l'impact. Le module de détection du SSD de STAR doit posséder une capacité à fonctionner dans un environnement très dense concernant les taux des particules chargées en termes d'efficacité et de pureté de reconstruction des traces. Une description graphique du détecteur est montrée sur la Figure 2.14. Le détecteur en silicium constitue la partie sensible, aux particules chargées, du module de détection. La surface active est circonscrite à l'intérieur des anneaux de polarisation situés (pour chaque face) à 1 mm du bord du détecteur. Le substrat de silicium (volume du détecteur) est de $300\text{ }\mu\text{m}$ d'épaisseur.

12.3 Motivation pour l'étude de correlations angulaires

Une des découvertes les plus importantes et en même temps inattendue auprès du collisionneur RHIC, était l'observation de la suppression anomale de jets produite par la matière *dense et chaude* crée pendant les collisions des noyaux-noyaux. Cette suppression est prédictive par les calculs théoriques d'être dépendante sur la masse de quarks, qui traversent le milieu. En particulier, la plus lourde la particule le plus faible la perte d'énergie de quarks devient. La suppression de jets est utile pour l'étude de la densité de gluons dans le milieu partonique traversé par le quark. En ayant comme but la mesure de cette densité, les prédictions par les modèles théoriques doivent être comprises et comparées avec les données réels divers, pour obtenir une image complétée et

cohérente. Une façon de comparer la théorie avec les données réels est l'investigation de la suppression de jets en fonction de la masse des quarks dans les données et la comparaison ensuite avec les modeles theoriques.

La mesure des quarks lourds (charme et la beauté) en exploitant les électrons non-photoniques dans les collisions des noyaux lourds en énergie à $\sqrt{s_{\text{NN}}} = 200 \text{ GeV}$, demon-trent une suppression plus élevé qu'attendue. Dans le cadre de la comprehension de cet enigme, la separation de la dependance de la suppression dans le domaine de saveur de quarks. En parallel avec les études de la production du *charme direct*, l'expérience STAR permet l'application de deux méthodes bien séparés pour effectuer l'étude décrite au-dessus. En particulier:

- Les corrélations électron-hadron ($e-h$); et
- les corrélations angulaires azimutales entre l'électron et la particule charmée ($e-D^0$).

La production du quark charme (dans les paires *ccbar*) a lieu dans les premières étapes de la collision, par l'intermediaire de la fusion des gluons $gg \rightarrow c\bar{c}$ [Abelev 08]. Grâce au fait que le taux de la production du charme est affectée par les conditions initiales de la collision, la mesure de la production du charme offre un outil d'étude pour la description de ces conditions. En plus grâce au fait que la masse des quarks charmés est élevée ($m > 1 \text{ GeV}/c^2$) les quarks lourds (charme et bottom, souvent abrégés en quarks *cet b*), sont générés par les processus de la diffusion dure (transfert d'énergie élevée) dans les premières moments de la collision. Ils sont sensibles à la densité initiale de gluons. La production de quarks lourds par les processus thermiques plus tard après la collision, ne contribue pas à la production totale, car l'énergie disponible dans le milieu ($\sim 0.5 \text{ GeV}/c^2$) est inférieure au seuil pour la production d'une paire de quarks lourds ($> 2.4 \text{ GeV}/c^2$). L'étude de la perte d'énergie des partons dans le chaud et dense matière de QCD peut être atteinte dans l'énergie ($\sqrt{s} = 200 \text{ GeV}$) au RHIC. La perte d'énergie d'un quark lourd est considérée plus faible que celle de quarks légers. Ce résultat est explique grâce au phénomène appelle *dead-cone* [Dokshitzer 01, Djordjevic 05], ergo la suppression de la radiation de gluons dans les petites angles**. En outre on doit mentioner que la production du J/ψ dans les collisions est supprimé à cause de l'écrantage du Debye provoqué par les paires $c\bar{c}$ a son entourage.

12.4 Méthode d'analyse des données

Dans cette thèse l'application des méthodes *microvertexing* sont aussi appliqués dans les données des collisions Cu+Cu et Au+Au à $\sqrt{s_{\text{NN}}} = 200 \text{ GeV}$. Cette méthode permet

**L'émission des gluons—selon le modèle du *dead-cone*—est interdite plutôt à la direction colinéaire en ce qui concerne l'impulsion initiale du quark.

l'amélioration d'extraction du signal du D^0 en exploitant la reconstruction du vertex secondaire. En plus, l'analyse des données concerne aussi la correlation azimutale $e-D^0$ dans les collisions Cu+Cu et Au+Au. Concernant la qualité de la méthode *microvertexing*, il était assuré en utilisant des données Monte Carlo (MC) et en faisant la comparaison avec les données réels (Au+Au à $\sqrt{s_{\text{NN}}} = 200 \text{ GeV}$). Les distributions des variables (e.g. DCA) aient été comparées entre les deux situations et la variation de l'importance du signal du D^0 en fonction de coupures imposées sur les variables du *microvertexing* ont été étudiées aussi. L'étude des données MC permet l'optimisation des valeurs des coupures sur les variables et la construction d'un ensemble de coupures qui seront appliquées sur les données.

12.4.1 Selection des événements

Une sélection primaire des événements est faite pour améliorer l'échantillon des événements. D'abord on effectue une coupure sur la multiplicité des événements. Plus particulièrement, la coupure possède la forme (3.1) et il sert pour effectuer l'étude de notre analyse en basses ou hautes multiplicités. Les multiplicités sont calculées par le modèle de Glauber (cf. Section 1.10) et démontre une mesure du nombre des traces de particules chargées. La plus haute la multiplicité, la plus centrale la collision devienne et cependant le nombre des particules est plus élevée. On effectue une coupure sur la composante z (l'axe du faisceau) du vertex primaire et en particulier on demande qu'il dépasse pas le $|z - \text{vertex}| < 20$ ou 30 cm (selon l'espèce de noyaux. En p+p et Cu+Cu la coupure imposée est de 30 cm et en Au+Au et d+Au la limite est de 20 cm). En plus on demande que l'événement appartient dans le déclencheur (*online trigger*) du BEMC. Concernant la qualité de traces, ils doivent être contenus dans la région $|\eta| < 1$ et le nombre des hits enregistrés par la TPC doit respecter (3.2). Cette coupure est appliquée pour éviter les traces *split* et aussi pour obtenir des traces qui contiennent une mesure sur l'impulsion plus élevée, puisque la mesure est proportionnelle au nombre de *hits* enregistrés.

12.4.2 Identification des hadrons

L'identification des particules joue un rôle important sur notre étude. Le but final de notre étude, est la reconstruction de la masse invariante du D^0 en respectant la (3.6). Pour cette raison la classification de particules en hadrons (K et π) est nécessaire. On utilise l'information sur la perte d'énergie obtenue par la TPC. Cette information est donnée sous forme de distribution gaussien pour chaque particule (appellation nSigmaKaon, nSigmaPion, nSigmaProton, etc.). Ces distributions (cf. Figure 3.10) sont créées à partir de l'hypothèse de la masse de chaque particule, et en prenant sous compte la valeur de la perte d'énergie. Pour une masse différente on obtient une différence entre la valeur théorique obtenue avec l'équation de Bethe-Bloch (2.1) et la

valeur actuelle. On souligne l'importance que les coupures sur la perte d'énergie—sous forme (3.7)—permettent la particule d'être candidat pour tous les deux espèces: pions et kaons. Cependant chaque coupure n'empêche pas que la particule appartient en même temps dans tous paires différentes comme une particule différente. Finalement la perte d'énergie de différentes espèces de particules en fonction de l'impulsion est montrée sur Figure 2.19.

12.4.3 Identification des électrons

Pour l'identification des électrons une méthode plus sophistiquée est utilisée. On applique les coupures suivantes pour obtenir un échantillon des électrons le plus propre possible. Tous les coupures suivantes doivent être satisfaites, sinon l'événement est rejeté.

1. L'événement doit contenir un *hit* dans un des modules du BEMC avec l'énergie E ou E_T ^{††} supérieure au seuil imposé. En particulier les événements qui contiennent *High Tower* (pour le Cu+Cu) ou *Btag* (pour le Au+Au). Les valeurs du seuil sont mentionnées dans le Tableau 3.3;
2. Une coupure dans la perte d'énergie de chaque particule dans la TPC qui doit être entre les valeurs $\frac{dE}{dx} \in [3.5, 5.0]$ [keV/cm]. En même temps l'impulsion doit être supérieure à $p \geq 1.5$ GeV/c;
3. Une coupure concernant le profil du gerbe électromagnétique. En utilisant le sous-détecteur SMD du calorimètre, on demande que le gerbe se disperse sur plusieurs fils (*strips*) en η et ϕ . Le gerbe électromagnétique possède un profil plus dispersé géométriquement. Avec la coupure suivante, on jette les gerbes créées par les hadrons, leurs profil étant plus focalisé. Le détecteur doit avoir au moins un *hit* dans tous les deux niveaux. Cependant: $SMD_\eta > 1$ et $SMD_\phi > 1$;
4. Une coupure sur le rapport $0 < \frac{p}{E_{\text{TOWER}}} < 2$, p mesure par la TPC et E_{TOWER} par le calorimètre BEMC, puisque les électrons perdent la totalité de leur énergie dans les cellules du calorimètre, cependant $p/E \sim 1$;
5. La propagation du trace par les cellules du calimètre jusqu'à la TPC doit avoir une trace dans la TPC. Cette trace est considérée comme un électron;
6. Finalement, après effectuer toutes les coupures précédentes, on a besoin que notre échantillon contient uniquement les électrons non-photoniques. Dans ce cadre, on crée la masse invariante pour les paires des électrons en même signe mais aussi pour la signe opposée. Pour étudier cette coupure, on superpose les

^{††}Energie transverse décrite par (1.14)

deux masses invariantes. Une coupure pour la masse invariante de di-électrons est applique pour le même signe ($e^\pm e^\pm$) est signe oppose ($e^\pm e^\mp$). L'échantillon des électrons est rejeté si au moins une des deux particules forment une masse invariante $m_{e^+e^-} \leq 150 \text{ MeV}/c^2$. Le dernier cas avec la coupure imposée, est montre sur la Figure 3.9.

12.4.4 La reconstruction de la masse invariante du D^0

Après la reconstruction de la masse invariante de paires $K^\pm\pi^\mp$, on a besoin d'extraire le signal du D^0 . Pour cette raison on a besoin la création de la distibution du bruit du fond. On utilise trois méthodes bien distinguées qui vont servir à la soustraction par la masse invariante initiale pour obtenir le signal de la masse du D^0 ($1865 \text{ MeV}/c^2$).

- Masse invariante de rotation. On utilise l'impulsion du kaon en faisant une rotation de 180° respectant le même niveau de désintegration. La masse invariante rotationnelle devient selon (3.11);
- Masse invariante de paires de même signe. En utilisant la (3.10), on peut construire une nouvelle masse invariante puisque le D^0 ne désintegre pas ni en $K^+\pi^+$ ni en $K^-\pi^-$;
- Le polynôme de n^{ème} degré $\text{pol}[n]$. Un fit est applique à coté—à gauche et à droite—de la region de $1865 \text{ GeV}/c^2$. La valeur du degré utilise varie selon la qualité du fit: $\chi^2/\text{d.d.l}^{\ddagger\ddagger} \sim 1$. La méthode est bien décrite en détails dans la Section 3.9.3.

Souvent les distributions de la masse invariante sous forme dN/dm (B) de bruit du fond obtenus sont eloignes par la masse invariante du D^0 ($S + B$) en termes de population. On utilise la méthode de mise à l'échelle d'un de deux distributions (on a choisi la distribution de la masse invariante qui correspond au bruit du fond). Plus particulierement, dans la region predefinie: [1.7, 1.8] et [1.9, 2.0] on performe l'integral pour le $S + B$ ainsi que pour le B . Le rapport des populations $(S + B)/B$ donne un facteur avec lequelle la mise à l'échelle est mise en œuvre. Finalement la soustraction du bruit du fond est realisé apres la mise à l'échelle et qui va devoiler l'existence du méson charme, notamment le D^0 . On décrit la méthode dans la Section 3.10.

12.5 La méthode du *microvertexing*

Les trajectoires des particules chargées qui se propagent dans un champ magnétique peuvent être décrites mathématiquement avec les hélices. Dans l'ensemble de (4.1),

^{††}degrés de liberté

l'équation de mouvement de la particule sous forme algébrique est présentée. Notre méthode du *microvertexing* exploite l'idée d'hélice et calcule les variables cinématiques: la DCA et cependant le point où se trouve le vertex secondaire de désintégration. En plus cette méthode fournit l'information sur les DCA transverses et sur l'axe z (respectivement la DCA_{xy} et la DCA_z) en ce qui concerne le vertex primaire. En plus la longueur de la désintégration de la particule peut-être aussi calculée à partir du moment que les coordonnées du vertex secondaire sont calculées. La méthode du *microvertexing* est expliquée en détail dans la Section 4.2. Aussi d'autres variables comme le $\cos\theta_{\text{POINTING}}$ ou bien le $\cos\theta^*$ des particules filles et la DCA_{D^0} pour la particule initiale, sont calculées (cf. Annexe A.3).

Dans le plan transverse xy , l'hélice est projetée comme l'arc d'un cercle. Concernant les plans parallèles au axe z , le trajet de la particule est une fonction sinusoïdale. Une particule avec haute impulsion transverse, possède une relativement petite courbure $1/R$ (cf. Annexe B.2). Les traces avec une impulsion plus faible—appelées *loopers* et qui sont la majorité pour les traces du STAR—are courbes dans l'ensemble de la TPC. À ce point, tous les traces reconstruites, sont appelées globales, puisque seulement l'information obtenue par la TPC est utilisée. Les traces sont soumises à un fit de nouveau en utilisant l'algorithme du Kalman [Lisa 96]. La trace passe le filtre du fit trois fois consécutives. En premier temps, et pendant la première fit le calcul de la proximité des points à la courbe du fit. Dans un deuxième temps, toutes les distorsions provoquées par les malformations du champ, la perte d'énergie moyenne des électrons dans le matériau et la diffusion multiple sont prises en compte. Finalement, pendant le troisième fit, le trace est optimisé et amélioré en termes de trajet. Pendant ce dernier pas, la trajectographie du STAR, permet de séparer les traces selon le fit en traces primaires et globales. Le critère pour ce distinction, est si le point de vertex primaire a été utilisé ou pas pour la reconstruction [Pruneau 03]. Plus particulièrement, si ce point est inclus la trace est considérée comme primaire. En même temps, la trace possède une $DCA \leq 3 \text{ cm}$.

12.5.1 Étude de Simulation

Pour tester notre algorithme d'analyse de données, on a appliqué notre méthode dans les données en simulation. Pour cette raison on a utilisé le logiciel STARSIM qui était développé pour l'expérience STAR. Ce logiciel utilise GEANT [Apostolakis 93] pour le passage de particules à travers de matériau. En plus pour la génération de particules initiales les possibilités du logiciel PYTHIA [Sjöstrand 10] sont aussi exploitées. En total on a généré 400.000 événements environ, chaque événement contient la particule D^0 qui désintègre dans le canal hadronique (Pour des raisons de simplicité on a produit seulement la réaction $D^0 \rightarrow K^-\pi^+$ et pas l'antiparticule $\bar{D}^0 \rightarrow K^+\pi^-$) avec un rapport d'embranchement de 100%. La distribution du vertex primaire pour les événements est une distribution aléatoire restreinte entre $|z - \text{vertex}| < 30 \text{ cm}$. Les traces générées se

trouvent dans la région $|\eta| < 1$ et en plein azimute. Chaque événement contient deux traces maximum. Puisque on a utilisé seulement la désintégration du D^0 , ça veut dire que les traces négatifs sont les kaons et les positifs les pions. Cependant on peut aussi étudier les variables pour chaque particule indépendamment (e.g. $\cos\theta^*$, cf. Section 4.2). Pour comparer la méthode du *microvertexing*, pour chaque paire, GEANT nous fournit avec l'information sur l'impulsion, le longeur de désintégration du D^0 et les coordonnées du vertex secondaire (Figure 5.4). En même temps, notre méthode permet le calcul des variables du *microvertexing*. Après ce calcul, une comparaison de valeurs—événement par événement *Ebye: Event by event*—est faite.

Lorsque une particule chargée traverse un milieu, elle est soumise à la diffusion de Coulomb multiple (MCS, notamment *Multiple Coulomb Scattering*). Le résultat de cette déviation angulaire de la particule créée par la somme de forces électromagnétiques d'atomes. L'angle de deviation est décrite par la (4.15) et est inverse proportionnelle à l'impulsion. La résolution de la trajectographie dépend par l'impulsion via la (4.18). La résolution peut être considérée comme l'erreur—en coordonnées cylindriques—décrite en plan transverse (r, θ) (4.13) et en composante θ par (4.14). En plus, dans le cadre d'étudier l'impact de l'inclusion de silicium dans les variables du microvertexing, on demande explicitement que chaque trace ait exactement la coupure SVT+SSD= n (ou $n=0-4$). On construit les distributions pour la liste des variables ci-dessous.

- i. La DCA entre la trace de la particule-fille, comme c'est présentée dans la Figure 5.13 (a);
- ii. le longeur de désintégration de la particule D^0 , dans la Figure 5.13 (b); et
- iii. la DCA du D^0 en ce qui concerne le primary vertex démontre dans la Figure 5.13 (c).

Le calcul de la DCA du D^0 est effectué en prenant sous compte l'extrapolation linéaire (4.3). Comme il a déjà été discuté (Section 5.5), la coupure sur le nombre total de SVT+SSD d'une trace a un impact sur la reconstruction de variables du microvertexing. Les valeurs moyennes de ces variables sont présentées dans Tableau 5.2 en appliquant la méthode microvertexing, dans l'échantillon MC.

Afin de améliorer les coupures qui vont servir plus tard pour l'analyse des données réels concernant la reconstruction du D^0 , une étude est effectuée dans l'échantillon MC, concernant ces valeurs, cf. Section 4.2. Les détails de cette méthode sont présentées ci-dessous. On considère la distribution d'une variable a dans la région de MC et des données réels (dans l'échantillon MC, la valeur est dénotée par a_{mc}). Cette valeur, peut être considérée comme le *signal* (S). Pour les données réels (dans les collisions Cu+Cu) la même valeur est a_{data} et est appellée *bruit du fond* (B). Tout les deux cas, sont présentes sous une forme de distribution unidimensionnelle $\frac{da}{dN}$, avec l'intégrale soit normalisé à l'unité (e.g. Figure 5.14 (a) pour la DCA entre les traces). Le but de

cette étude est l'investigation de l'impact d'une coupure inclusive, en gardant la région $\Delta a \equiv [a_1, a_2]$, même de S et de B . Pour cette raison, on étudie la variation de la variable (5.1) dans l'intervalle pré-déterminé Δa . En plus on étudie la variation du rapport $\frac{S}{B}$ mais aussi du $\frac{S}{\sqrt{B}}$. Finalement la variable de pourcentage de survie (notée par SP); ergo le pourcentage inclus de la variable pour les deux cas (MC et données réels) dans la région Δa est aussi présentée pour chaque variable du microvertexing.

En outre, l'impact d'inclusion de points de détecteurs en silicium pour chaque trace sur le calcul de variables du microvertexing est aussi investi—en répétant la méthode décrite ci-dessus—pour chaque situation de SVT+SSD. L'échantillon de MC qui est utilisé pour cette étude, est décrit dans la Section 5.1. Pour la comparaison entre les données réels, on a utilisé les collisions en Cu+Cu à $\sqrt{s_{\text{NN}}} = 200 \text{ GeV}$. Plus particulièrement l'ensemble des événements qui sont sélectionnés par le déclencheur *High Tower*, (cf. Chapitre 6). Le calcul des variables pour les MC et les données réels est effectué en utilisant le même algorithme décrit dans la Section 4.2. Les variables utilisées pour cette étude sont mentionnées dans la liste ci-dessus. En plus on va considérer les deux régions suivantes pour effectuer cette étude: $[0, 1] \text{ (cm)}$ et $[0, 0.1] \text{ (cm)}$.

La résolution de la trajectographie interne de l'expérience STAR, est $250\text{--}300 \mu\text{m}$ concernant la DCA (*distance of closest approach*) des traces au vertex primaire. Cette valeur est plus grande que le longueur du trajet de la particule D^0 dans le référentiel du laboratoire: $\beta\gamma c\tau \simeq 70 \mu\text{m}$ pour une impulsion du D^0 moyenne (longeur de désintégration propre $c\tau = 120 \mu\text{m}$). Malgré ce fait, il était démontré que le rapport du signal (S) bruit du fond (B) pour la désintégration $D^0 \rightarrow K^- \pi^+$ est augmentée sans contribuer au perte du signal pour les coupures imposées. Par exemple, les coupures suivantes ont été appliquées sur la longueur de désintégration du D^0 , la DCA de traces au vertex primaire en profil transverse (DCA_{xy}) ainsi que en composante z (notée par DCA_z).

12.6 Résultats

On a obtenu comme résultat un signal du D^0 avec $\frac{S}{\sqrt{S+B}} = 3.71$ dans les données de $2.5 \cdot 10^6 \text{ Au+Au}$ événements, après imposer le *minimum bias trigger* et la coupure sur la composante du vertex primaire $|z - \text{vertex}| < 20 \text{ cm}$ et la demande du *hit* dans les détecteurs en silicium (SVT et SSD) soit supérieur ou égale à un. En même temps l'application de la méthode du *microvertexing* a été aussi implementée pour réduire le bruit du fond. L'importance du signal devient plus grande avec la population des événements, respectant la prédiction pour le vrai signal. En plus, on souligne que dans les événements *minimum bias* l'électron est absent ne permettant pas l'application de la méthode de la corrélation $e-D^0$.

Dans les données Cu+Cu et Au+Au, la particule-déclencheur (*trigger particle*)

de haute impulsion était choisi par le calorimètre électromagnétique (BEMC). Les événements qui étaient choisis s'appellent *Btag* et *High Tower* pour les espèces de noyaux de collision Au+Au et Cu+Cu. Le BEMC a été utilisé pour la rejet du bruit du fond et la sélection finale de la particule e^\pm . Le bruit du fond provient de la désintégration de mesons neutres (π^0 et η) en photons. Une deuxième source de contamination est la contribution de matériau dans lequel les photons se désintègrent suivant le canal $\gamma \rightarrow e^-e^+$, en justifiant le terme *photonnique*. Concernant le chemin suivi pour l'algorithme, la masse invariant du D^0 est reconstruite après l'identification d'électron. Les hadrons sont aussi classifiés en *pions* π^\pm et *kaons* K^\mp pour construire la masse invariante pour le canal $D^0 \rightarrow K^-\pi^+$. En même temps les corrélations du électron e et du D^0 sont aussi appliquées en azimut ($\Delta\phi$). Plus spécifiquement, pour les électrons et les kaons avec le même signe une corrélation angulaire à 0° est appliquée. Ce cas implique la génération du D^0 par une désintégration de quarks $b\bar{b}$, appellée la contribution de la beauté. Quand l'électron et le kaon ont le signe contraire, une corrélation $\Delta\phi = 180^\circ$ est imposée pour extraire le signal du D^0 provenant de la contribution du charme ($c\bar{c}$). Le résultat obtenu avec les méthodes précédentes est

d'une importance $\frac{S}{\sqrt{S+B}} = 2.2$. Les événements initiaux examinés sont $1.5 \cdot 10^6$.

Après les coupures impliquées on a obtenu dans les collisions Au+Au (*Btag trigger*) est ~ 90000 , et le même chiffre devient ~ 26000 pour les collisions Cu+Cu (*High Tower*). Comme conséquence, les données qui contiennent les électrons sont inférieures si elles sont comparées aux données de *minimum bias*. En plus les données prises pendant les collisions en Au+Au sont supérieurs aux autres prises pendant les collisions Cu+Cu en termes de l'acceptance du calorimètre. En 2005 (Cu+Cu) le détecteur couvrait seulement la région en pseudorapidité $0 < \eta < 1$ mais en 2007 (Au+Au) la couverture de cette région arrivait jusqu'à $-1 \leq \eta \leq +1$.

L'étude des plusieurs ensembles de coupures qui étaient appliquées était aussi effectuée, en obtenant comme résultat l'observation de plusieurs pics candidats pour le D^0 . Par exemple, l'observation du D^0 est faite pour l'azimut de $\Delta\phi \simeq \pi$ entre l'électron et la paire de $K\pi$ pour le cas de même signe: $\text{sgn}(e) = \text{sgn}(K)$. Ce cas signifie la production par la fragmentation du $c\bar{c}$ dans les données obtenues dans les collisions Cu+Cu. Pour les données en collisions Au+Au le pic obtenu est observé pour le $\Delta\phi \simeq 0$ entre la particule-déclencheur (e^\pm) et le D^0/\bar{D}^0 . Dans le dernier cas, on choisit la corrélation entre les signes des K et des électrons qu'elle soit $\text{sgn}(e) \neq \text{sgn}(K)$. Avec cette sélection des particules, on est capable d'obtenir un pic du D^0 provenant de fragmentation du $b\bar{b}$. Des études plus approfondies en utilisant les corrections obtenues par la méthode de *embedding* sont indispensables pour les deux cas décrits ci-dessus. La production des données de *embedding* sont en cours de *quality assurance* par la collaboration STAR. L'*embedding* va servir dans les signaux obtenus en Au+Au en corrigeant l'acceptance et l'efficacité des détecteurs. En plus cette méthode va servir pour le calcul de la section efficace de la production du charme.

Les résultats dans les collisions Cu+Cu et Au+Au en exploitant les possibilités de la méthode du *microvertexing* ont été obtenus grâce à la performance excellente que les détecteurs en silicium (SVT et SSD) ont démontre pendant la prise des données. En particulier le SSD offrait des *hits* supplémentaires qui aidaient sur la reconstruction entre la TPC et la SVT en diminuant les phantômes (*ghost hits*) qui apparaissent dans le SVT. Dans cette thèse, on a étudié les corrélations azimutales angulaires $e-D^0$ pour les données en p+p et d+Au à $\sqrt{s} = 200 \text{ GeV}$. Il était observé un pic du D^0 pour tous les deux cas de *charme* et la *beauté*. Ces résultats contribuent dans les analyses précédentes qui ont aussi observé le signal de la particule D^0 et il était démontre que la contribution de la *beauté* augmente avec la impulsion transverse (p_T) et est comparable à la *charme* environ à $p_T \sim 5.5 \text{ GeV}/c$. La contribution de la beauté calculée par les données est compatibles avec les calculs qui sont effectués dans le cadre de FONLL. Le dernier résultat est de grande importance pour la comprehension de la suppression de jets dans les collisions des noyaux. En outre il souligne l'importance pour résoudre l'éénigme de cette suppression dans la physique d'ions lourds ne peut pas être lié à l'absence de la beuté dans le collisions p+p dans la region de la même impulsion transverse.

12.7 Nouvelle méthode de collecte des amas de charge pour le SSD

Concernant la partie technique de la thèse, on s'intéresse sur une nouvelle méthode concernant la collecte des amas de charge pour le SSD en utilisant la classe de ROOT appellée **TSpectrum**. L'algorithme implementé dans cette classe, utilise la notion de la chaîne du Markov exprimée par (10.5) et peut distinguer des pics dans un spectre bruyant. Dans la Figure 10.2 c'est démontre la mise en évidence de la méthode de la chaîne Markov par le **TSpectrum**.

En particulier cette nouvelle méthode de collecte, cherche les amas dans les deux pistes des détecteurs mais sans prendre sous considération ni la correlation topologique, ni la correlation entre les signaux provenant de chaque piste. Des résultats préliminaires ont dévoilé un taux d'augmentation sur le nombre des amas enregistrés. Plus particulier une augmentation de 40% sur ce nombre est obtenue avec la nouvelle méthode. Les données qui ont été traitées provenaient de collisions Au+Au à $\sqrt{s_{\text{NN}}} = 200 \text{ GeV}$ (run VII). La nouvelle méthode peut servir pour la reproduction de ces données ainsi que pour la future mise à niveau de détecteurs du vertex du STAR, le futur HFT (*Heavy Flavor Tracker*). La troisième couche de silicium sur HFT, sera le SSD.

12.8 Conclusion

Pendant les années 2009–2010 le détecteur TOF (*Time of Flight*) a été déployé en pleine couverture pour la première fois en permettant l’identification des particules provenant par la *charme* et la *beauté*. Comme conséquence les études sur ce domaine auront une meilleure résolution concernant les résultats. En supplément, la future mise à niveau de détecteurs en silicium, le HFT—actuellement sous développement—va offrir une amélioration sur la résolution en impulsion et une précision plus importante concernant la position du vertex secondaire, élément indispensable pour les études sur la physique du *charme*. Il faut souligner que le détecteur de vertex du STAR n’était pas conçu pour la physique des saveurs lourdes.

La performance excellente du détecteur SSD, qui a aidé à obtenir les résultats enregistrés dans cette thèse assure l’inclusion du SSD sur l’ensemble du HFT. Le détecteur d’avenir (HFT) est designé pour mesurer avec précision les variables du *microvertexing* pour la reconstruction de *charme* et de la *beauté*. Les nouvelles développements présentent auprès de cette thèse, notamment pour la reconstruction du vertex secondaire, vont servir pour l’extraction du signal du D^0 dans les collisions d’ions lourds. Finalement la nouvelle application pour la recherche des amas de charge pour le SSD, démontre que les études de *charme* et de la *beauté*, peuvent être effectuées dans l’environnement dense de collisions d’ions lourds, malgré la haute densité des particules chargées qui traversent le détecteur et poussent à ses limites l’expérience actuelle qui était loin de son but initial. En plus, ces résultats, serviront pour la future mise à niveau du détecteur HFT.

Appendices

Appendix **A**

A.1 Rapidity Relation Between Two Reference Frames

Let us consider two inertial reference frames moving with velocity \vec{v} with respect to each other. Let us also consider a Lorentz boost parallel to the axis z , $\vec{\beta} = (0, 0, \frac{v}{c})$. The relations between the 4-momenta components become:

$$\begin{aligned} E' &= \gamma(E - \beta p_z) \\ p'_x &= p_x \\ p'_y &= p_y \\ p'_z &= \gamma(p_z - \beta E) \end{aligned} \tag{A.1}$$

We begin the proof by using $y = \frac{1}{2} \ln \frac{E + p_{\text{L}}}{E - p_{\text{L}}}$ and considering y' as the rapidity in the moving frame.

Proof.

$$\begin{aligned} y' &= \frac{1}{2} \ln \frac{E' + p'_z}{E' - p'_z} \\ &= \frac{1}{2} \ln \frac{\gamma(E - \beta p_z) + \gamma(p_z - \beta E)}{\gamma(E - \beta p_z) - \gamma(p_z - \beta E)} \\ &= \frac{1}{2} \ln \frac{(E + p_z)(1 - \beta)}{(E - p_z)(1 + \beta)} \\ &= \frac{1}{2} \ln \frac{E + p_z}{E - p_z} + \frac{1}{2} \ln \frac{1 - \beta}{1 + \beta} \\ &= y + \xi \end{aligned}$$

□

Therefore the distribution $\frac{dN}{dy}$ remains invariant between the relative inertial frames:

$$\frac{dN'}{dy} = \frac{dN}{dy} \quad (\text{A.2})$$

A.2 The Case when $y \approx \eta$.

Let us begin the proof using the expression $\eta = -\ln \tan \frac{\theta}{2}$. We shall also consider the case that $\beta \rightarrow 1$, therefore $E \simeq p$. Let us note that $\cos \theta = \frac{p_z}{p}$ and also the following trigonometric expressions:

$$\begin{aligned} 1 + \cos \theta &= 2 \cos^2 \frac{\theta}{2} \\ 1 - \cos \theta &= 2 \sin^2 \frac{\theta}{2} \end{aligned}$$

Proof.

$$\begin{aligned} y &= \frac{1}{2} \ln \frac{E + p_z}{1 - p_z} \\ &= \frac{1}{2} \ln \frac{1 + \frac{p_z}{E}}{1 - \frac{p_z}{E}} \\ &\simeq \frac{1}{2} \ln \frac{1 + \frac{p_z}{p}}{1 - \frac{p_z}{p}} \\ &= \frac{1}{2} \ln \frac{1 + \cos \theta}{1 - \cos \theta} \\ &= \frac{1}{2} \ln \frac{\cos^2 \frac{\theta}{2}}{\sin^2 \frac{\theta}{2}} \\ &= \frac{1}{2} \ln \frac{1}{\tan^2 \frac{\theta}{2}} \\ &= -\ln \tan \frac{\theta}{2} \\ &= \eta \end{aligned}$$

□

A.3 The angle θ^*

The angle θ^* is defined as the angle between the momentum of the parent particle in the lab frame, and the momentum of the daughter particle in the CMS, as stated in (A.3) for the case of the kaon. Let us consider the Gottfried-Jackson reference frame.

$$\cos \theta_K^* \equiv \frac{\vec{p}'_K \cdot \vec{P}_{D^0}}{|\vec{p}'_K| |\vec{P}_{D^0}|} \quad (\text{A.3})$$

In the laboratory frame we measure only the \vec{p}' for the daughters and reconstruct the parent \vec{P} . Concerning the center of mass system (CMS), the same daughter particle momentum is denoted by p' and the decay of $D^0 \rightarrow K^- \pi^+$ results for the decay particles to be emitted in a *back-to-back* orientation. By applying the inverse Lorentz boost described by (A.1) we can calculate the momentum of the daughter particle in the CMS, e.g. \vec{p}'_K for the K candidate. Hence (A.3) can be re-written as (A.4).

$$\begin{aligned} \cos \theta_K^* &= \frac{(\vec{p}_K + \vec{\beta}_{D^0} E_K) \cdot \vec{P}_{D^0}}{|\vec{p}_K + \vec{\beta}_{D^0} E_K| |\vec{P}_{D^0}|} \\ &= \frac{\vec{p}_K \cdot \vec{P}_{D^0} + P_{D^0}^2 \frac{E_K}{E_{D^0}}}{|\vec{p}_K + \vec{\beta}_{D^0} E_K| |\vec{P}_{D^0}|} \\ &= \frac{|\vec{p}_K| \cos \theta_K + P_{D^0} \frac{E_K}{E_{D^0}}}{|\vec{p}_K + \vec{\beta}_{D^0} E_K|} \\ &= \frac{|\vec{p}_K| \cos \theta_K + \beta_{D^0} E_K}{|\vec{p}_K + \vec{\beta}_{D^0} E_K|} \end{aligned} \quad (\text{A.4})$$

Let us note that the angle θ_K is calculated in the lab frame as the angle between the momentum of the K and that of the D^0 as described by (A.5).

$$\cos \theta_K = \frac{\vec{p}_K \cdot \vec{p}_{D^0}}{|\vec{p}_K| |\vec{p}_{D^0}|} \quad (\text{A.5})$$

Therefore (A.4), is transformed into (A.6).

$$\cos \theta_K^* = \frac{\frac{\vec{p}_K \cdot \vec{p}_{D^0}}{|\vec{p}_{D^0}|} + \beta_{D^0} E_K}{|\vec{p}_K + \vec{\beta}_{D^0} E_K|} \quad (\text{A.6})$$

Concerning the calculation of the D^0 energy, the mass is considered to be the invariant mass of the $K\pi$ pair: $M_{K\pi}$ as stated in (A.7).

$$M_{K\pi} = \sqrt{E_K E_\pi - \vec{p}_K \cdot \vec{p}_\pi} \quad (\text{A.7})$$

In particular the energy of the parent particle is given by (A.8).

$$E_{D^0} = \sqrt{(\vec{p}_K + \vec{p}_\pi)^2 + M_{K\pi}^2} \quad (\text{A.8})$$

On the other hand, for the calculation of the energy of the daughter K (and of the π), the energy is calculated by using the nominal mass values of $m_K = 0.493 \text{ GeV}/c^2$ ($m_\pi = 0.140 \text{ GeV}/c^2$) and the (A.9).

$$E_{K,\pi} = \sqrt{p_{K,\pi}^2 + m_{K,\pi}^2} \quad (\text{A.9})$$

A.4 Energy in the Center of Mass for Fixed Target and Collider Experiments

Let E_1 be the energy of the beam of particles m_1 that hit particles of mass m_2 with E_2 . The energy at the CMS can be calculated using the square of the 4 momenta, as expressed below, in the laboratory frame.

$$\begin{aligned} p^\mu p_\mu &= E_{\text{TOT}}^2 - \vec{p}_{\text{TOT}}^2 \\ &= (E_1 + E_2)^2 - (\vec{p}_1 + \vec{p}_2)^2 \\ &= p_1^2 + m_1^2 + p_2^2 + m_2^2 + 2E_1 E_2 - (p_1^2 + p_2^2 + 2\vec{p}_1 \cdot \vec{p}_2) \\ &= m_1^2 + m_2^2 + 2(E_1 E_2 - \vec{p}_1 \cdot \vec{p}_2) \end{aligned} \quad (\text{A.10})$$

In the center of mass the invariant mass is given by (A.11).

$$p^\mu p_\mu = \tilde{E}_{\text{TOT}}^2 - \tilde{\vec{p}}_{\text{TOT}}^2 \quad (\text{A.11})$$

Since in the CMS the total momentum is $|\vec{p}_{\text{TOT}}| = 0$ then (A.11), is transformed into (A.12).

$$p^\mu p_\mu = \tilde{E}_{\text{TOT}}^2 \quad (\text{A.12})$$

Since the quantity $p^\mu p_\mu$ is invariant, relations (A.12) and (A.10) are equal, yielding:

$$\tilde{E}_{\text{TOT}}^2 = m_1^2 + m_2^2 + 2(E_1 E_2 - \vec{p}_1 \cdot \vec{p}_2) \quad (\text{A.13})$$

Furthermore we distinguish the two separate cases: for fixed target and collider.

A.4.1 Fixed Target

For the fixed target experiment, we can consider that $|\vec{p}_2| = 0$ yielding $E_2 = m_2$. Therefore, (A.13) is transformed into (A.14).

$$\tilde{E}_{\text{TOT}} = \sqrt{m_1^2 + m_2^2 + 2E_1 m_2} \quad (\text{A.14})$$

In the ultra-relativistic regime where $E_1 \gg m_1, m_2$ then the available energy (A.14), in the center of mass (CMS) is a function of the square root of the colliding energy beam ($\sqrt{E_1}$) for a given target mass m_2 .

A.4.2 Collider

In the case of a collider, there are two anti parallel beams of (E_1, p_1) and (E_2, p_2) , with $\vec{p}_1 \uparrow\downarrow \vec{p}_2$. Therefore (A.13), becomes (A.15).

$$\tilde{E}_{\text{TOT}} = \sqrt{2(E_1 E_2 + |\vec{p}_1||\vec{p}_2|) + m_1^2 + m_2^2} \quad (\text{A.15})$$

In the ultra-relativistic limit $p \rightarrow E$ or equivalently $m \rightarrow 0$, yields (A.16).

$$\tilde{E}_{\text{TOT}} = \sqrt{4E_1 E_2} \quad (\text{A.16})$$

Finally in the case of equal energy beams ($E_1 = E_2 = E$), the available energy \tilde{E}_{TOT} is only a function of the $2E$. As a graphical representation, Figure A.1 depicts both cases (fixed target and collider) concerning the available energy at the CMS \sqrt{s} as a function of the E . In Table A.1 it is depicted the values of the energies in collisional and fixed target experiments used in heavy-ion physics.

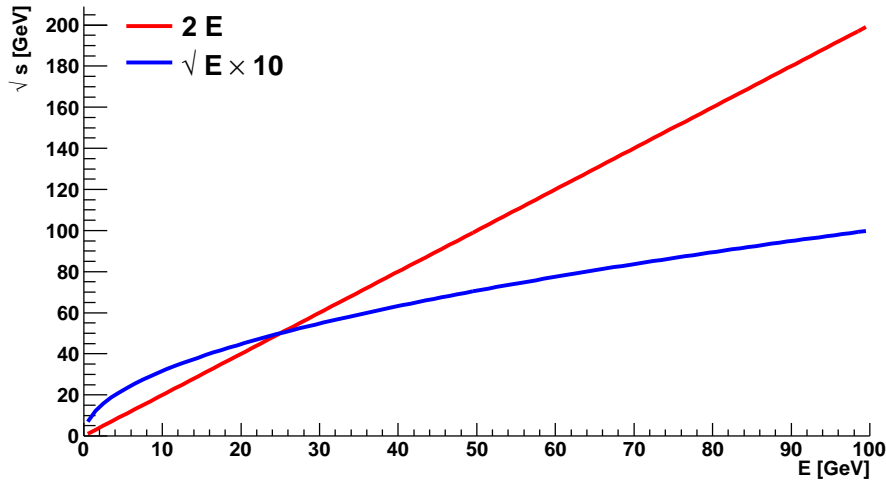


FIG. A.1: Available energy at the CMS (\sqrt{s}) as a function of the energy (E) of the incident beams, for the collider $E_1 = E_2 \equiv E$ (red line) and for fixed target (blue line) cases. Let us note that in the latter case the mass of the target is considered to be $m_2 = 50 \text{ GeV}/c^2$, hence the multiplication factor.

TAB. A.1: Characteristics of heavy ion experiments. Available energy in the CMS per nucleon pair ($\sqrt{s_{\text{NN}}}$) and energy density ε . Values taken from [Aurenche 05].

| | AGS | SPS | RHIC | LHC |
|------------------------------|--------------|--------------|----------|----------|
| operational year | 1992 | 1994 | 2001 | 2010 |
| | fixed target | fixed target | collider | collider |
| Circumference [km] | 0.8 | 7.0 | 4.6 | 27.0 |
| Colliding species | Au+Au | Pb+Pb | Au+Au | Pb+Pb |
| $\sqrt{s_{\text{NN}}}$ [GeV] | 4.8 | 17.3 | 200 | 5500 |

Appendix B

B.1 Isotropic Decay

Let us consider the angle of the emission of a particle between the momentum of the particle and a given vector. By *isotropic* decay, we refer to the constant angular distribution of the particle emission in that frame, regardless of the position in space, where the detection takes place. In particular: $\frac{dN}{d\Omega} = \mathbb{C}$, where \mathbb{C} is a constant and the solid angle is defined as $d\Omega = d\phi d(\cos\theta)$.

$$\frac{dN}{d\Omega} = \frac{dN}{d\phi d\cos\theta} = \frac{dN}{d\phi d\theta} \frac{1}{\frac{d\cos\theta}{d\theta}} = -\frac{1}{\sin\theta} \frac{dN}{d\phi d\theta} \propto \frac{1}{\sin\theta} \frac{dN}{d\theta}$$

yielding:

$$\frac{dN}{d\theta} \propto \sin\theta \quad (\text{B.1})$$

Since $\frac{dN}{d\theta} = -\frac{dN}{d\cos\theta} \sin\theta$ and using (B.1), yields $\frac{dN}{d\cos\theta} \propto \mathbb{M}$, with \mathbb{M} a constant. Therefore the isotropic decay distribution is flat in $\cos\theta$ but not in θ as can be observed in Figure B.1.

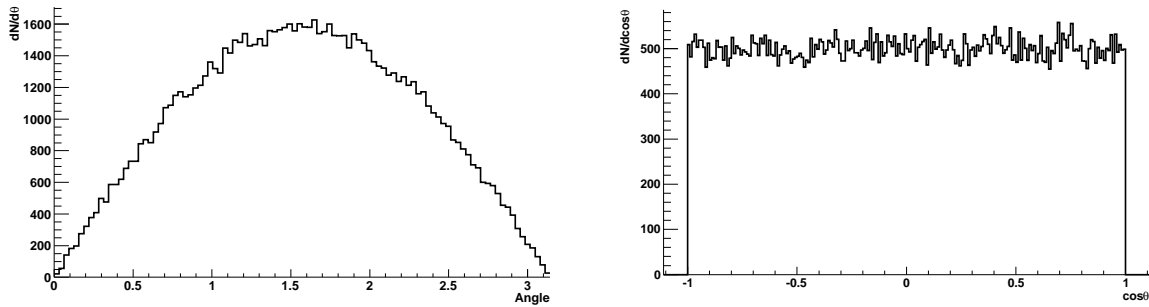


FIG. B.1: Distribution of the angle θ (left) and $\cos\theta$ (right) for the case of an isotropic decay. Plots created using pseudo-random numbers.

B.2 Sagitta

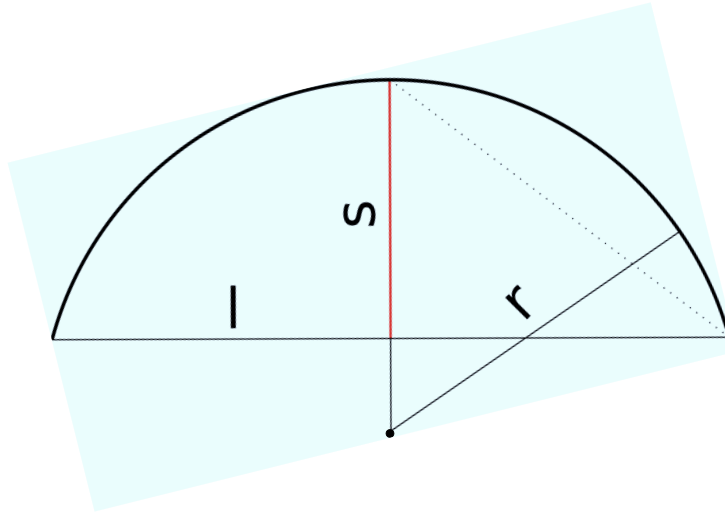


FIG. B.2: Cartoon depicting the sagitta (s) of a track, the half length of the base of the arc (l) and the radius of the circle (r). Figure taken from [Rursus 10].

In the transverse plane ($r-\phi$) the track of a charged particle, can be projected as a circular arc, as shown Figure B.2, under the influence of the magnetic field B_z . By *sagitta* we refer to the depth of an arc given by (B.2).

$$s = r - \sqrt{r^2 - l^2} \quad (\text{B.2})$$

The transverse momentum of a track can be related to the sagitta. In particular, if we consider the p_T calculation given by (2.2) and that all the tracks are charged with $\pm|q_e|$. Putting all these together, yields for the value of the sagitta s [m]:

$$s = \frac{1}{\lambda} \left[p_T - \sqrt{p_T^2 - (\lambda l)^2} \right] \quad (\text{B.3})$$

where p_T is measured in [GeV/c]. In the case of the magnetic field $B_z = 0.5 \text{ T}$ —like in the STAR detector—and for a positive charged track ($+q_e$), the constant is $\lambda = 0.15 \text{ GeV/m}$. In addition in Figure B.3, it is shown the distribution of the sagitta s for the different transverse lengths l as a function of the p_T of the track, calculated by (B.3). In Table B.1 the values of the sagitta s are summarized for various p_T and transverse track length l .

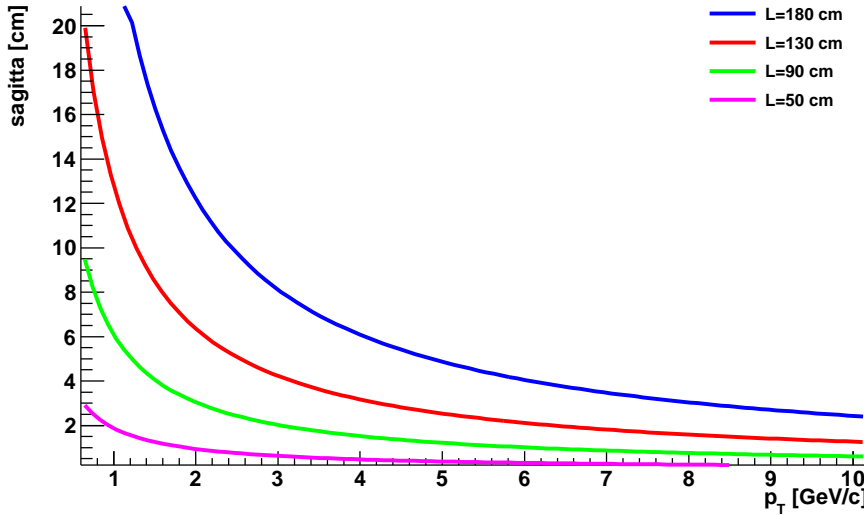


FIG. B.3: Plots of the sagitta s as a function of the transverse momentum p_T and for the different transverse track lengths l : 180 cm (blue), 130 cm (red), 90 cm (green), and 50 cm (magenta). Calculated by (B.3). The magnetic field is considered to be $B_z = 0.5$ T.

TAB. B.1: Sagitta s values of the tracks as a function of the radius r , the transverse momentum p_T and the curvature κ , for the magnetic field of 0.5 T. Also the ratio s/r is given in [%]. The transverse track length l is considered to be fixed at 180 cm.

| p_T [GeV/c] | s [cm] | r [cm] | κ [cm $^{-1}$] | s/r [%] |
|---------------|----------|----------|------------------------|-----------|
| 0.61 | 42 | 407 | 0.00246 | 10.31 |
| 0.72 | 35 | 480 | 0.00208 | 7.29 |
| 0.99 | 25 | 660 | 0.00151 | 3.78 |
| 1.23 | 20 | 820 | 0.00121 | 2.43 |
| 1.36 | 18 | 909 | 0.00110 | 1.98 |
| 1.53 | 16 | 1020 | 0.00097 | 1.56 |
| 3.04 | 8 | 2029 | 0.00049 | 0.39 |
| 6.08 | 4 | 4052 | 0.00024 | 0.09 |
| 8.10 | 3 | 5402 | 0.00018 | 0.05 |
| 11.0 | 2 | 7333 | 0.00013 | 0.0002 |

C.1 The Uniform Distribution

Let us consider the case where the variable x is equally distributed, among the interval $[a, b]$, following the *uniform* distribution. The probability density function $f(x)$ is given by (C.1).

$$f(x) = \begin{cases} \mathcal{K}, & a \leq x \leq b \\ 0, & \text{otherwise} \end{cases} \quad (\text{C.1})$$

let be \mathcal{K} a constant. The normalization of the function $f(x)$ imposes that

$$\int_a^b dx f(x) = 1 \quad (\text{C.2})$$

yielding

$$\mathcal{K} = \frac{1}{b - a} \quad (\text{C.3})$$

The mean value is given by (C.4)

$$\langle x \rangle \equiv \int_a^b dx x f(x) \quad (\text{C.4})$$

or equivalently

$$\langle x \rangle = \mathcal{K} \frac{x^2}{2} \Big|_a^b = \frac{1}{b - a} \frac{b^2 - a^2}{2} = \frac{b + a}{2} \quad (\text{C.5})$$

In order to calculate the *variance* given by (C.6)

$$\sigma^2 = \langle x^2 \rangle - \langle x \rangle^2 \quad (\text{C.6})$$

first we have to calculate the quantity

$$\langle x^2 \rangle = \int_a^b dx x^2 f(x) \quad (\text{C.7})$$

therefore

$$\langle x^2 \rangle = \mathcal{K} \frac{x^3}{3} \Big|_a^b = \frac{1}{b-a} \frac{b^3 - a^3}{3} = \frac{1}{3}(a^2 + ab + b^2) \quad (\text{C.8})$$

The variance then becomes:

$$\sigma^2 = \frac{1}{3}(a^2 + ab + b^2) - \frac{(b+a)^2}{4} = \frac{1}{12}(a-b)^2 \quad (\text{C.9})$$

Finally accepting the non negative roots of (C.9), the *standard deviation* is given by (C.10).

$$\sigma = \frac{|a-b|}{\sqrt{12}} \quad (\text{C.10})$$

For the case where $a = 0$, $b = 1$, $\langle x \rangle = 0.5$ and $\sigma = \frac{1}{\sqrt{12}}$ as it is graphically depicted in Figure C.1.

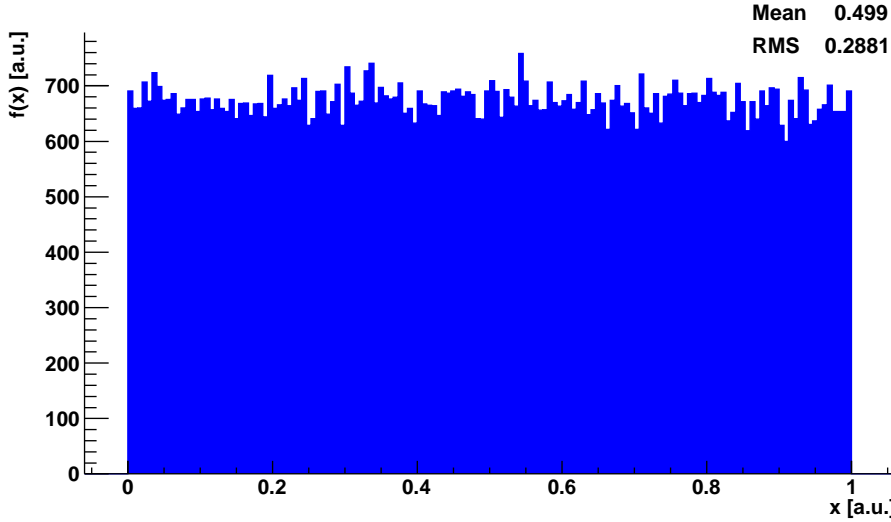


FIG. C.1: Constant distribution of pseudo-random number within the interval $[0, +1]$. The mean value is $\langle x \rangle = 0.5$ and the standard deviation $\sigma = \frac{1}{\sqrt{12}} \simeq 0.288$.

D.1 Helix Parameterization

The trajectory of a charged particle in a static uniform magnetic field with $\vec{B} = (0, 0, B_z)$ is a helix. In principle five parameters are needed to define such a helix [van Buren 06]. From the various possible parameterizations we describe here the version which is well suited for the geometry of a collider experiment and therefore used for the implementation of the StHelix class. This parameterization describes the helix in Cartesian coordinates, where x, y and z are expressed as functions of the track length (s). In particular it is defined:

$$x(s) = x_0 + \frac{1}{\kappa} [\cos(\Phi_0 + h s \kappa \cos \lambda) - \cos \Phi_0] \quad (\text{D.1})$$

$$y(s) = y_0 + \frac{1}{\kappa} [\sin(\Phi_0 + h s \kappa \cos \lambda) - \sin \Phi_0] \quad (\text{D.2})$$

$$z(s) = z_0 + s \sin \lambda \quad (\text{D.3})$$

The following variables are also defined and will be used from now on:

s is the path length along the helix;

x_0, y_0, z_0 is the starting point at $s = s_0 = 0$;

λ is the dip angle;

κ is the curvature, i.e. $\kappa = 1/R$;

B is the z component of the homogeneous magnetic field $B = (0, 0, B_z)$;

q is charge of the particle in units of positron charge;

h is the sense of rotation of the projected helix on the transverse (xy) plane taking into account the charge q and the magnetic field B , i.e. $h = -\text{sgn}(q \cdot B) = \pm 1$;

Φ_0 is the azimuth angle of the starting point (in cylindrical coordinates) with respect to the helix axis: $\Phi_0 = \Psi - h\pi/2$; and

Ψ is the arctan $\frac{dy}{dx} \Big|_{s=0}$, i.e. the azimuthal angle of the track direction at the starting point.

The meaning of the different parameters is visualized in Figure D.1.

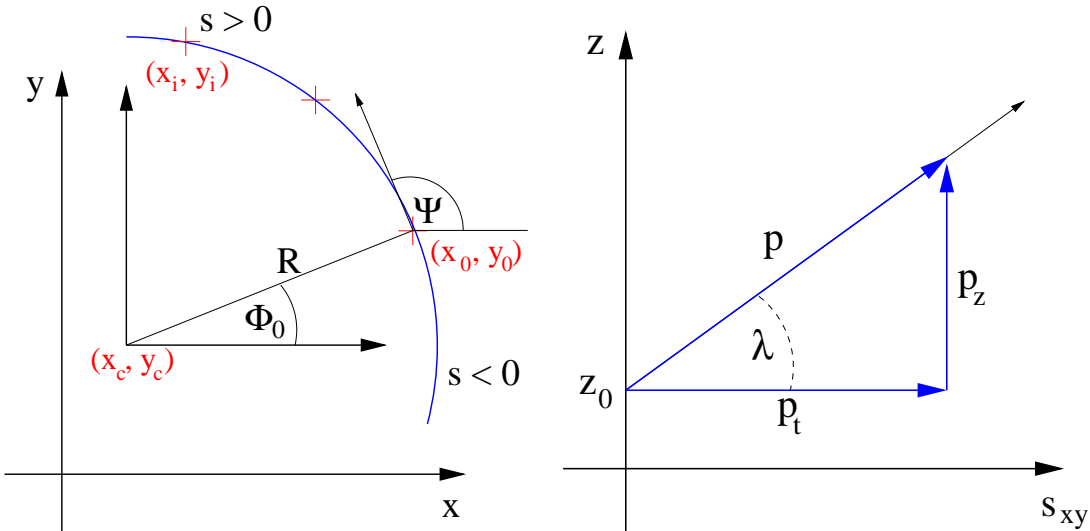


FIG. D.1: Helix parameterization. *Left:* Projection of a helix on the xy -plane. The crosses mark possible data points. *Right:* Projection of a helix on the sz -plane.

D.2 Calculation of the Particle Momentum

The circle fit in the xy -plane gives the center of the fitted circle (x_c, y_c) and the curvature $\kappa = 1/R$ while the linear fit gives the values of z_0 and $\tan \lambda$. The phase of the helix (cf. Figure D.1) is defined as follows:

$$\Phi_0 = \arctan \frac{y_0 - y_c}{x_0 - x_c} \quad (\text{D.4})$$

The reference point (x_0, y_0) is then calculated as follows:

$$x_0 = x_c + \frac{\cos \Phi_0}{\kappa} \quad (\text{D.5})$$

$$y_0 = y_c + \frac{\sin \Phi_0}{\kappa} \quad (\text{D.6})$$

and the helix parameters can be evaluated as:

$$\Psi = \Phi_0 + h\pi/2 \quad (\text{D.7})$$

$$p_\perp = c q B/\kappa \quad (\text{D.8})$$

$$p_z = p_\perp \tan \lambda \quad (\text{D.9})$$

$$p = \sqrt{p_\perp^2 + p_z^2} \quad (\text{D.10})$$

where κ is the curvature in $[\text{m}^{-1}]$, B the value of the magnetic field in $[\text{T}]$, c the speed of light in $[\text{m/ns}]$ (≈ 0.3) and p_\perp and p_z are the transverse and longitudinal momentum in $[\text{GeV}/c]$.

D.3 Distance Measurement Between a Point and a Helix

The minimal squared distance M_i between a helix and a point i with position (x_i, y_i, z_i) is given by

$$M_i = M_i^{(xy)} + M_i^{(z)} \quad (\text{D.11})$$

$$M_i = [x_i - x(s')]^2 + [y_i - y(s')]^2 + [z_i - z(s')]^2 \quad (\text{D.12})$$

In literature one finds the following approach to solve this problem analytically by neglecting $M_i^{(z)}$ in the derivatives.

$$\frac{dM_i^{xy}}{ds} = 0 \quad (\text{D.13})$$

This formula can only serve to derive an approximation for the real distance. For large dip angles the errors become large depending also on the actual helix parameters. The advantage is that s' can be calculated analytically:

$$s' = \frac{1}{h\kappa \cos \lambda} \arctan \frac{(y_i - y_0) \cos \Phi_0 - (x_i - x_0) \sin \Phi_0}{1/\kappa + (x_i - x_0) \cos \Phi_0 + (y_i - y_0) \sin \Phi_0} \quad (\text{D.14})$$

Note, that this formula can **not** be used to derive the distance of closest approach to a point. In order to derive the distance of closest approach the following equation has to be solved:

$$\frac{dM_i}{ds} = 0 \quad (\text{D.15})$$

which can be written as

$$\begin{aligned} & 2 \left(x_i - x_0 - \frac{\cos(\Phi_0 + hs\kappa \cos \lambda) - \cos \Phi_0}{\kappa} \right) \sin(\Phi_0 + hs\kappa \cos \lambda) h \cos \lambda - \\ & 2 \left(y_i - y_0 - \frac{\sin(\Phi_0 + hs\kappa \cos \lambda) - \sin \Phi_0}{\kappa} \right) \cos(\Phi_0 + hs\kappa \cos \lambda) h \cos \lambda - \\ & 2 (z_i - z_0 - s \sin \lambda) \sin \lambda = 0 \end{aligned} \quad (\text{D.16})$$

The root of (D.16) can easily be found with the Newton or *regula falsi* method with s' from (D.14) as starting value. For the Newton method the second derivative is needed as well.

$$\frac{d^2 M_i}{ds^2} = 0 \quad (\text{D.17})$$

which is

$$\begin{aligned} & 2 (\sin(\Phi_0 + hs\kappa \cos \lambda))^2 h^2 \cos^2 \lambda + \\ & 2 \left(x_i - x_0 - \frac{\cos(\Phi_0 + hs\kappa \cos \lambda) - \cos \Phi_0}{\kappa} \right) \\ & \cos(\Phi_0 + hs\kappa \cos \lambda) h^2 \kappa \cos^2 \lambda + \\ & 2 (\cos(\Phi_0 + hs\kappa \cos \lambda))^2 h^2 \cos^2 \lambda + \\ & 2 \left(y_i - y_0 - \frac{\sin(\Phi_0 + hs\kappa \cos \lambda) - \sin \Phi_0}{\kappa} \right) \\ & \sin(\Phi_0 + hs\kappa \cos \lambda) h^2 \kappa \cos^2 \lambda + \\ & 2 \sin^2 \lambda = 0 \end{aligned} \quad (\text{D.18})$$

D.4 Distance of Closest Approach Between Two Helices

The closest distance between two helices \mathbf{H}_1 and \mathbf{H}_2 is a problem which again can be solved analytically only in 2 dimensions, i.e. in the xy -plane, (cf. Figure D.2). The solution in 3 dimensions cannot even be solved by standard numerical methods (as the Newton method) but requires a more sophisticated method since we have to find 2 unknown parameters, namely the s_1 and s_2 in

$$\frac{d^2 M(s_1, s_2)}{ds_1 ds_2} = 0 \quad (\text{D.19})$$

where M is the distance between the two helices at s_1 and s_2 .

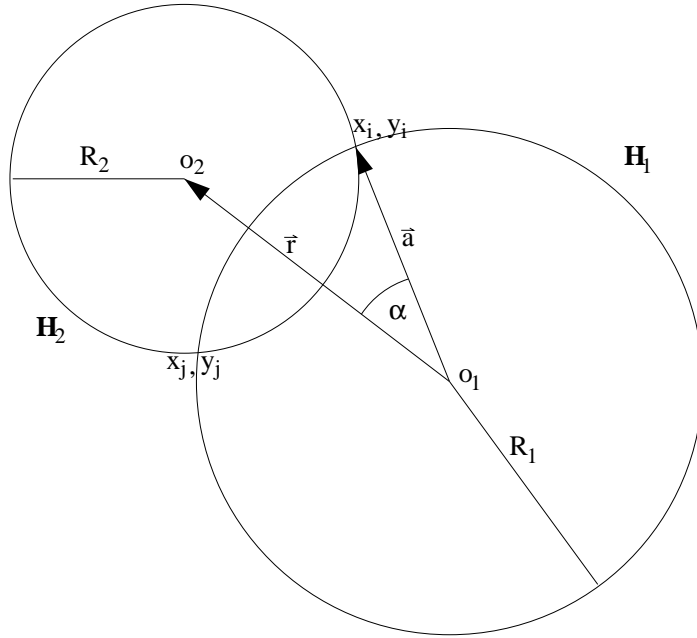


FIG. D.2: Cartoon of the two intersecting helices in the transverse (xy) plane.

D.4.1 In the Transverse Plane

Given two helices with radii R_1 and R_2 and centers in the xy plane $O_1 = (x_{c_1}, y_{c_1})$ and $O_2 = (x_{c_2}, y_{c_2})$ we have to find the vector \vec{a} as depicted in Figure D.2. The angle α can be therefore calculated as:

$$\cos \alpha = \frac{R_1^2 + |\vec{r}|^2 - R_2^2}{2R_1|\vec{r}|} \quad (\text{D.20})$$

where \vec{r} is the vector between the two centers. The absolute coordinates of one intersection point (measured from o_1) can be obtained by calculating vector \vec{a} and adding o_1 .

$$x_i = x_{c_1} + R_1[(x_{c_2} - x_{c_1}) \cos \alpha - (y_{c_2} - y_{c_1}) \sin \alpha] / |\vec{r}| \quad (\text{D.21})$$

$$y_i = y_{c_1} + R_1[(x_{c_2} - x_{c_1}) \sin \alpha + (y_{c_2} - y_{c_1}) \cos \alpha] / |\vec{r}| \quad (\text{D.22})$$

If $\cos \alpha = 1$ we have only one solution. For the case where $\cos \alpha < 1$, we get two valid intersection points (x_i, y_i) and (x_j, y_j) where the latter is simply given by:

$$x_j = x_{c_1} + R_1[(x_{c_2} - x_{c_1}) \cos \alpha + (y_{c_2} - y_{c_1}) \sin \alpha] / |\vec{r}|; \quad (\text{D.23})$$

$$y_j = y_{c_1} + R_1[(y_{c_2} - y_{c_1}) \cos \alpha - (x_{c_2} - x_{c_1}) \sin \alpha] / |\vec{r}|; \quad (\text{D.24})$$

In the case of $\cos \alpha > 1$, the circles do not intersect. Therefore the distance of closest approach is simply given by the intersection of a line between the two centers and the two helices. Consequently, for the helix \mathbf{H}_1 we get:

$$x = x_{c_1} + R_1(x_{c_2} - x_{c_1}) / |\vec{r}|; \quad (\text{D.25})$$

$$y = y_{c_1} + R_1(y_{c_2} - y_{c_1}) / |\vec{r}|; \quad (\text{D.26})$$

D.4.2 In 3 Dimensions

Usually an iteration method is applied which uses the intersection points in the xy -plane as start values. Care has to be taken if both helices have different dip angle λ since the start values then significantly deviate from the actual solution.

D.5 Intersection with a Cylinder ($\rho=\text{const}$)

In order to obtain the path length s at which the helix intersects with a cylinder of given radius ρ we have to solve the following equation:

$$\rho^2 = x(s)^2 + y(s)^2 \quad (\text{D.27})$$

Using (D.1) and (D.2) we obtain the two analytic solutions for s_1 and s_2 :

$$\begin{aligned} s_{1/2} = & -(\Phi_0 + 2 \arctan [\{2 y_0 \kappa - 2 \sin \Phi_0 \pm (-\kappa^2 (-4 \rho^2 + 4 y_0^2 - 2 \rho^2 \kappa^2 x_0^2 - \\ & 2 \rho^2 \kappa^2 y_0^2 + 2 x_0^2 \kappa^2 y_0^2 + \rho^4 \kappa^2 + x_0^4 \kappa^2 + y_0^4 \kappa^2 - 4 x_0^3 \kappa \cos \Phi_0 + \\ & 4 x_0^2 \cos^2 \Phi_0 - 4 y_0^2 \cos^2 \Phi_0 - 4 y_0^3 \kappa \sin \Phi_0 + 4 \rho^2 \kappa x_0 \cos \Phi_0 + \\ & 4 \rho^2 \kappa y_0 \sin \Phi_0 - 4 x_0^2 \kappa y_0 \sin \Phi_0 - 4 y_0^2 \kappa x_0 \cos \Phi_0 + \\ & 8 x_0 \cos \Phi_0 y_0 \sin \Phi_0)]^{1/2}\} / \\ & (-\rho^2 \kappa^2 + 2 + x_0^2 \kappa^2 + 2 \cos \Phi_0 + y_0^2 \kappa^2 - \\ & 2 x_0 \kappa - 2 x_0 \kappa \cos \Phi_0 - 2 y_0 \kappa \sin \Phi_0]) h^{-1} \kappa^{-1} (\cos \lambda)^{-1} \end{aligned} \quad (\text{D.28})$$

D.6 Intersection with a Plane

Any plane can be described by its normal vector \vec{n} (orientation) and an arbitrary point in this plane \vec{r} (position). The vector \vec{p} which describes the intersection point must fulfill:

$$\vec{p} \cdot \vec{n} = 0. \quad (\text{D.29})$$

Hence:

$$(\vec{a} - \vec{r}) \cdot \vec{n} = 0. \quad (\text{D.30})$$

where \vec{a} is given by $\vec{a} = (x(s'), y(s'), z(s'))$ as described in (D.1)–(D.3). In order

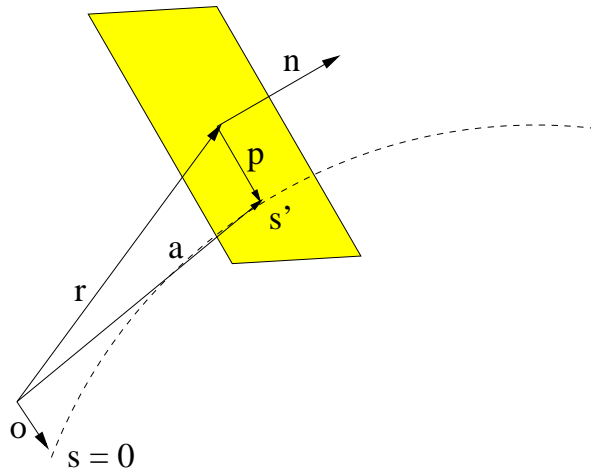


FIG. D.3: Sketch depicting the intersection of a helix with a plane.

to obtain the path length s' where the helix intersects with the plane the following equation has to be solved:

$$\begin{aligned} x(s)n_x + y(s)n_y + z(s)n_z - \vec{r} \cdot \vec{n} &= \\ A + n_x \cos S + n_y \sin S + \kappa s n_z \sin \lambda &= 0 \end{aligned} \quad (\text{D.31})$$

where:

$$A = \kappa(\vec{o} \cdot \vec{n} - \vec{r} \cdot \vec{n}) - n_x \cos \Phi_0 - n_y \sin \Phi_0 \quad (\text{D.32})$$

$$S = h s \kappa \cos \lambda + \Phi_0 \quad (\text{D.33})$$

The root of (D.31) can now easily be determined by a suitable numerical method (Newton).

D.7 Limitations

The only non-numerical limitations of this parameterization are:

$$-\pi/2 < \lambda < \pi/2 \quad (\text{D.34})$$

$$\kappa > 0 \quad (\text{D.35})$$

D.8 The Case of the Absence of the Magnetic Field

For the special case $B = 0$ the trajectory becomes a straight line, i.e. $\kappa = 0$ and $R = \infty$. Care must be taken in the numerical calculation of the parameterization because of the singularity in (D.1) and (D.2). The correct form is:

$$x(s) = x_0 - sh \cos \lambda \sin \Phi_0 \quad (\text{D.36})$$

$$y(s) = y_0 + sh \cos \lambda \cos \Phi_0 \quad (\text{D.37})$$

$$z(s) = z_0 + s \sin \lambda \quad (\text{D.38})$$

Important: For $B = 0$ the sense of rotation is ill defined. All what matters is that $\Phi_0 = \Psi - h\pi/2$ is done correctly, i.e. with the same arbitrary h . In the following we assume $h = +1$ for convenience then (D.14) reads as:

$$s' = \frac{1}{\cos \lambda} [(y_i - y_0) \cos \Phi_0 - (x_i - x_0) \sin \Phi_0] \quad (\text{D.39})$$

Finally (D.16) can now be solved analytically.

$$\frac{dM_i^{\text{DCA}}}{ds} = 0 \quad (\text{D.40})$$

yielding

$$s^{\text{DCA}} = \cos \lambda \cos \Phi_0 (y_i - y_0) - \cos \lambda \sin \Phi_0 (x_i - x_0) + \sin \lambda (z_i - z_0) \quad (\text{D.41})$$

The solution for the intersection with a cylinder (D.28) now reads:

$$\begin{aligned} s_{1/2} = & \cos^2 \lambda \{ x_0 \cos \lambda \sin \Phi_0 - y_0 \cos \lambda \cos \Phi_0 \pm \\ & [-\cos^2 \lambda (2x_0 \cos \Phi_0 y_0 \sin \Phi_0 - \rho^2 + y_0^2 - y_0^2 \\ & \cos^2 \Phi_0 + x_0^2 \cos^2 \Phi_0)]^{1/2} \} \end{aligned} \quad (\text{D.42})$$

The same holds for the intersection of a helix with a plane where in the case of zero curvature, (D.31) can then be solved analytically.

$$s' = \frac{\vec{r} \cdot \vec{n} - \vec{o} \cdot \vec{n}}{-n_x \cos \lambda \sin \Phi_0 + n_y \cos \lambda \cos \Phi_0 + n_z \sin \lambda} \quad (\text{D.43})$$

Appendix E

E.1 Track Fitting

In the xy plane the helix projection is represented by an arc of a circle. In any of the planes parallel to the z -axis, the track trajectory is a section of a sinusoidal curve. A high p_T track (e.g. for $p_T > 3 \text{ GeV}/c$) has a relatively small curvature (Appendix B.2). Tracks with lower p_T (which are a majority of those seen in STAR) are visibly curved. At this point the tracks found by the tracking algorithm (all called *global* tracks, as no information other than their TPC hits are used in the track finding). The tracks are refitted using a Kalman filter algorithm [Lisa 96]. The track passes through the Kalman filter three times. In the first pass, the calculation of the proximity of the points to the fitted curve is performed. On the second pass, all the distortions due to the field non-uniformities, the average energy loss and the multiple scattering of the electrons in the material are taken into account. Finally, on the third pass of the fitter, the track is smoothed and the fit is used to calculate the optimal particle trajectory. This means that the track's fit points include an extra hit, the primary vertex. In addition, the STAR software labels the track as *primary* if the distance of closest approach (DCA) of the tracks to the primary vertex is less than DCA<3 cm. The main difference between *global* and *primary* tracks is the usage of primary vertex as measurement in the track parameter fit. The global tracks don't use the vertex position in fit [Pruneau 03].

Appendix F

F.1 Introduction

We present the results of signal and noise for a given ladder and the set of wafers for the SSD of the *low multiplicity* run 8120057 of Au+Au at $\sqrt{s_{\text{NN}}} = 200 \text{ GeV}$. A description of the detector can be found at Section 2.10. We examine 1000 events and the detector raw hits plot can be seen in Figure F.1 both in 3D and 2D.

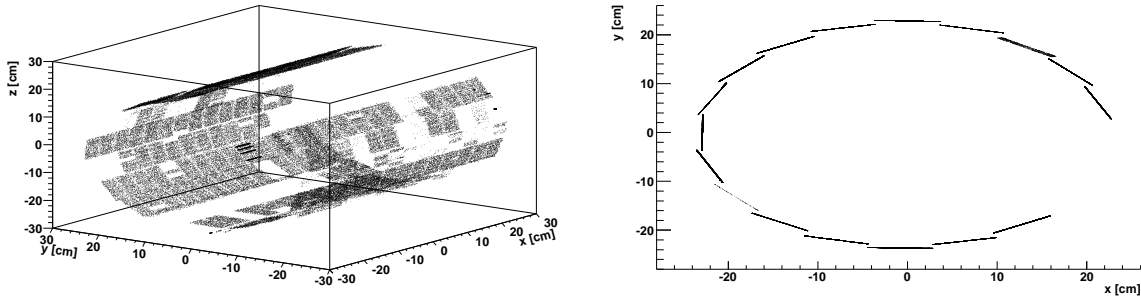


FIG. F.1: 3D (left) and 2D (right) depiction of SSD raw hits in global STAR coordinates $\{xg, yg, zg\}$ and for 1000 events of run 8120057 of Au+Au at $\sqrt{s_{\text{NN}}} = 200 \text{ GeV}$.

F.2 Signal and Noise vs. Strips for the Selected Wafers

Concerning the ladder 03, both sides (n and p) for the wafers: $\{5, 6, 8, 9 \text{ and } 10\}$ the signal of each strip (in ADC units) is depicted in Figure F.2 (in green dots) along with the noise (in black error bars).

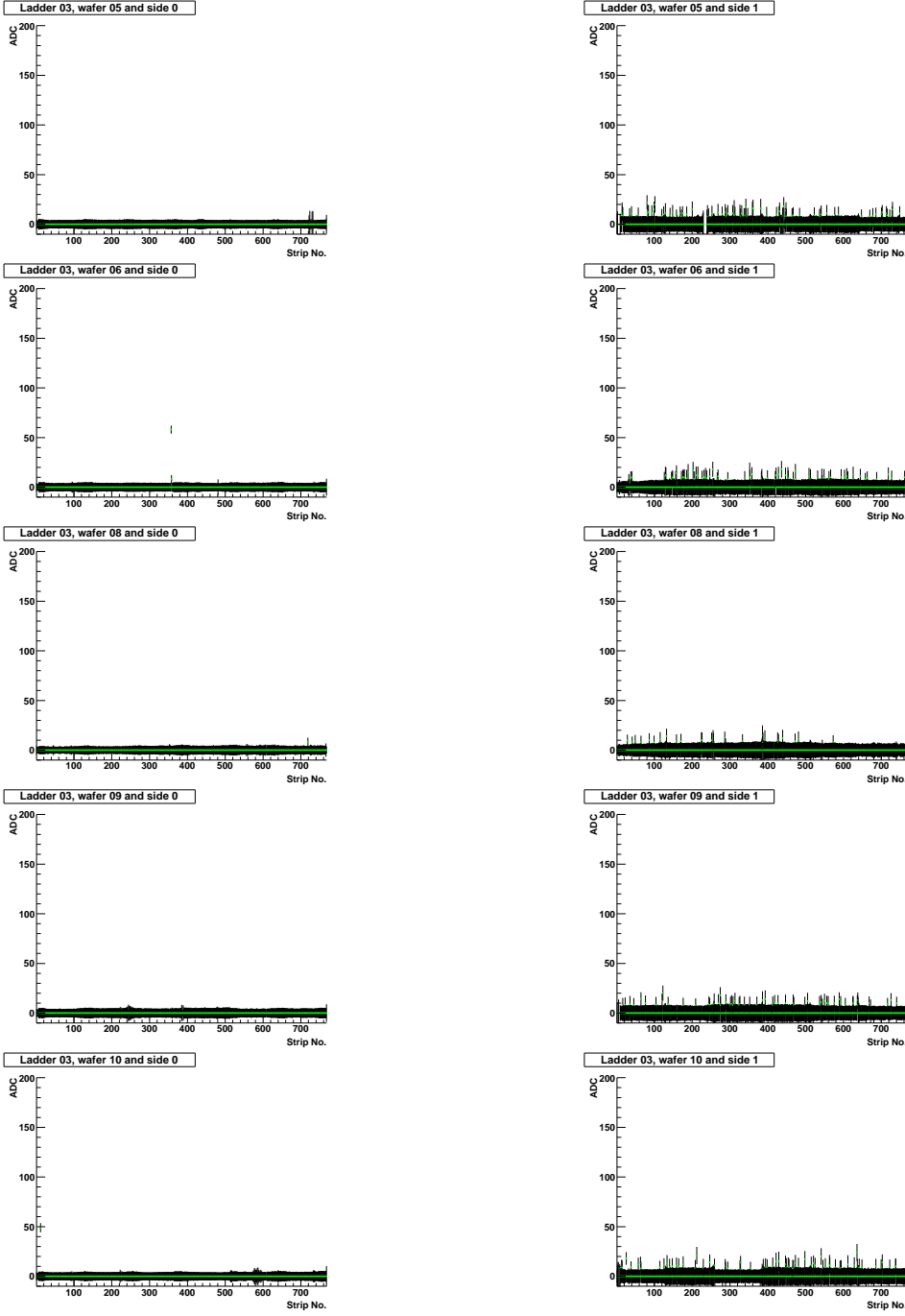


FIG. F.2: Fired strips (green) along with noise for every strip (black errors bars), for ladder 3 and wafers: {5, 6, 8, 9 and 10}, for the *p* (left) and *n* (right) side. Data is taken from 1 event of the *low luminosity* run 8120057, Au+Au at $\sqrt{s_{\text{NN}}} = 200$ GeV (run VII).

F.3 Noise Distribution for the Selected Wafers

For the total sum of 1000 events from run 8120057, we present the noise distribution of wafers $\{5, 6, 8, 9\}$ and 10 of ladder 3 in Figure F.3.

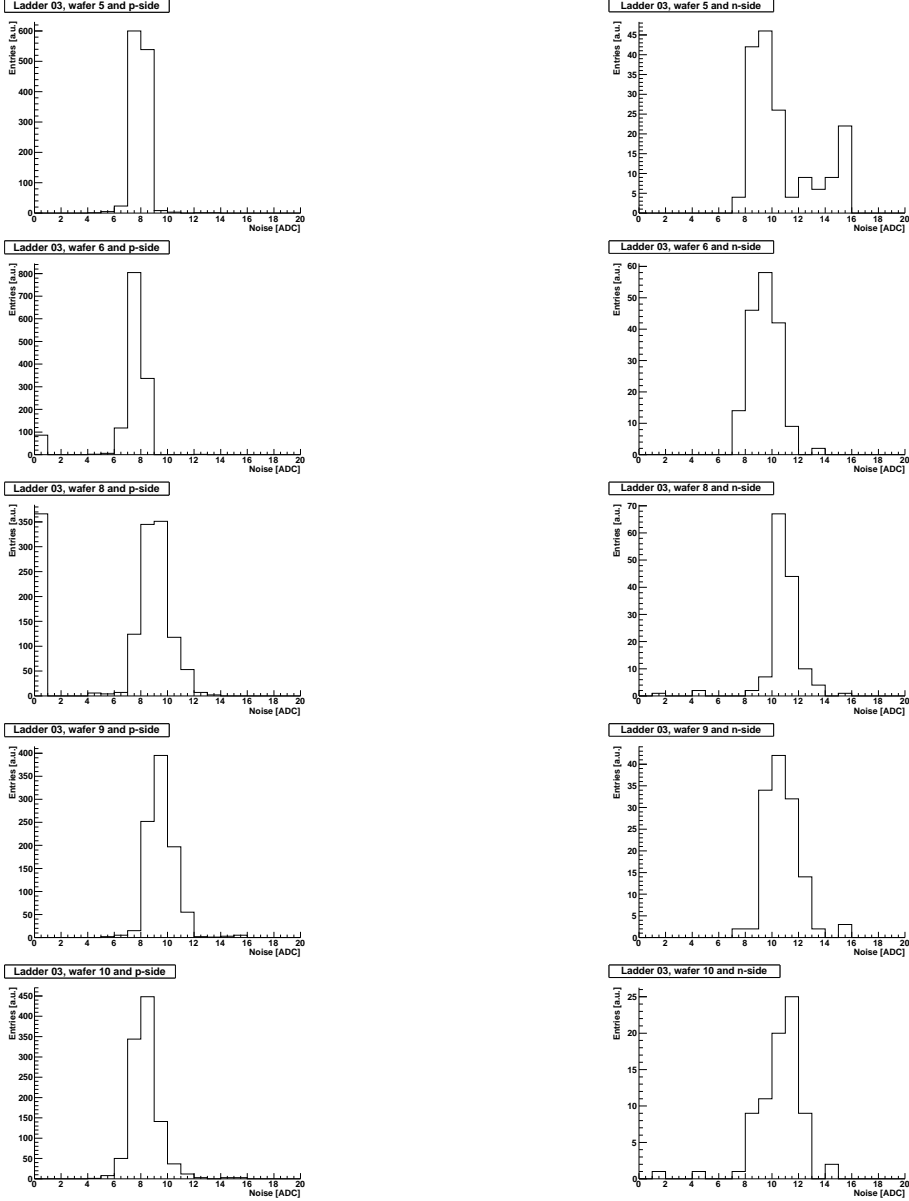


FIG. F.3: Overall noise distribution for wafers $\{5, 6, 8, 9\}$ and 10 belonging to ladder 3, for both sides p (*left*) and n (*right*). The n side exhibits more noisy behavior compared to the p side. The data is collected from 1000 events of the *low luminosity* run 8120057, Au+Au at $\sqrt{s_{NN}} = 200$ GeV (run VII).

Index

- StHelix, 231
- TSpectrum, 181
- regula falsi*, 234
- AGS, 6, 23, 198, 224
- asymptotic freedom, 4
- atom
 - pentavalent, 34
 - trivalent, 35
- Azimuthal correlation
 - probe side, 19
 - trigger side, 19
- BBC, 32
- beam halo, 32
- Bethe-Bloch, 42, 209
- Bjorken, 7, 16
- BNL, 17
- Booster, 23
- bottomonium, 10
- BRAHMS, 27, 199
- calorimetry, 48
 - BEMC, 49, 65, 204
 - distance of cell to track, 70
 - towers, 16
 - BPRS, 50
 - BSMD, 51
 - EEMC, 48, 204
 - EPSD, 49
 - ESMD, 49, 204
 - shower
- electromagnetic, 68
- hadronic, 68
- charmonium, 10, 17, 200
- Cherenkov, 27, 28, 200
- chiral symmetry, 13
- CMOS, 57
- CMS, 221, 222
- collisional energy density, 16
- color
 - factors, 3
 - octet, 3
 - singlet, 2
- coplanarity, 87
- COSTAR, 41
- CTB, 33
- DAQ1000, 58
- dca, 187, 233
 - dca between helices
 - see dca, 235
 - dead-cone effect, 17
 - deflection angle, 92
 - dileptons, 12, 199
 - Drell-Yan, 12
 - drift chambers, 28
 - drift velocity, 47
- EEMC, 48
- effective charge, 42
- electron
 - bremsstrahlung, 42

- non photonic, 187
- discrimination, 68
- particle identification of, 66
- photonic, 71
- FGT, 53
- FMS, 52
- FONLL, 163
- freeze-out
 - chemical, 12
 - kinetic, 11
 - thermal, 12
- FTPC, 47, 201
- Glauber model, 13, 63
- gluon, 1
 - bremsstrahlung, 10, 17, 196
- Gottfried-Jackson, 221
- helix, 83
 - dip angle, 83
 - path length, 231
 - phase, 232
- HFT, 57, 216
- impact parameter, 33
- intrinsic resolution, 39
- ionization, 42
 - gas, 43
- isotropic decay, 225
- IST, 57
- jet quenching, 10, 187
- Kalman filter, 29, 239
- kapton, 41, 71
- LHC, 224
- Linac, 23
- loopers, 211
- luminosity, 17
- Markov
- chain, 181
- process, 181
- MCS, 92
- meson
 - bottom
 - Υ , 10
 - charmed
 - J/ψ , 10
 - D^0 , 61
 - neutral
 - π^0 , 48
 - vector
 - decay of, 56
- microvertexing, 83
- MinuitVF, 59
- MIP, 39, 46, 49, 206
- MRPC, 54, 56
- MTD, 56
- multiplicity
 - of neutrons, 31
 - in collisions of
 - Au+Au, 63
 - Cu+Cu, 63
 - d+Au, 63
 - p+p, 63
- muon
 - arms, 28
 - bremsstrahlung, 56
 - identifier, 28
 - spectrometers, 28
 - tracker, 28
- MWPC, 43, 51, 201
- Nuclear Modification Factor, 13
- P10, 44, 203
- parton, 7, 197, 198
- PHENIX, 28, 199
- PHOBOS, 25, 198
- photon
 - γ discrimination, 48

- direct, 11
- pile up, 45, 59
- PMT, 57
- PPV, 59
- PSD, 204
- pseudo-random numbers, 225, 230
- pseudorapidity, 15
- pVPD, 57
- QCD, 1
 - in lattice, 6, 193
 - Lagrangian, 2
 - phase diagram of, 6
- QGP, 9
- quark, 1
 - bottom, 19
 - charm, 17, 19
 - condensate, 13
 - confinement, 3
 - deconfinement, 6, *see* asymptotic freedom
 - energy loss, 187
 - fragmentation, 19
 - strange, 10
 - enhancement of, 10
- rapidity, 15
- RHIC, 6, 17, 23, 198, 224
- ROOT, 181
- Running Coupling Constant, 3
- sagitta, 92, 226
- saturation, 197
- semiconductor
 - doping, 34
 - n-type, 35
 - p-type, 35
 - gap band, 34
 - pn junction, 36
 - principle, 33
 - valence band, 33
- siberian snakes, 23
- Silicon Detectors, *see* SVT and SSD
- SIS, 6
- SMD, 68, 204
- spinor, 2
- SPS, 6, 198, 224
- SSD, 39, 204
 - Cluster Finder
 - Novel, 182
 - Standard, 181
- Cluster reconstruction, 182
- pulser, 42
- STAR, 29, 200
 - Trigger Levels, 30
- stopping power, 37
- SVT, 38, 215
- synchrotron, 198
- Tandem, 23
- TOF, 25, 27, 54
- TPC, 27, 43, 200
 - anode grid, 202
 - gated grid, 203
 - laser, 46, 203
 - shield grid, 202
- tracks
 - curvature, 83, 231
 - dip angle, 231
 - global, 84, 89, 149, 161, 167, 239
 - primary, 89, 161, 172, 239
 - split, 64
- transverse
 - energy, 16
 - mass, 16
 - momentum, 16
- Van de Graaff, 23
- WLS, 50
- Woods-Saxon, 13
- ZDC, 31
- zero suppression, 179

Glossary

AGS Alternate Gradient Synchrotron (at BNL)

ATR AGS to RHIC

BBC Beam Beam Counters

BEMC Barrel Electromagnetic Calorimeter

BNL Brookhaven National Laboratory

BPRS Barrel Pre Shower Detector

BR Branching Ratio

BRAHMS Broad Range Hadron Magnetic Spectrometer (at BNL)

Bremsstrahlung Emission of radiation due to the acceleration of charged particles

BSMD Barrel Shower Maximum Detector

CERN Centre Européen pour la Recherche Nucléaire—European Organisation for Nuclear Research

CMOS Complementary Metal Oxide Semiconductor

CMS Center of Mass System

COSTAR Control for STAR—Monitors the low and high voltage of the SSD

CTB Central Trigger Barrel

DAQ Data Acquisition

DC Drift Chamber

- DCA Distance of Closest Approach
- DESY Deutsches Elektronen Synchrotron—German ElectronSynchrotron
- EBIS Electron Beam Ion Source
- EEMC Endcap Electromagnetic Calorimeter
- EPRS Endcap Pre Shower Detector
- ESMD Endcap Shower Maximum Detector
- FEE Front End Electronics
- FGT Forward GEM Tracker
- FMS Forward Meson Spectrometer
- FONLL Fixed Order Next to Leading Log
- FTPC Forward Time Projection Chamber
- GEANT Geometry and Tracking—Detector description and simulation tool
- GEM Gas Electron Multiplier
- Gluons Exchange particles that carry the strong force between the nuclear constituents
- GSI Gesellschaft für Schwerionenforschung—Heavy ion research center
- HBT Hanbury-Brown and Twiss (used for particle correlation function)
- HF Heavy Flavor
- HFT Heavy Flavor Tracker
- IEEE Institute of Electrical and Electronics Engineers
- IST Intermediate Strip Tracker
- ITTF Integrated Tracker Tast Force
- LHC Large Hadron Collider (at CERN)
- LINAC Linear Accelerator
- Loopers Low-momentum charged particles that curl inside the volume of the TPC

LS Like Sign

MARS Modular Array for RHIC spectroscopy (at BNL)

MCS Multiple Coulomb Scattering

MINUIT A physics analysis tool for function minimization

MIP Minimum Ionizing Particle

MRPC Multi Resistive Plate Chamber

MRS Mid Rapidity Spectrometer

MTD Muon Telescope Detector

MUVTX Micro Vertexing

MWPC Multi Wire Proportional Chamber

NIM Nuclear Instruments and Methods

NLO Next to Leading Order

NMF Nuclear Modification Factor

NPE Non Photonic Electrons

P10 Gaz mixture of Ar and CH₄ in a 90 : 10 proportion used in the STAR TPC

Partons A quark or a gluon inside the hadron

PDG Particle Data Group

PHENIX Pioneering High Energy Nuclear Interaction Experiment (at BNL)

PID Particle Identification

Pitch The distance between two consecutive detection modules

PMD Photon Multiplicity Detector

PMT Photo Multipliers Tubes

PPV Proton Proton Vertex

PRS Pre Shower Detector

PV Primary Vertex

PVD Pseudo Vertex Detector

PWG Physics Working Group

PYTHIA Program for the generation of high-energy physics events

QA Quality Assurance

QCD Quantum Chromodynamics

QGP Quark Gluon Plasma

Quarks Elementary constituents of nuclear matter

RDO Read Out (for boards)

RHIC Relativistic Heavy Ion Collider (at BNL)

RICH Ring Imaging Cherenkov (Detector)

ROOT An object oriented framework for large scale data analysis

SIS Schwerionensynchrotron (at GSI)

SMD Shower Maximum Detector

SPS Super Proton Synchrotron (at CERN)

SSD Silicon Strip Detector

STAR Solenoid Tracker at RHIC (at BNL)

STARSIM Dedicated Simulation Package for the STAR experiment

SVT Silicon Vertex Tracker

TOF Time of Flight

TPC Time Projection Chamber

ULS Unlike Sign

VPD Vertex Position Detector

WLS Wave Length Shifting

ZDC Zero Degree Calorimeter

Bibliography

- [Abele 03] J. Abele *et al.* *The laser system for the STAR time projection chamber.* Nucl. Instrum. & Meth. Phys. Res. A, vol. 499, no. 2–3, pages 692–702, 2003. Available from <http://tinyurl.com/35btppx>.
- [Abelev 07] B. I. Abelev & for the STAR Collaboration. *Transverse Momentum and Centrality Dependence of High- p_{T} Nonphotonic Electron Suppression in Au+Au Collisions at $\sqrt{s_{\text{NN}}} = 200 \text{ GeV}$.* Phys. Rev. Lett., vol. 98, no. 19, page 192301, 2007. Available from <http://tinyurl.com/34mtw44>.
- [Abelev 08] B. I. Abelev & for the STAR Collaboration. *Charmed hadron production at low transverse momentum in Au+Au collisions at RHIC,* 2008. Available from <http://tinyurl.com/yayohw5>.
- [Ackermann 03] K. Ackermann. *The forward time projection chamber in STAR.* Nucl. Instrum. & Meth. Phys. Res. A, vol. 449, no. 2–3, pages 713–719, 2003. Available from <http://tinyurl.com/23ztu3d>.
- [Adamczyk 03] M. Adamczyk *et al.* *The BRAHMS experiment at RHIC.* Nucl. Instrum. & Meth. Phys. Res. A, vol. 499, no. 2–3, pages 437–468, 2003. Available from <http://tinyurl.com/3xrrshs>.
- [Adams 96] M. Adams *et al.* *A new detector technique using triangular scintillating strips to measure the position of minimum ionizing particles.* Nucl. Instrum. & Meth. Phys. Res. A, vol. 378, pages 131–142, 1996. Available from <http://tinyurl.com/23owvv7>.
- [Adams 03] J. Adams *et al.* *Evidence from $d + \text{Au}$ Measurements for Final-State Suppression of High- p_{T} Hadrons in Au + Au Collisions at RHIC.* Phys. Rev. Lett., vol. 91, no. 7, page 072304, Aug 2003. Available from <http://tinyurl.com/yz3ue4k>.

- [Adams 05] J. Adams & for the STAR Collaboration. *Experimental and Theoretical Challenges in the Search for the Quark Gluon Plasma: The STAR Collaboration's Critical Assessment of the Evidence from RHIC Collisions.* Nucl. Phys. A, vol. 757, page 102, 2005. Available from <http://tinyurl.com/y9mwyxo>.
- [Adare 07] A. Adare. *Energy Loss and Flow of Heavy Quarks in Au+Au Collisions at $\sqrt{s_{\text{NN}}} = 200 \text{ GeV}$.* Phys. Rev. Lett., vol. 98, no. 17, page 172301, 2007. Available from <http://tinyurl.com/2cr5794>.
- [Adcox 03] B. Adcox *et al.* *PHENIX Central Arm Tracking Detectors.* Nucl. Instrum. & Meth. Phys. Res. A, vol. 499, no. 2–3, pages 489–507, 2003. Available from <http://tinyurl.com/38jvo67>.
- [Adil 07] A. Adil & I. Vitev. *Collisional dissociation of heavy mesons in dense QCD matter.* Phys. Lett. B, vol. 649, no. 2–3, pages 139–146, 2007. Available from <http://tinyurl.com/2aomynq>.
- [Adler 01] C. Adler. *The RHIC Zero Degree Calorimeter.* Nucl. Instrum. & Meth. Phys. Res. A, vol. 470, pages 488–499, 2001. Available from <http://tinyurl.com/379rrpx>.
- [Adler 03] C. Adler *et al.* *The STAR Level-3 trigger system.* Nucl. Instrum. & Meth. Phys. Res. A, vol. 499, no. 2–3, pages 778–791, 2003. Available from <http://tinyurl.com/2vyj85w>.
- [Aggarwal 10] M. M. Aggarwal & for the STAR Collaboration. *Measurement of the Bottom contribution to non-photonic electron production in p+p collisions at $\sqrt{s} = 200 \text{ GeV}$.* 2010. Available from <http://tinyurl.com/2d4sjk6>.
- [Alessi 05] J. G. Alessi. *Progress on test EBIS and the Design of an EBIS-based RHIC Preinjector.* 21st Particle Accelerator Conference, PAC05, Knoxville, TN, USA, 2005. Available from <http://tinyurl.com/ya2me9x>.
- [Allgower 03] C. E. Allgower. *The STAR Endcap Electromagnetic Calorimeter.* Nucl. Instrum. & Meth. Phys. Res. A, vol. 449, no. 2–3, pages 740–750, 2003. Available from <http://tinyurl.com/337xk1c>.
- [Amsler 08] C. Amsler *et al.* *Particle Data Group.* Phys. Lett. B, vol. 667, page 1, 2008. Available from <http://tinyurl.com/2v56mwz>.

- [Anderson 03] M. Anderson. *The STAR time projection chamber: a unique tool for studying high multiplicity events at RHIC.* Nucl. Instrum. & Meth. Phys. Res. A, vol. 449, pages 659–678, 2003. Available from <http://tinyurl.com/39ect4r>.
- [Apostolakis 93] J. Apostolakis. Geant—detector description and simulation tool [Web-page]. 1993. Available from <http://tinyurl.com/yk1kg12> [Last cited on October 22, 2010].
- [Armesto 06] N. Armesto, M. Cacciari, A. Dainese, C. A. Salgado & U. A. Wiedemann. *How sensitive are high- p_T electron spectra at RHIC to heavy quark energy loss?* Phys. Lett. B, vol. 637, no. 6, pages 362–366, 2006. Available from <http://tinyurl.com/26fh6kw>.
- [Arnold 03] L. Arnold *et al.* *The STAR silicon strip detector (SSD).* Nucl. Instrum. & Meth. Phys. Res. A, vol. 449, no. 2–3, pages 652–658, 2003. Available from <http://tinyurl.com/2erek9c>.
- [Arsene 05] I. Arsene *et al.* *Quark-gluon plasma and color glass condensate at RHIC? The perspective from the BRAHMS experiment.* Nucl. Phys. A, vol. 757, no. 1–2, 2005. Available from <http://tinyurl.com/2bhuttc>.
- [Aurenche 05] P. Aurenche, O. Pene, F. Gulminelli, B. Moussallam, J.M. Le Goff, R. Granier De Cassagnac, C. Roy & P. Dupieux. *Ecole Joliot-Curie De Physique Nucléaire 2005—La QCD à l’œuvre: Des hadrons au plasma.* 2005. Available from <http://tinyurl.com/3ydu8n3>.
- [Back 03] B. B. Back *et al.* *The PHOBOS detector at RHIC.* Nucl. Instrum. & Meth. Phys. Res. A, vol. 499, pages 603–623, 2003. Available from <http://tinyurl.com/2wj53cp>.
- [Beddo 03] M. Beddo *et al.* *The STAR Barrel Electromagnetic Calorimeter.* Nucl. Instrum. & Meth. Phys. Res. A, vol. 449, no. 2–3, pages 725–739, 2003. Available from <http://tinyurl.com/2w7c8jz>.
- [Bellwied 03] R. Bellwied *et al.* *The STAR Silicon Vertex Tracker: A large area Silicon Drift Detector.* Nucl. Instrum. & Meth. Phys. Res. A, vol. 449, no. 2–3, pages 640–651, 2003. Available from <http://tinyurl.com/2c49ewp>.
- [Beole 00] S. Beole. *Latest results from NA50 on J/ψ suppression and multiplicity distributions in Pb-Pb collisions at 158GeV/c.* In Ricerca Scientifica ed Educazione Permanente Supplemento International Winter Meeting on Nuclear Physics 38, volume 116, pages 231–240c, Bormio Italie, 2000. NA50 LYCEN 2000–123. Available from <http://tinyurl.com/yzyqxrg>.

- [Bethke 03] S. Bethke. α_s 2002. Nucl. Phys. Proc. Suppl., vol. 121, pages 74–81, 2003. Available from <http://tinyurl.com/yajfxlo>.
- [Bichsel 06] H. Bichsel. *A method to improve tracking and particle identification in TPCs and silicon detectors*. Nucl. Instrum. & Meth. Phys. Res. A, no. 1, pages 154–197, 2006. Available from <http://tinyurl.com/35xqgmq>.
- [Bielcik 06] J. Bielcik. *Centrality dependence of heavy flavor production from single electron measurement*. Nucl. Phys. A, vol. 774, page 697, 2006. Available from <http://tinyurl.com/2bmcnu8>.
- [Bieser 03] F. S. Bieser. *The STAR trigger*. Nucl. Instrum. & Meth. Phys. Res. A, vol. 449, no. 2–3, pages 766–777, 2003. Available from <http://tinyurl.com/2cabt4u>.
- [Bjorken 82] J. D. Bjorken. *QCD and the Space-Time Evolution of High-Energy e^+ , e^- , p anti- p , and Heavy Ion Collisions*. 1982. Presented at 2nd Int. Conf. on Physics in Collisions: High Energy ee/ep/pp Interaction, Stockholm, Sweden, Jun 2–4.
- [Bjorken 83] J. D. Bjorken. *Highly relativistic nucleus-nucleus collisions: The central rapidity region*. Phys. Rev. D, vol. 27, no. 1, pages 140–151, 1983. Available from <http://tinyurl.com/28gas5t>.
- [Bland 99] L. C. Bland *et al.* *An Endcap Electromagnetic Calorimeter for STAR*. 1999. CDR-ST_AR Note 401. Available from <http://tinyurl.com/29wfw8w>.
- [Bland 05] L. C. Bland *et al.* *Future of low- x forward physics at RHIC*. Eur. Phys. Journ. C, vol. 43, page 427, 2005. Available from <http://tinyurl.com/y9aw8r3>.
- [Bonner 03] B. Bonner *et al.* *A single Time-of-Flight tray based on multigap resistive plate chambers for the STAR experiment at RHIC*. Nucl. Instrum. & Meth. Phys. Res. A, vol. 508, pages 181–184, 2003. Available from <http://tinyurl.com/2e8k2tn>.
- [Bonner 04] B. Bonner *et al.* *Proposal for a Large Area Time of Flight System for STAR*. 2004. Available from <http://tinyurl.com/2fm9kty>.
- [Bouchet 07] J. Bouchet. *Performances du détecteur en silicium à micropistes de l'expérience STAR à RHIC*. Ph.D. Thesis, SUBATECH, École des Mines de Nantes, 2007. Available from <http://tinyurl.com/yetlj2r>.

- [Bouchet 09] J. Bouchet & for the STAR Collaboration. *Heavy Flavor Tracker HFT: A new inner tracking device at STAR*. Nucl. Phys. A, vol. 830, page 636c, 2009. Available from <http://tinyurl.com/ycamwwc>.
- [Brun 06] R. Brun & F. Rademakers. ROOT TSpectrum Class [Webpage]. 2006. Available from <http://tinyurl.com/y8zkm8d> [Last cited on October 22, 2010].
- [Cacciari 05] M. Cacciari, P. Nason & R. Vogt. *QCD Predictions for Charm and Bottom Quark Production at RHIC*. Phys. Rev. Lett., vol. 95, no. 12, page 122001, 2005. Available from <http://tinyurl.com/3ahhx6>.
- [Choi 09] K. Choi. Gamma-conversion tomography of STAR Silicon detector in Cu+Cu Collisions [Webpage]. 2009. Available from <http://tinyurl.com/yzp8647> [Last cited on October 22, 2010].
- [Cottingham 01] W. N. Cottingham & D. A. Greenwood. An introduction to Nuclear Physics. Cambridge University Press, Cambridge, 2nd edition, 2001.
- [DePhillips 07] M. DePhillips. Run Log for STAR at RHIC [Webpage]. 2007. Low Multiplicity run: 8120057 for run VII: Au+Au at $\sqrt{s_{\text{NN}}} = 200 \text{ GeV}$. Available from <http://tinyurl.com/ye2vpzw> [Last cited on October 22, 2010].
- [Didenko 08] L. Didenko. Production Status Update for run 2007/2008 [Webpage]. 2008. Available from <http://tinyurl.com/yb361v2> [Last cited on October 22, 2010].
- [Didenko 10] L. Didenko, V. Perevoztchikov & J. Lauret. Star geometry in simulation and reconstruction [Webpage]. 2010. Available from <http://tinyurl.com/y8qppzz> [Last cited on October 22, 2010].
- [Djordjevic 05] M. Djordjevic, M. Gyulassy & S. Wicks. *Open Charm and Beauty at Ultrarelativistic Heavy Ion Colliders*. Phys. Rev. Lett., vol. 94, no. 11, page 112301, 2005. Available from <http://tinyurl.com/ycynvsq>.
- [Djordjevic 06] M. Djordjevic, M. Gyulassy, R. Vogt & S. Wicks. *Influence of bottom quark jet quenching on single electron tomography of Au+Au*. Phys. Lett. B, vol. 632, no. 1, pages 81–86, 2006. Available from <http://tinyurl.com/2czr232>.
- [Dokshitzer 01] Y. L. Dokshitzer & D. E. Kharzeev. *Heavy-quark colorimetry of QCD matter*. Phys. Lett. B, vol. 519, no. 3–4, page 199, 2001. Available from <http://tinyurl.com/2aoe7ho>.

- [Dunlop 05] J. Dunlop. Cu+Cu year 5 FAQ [Webpage]. 2005. Available from <http://tinyurl.com/ybx2ks> [Last cited on October 22, 2010].
- [Dunlop 06] J. Dunlop. 2006 p+p run (run 6) Trigger FAQ [Webpage]. 2006. Available from <http://tinyurl.com/ydhn6vg> [Last cited on October 22, 2010].
- [Dunlop 08a] J. Dunlop. BEMC triggers in STAR [Webpage]. 2008. Available from <http://tinyurl.com/yduevu3> [Last cited on October 22, 2010].
- [Dunlop 08b] J. Dunlop. Streams in 2008 [Webpage]. 2008. Available from <http://tinyurl.com/yf2shko> [Last cited on October 22, 2010].
- [Ferbel 87] T. Ferbel. Experimental techniques in high-energy nuclear and particle physics. Addison-Wesley Publishing Company, Singapore, 1st edition, 1987.
- [Fisyak 07] Y. V. Fisyak *et al.* *Overview of the Inner Silicon detector alignment procedure and techniques in the RHIC/STAR experiment*. Journal of Physics: Conference Series, vol. 119, 2007. International Conference on Computing in High Energy and Nuclear Physics. Available from <http://tinyurl.com/23mv6bn>.
- [Franz 06] A. Franz. *Five Years of Tracking Heavy Ion Collisions at RHIC*. Nucl. Instrum. & Meth. Phys. Res. A, vol. 566, pages 54–61, 2006. Available from <http://tinyurl.com/yksgtfu>.
- [Franz 08] A. Franz. *Highlights from PHENIX*. Quark Matter 2008, Jaipur, India, 2008. Available from <http://tinyurl.com/yhq4t94>.
- [Germain 02] M. Germain *et al.* *Radiation damages in double-sided silicon strip module*. Nucl. Instrum. & Meth. Phys. Res. A, vol. 485, no. 1–2, pages 121–125, 2002. Available from <http://tinyurl.com/y9bqc1b>.
- [Geromitsos 09] A. Geromitsos & for the STAR Collaboration. *Non Photonic e-D⁰ correlations in p+p and Au+Au collisions at $\sqrt{s_{\text{NN}}} = 200 \text{ GeV}$* . volume 1182, pages 787–790. AIP, 2009. Available from <http://tinyurl.com/yadvuy4>.
- [Glauber 59] R. J. Glauber. *High Energy Collision theory*. vol. 1, 1959.
- [Gyulassy 91] M. Gyulassy & M. Plumer. *Jet Quenching as a probe of dense matter*. Nucl. Phys. A, vol. 527, pages 641–644, 1991. Available from <http://tinyurl.com/28yf2x6>.

- [Gyulassy 05] M. Gyulassy & L. McLerran. *New forms of QCD matter discovered at RHIC*. Nucl. Phys. A, vol. 750, pages 30–63, 2005. Available from <http://tinyurl.com/yjwn8bs>.
- [Harrison 03] M. Harrison, T. Ludlam & S. Ozaki. *RHIC Project Overview*. Nucl. Instrum. & Meth. Phys. Res. A, vol. 449, no. 2-3, pages 235–244, 2003. Available from <http://tinyurl.com/26ulh4z>.
- [Iarocci 83] E. Iarocci. Nucl. Instrum. & Meth. Phys. Res., vol. 217, page 30, 1983. Available from <http://tinyurl.com/yko5yng>.
- [Jacobs 09] W. W. Jacobs. *STAR Calorimetry*. Journal of Physics: Conference Series, vol. 160, page 012008 (8pp), 2009. Available from <http://tinyurl.com/ycu64zj>.
- [James 06a] F. James. ROOT Minuit: physics analysis tool for function minimization [Webpage]. 2006. Available from <http://tinyurl.com/yzzxfy5> [Last cited on October 22, 2010].
- [James 06b] F. James. Statistical methods in experimental physics. World Scientific, Singapore, 2nd edition, 2006.
- [Judd 03] E. Judd. STAR Trigger Introduction [Webpage]. 2003. Available from <http://tinyurl.com/ye9nmh4> [Last cited on October 22, 2010].
- [Kurnadi 10] P. Kurnadi, 2010. Private Communication.
- [Leo 92] W. R. Leo. Techniques for Nuclear and Particle Physics Experiments. Springer-Verlag, 2nd edition, 1992.
- [Liko 92] D. Liko. *Track Fitting in the STAR Detector using the Kalman Filter Method*. 1992. STAR Note 87. Available from <http://tinyurl.com/y8h44db>.
- [Lin 95] Z. Lin & M. Gyulassy. *Open charm as a probe of preequilibrium dynamics in nuclear collisions*. Phys. Rev. C, vol. 51, no. 4, pages 2177–2187, 1995. Available from <http://tinyurl.com/2cumw4s>.
- [Lin 09] G. Lin. *Electro-magnetic Physics Studies at RHIC: Neutral Pion Production, Direct Photon HBT, Photon Elliptic Flow in Au+Au Collisions at $\sqrt{s_{\text{NN}}} = 200 \text{ GeV}$ and the Muon Telescope Detector Simulation*. Ph.D. Thesis, Yale University, 2009. Available from <http://tinyurl.com/yb79696>.

- [Lisa 96] M. Lisa. *The STAR-TPC Clusterfinder/Hitfinder*. 1996. STAR Note 238. Available from <http://tinyurl.com/y8jjstv>.
- [Martin 02] L. Martin. *SSD documentation-SSD Module*. 2002. Available from <http://tinyurl.com/ygztwy8>.
- [Matis 95] H. Matis. *STAR Geometry*. 1995. STAR Controlled Note 229A. Available from <http://tinyurl.com/ydtr3xh>.
- [Matsui 86] T. Matsui & H. Satz. *J/ψ suppression by quark-gluon plasma formation*. Phys. Lett. B, vol. 178, no. 4, pages 416–422, 1986. Available from <http://tinyurl.com/26htrc5>.
- [Mischke 07] A. Mischke. *Topological reconstruction of open charm mesons using electron tagging*. 2007. Available from <http://tinyurl.com/yc4o5cw>.
- [Mischke 09a] A. Mischke. *A new correlation method to identify and separate charm and bottom production processes at RHIC*. Phys. Lett. B, vol. 671, page 361, 2009. Available from <http://tinyurl.com/ydbbttoy>.
- [Mischke 09b] A. Mischke & for the STAR Collaboration. *Studying the relative bottom contribution via heavy-quark decay electron measurements in STAR*. Eur. Phys. Journ. C—Particles and Fields, vol. 61, pages 807–809, 2009. Available from <http://tinyurl.com/yfmkydv>.
- [Mohanty 09] B. Mohanty. Collaboration wide bad run list for Au+Au 200 GeV run 7 [Webpage]. 2009. PWG Convenors list. Available from <http://tinyurl.com/y9v13vb> [Last cited on October 22, 2010].
- [Morháč 97a] M. Morháč. *Background elimination methods for multidimensional coincidence gamma-ray spectra*. Nucl. Instrum. & Meth. Phys. Res. A, vol. 401, no. 1, pages 113–132, 1997. Available from <http://tinyurl.com/273hyoc>.
- [Morháč 97b] M. Morháč. *Efficient one—and two—dimensional Gold deconvolution and its application to gamma-ray spectra decomposition*. Nucl. Instrum. & Meth. Phys. Res. A, vol. 401, no. 1, pages 385–408, 1997. Available from <http://tinyurl.com/2e5wu5a>.
- [Musa 03] L. Musa *et al.* *The ALICE TPC Front End Electronics*. 2003. IEEE Nuclear Science Symposium. Available from <http://tinyurl.com/yhd86bf>.
- [Papoulis 02] A. Papoulis & U. Pillai. Probability, random variables, and stochastic processes with errata pages. McGraw-Hill, 4th revised edition, 2002.

- [Perevoztchikov 10] V. Perevoztchikov. Simulation | the STAR Experiment [Webpage]. 2010. Available from <http://tinyurl.com/yzmnhg4> [Last cited on October 22, 2010].
- [Potekhin 06] M. Potekhin. STAR simulation pages [Webpage]. 2006. Available from <http://tinyurl.com/ye6lmy4> [Last cited on October 22, 2010].
- [Pruneau 03] C. Pruneau. *Tracker for dummies—STAR Integrated Tracker*. pages 16–26, 2003. Integrated Tracker Task Force. Available from <http://tinyurl.com/yjy6fsy>.
- [Rafelski 82] J. Rafelski & B. Müller. Phys. Rev. Lett. B, vol. 48, page 1066, 1982.
- [Rajagopal 09] K. Rajagopal, 2009. Private Communication.
- [Reed 09] R. Reed *et al.* *Vertex finding in pile-up rich events for p + p and d + Au collisions at STAR*. 17th International Conference on Computing in High Energy and Nuclear Physics, Prague, Czech Republic, 2009. Available from <http://tinyurl.com/391o8s5>.
- [Ruan 08] L. Ruan & for the STAR Collaboration. *Prototype Performance of Novel Muon Telescope Detector at STAR*. 2008. Available from <http://tinyurl.com/ybzo3na>.
- [Rursus 10] User Rursus. Sagitta (geometry) [Webpage]. 2010. From Wikipedia, the free encyclopedia. Available from <http://tinyurl.com/3363ssn> [Last cited on October 22, 2010].
- [Sakuma 10] T. Sakuma [Webpage]. 2010. Available from <http://tinyurl.com/yco3t39> [Last cited on October 22, 2010].
- [Shuryak 78] E. V. Shuryak. *Quark-Gluon Plasma and Hadronic Production of Leptons, Photons and Psions*. Phys. Lett. B, vol. 78, no. 1, pages 150–153, 1978. Available from <http://tinyurl.com/2vx8g9x>.
- [Sjöstrand 10] Torbjörn Sjöstrand, S. Ask, R. Corke, S. Mrenna & P. Skands. *PYTHIA software package*, 2010. Available from <http://tinyurl.com/ycffqba>.
- [Suire 01] C. Suire. *Conception et réalisation de modules de détection pour le trajectographe interne de l'expérience STAR*. Ph.D. Thesis, Université Louis Pasteur, Strasbourg, juin 2001. Available from <http://tinyurl.com/ybjagwo>.
- [Surrow 07] B. Surrow *et al.* *FGT A Forward Tracking Upgrade Proposal for the STAR experiment*. 2007. Available from <http://tinyurl.com/yccrhyk>.

- [Timmings 06] A. Timmins. Centrality Study for P06ib Cu+Cu at $\sqrt{s_{\text{NN}}} = 200 \text{ GeV}$ events [Webpage]. 2006. Available from <http://tinyurl.com/y9gmm5f> [Last cited on October 22, 2010].
- [Timmings 09a] A. Timmins. *Overview of Strangeness Production at the STAR Experiment*. J. Phys. G, vol. 36, page 064006, 2009. Available from <http://tinyurl.com/ye44ow>.
- [Timmings 09b] A. Timmins. Year 7 Au+Au Centrality [Webpage]. 2009. Available from <http://tinyurl.com/yczhqks> [Last cited on October 22, 2010].
- [van Buren 06] G. van Buren *et al.* *STAR C++ Class Library*. pages 109–116, 2006. User Guide and Reference Manual Revision: 1.23. Available from <http://tinyurl.com/36sfcpo>.
- [van Buren 08] G. van Buren. *STAR EMC Calibration Workshop*, 2008. Available from <http://tinyurl.com/yapadpn>.
- [van Hess 06] H. van Hess, V. Greco & R. Rapp. *Heavy-quark probes of the quark-gluon plasma and interpretation of recent data taken at the BNL Relativistic Heavy Ion Collider*. Phys. Rev. C, vol. 73, no. 3, page 034913, 2006. Available from <http://tinyurl.com/26od6b4>.
- [Vogt 08] R. Vogt. *The total charm cross section*. Eur. Phys. Journ.—Special Topics, vol. 155, pages 213–222, 2008. Available from <http://tinyurl.com/3ajmm9d>.
- [Wicks 07] W. Wicks, W. Horowitz, M. Djordjevic & M. Gyulassy. *Elastic, inelastic, and path length fluctuations in jet tomography*. Nucl. Phys. A, vol. 784, pages 426–442, 2007. Available from <http://tinyurl.com/2u5hvxd>.
- [Xu 08a] Y. Xu *et al.* *Improving the dE/dx calibration of the STAR TPC for the high- p_T hadron identification*. 2008. Available from <http://tinyurl.com/ydjnbrs>.
- [Xu 08b] Z. Xu *et al.* *A Heavy Flavor Tracker for STAR*. 2008. Available from <http://tinyurl.com/y9nlccc>.
- [Zhang 03] H. Zhang. *$K^*(892)$ Resonance Production in Au+Au and $p+p$ Collisions at $\sqrt{s_{\text{NN}}} = 200 \text{ GeV}$ at the Relativistic Heavy Ion Collider*. Ph.D. Thesis, Yale University, 2003. Available from <http://tinyurl.com/2eghdp5>.



